



HAL
open science

Automated lung screening system of multiple pathological targets in multislice CT

Kuang Che Chang Chien

► **To cite this version:**

Kuang Che Chang Chien. Automated lung screening system of multiple pathological targets in multislice CT. Other. Institut National des Télécommunications, 2011. English. NNT : 2011TELE0021 . tel-01182693

HAL Id: tel-01182693

<https://theses.hal.science/tel-01182693>

Submitted on 2 Aug 2015

HAL is a multi-disciplinary open access archive for the deposit and dissemination of scientific research documents, whether they are published or not. The documents may come from teaching and research institutions in France or abroad, or from public or private research centers.

L'archive ouverte pluridisciplinaire **HAL**, est destinée au dépôt et à la diffusion de documents scientifiques de niveau recherche, publiés ou non, émanant des établissements d'enseignement et de recherche français ou étrangers, des laboratoires publics ou privés.



Ecole Doctorale EDITE

**Thèse présentée pour l'obtention du diplôme de
Docteur de Télécom & Management SudParis**

Doctorat conjoint Télécom & Management SudParis et Université Pierre et Marie Curie

Spécialité : *Informatique appliquée*

Par Kuang Che CHANG CHIEN

Automated Lung Screening System of Multiple Pathological Targets in Multislice CT

Soutenue le 30 septembre 2011 devant le jury composé de :

**Pr. Eric PETIT
Pr. Marc THIRIET
Pr. Philippe GRENIER
Pr. Pierre-Yves BRILLET
Dr. Catalin FETITA
Pr. Françoise PRETEUX**

Rapporteur
Rapporteur
Examineur
Examineur
Examineur, encadrant
Directeur de thèse

Thèse n° 2011TELE0021



Ecole Doctorale EDITE

**Thèse présentée pour l'obtention du diplôme de
Docteur de Télécom & Management SudParis**

**Doctorat conjoint Télécom & Management SudParis et Université Pierre
et Marie Curie**

**Automated Lung Screening System of Multiple
Pathological Targets in Multislice CT**

by Kuang-Che CHANG CHIEN

Ph. D Thesis

Prof. Eric PETIT

Reviewer

Prof. Marc THIRIET

Reviewer

Prof. Philippe GRENIER

Examiner

Prof. Pierre-Yves BRILLET

Examiner

Dr. Catalin FETITA

Thesis supervisor, Examiner

Prof. Françoise PRETEUX

Thesis director

Acknowledgement

Supported by a joint grant from Institute Français de Taipei (FIT) and National Science Council (NSC) in Taiwan, this thesis would not have been possible without the guidance and the support of many people who in one way or another contributed and extended their valuable assistance in the preparation and completion of this study. It is a pleasure to express my gratitude to them in my humble acknowledgement.

First and foremost, I would like to record my utmost gratitude to my supervisor, Dr. Catalin FETITA, Associate Professor with ARTEMIS Department of TELECOM SudParis, who had a crucial contribution to this research. With his patient supervision, precious guidance and unfailing support he provided from the beginning stage of this research, I could successfully achieve this study.

I gratefully acknowledge my thesis Director, Prof. Françoise PRETEUX, Head of ARTEMIS Department of TELECOM SudParis, and Prof. Ruey-Feng CHANG, Professor with CSIE Department of National Chung Cheng University, for their confidence and the opportunity they gave to me to enroll into this double degree PhD study which provided valuable research experience in a new cultural environment.

I would also like to thank Prof. Eric PETIT and Prof. Marc THIRIET for having accepted the difficult task of reviewing this manuscript, and Prof. Philippe GRENIER for his participation to the jury and his help in welcoming this thesis defense in his Radiology Department at Pitié Salpêtrière Hospital in Paris.

I heartily thank Prof. Pierre-Yves BRILLET, Radiologist with the Avicenne Hospital in Bobigny, who provided the experimental dataset and medical-related information in this research. With his guidance, I could acquire the knowledge concerning interstitial lung diseases, especially in disease characteristics on CT images, which allowed completing the CAD system in this research.

I would also like to express my gratitude to Evelyne TARONI and Why-in CHEN, Manager Assistants of ARTEMIS Department in TELECOM SudParis and Center of International Affairs and Exchange in National Chung Cheng University, respectively. They assisted me to handle the related official documents and applications of the school.

For the members of the ARTEMIS group, all of you were friendly and vivacious, and gave me so many pleasant memories, not only at the office but also during some festival parties and outdoor activities. I will keep these forever. Here, I would like to thank all of you and say that you are the best research group in my mind.

In addition, for my friends in Paris, I am really happy to know you in this

foreign city. Because of you, I could familiarize progressively the life in Paris and Europe, and could successfully solve typical expatriate difficulties. Especially to Song-Po SONG, Dian-Le Zhou, Xiao-Chen LAI, Jian HOU, Yu LU, Chen-Chen SUN, and so on, the friends at the beginning period in France, I only say thanks for the wonderful period in MAISEL that you brought to me.

My parents deserve special mention for their inseparable prayers and support. They always sincerely raised me with their caring and gently love. With each phone call at the weekend, I still could remain close to my family activities so that I did not feel lonely abroad.

Words fail me to express my gratitude to my dear Yu-Jia CHENG. With your support and persistent confidence, I could face to the pressure of the work and overcome the difficult moments during this 5-years period. I am fortunate to own you in my life, thank you for everything you did for me.

Finally, I would like to thank everyone who has a direct or indirect involvement in the successful accomplishment of this thesis, and express my apology to people that I can not mention personally in this acknowledgement.

TABLE OF CONTENTS

INTRODUCTION.....	9
Chapter I.....	11
Emphysema and Infiltrative Lung Diseases: anatomical description and investigation techniques	11
I.1 Emphysema and Idiopathic Interstitial Pneumonias.....	11
I.2.1 Emphysema.....	11
I.1.2 Idiopathic interstitial pneumonias	14
I.2 Clinical investigation techniques of lung pathologies	17
I.2.1 Pulmonary Function Tests	17
I.2.2 Multi-slice computed tomography (MSCT).....	18
Chapter II	27
Detection of lung disease with MDCT: State of the Art.....	27
II.1 Lung Region Segmentation	28
II.1.1 Optimal thresholding.....	28
II.1.2 Region growing	29
II.1.3 Edge tracking	30
II.2 Lung Parenchyma Analysis.....	30
II.2.1 Lung partitioning.....	31
II.2.2 Classification Approaches	34
II.3 Validation Approaches.....	45
II.4 Summary.....	47
Chapter III.....	51
Multi-resolution Approach for Characterization of Lung Diseases	51
III.1 Pre-processing.....	55
III.1.1 Anisotropic Diffusion Operator	55
III.1.2 Stick Operator	56
III.2 Lung field segmentation.....	58
III.2.1 Definitions	58
III.2.2 Segmentation of the lung mask with discrimination of large airways and high density structures	63
III.3 Multi-resolution Decomposition Scheme	67
III.3.1 Flood size-drain leveling	68
III.3.2 The Multi-resolution Decomposition Approach	71

III.4 Hierarchic Description.....	79
III.4.1 Definition.....	80
III.4.2 Hierarchic Tree Structure.....	81
III.5 Fuzzy Classification.....	85
III.5.1 Definition.....	86
III.5.2 Lung Disease Classification.....	88
III.6 Spatial lung partitioning.....	98
III.6.1 Box partitioning.....	98
III.6.2 Texture-based partitioning.....	104
III.7 Conclusion.....	106
Chapter IV.....	109
Clinical assessment.....	109
IV.1 Influence of the method parameter setup.....	109
IV.2 Influence of the CT acquisition protocol.....	113
IV.2.1 Impact of the reconstruction kernel.....	113
IV.2.2 Impact of the X-ray beam collimation.....	116
IV.3 Radiologist expert versus the CAD system.....	121
IV.4 Longitudinal follow-up studies.....	128
IV.5 Concluding remarks.....	137
Conclusion and Perspectives.....	151
Publications.....	155
References.....	157

List of Abbreviations

1-D	one-dimensional
2-D	two-dimensional
3-D	three-dimensional
A1A	Alpha-1 antitrypsin
A1AD	Alpha-1 antitrypsin deficiency
AMFM	adaptive multiple feature method
ANN	artificial neural network
AW	large airway
CAD	computer-aided diagnosis
CO ₂	carbon dioxide
COPD	chronic obstructive pulmonary disease
CT	computed tomography
DLCO	diffusion capacity
DPLD	diffuse parenchymal lung disease
EF	mixture of emphysema and fibrosis/honeycombing
EM	emphysema
FEF	forced expiratory flow
FEV ₁	forced expiratory volume in 1 second
FHC	fibrosis/honeycombing
FN	false negative
FOV	field of view
FP	false positive
FSD	flood size-drain leveling
FVC	forced vital capacity
GDG	ground glass
GL	gray-level value
HD	high density
HU	Hounsfield unit
IIP	idiopathic interstitial pneumonia
ILD	interstitial lung disease
IPF	idiopathic pulmonary fibrosis
LD	low density
MD	medium density
MEM	mild emphysema

MF	mild fibrosis/honeycombing
MRI	magnetic resonance imaging
MSCT	multi-slice computed tomography
MVV	maximal voluntary ventilation
N	normal pulmonary tissue
NPV	negative predictive value
PEFR	peak expiratory flow rate
PFT	pulmonary function test
PPV	positive predictive value
ROC	receiver operating characteristic
ROI	region of interest
SE	structuring element
SFD	stochastic fractal dimension
SVM	support vector machine
TLC	total lung capacity
TN	true negative
TP	true positive
TSK	Takagi-Sugeno-Kang
TV	tidal volume
VOI	volume of interest

INTRODUCTION

This research focuses on the study of a specific category of non-neoplastic lung pathologies including emphysema and interstitial lung diseases (ILDs), and especially on **idiopathic interstitial pneumonias (IIPs)** [1] – a variety of ILDs, and aims at developing a computer-aided diagnosis system of these pathologies exploiting the computed tomography imaging technology.

The motivation of such a research comes from the increasing healthcare burden associated with this category of chronic diseases (most of them being considered until few years ago as “orphan” diseases, i.e. with a prevalence less than 0.2% over population, and thus receiving small research funding¹) and from an unmet clinical need of efficient diagnosis and follow-up tools. In United States, 3.7 million people have been diagnosed with emphysema, of which 16700 deaths registered, whereas other studies reported that 80.9 per 100000 men and 67.2 per 100000 women suffer from ILDs with 31.5 and 26.1 new cases diagnosed per 100000 persons per year, respectively.

It is important to note that emphysema and IIPs are irreversible diseases that can be slowed but not stopped, and to date, no efficient treatment is available for most of IIPs. Such diseases affect the tissue and space within and around the alveoli (air sacs) and sometimes also the airways, the blood vessels and the pleura, leading to profound impairment in lung physiology. Unfortunately, if the initiated injury or abnormal repair from injury is not halted, progressive tissue damage can lead to worsening physiologic impairment and even death. In this context, early diagnosis and follow-up of these pathologies are the key issues for increasing the quality of life and the survival chances of the patient. If the suspicion of lung disease can be clinically confirmed or rejected by performing pulmonary function tests and chest radiography, to date only the computed tomography (CT) investigation allows an accurate diagnosis of the type of pathology (IIPs including more than 200 different disease entities). In addition, the visual feed-back provided by CT is very valuable due to the high spatial resolution of this imaging technique which allows accurately depiction and spatial localization of the disease patterns.

However, if CT allows diagnosing these pathologies, a quantitative analysis is needed in order to monitor the disease progression over time (longitudinal follow-up) or the response to a therapy. Such a quantitative investigation can only be ensured by computer-aided diagnosis (CAD) systems [2-10] exploiting the CT image data. It is well known [11-14] that the CAD systems not only avoid diagnosis failure due to human factors such as fatigue or oversight because of hundreds of images to screen, but they offer the radiologist a reference

¹ According to European Lung Foundation, <http://www.european-lung-foundation.org/>

opinion in the initial diagnosis stage or as a second reader to increase the accuracy and the confidence in the diagnostic. But the major advantage of the CAD systems over the radiologists is their quantification ability mandatory in follow-up studies, which cannot be provided by the clinicians using interactive delineation tools because of the task complexity related to the type of the pathology and the unavoidable inter- and intra-user variability of the measurement result.

Although several teams in the medical research and image processing (CAD developers) have studied the problem and proposed several solutions, the issue of an accurate and robust CAD system targeting IIPs and emphysema remains open. Our research is placed in this context and the solution we proposed is presented in the next chapters of this manuscript. In order to thoroughly capture the characteristics of the diseases we studied and their translation in terms of image analysis, Chapter I introduces the main aspects of the physiology of emphysema and targeted IIPs from both anatomical point of view and the investigation techniques used. Then, Chapter II analyses the state-of-the-art in the field of the CAD system development for lung pathology assessment with CT, and orients the research towards the proposed solution. Chapter III presents in detail the developed innovative 3D automated approach for emphysema and IIPs detection and quantification, based on 3D morphological segmentation and graph-description fuzzy reasoning. The performances of the proposed solution according to the parameter selection are discussed in Chapter IV and the results presented for a clinical cohort. The manuscript ends with a global conclusion and opens several perspectives of this work.

Chapter I

Emphysema and Infiltrative Lung Diseases: anatomical description and investigation techniques

This chapter introduces the anatomical characteristics of the lung pathologies we are interested in throughout this work and the clinical investigation techniques currently employed for their detection and analysis. Among them, CT imaging technique became the reference modality in lung investigation, due to its ability to depict the anatomo-pathological regions of the lung parenchyma. The chapter starts with a description of emphysema and the infiltrative diseases (Section I.1) followed by a presentation of the clinical investigation techniques (Section I.2), the pulmonary function tests (Section I.2.1) and the multi-slice computed tomography (MSCT) imaging technique (Section I.2.2) where image appearance of the normal and pathological tissues is discussed with respect to the parameters of the acquisition protocol.

I.1 Emphysema and Idiopathic Interstitial Pneumonias

Emphysema and interstitial lung diseases (IIPs) are both the lung diseases caused by destruction of the alveoli in the lungs. In people with such diseases, the lung tissue involved in exchange of gases is impaired. In this section, emphysema and targeted IIPs are described in detail, with discussion on their causes, symptoms, and types.

I.2.1 Emphysema

Emphysema is a type of chronic obstructive pulmonary disease (COPD) [15-18] linked to cigarette smoking, that causes a permanent enlargement of the airways in lungs, accompanied by destruction of the walls of the alveoli, the tiny air sacs in the lungs, where performs the crucial task of replenishing the blood with oxygen via inhalation and ridding the body of carbon dioxide (CO₂) via exhalation [19].

The first sign of a person with emphysema is shortness of breath, even taking a rest. As emphysema progresses, the following symptoms occur:

- Difficulty of breathing,
- Coughing with or without sputum,
- Wheezing,
- Excess mucus production,
- A bluish tint to the skin.

Moreover, emphysema may affect the brain. Low oxygen levels in the blood may mean that the brain is not getting enough oxygen. The end result can be grumpiness, irritability, and impaired mental ability. Also, high CO₂ levels in the blood leads to headaches and sleeplessness. All the symptoms of emphysema are caused by decrease of the lung elasticity. This prevents the alveoli from deflating completely, and the person has difficulty in exhaling. Hence, the next breath is started with a smaller capacity of the lungs while the trapped “old” air take up space of the lungs. So, the alveoli are unable to fill with enough fresh air to supply the body with needed oxygen.

The underlying cause of emphysema is believed to be an unbalance in the activities of proteolytic and antiproteolytic enzymes in lung tissue [20, 21]. Emphysema is produced as a result of the enzymatic destruction of lung elastin and collagen by neutrophil and microphage elastases. The primary cause of this imbalance of proteolytic and antiproteolytic enzymes is cigarette smoking. Cigarette smoking has been shown to produce an increase in the number of neutrophils in lung tissue and to stimulate the release of neutrophil elastase. It inhibits α_1 -antitrypsin (A1A) and interferes with the repair of damaged elastin and collagen. Note that only 10% to 15% of smokers develop emphysema. Exposure to the polluted and industrialized environments is also a recognized cause of emphysema, even in nonsmoker. It is believed that cigarette smoking has a longer clearance time from the upper lobes of the lungs, and this accounts for the increased incidence of emphysema in the upper lobes in smokers [22].

Alpha-1 antitrypsin deficiency (A1AD) was first discovered as another cause of emphysema in 1963 [20]. A1AD is actually a primary liver disease where the A1A enzyme can not get out of the hepatocyte because of a point mutation that induces polymerization of the enzyme within the hepatocyte. This leads to a deficiency of the enzyme in plasma and it is unavailable in sufficient quantities to inactivate the neutrophil elastase in the lungs. The abundance of activated neutrophil elastase leads to destruction of alveolar walls and a typical lower lobe panacinar emphysema in patients with A1AD. Cigarette smoking increases the risk of developing emphysema in patients with reduced serum levels of A1A enzyme. The lower lobe distribution of emphysema is thought to be caused by the increased amount of blood flow and resultant increase in neutrophil activity in the lower lobes. The macrophages are concentrated in the centriacinar portion of the lung, in the area of the respiratory bronchiole, which is the area where cigarette smoking-induced emphysema begins. The macrophage and neutrophil are likely both important in the development of emphysema.

Generally, emphysema can be classified as three anatomic types, namely centriacinar, panacinar, and distal acinar, based on the portion of the pulmonary acinus that is involved, and the three types are briefly described in the following.

— The **Centriacinar emphysema** involves the proximal portion of the acinus in the area of the respiratory bronchiole [18]. It affects the upper lobes of the lungs. These get enlarged and dilated, and thereby causing an obstruction for the air to pass while entering and leaving the lungs, and causing a discomfort while breathing. Centriacinar emphysema is more commonly found among cigarette smoker and coal miners.

Fig. 1 is a diagram of the lungs with centriacinar emphysema. The appearance of centriacinar emphysema is low attenuation holes like “moth-eaten” regions, and without obvious walls with centriacinar artery identified in holes.

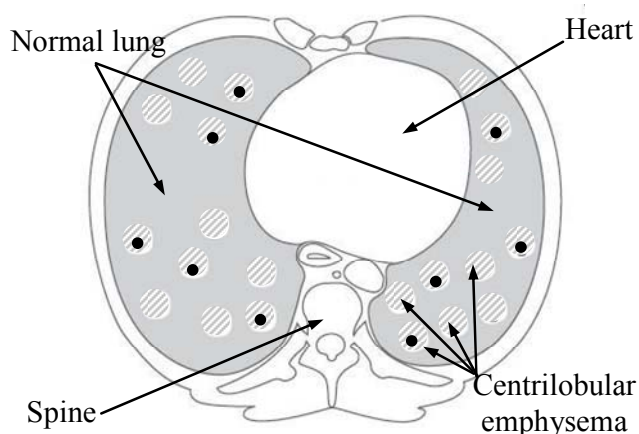


Fig. 1 A diagram of centriacinar emphysema.

— The **Panacinar emphysema** involves the pulmonary acinus in a diffuse and uniform way [18]. It mainly affects the lower lobes of the lungs, and may accompany the centriacinar emphysema in cigarette smokers. This type of emphysema is the most widespread destructive type with the greatest physiologic progressive destruction because the entire acini are affected, and it is caused primarily by the A1AD. Panacinar emphysema is less common, and may be found in people who never smoked in their lives.

Fig. 2 is a diagram of the lungs with panacinar emphysema. The appearance of panacinar emphysema is a large area of low attenuation associated with deranged tissue surrounding blood vessels, and obvious walls are around the area.

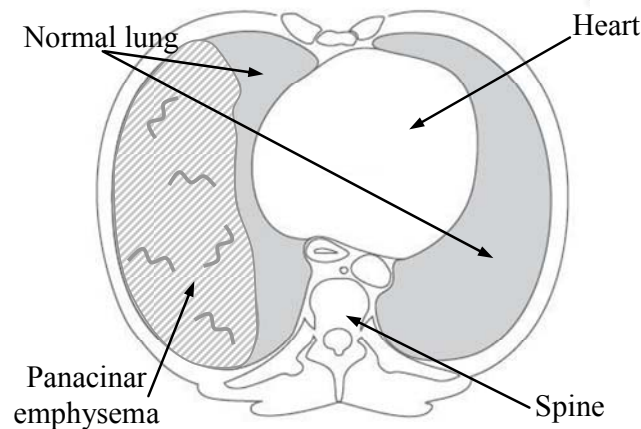


Fig. 2 A diagram of panacinar emphysema.

- The **Distal acinar emphysema** involves primarily the alveolar ducts and sacs, and does not affect the area of the respiratory bronchiole as does centriacinar emphysema [18]. It is often associated with extensive bulla formation with only mild decreases in airflow and also is associated with spontaneous pneumothorax in young adults.

Fig. 3 is a diagram of the lungs with distal acinar emphysema. The appearance of distal acinar emphysema is low attenuation holes with obvious walls like “saw-toothed” regions.

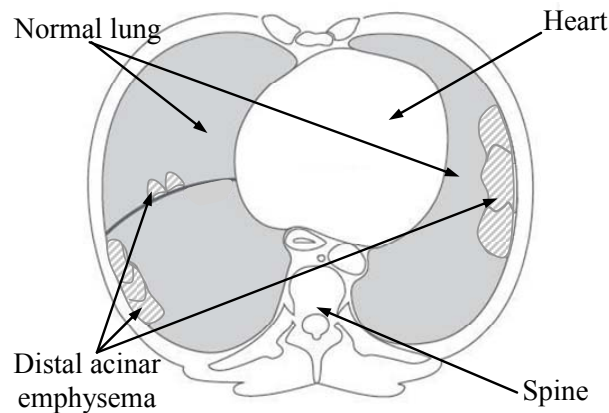


Fig. 3 A diagram of distal acinar emphysema.

The major physiological effect in emphysema is an increase in lung volumes and a decrease in elastic recoil of parenchyma. These result in decreased maximum expiratory airflow, hyperinflation, and air-trapping, which can be evaluated by pulmonary function tests (PFTs).

I.1.2 Idiopathic interstitial pneumonias

The IIPs (also called interstitial lung diseases) [1] are a group of diffuse parenchymal

lung diseases (DPLDs) referring to the inflammation of the interstitium of the lungs. The interstitium is the tissue that surrounds and separates the tiny air sacs (alveoli) of the lung parenchyma. Note that IIPs involves the inflammation of the tissue between air sacs rather than inflammation in the air sacs. The IIPs gradually develop and cause two conditions, interstitial inflammation and accretion. Interstitial inflammation is typically a diffuse process that occurs all over the lungs and is not confined locally, and results in edema and fibrosis formation. Accretion is organization of exudate within the alveolar space, which is converted to fibrous connective tissue and is incorporated into the interstitium. Three pathologies of the IIPs, namely idiopathic pulmonary fibrosis, honeycombing, and ground-glass opacity, are resulted by such conditions, and are briefly described as follows, respectively.

- **Idiopathic pulmonary fibrosis** (IPF) [23] is a chronic disease resulting in swelling and scarring of the interstitium of the lungs. The most frequent causes of pulmonary fibrosis are related to occupational diseases. People working with asbestos, ground stone or metal dust, inhale the small particles of these materials. Such materials damage the alveoli in the lung and cause fibrosis. Also, certain strong medicines, such as nitiofurantoin, amiodarone, and bleomycin, may have the undesirable side effect of causing pulmonary fibrosis. In some people, however, the pulmonary fibrosis develops without identifiable cause. The fibrosis with this situation is called idiopathic pulmonary fibrosis. Generally, the pulmonary fibrosis usually affects people between the ages of 40 and 70, and men and women are equally affected. The prognosis for patients with this disease is poor, and the survival time usually expected to an average of only 4 to 6 years after diagnosis.
- **Honeycombing** is one of the characteristic appearances of pulmonary fibrosis in the end-stage, and is extensive pulmonary fibrosis with alveolar destruction resulting in a loss of alveolar walls. Bronchiolectasis in patients with honeycombing results at least partially from traction on the bronchiolar walls by surrounding fibrosis tissue. As the pulmonary fibrosis progresses, honeycombing becomes more prominent. Honeycombing is most commonly caused by the IPF, the collagen vascular disease, hypersensitivity pneumonitis in the end-stage, or asbestosis. In the cases of drug-related fibrosis and hypersensitivity pneumonitis, the appearance of honeycombing have an atypical distribution, and the focal area is similar to cicatrizing emphysema.
- **Ground-glass opacity** is a nonspecific term referring to the appearance of hazy lung opacity, and is obvious in vision because of the presence of the thickening alveolar interstitium, or the presence of the fluid partially filling the alveolar spaces. In histology, ground-glass opacity has been seen in patients with the findings of mild or early interstitial inflammation or infiltration, and should be considered as consistent with active

inflammation only when there are no superimposed findings of fibrosis such as reticulation, architectural distortion, or traction bronchiectasis. The causes of ground-glass opacity include honeycombing cysts filled with secretions, superimposed diffuse alveolar damage, and a superimposed complication such as an infection and drug reaction.

Each pathological target mentioned above results in a lung tissue becoming stiff and thick, and then breathing efficiency would be reduced, leading to the reduction of oxygen levels in the blood. Therefore, the most common symptoms of the IIP are shortness of breath, persistent dry cough, fatigue, loss of weight, and discomfort in chest.

According to the classification of [24], the appearance of the pulmonary disease is categorized into three types. In the peripheral type, as shown in Fig. 4 (a), parenchyma opacification appears in the inner peripheral zone adjacent to pre-existing honeycombing. In the multifocal type, as shown in Fig. 4 (b), parenchyma opacification appears in central and peripheral regions. Sometimes, it is not adjacent to honeycombing if it appears around bronchial or vascular branches. The diffuse type has generalized pulmonary involvement but regional inhomogeneity, in Fig. 4 (c).

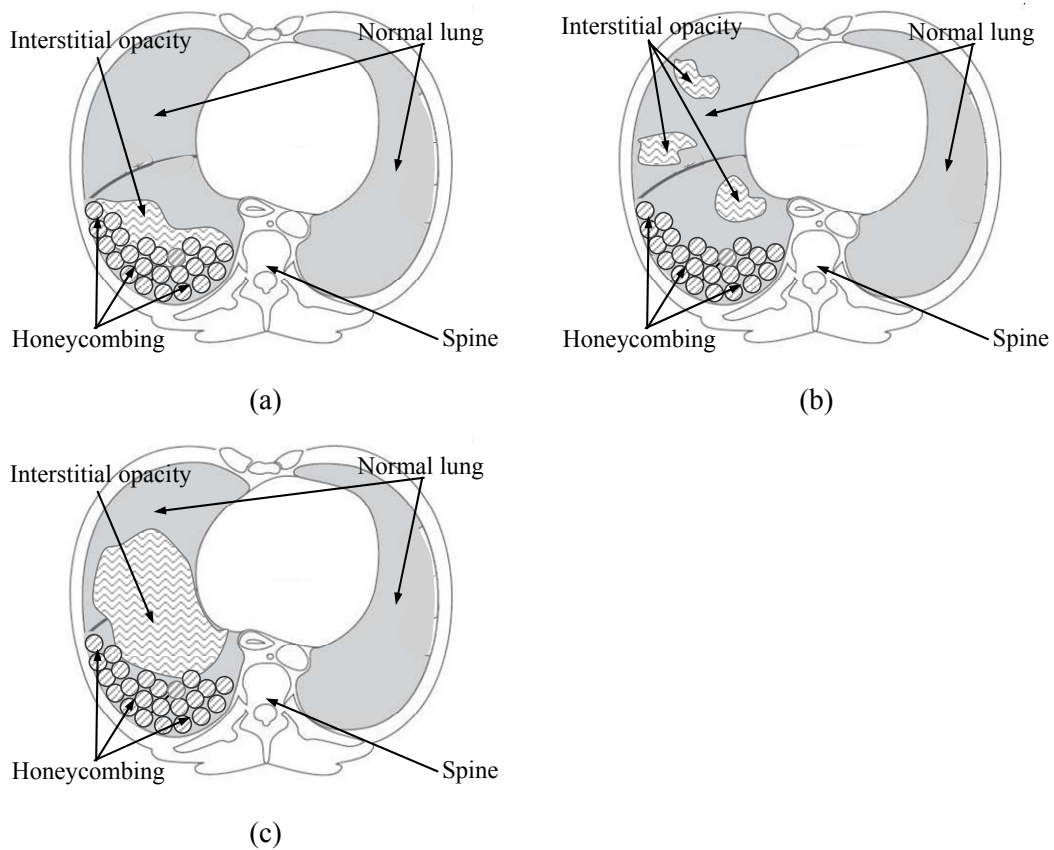


Fig. 4 A diagram of the pulmonary fibrosis with (a) peripheral, (b) multifocal, and (c) diffuse parenchyma opacification.

I.2 Clinical investigation techniques of lung pathologies

In clinical routine, lung dysfunction or the presence of pulmonary diseases is generally assessed by means of two major approaches. The first one consists of acquiring global measurements of the lung function by monitoring the airflow during inspiration and expiration – the pulmonary function tests. The second one is based on an imaging technique providing visual local information of the lung morphology – the computed tomography (CT). These approaches are briefly discussed in the next sections with a focus on the CT which is the investigation modality exploited by the computer-aided diagnosis systems in general.

I.2.1 Pulmonary Function Tests

The pulmonary function test (PFT) is a major step for assessing the functional status of the lungs. The measurement of PFT is based on several conditions stated as follows:

- The inspiration and expiration capacities of the lungs,
- The velocity of the air moving in and out of the lungs,
- The elasticity of the lungs and chest wall,
- The diffusion characteristics of the membrane through which the gas moves,
- The evaluation for the lungs responding to chest physical therapy procedures.

PTFs is a generic term used to indicate a series of maneuvers that are performed using standardized equipment to measure lung function. Generally, PFTs includes spirometry, lung volume measurement, and diffusion capacity for carbon monoxide. During spirometry, the examinee takes a deep breath in and then blow out as hard and as fast as he/she can into a tube connected to a machine called spirometer. The spirometer and lung volume assessment measure how fast and how much air the examinee can blow out from his/her lungs by several function tests defined in the following:

- **Forced vital capacity (FVC)** is the volume of air which can be forcibly and maximally expired out of the lungs until no more can be expired after the examinee has taken in the deepest possible breath.
- **Forced expiratory volume in 1 second (FEV1)** is the volume of air which can be forcibly expired from the lungs in the first second of a forced expiration.
- **FEV1 percent (FEV1/FVC)** is the ratio of FEV1 to FVC. It indicates what percentage of the total FVC is expelled from the lungs during the first second of a forced expiration.
- **Peak expiratory flow rate (PEFR)** is maximum flow rate achieved by the patient during the FVC beginning after full deep inspiration and starting and ending with maximal expiration.
- **Forced expiratory flow (FEF)** is a flow rate to measure how much air can be expired from the lungs. The FVC expiratory curve is divided into quartiles and therefore there is a FEF that exists for each quartile. The quartiles are expressed as FEF25%, FEF50%, and FEF75% of FVC.

- **Tidal volume** (TV) is the specific volume of air inspired into the lungs, and then expired out during normal tidal breathing.
- **Total lung capacity** (TLC) is the maximum volume that the lung can be expanded with the greatest possible inspiration effort.
- **Diffusion capacity** (DLCO) is the rate of carbon monoxide uptake from a single inspiration in a standard time. In principle, the total diffusing capacity of the whole lung is the sum of the diffusing capacity of the pulmonary membrane component and the capacity of the pulmonary capillary blood volume [25].
- **Maximal voluntary ventilation** (MVV) is determined by having the patient breath in and out as rapidly and fully as possible for 12 - 15 seconds. This test parameter reflects the status of the respiratory muscles, compliance of the thorax-lung complex, and airway resistance. A poor performance on this test suggests that the patient may have pulmonary problems postoperatively due to muscle weakness. MVV can therefore be viewed as a measure of respiratory muscle strength.

Sometimes, additional pulmonary function test is performed. Arterial blood gases test is used to measure amounts of oxygenation and CO₂ by analyzing blood from an artery. This test is often used in more advanced stages of emphysema to help determine if a person needs supplemental oxygen.

I.2.2 Multi-slice computed tomography (MSCT)

Among the medical imaging techniques today available, computed tomography (CT) has imposed itself as the reference imaging modality for the lung morpho-pathological assessment due to its high spatial resolution and the ability to depict air-filled regions for which other imaging modalities such as magnetic resonance imaging or echography fail. In the sequel, we shall briefly present the principle of the CT without insisting on the theoretical aspects, but instead focusing on the acquisition parameters and their influence on the image appearance and quality.

The CT imaging was invented and introduced into clinical practice by Godfrey Hounsfield (British engineer at the Central Research Laboratories of EMI, England) and Allan Mc Cormack (South Africa-born physicist at Tufts University, Massachusetts) in 1972. The CT imaging produces high quality data of the inside of the body in cross sectional views by exploiting the principle of image reconstruction from projections [26] . The projections are obtained as the attenuation profiles of an X-ray beam traversing the body and recorded by a detector for a multitude of directions (theoretically an infinite number of projections), generally along a cross-section plane, in Fig. 5. The reconstructed radiographic image thus produces a cross-sectional view of the body which depicts the local X-ray attenuation coefficients of the tissue. These attenuation coefficients, proportional with the physical density of the tissue, are expressed as a relative variation with respect to the water attenuation

coefficient, leading to a measure unit in CT called the Hounsfield unit, HU:

$$1HU = \frac{\mu - \mu_w}{\mu_w} \times 1000 \quad (1.1)$$

where μ denotes the X-ray attenuation coefficient of a tissue and μ_w the water attenuation coefficient.

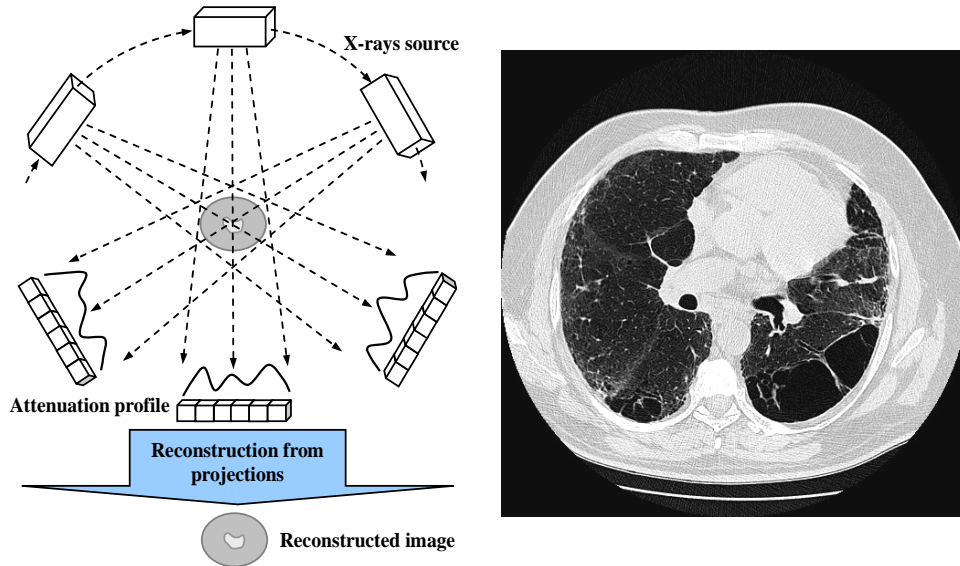


Fig. 5 Principle of the CT imaging technique and an example of a lung cross-section reconstructed image (emphysema case).

Major advances were obtained in 1998 with the introduction of the multi-slice CT acquisition technique and half-second rotation times of the couple X-ray source – detector. Continuing technical developments have resulted in a reduction of the rotation time to 0.4 seconds and the increase in the number of simultaneously acquired slices to 16 in 2003 and up to 64 and 128 nowadays. MSCT [27-34] with sub-second rotation times allows for shorter scan times, a reduction in motion artifacts, and the scanning of longer body ranges. A series of adjacent cross sections in MSCT is easily obtained during so-called volumetric acquisitions, and provide real 3-D information for medical analysis.

According to the type of the X-ray beam and the arrangement of the detectors, the CT scanners are divided into four generations. In the first generation scanner, as shown in Fig. 6 (a), a pencil X-ray beam is produced from a source, and a detector is used to receive the signal. In each projection, the X-ray source and the detector move along a straight line and change the directions with 1° angle. In the second generation scanner, as shown in Fig. 6 (b), a fan beam is produced instead of the pencil beam, and the total scanning time is reduced due to the multiple detectors. In Fig. 6 (c), the third generation scanner uses a sharply increased number of detectors arranged in a curve. The X-ray source and detectors rotate through 360° .

The fourth generation scanner, Fig. 6 (d), uses a complete ring of detectors to surround the patient.

In the MSCT scanner system, the X-ray source also produces a fan beam. The MSCT scanner uses multiple detector arrays instead of a single detector array (third generation scanner) to record the X-rays through the section of the examined body at one angular position of the source. The X-ray attenuation profiles from many different angles of the source are collected to reconstruct several cross sectional slices during one complete rotation. The MSCT scanner principle is illustrated in Fig. 7.

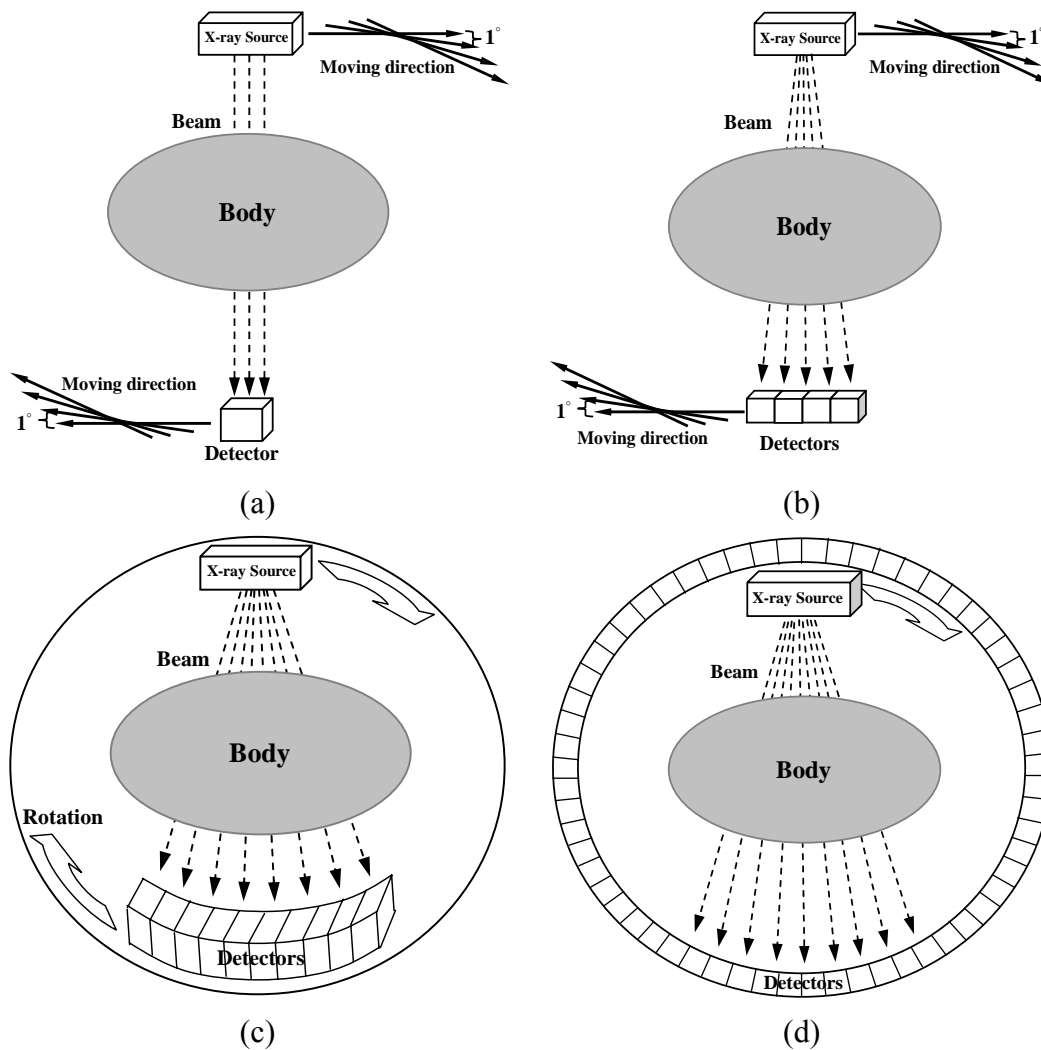


Fig. 6 The four generation scanners: (a) the first generation, (b) the second generation, (c) the third generation, and (d) the fourth generation.

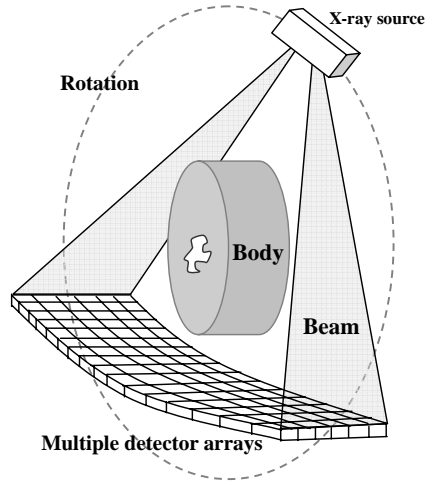


Fig. 7 Principle of the multi-slice CT scanner.

Several parameters of the acquisition protocol in MSCT influence the image quality and the spatial resolution, and thus need to be discussed and taken into account in our study.

- The X-ray **beam collimation** is responsible of the partial volume effect. An increase in beam collimation has as consequence a decrease in spatial resolution and also in the noise level, Fig. 8.

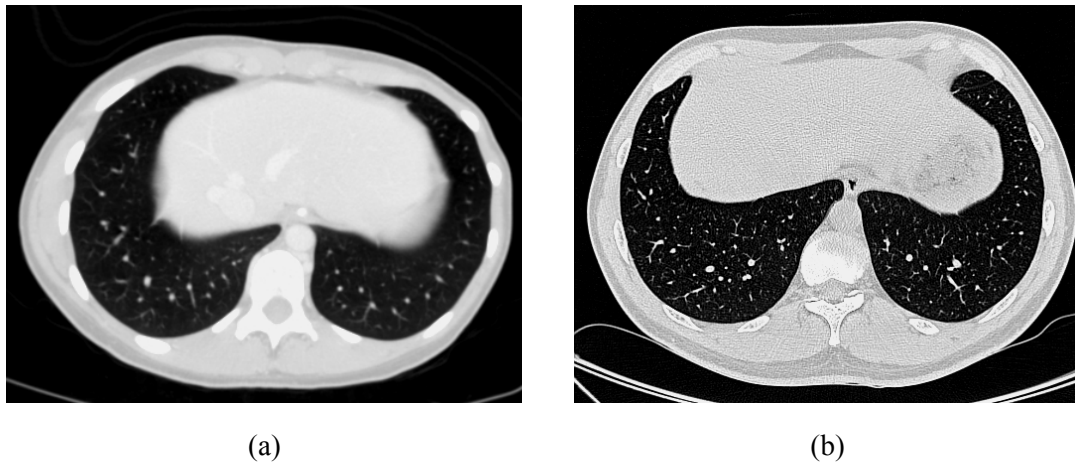


Fig. 8 Effect of the X-ray beam collimation on the reconstructed image: (a) 2 mm collimation, (b) 0.6 mm collimation.

- The image **reconstruction kernel** or the frequency filter used in the filter backprojection approaches influences the level of details captured by the image and the noise level, irrespective to the X-ray beam collimation. The kernel setting can be changed offline at will, and do not require additional patient exposure. Fig. 9 shows a reconstruction example using a “SOFT” (low frequency) and a “HARD” (high frequency) kernel.

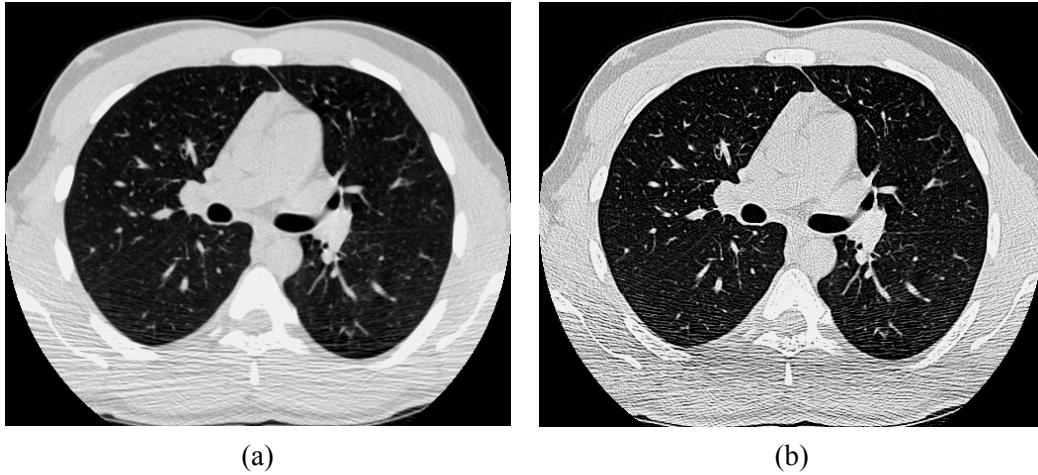


Fig. 9 Influence of the reconstruction kernel on the CT image: (a) “SOFT” kernel, (b) “HARD” kernel.

- The image **reconstruction matrix** (image size) and the selected **field of view** impact on the image axial resolution. Typical matrix size is 512x512 pixels but larger matrices are also available on current CT scanners – 768x768 pixels and 1024x1024 pixels. For a given matrix size, a reduced field of view can focus on a region of the body and provides a higher axial resolution (smaller pixel size), Fig. 10. However, in our study, the field of view has to capture both lungs for the whole body volume, Fig. 11 , which prevents us from exploiting this parameter for increasing the axial resolution.

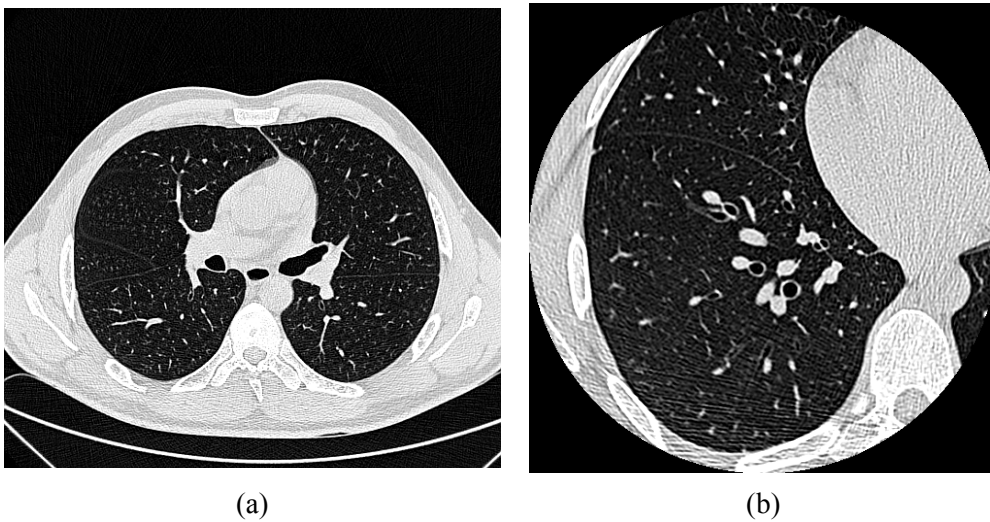


Fig. 10 Axial resolution with respect to the field of view (FOV) for the same reconstruction matrix: (a) FOV capturing both lungs – 0.77 mm/pixel resolution, (b) FOV focused on the right lung – 0.35 mm/pixel resolution.

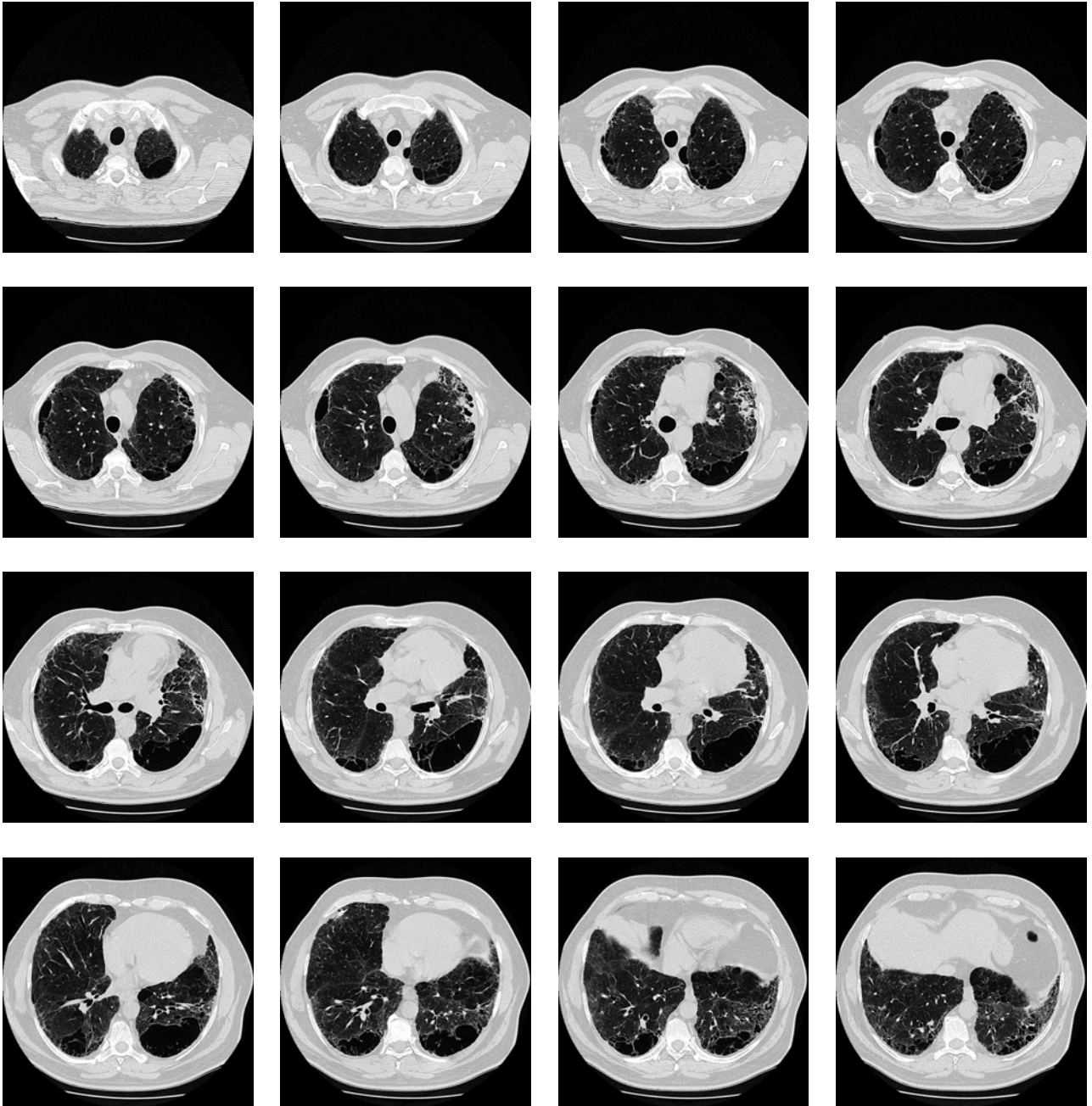


Fig. 11 Sixteen MSCT axial images equally spaced in the longitudinal direction throughout the lung and showing the variability in the lung cross-section size, imposing a large FOV for the CT acquisition. Note that this subject is with emphysema and pulmonary fibrosis.

- The **longitudinal sampling interval** for axial image reconstruction impacts on the image resolution in the z -direction (cranio-caudal direction). It should be set-up with respect to the beam collimation by fulfilling the Nyquist criterion, namely providing at least two axial images per collimation width (note that generally, overlapped reconstructions are accepted in clinical routine). Moreover, ideally, the sampling step should be set-up

according to the axial pixel dimension in order to obtain isotropic volume data. Unfortunately, in clinical practice there is a large variability concerning this setting.

- The **radiation dose** affects the signal-to-noise ratio in the image. It is measured as the product between the X-ray tube current and the exposure time and expressed in mAs units. Higher doses ensure better image quality (Fig. 12) but they are generally in conflict with clinical recommendations which stipulate low doses, especially for the patients having a longitudinal follow-up (repeated CT examinations over time). Such parameter setting is a compromise between image quality and accepted patient dose, and depends on the patient body weight. Consequently, a CAD analysis software should be able to overcome the variability imposed by such parameter.

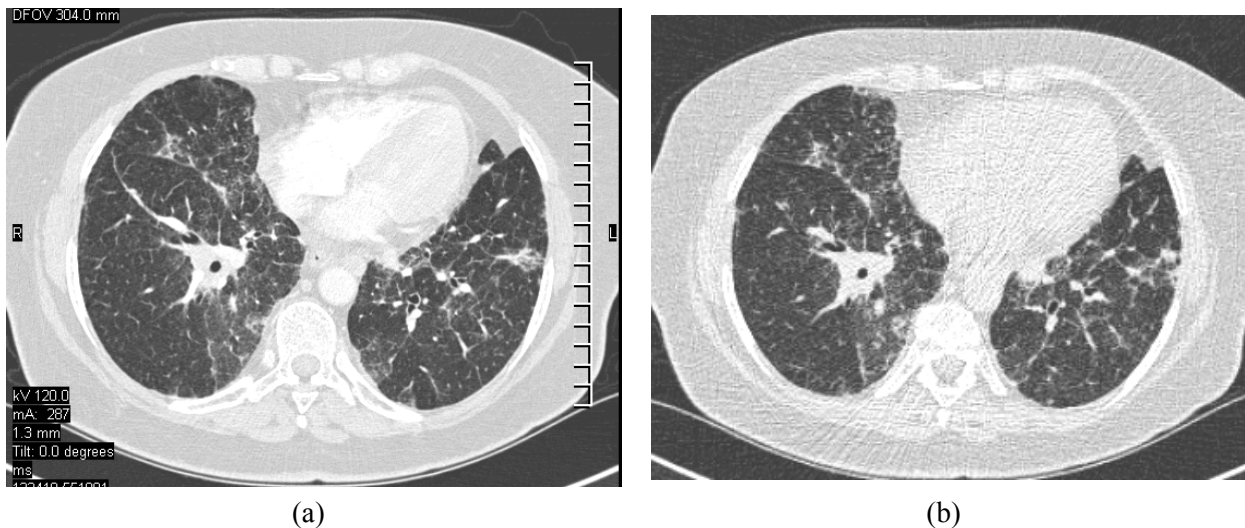
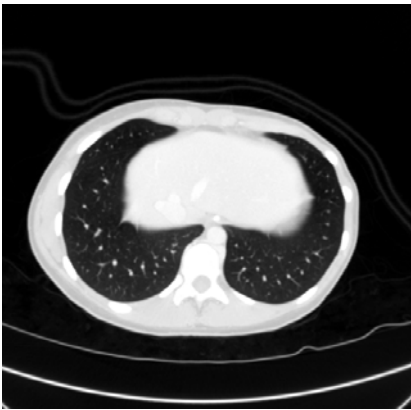
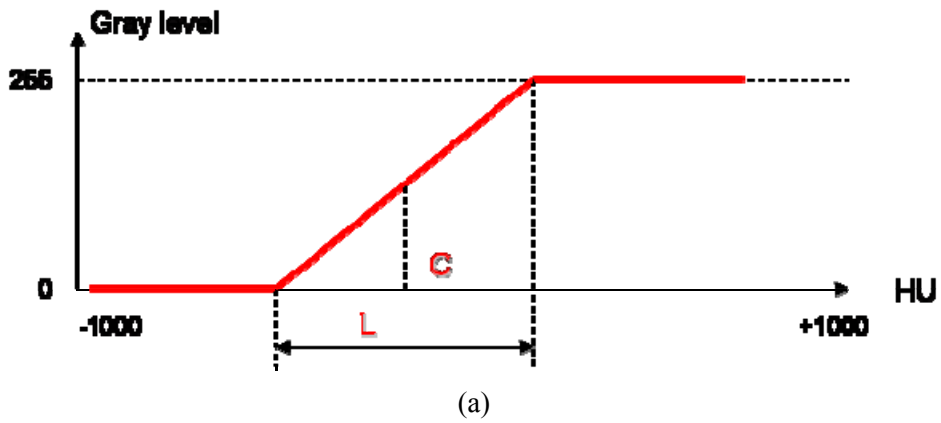


Fig. 12 Influence of the radiation dose on the image quality: (a) normal dose, 287 mAs, (b) low dose, 57 mAs. Courtesy of Dr. Catherine Beigelman-Aubry, Pitié-Salpêtrière Hospital, Paris.

- The **display window setting** provides the tissue density range that is visualized on the computer display with a compressed dynamics of 256 gray level values out of 2000 HU values, as illustrated in Fig. 13. Such display window setting can also be used by the CAD system in processing the CT data, due to the memory size reduction.

To summarize, the appearance of the lung tissues on the MSCT images depends on their intrinsic physical density and the CT acquisition protocol settings. Such image properties will be discussed in detail later on, in Chapter III, where the proposed CAD system will be presented.



(b)



(c)



(d)

Fig. 13 Display window setting for CT images: (a) Transfer function, (b) “LUNG” window, $C = -600$ HU, $L = 1600$ HU, (c) “LIVER” window, $C = 100$ HU, $L = 200$ HU, (d) “BONE” window, $C = 400$ HU, $L = 2000$ HU.

In conclusion, the CAD system targeting lung parenchyma pathologies in MSCT images has to take into account the variability induced by the CT image protocol used in order to provide a robust detection (or to recommend the CT protocol adapted to the lung investigation). Also, it is important to ensure detection accuracy and discriminative power with respect to the type of pathology itself, independent of the variability in image appearance of these pathologies. The following chapter analyses the state of the art in this field and sets up the direction considered in this work for the developed approach presented in Chapter III.

Chapter II

Detection of lung disease with MDCT: State of the Art

The purpose of this research is the automated detection and classification of different lung parenchyma patterns as normal tissue and pathological regions, where these latter focus on emphysema, fibrosis, and ground glass. For this objective, two challenges, lung segmentation and classification of lung tissues, need to be achieved.

Lung segmentation addresses two main aspects, namely lung region segmentation and partition of the lung region. The purpose of lung region segmentation is to accurately extract the lung parenchyma regions, where the analysis focuses on, from thorax CT images. The entire lung region provides full photometric information of lung parenchyma for the following analysis, even at the periphery of lungs. In general, pathological changes occur locally in the lung so that the appearances of regions with normal tissue and pathological changes are different in CT images. Hence, lung region partitioning aims at splitting an entire lung region into regions of interest (ROIs) according to the photometric properties of each point within the lung region, such as intensity and spatial neighborhood texture. While the points within a given ROI are associated with similar photometric properties, the differentiability among ROIs is increased. Such differentiability can be extracted as texture features to enhance the accuracy of ROI classification.

Further on, the purpose of the lung tissue classification is to recognize that lung tissue inside a ROI is normal or pathological. The analysis can be divided into two steps, feature extraction and ROI classification. Feature extraction is to obtain gray-level and texture information from ROIs. Such features should provide specificities for ROIs with normal tissue and pathologies for their efficient discrimination. The more the distinguishability of a feature is higher, the more the confidence is higher and the accuracy of classification is higher. Therefore, we need to define various features and select the useful and confident ones. In classification, a potential classifier is used for discrimination of ROIs based on the extracted features. While there are several well-known classifiers, we need to select an appropriate one for our CAD system.

In this chapter, we present and discuss existing techniques related to the detection and classification of lung diseases. Following the procedure of a classification system, we first introduce lung region segmentation (Section II.1), which is a step to extract an entire lung from a CT volumetric acquisition. In this section, three methods including optimal thresholding (Section II.1.1), region growing (Section II.1.2), and edge tracking (Section II.1.3), are briefly described. Then, in Section II.2, we introduce the concepts of related techniques for lung parenchyma analysis, which are divided into two categories, lung

partitioning and classification approaches. The section on lung region partitioning (Section II.2.1) addresses the detection of regions of interest (ROIs) in the lung parenchyma related with textural properties. The classification approaches (Section II.2.2) introduce the methods for feature extraction and the potential classifiers used to categorize the previously defined ROIs.

For a CAD system, the evaluation of overall performance is indeed important, both in terms of accuracy and robustness. Therefore, in Section II.3, several validation approaches are briefly introduced. Finally, the strengths and the weaknesses of each related technique are discussed and summarized in Section II.4.

II.1 Lung Region Segmentation

In a CAD system, lung region segmentation is a necessary first step. Armato *et al.* [35] explained the importance of an accurate lung segmentation in a CAD system. The pathologies that CAD systems focus on usually locate within specific lung regions or exist at the periphery of lungs. If the segmentation is inaccurate, the regions with pathologies or abnormalities may be excluded so that the analysis result is incorrect. Second, based on this segmentation, only the lung parenchyma region will be processed, which will greatly reduce the computation time, since lung regions occupy only a reduced part of the total volume data of a CT scan.

In this section, we introduce several relevant approaches related to the lung region segmentation. These approaches include semi- and automated techniques, where the first category requires user interaction, such as seed-point initialization.

II.1.1 Optimal thresholding

Optimal thresholding [36] uses discriminant analysis to divide foreground and background by maximizing the discriminant measure function. In an image with L gray levels, the number of pixels at level i is denoted as n_i , and the total number of pixels is denoted as $N = n_1 + n_2 + \dots + n_L$. Hence, the probability distribution of level i can be computed by

$$P_i = n_i / N \quad (2.1)$$

The pixels of the image are divided into two classes, C_1 and C_2 , which include pixels with gray-level $[1, k]$ and $[k+1, L]$, respectively. The sum of the probabilities of classes C_1 and C_2 are calculated by

$$w_1(k) = \sum_{i=1}^k P_i \quad \text{and} \quad (2.2)$$

$$w_2(k) = \sum_{i=k+1}^L P_i, \quad (2.3)$$

where $w_1 + w_2 = 1$. Let μ_i be the gray-level mean of the class C_i , and μ_T be the gray-level mean of the original image. Then, the optimum threshold k^* is obtained by the following formulas,

$$k^* = \arg \max_{1 \leq k < L} \sigma^2(k), \text{ where} \quad (2.4)$$

$$\sigma^2(k) = \frac{[\mu_T w_1(k) - \mu_1(k)]^2}{w_1(k) \cdot w_2(k)}. \quad (2.5)$$

When $\sigma^2(k)$ reaches the maximum, k is the optimal thresholding value, k^* .

Optimal thresholding is usually employed to roughly dividing the CT image into two categories: the foreground and the background. Then, other (spatial discrimination) criteria are exploited to detect the right and left lungs. In [5], the authors applied optimal thresholding to automatically select a threshold value to separate the voxels of the CT image volume into two categories: (1) voxels within the dense body and chest wall structures (foreground), and (2) low-density voxels in the lungs or in the air surrounding the body (background). After applying the optimal thresholding, a spatial connectivity algorithm was exploited to exclude the background air which is the region connecting to the border of the image and retain the two largest components. Finally, topological analysis [37] was used to fill in the lung regions and eliminate the interior cavities. Leader *et al.* [38] proposed a similar lung segmentation scheme which was performed in three steps. First, image preprocessing was used to remove background pixels, and second, computation and application of a defined threshold was exploited to identify lung tissue. Third, according to the rules of size, circularity, and location, the preliminary segmented regions were refined by pruning incorrectly detected airways and separating fused right and left lungs.

II.1.2 Region growing

Region growing is a general class of segmentation approaches which performs points aggregation in the discrete space based on local spatial connectivity. Basically, the procedure starts from a seed point, and is continuously examining neighboring locations in order to determine whether they should be added to the seed class. The growing process is stopped when no more locations can be added to the expanding subset.

The seed point/subset is chosen depending on the nature of the problem, for example, if the target is the largest object in the image, the seed can be chosen as the point set for which the gray value corresponds to the strongest peak of image histogram. Alternatively, the seed point can be chosen manually by an operator. The aggregation criteria are usually based on the photometric characteristics of the region (the current point and its neighbors) such as mean intensity value and variance.

Several studies exploited the two-dimensional (2-D)/three-dimensional (3-D) region-growing approach for segmenting lung regions. Denison *et al.*[39] have proposed a

2-D region-growing approach for extracting lung regions using an operator-given seed point in each axial CT image. Then, the 3-D lung volume was recovered by composing the 2-D region-growing results, and was offered for estimating the total lung capacity. The result showed that the mean tissue volume of a lung was 431 ± 64 ml and the residual volume was 427 ± 63 ml. Hedlund *et al.* [40] presented a 3-D region-growing approach that automatically isolates the lung region of a CT scan. The method selected all lung voxels connected with a seed point. They first excluded the points within the heart and diaphragm areas using the criteria of the range $[-550, 1000]$ HU and average difference less than 50 HU. Then, the criteria were adjusted in the range $[-1000, 15]$ HU and average difference less than 55 HU.

II.1.3 Edge tracking

The edge tracking method is based on finding the path along the steepest gradients corresponding to an interface between tissues of different X-ray attenuation. The gradients are obtained by calculating the discrete approximation of the derivative in the local neighborhood. Then, the tracking starts from a seed point and proceeds by finding the edge points in the neighborhood, whose gradient values are within a specific range. Such methods aim to produce a closed contour around an anatomic structure. For example, Sandor *et al.* [41] proposed an automated computer analysis to measure bone mass and thickness around the calvaria. They exploited an edge-based algorithm to separate and characterize differences between trabecular and cortical bone, and then compared these quantities for the left and right sides of the skull. Hedlund *et al.* [40] applied edge tracking on lung region segmentation. Their approach is based on the steep density gradient between the lung (low) and the chest wall (high). Three general ranges are respectively defined for the lung parenchyma (less than 20 HU), the cardiac and diaphragm regions $[25, 45]$ HU, and the chest wall (greater than 50 HU). Then, tracking was to find the continuous edge path along image points with the density gradient greater than 55 HU and the intensity greater than -550 HU.

II.2 Lung Parenchyma Analysis

The objective of lung parenchyma analysis is to partition and class the lung region into normal and pathological regions. With respect to implementation, the analysis can be separate into two steps: lung partitioning and classification. In this section, several lung partitioning methods and classification schemes are described. The partitioning methods include ROI setting (Section II.2.1.1), watershed (Section II.2.1.2), and region-merging (Section II.2.1.3). In the classification scheme, texture features definition (Section II.2.2.1) is addressed, and several classifiers are presented, such as the Bayesian classifier (Section II.2.2.2), the artificial neural network (Section II.2.2.3), the support vector machine (Section II.2.2.4), the logistical

regression (Section II.2.2.5), and the fuzzy logic system (Section II.2.2.6).

II.2.1 Lung partitioning

In general, pathological changes occur locally inside the lung in the initial stage but may extend to a lung region or even spread throughout the entire lung. Hence, lung partitioning is exploited to separate the lung region, either directly (ROI setting, Section II.2.1.1) or according to photometric properties (watershed transform, Section II.2.1.2, and region merging, Section II.2.1.3). The points in a partitioning region have similar properties as the normal tissue or one of pathological targets. Thus, the differentiability between regions associated with normal or pathological tissues would be enhanced.

II.2.1.1 ROI setting

In image processing, a ROI is a subset of an image identified for a particular purpose. ROI setting is selected by a given boundary on a 2-D dataset or by a given surface defining an object on a 3-D dataset. In medical imaging, the concept of ROI definition is commonly associated with automatic or manual selection of target anatomical or pathological territories (e.g. tumor margin delineation).

For an automatic region analysis, the simplest ROIs are generally set up as rectangular grids with a fixed size and overlapped to ensure the texture information would not be missed during the analysis of the whole organ. In [42], in order to automatically detect and quantify ground-glass opacities on high-resolution CT images, the author partitioned the lung region into 9×9 pixels ROIs and calculated texture features in each ROI for classification. Xu *et al.* [43] separated the lung region into 31×31 pixels ROIs. The ROIs are overlapped by half and, thus, a whole lung slice is classified on 15×15 pixels ROIs. Then, 24 texture features were calculated for analyzing and classifying each ROI in emphysema and normal tissue.

II.2.1.2 Watershed transform

Watershed transform, introduced by Vincent and Soille [44], is one of region-based segmentation methods. The main idea of watershed is to find the boundary between regions associated with catchment basins in an image relief. If $m_i(I)$ denotes the regional minima of the image I , and $CB(m_i)$ denotes the catchments basin associated with these minima, the watershed transform is defined as:

$$WS(I) = (CB(m_i))^C, \quad (2.6)$$

where C denotes the complement operator.

Fig. 14 illustrates the concept of watershed. A simple topographic relief includes two

catchment basins associated with two local minima, A and B. When water falls on the relief and flows along a path to reach one of two local minima, the relief is slowly flooded by water rising. Eventually, the flooding will reach a top zone which is the boundary between two catchment basins on the relief, and such top zone is called a watershed line.

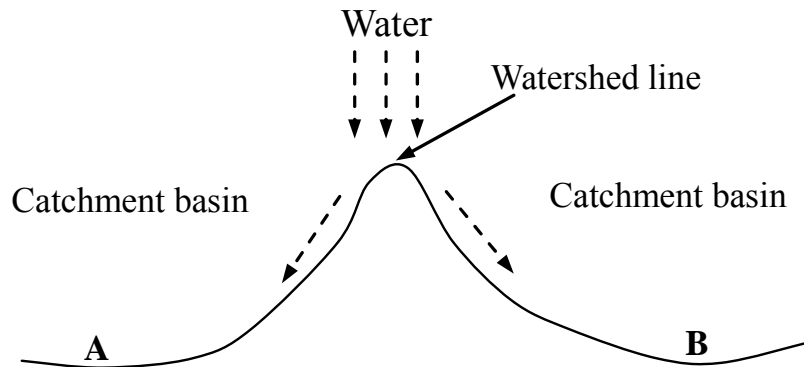


Fig. 14 The concept of watershed segmentation.

Generally, watershed segmentation would be roughly separated into two categories, immersion-based watershed and drainage rainfall watershed. In immersion watershed algorithms, water floods on the digital relief from lowlands (pixels of low gray level) to highlands (pixels of high gray level). When the water floods up to a pixel p with altitude h , there are three possible situations, as shown in Fig. 15: (a) p is a minimum in a new catchment basin if gray levels of all neighbors of p are larger or equal to h , Fig. 15 (a); (b) if there is only one catchment basin beside p , p would join to this catchment basin, Fig. 15 (b) ; (c) if p is between two catchment basins, a dam would be built on p , Fig. 15 (c).

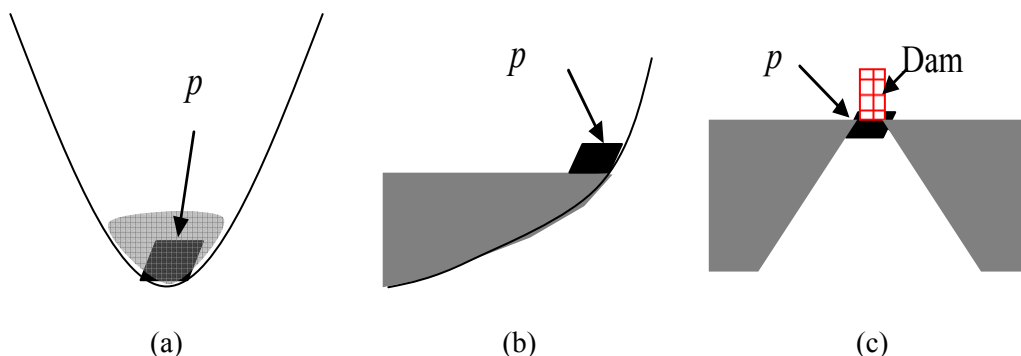


Fig. 15 Three situations of a pixel p during flooding: (a) p is a minimum; (b) p is on the hillside of a catchment basin; and (c) p is between two catchment basins.

The concept of drainage rainfall watershed is to simulate water flow. When water is on a rugged topography, it would flow down on the steepest downhill direction associated in the

area until a local minimum is reached. After all local minima are found, the drainage direction of each pixel is set according to gradient. As shown in Fig. 16, each pixel chooses the steepest downhill direction among its eight neighbors as its drainage direction. According to drainage directions, all pixels belong to two different catchment basins, and a boundary, watershed, between two basins could be obtained.

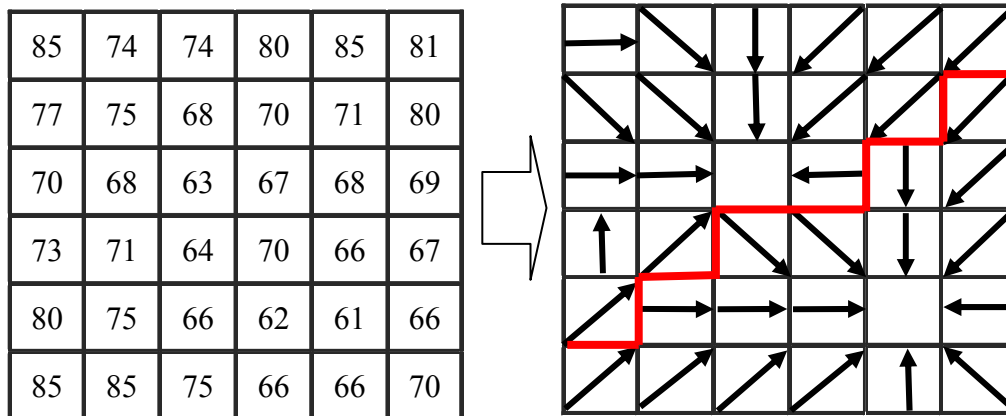


Fig. 16 An example of the drainage rainfall algorithm.

In order to enhance performance, several papers presented novel watershed segmentation methods by incorporating textural properties [45], and the framework of normalized cuts [46]. In [45], the authors used several channels to compute texture features for each pixel on the image. Then, gradient computation was exploited to select local minima pixels as starting points for the watershed segmentation. In [46], the authors exploited the generalized eigenvector to formulate the minimization of the graph-theoretic criterion which is defined for measuring the goodness of an image partition. Recently, watershed segmentation is applied to the lung CT image [47, 48]. Ukil *et al.* [47] developed an automated method for the segmentation and analysis of the pulmonary fissures. They applied a watershed transform on a vessel distance map combined with the original image to obtain an approximate segmentation of the lobar fissures. Then, the contrast information in the approximate fissure region was used to accurately detect the fissures.

II.2.1.3 Region Merging

The region-merging approach is based on a clustering concept. First, merging criteria are defined based on the priori knowledge for measuring the “fitness” degree between two clusters. Then, in a specific region, each point starts out as an individual cluster, and clusters are progressively merged into larger clusters if they satisfy the merging criteria. Based on this concept, Sluimer *et al.* [49] presented a region-merging approach to divide lung areas. Three

objectives were considered as the merging criteria: (1) the regions should be homogeneous in texture, (2) the sizes of regions should fall within a certain range, and (3) the shape of the regions should be constrained to a more compact form. Hence, the fitness degree was measured by three features, textural similarity, size, and compactness. Moreover, the total fitness is a weighted sum of the fitnesses associated with each of the three criteria. According to these criteria, the clusters showing the similar characteristics are merged into a larger cluster.

Alternatively, region-merging also can start with an over-segmented image and then merge regions into objects according to the pre-defined merging criteria (the priori knowledge). Tadikonda *et al.* [50] proposed a region-merging method for the semantic genetic image segmentation. Their method was based on the “hypothesize and verify” principle and was composed of the following steps organized in a feedback loop: (1) an image was over-segmented into primary regions, (2) the regions were represented in a primary region adjacency graph, and (3) primary regions were iterative merged according to image interpretation hypotheses generated by the genetic algorithm until the optimal segmentation was achieved.

II.2.2 Classification Approaches

In this section, several classification approaches are introduced. For classification implementation, two main challenges need to be addressed. The first is feature extraction, and the second is classifier selection.

In Section II.2.2.1, we present several methods generally employed in the literature for extracting features from the given image, which include gray-level statistics, co-occurrence matrices, run-length coding, and fractal measures. Then, from Section II.2.2.2 to Section II.2.2.6, we discuss several classifiers including Bayesian classifier, artificial neural network, support vector machine, logistic regression, and fuzzy logic systems, respectively.

II.2.2.1 Feature extraction

In image processing, feature extraction is an important step before classification and recognition. The main aim of feature extraction is to compute quantifiable characteristics of an image using one or several measure functions. By such extracted features, the dimension to represent an image is significantly reduced for understanding the content of the image so that it is easier to compare differences between images and to analyze objects in the image.

Various categories of features were proposed to represent images. These features are briefly described as follows:

- the **gray level distribution** provides a set of useful features derived from the grayscale image histogram. These features such as mean, variance, skewness, and kurtosis describe the shape of the first-order gray-level distribution regardless of spatial interdependencies [51]. Several approaches [52-56] exploited first-order features to analyze the distribution of gray levels in CT images. Sometimes, the authors used additional gray-level features to increase the accuracy. Malone *et al.* [54] added 6 first-order features, namely maximum, minimum, range, lower percentile, upper percentile, mean deviation. Also, Uppaluri *et al.* [55] defined four new features to calculate the number of voxels within given grayscale ranges and the ratios of the number of voxels in different categories.

- the **gray level co-occurrence matrix** is a second-order statistics for characterizing the occurrence of gray-level combinations in pairs of spatially related pixels [51]. An element at location (i, j) in the co-occurrence matrix specifies the frequency of occurrence of two gray-levels i and j separated by a given distance and a given direction from each other. Then, 13 features are calculated from a sub-matrix of the co-occurrence matrix: entropy, variance, contrast, correlation, sum average, sum variance, sum entropy, difference variance, difference entropy, angular second moment, inverse different moment, information measure of correlation 1, information measure of correlation 2 [57]. In 2-D analysis [58], the number of occurrences of pairs of gray-levels i and j are respectively accumulated in 4 directions, 0° , 45° , 90° , and 135° . Recently, in 3-D analysis [59], there are 13 directions for co-occurrence matrix computation, corresponding to the 26-connectivity.

- the **run-length statistics** is a second-order statistics to capture the coarseness of a texture in specified directions. A run is a set of consecutive pixels displaying the same gray-level intensity along a specified linear direction [60]. For 2-D analysis [61-63], an element at location (i, j) in a run-length matrix represents the number of runs associated with gray-level intensity i and length of run j along a specific direction. Note that there are 4 directions, 0° , 45° , 90° , and 135° . Generally, 11 features are extracted from the run-length matrices: short run emphasis, long run emphasis, low gray-level run emphasis, high gray-level run emphasis, short run low gray-level emphasis, short run high gray-level emphasis, long run low gray-level emphasis, long run high gray-level emphasis, gray-level non-uniformity, run length non-uniformity, and run percentage. Furthermore, for 3-D analysis, in the statistics, fine textures with similar gray-level intensities contain more short runs, while coarse textures with significantly different gray-level intensities produce more long runs [64].

- the concept of the **fractal dimension** developed by Mandelbrot [65] provides a

self-similarity measure of an object and allows to describe the surface of an object as fine, coarse, gained, or smooth. Roughly, fractal dimension is measured by the ratio of the log change in the object size and the log change in measurement scale. Five fractal image models have been presented for estimating the fractal dimension of an image: (1) box counting dimension [66], (2) blanket dimension [67], (3) fractal Brownian motion [68-70], (4) the fractal interpolation function system [71], and (5) affine transforms [72, 73]. For a region or an image, a small value of the fractal dimension indicates a “compact” object, and a large value indicates a “porous” object. Additionally, the fractal dimension can derive fractal features [74] such as mean, variance, skewness, kurtosis, and entropy from a constructed stochastic fractal dimension (SFD) image [75, 76]. The value of each point in the SFD image is calculated by the function of linear least-squares regression in log-log scale [77].

II.2.2.2 Bayesian Classifier

Bayesian decision theory is a fundamental statistical approach based on quantifying the tradeoffs between various classification decisions using probability and the costs that accompany such decisions and is usually applied to the classification problem [78]. In Bayesian formula, a posterior probability $P(\omega_i|x)$ represents the occurrence probability of the category ω_i when the feature vector x has been measured, and it can be calculated by

$$P(\omega_i | x) = \frac{P(x | \omega_i)P(\omega_i)}{P(x)}, \quad (2.7)$$

where $P(x|\omega_i)$ is the probability of assigning the category ω_i given x , $P(\omega_i)$ is the probability that the category ω_i appears in all data, and $P(x)$ is the probability that the feature vector x appears in all data. Fig. 17 shows an example representing different x values and the corresponding posterior probabilities $P(\omega_i|x)$ of a two-class problem. The feature vector x would be assigned to the category ω_i , if $P(\omega_i|x)$ is maximum over all others; that is

$$P(\omega_i|x) > P(\omega_j|x) \quad \text{for all } j \neq i. \quad (2.8)$$

The classifiers based on Bayesian decision theory provide competitive performance to deal with uncertainties. The naive Bayesian classifier is a simplified probabilistic classifier based on Bayesian theory which makes the assumption that attributes are all independent [79]. Thus, under the naive assumption, the classifying function is defined as eq. (2.7), but $P(x|\omega_i)$ should be replaced by

$$P(x|\omega_i) = \prod_{j=1}^d P(x_j | \omega_i), \quad (2.9)$$

where x_j is the feature vector x in the j -th dimension, and d is the number of the features.

Farag *et al.* [80] used deformable 2-D and 3-D templates of typical geometry and gray-level distribution to detect lung nodules. Then, in order to enhance the accuracy, a

Bayesian supervised classifier was exploited as post classification to train and test nodules. Uppaluri *et al.* [81] proposed a texture-based adaptive multiple feature method (AMFM) for evaluating pulmonary parenchyma from CT images. The AMFM divides a lung into 6 equal regions and employs a naïve Bayesian classifier to categorize each region as one of normal tissue and emphysema using extracted 2-D features. The 2-D features incorporate first-order and second-order 2-D statistical texture features and the geometric fractal dimension. Recently, Xu *et al.* [82] enhanced the ability of the AMFM to differentiate normal lung from pathologies including emphysema, honeycombing, and ground-glass, by extending 2-D texture features to 3-D.

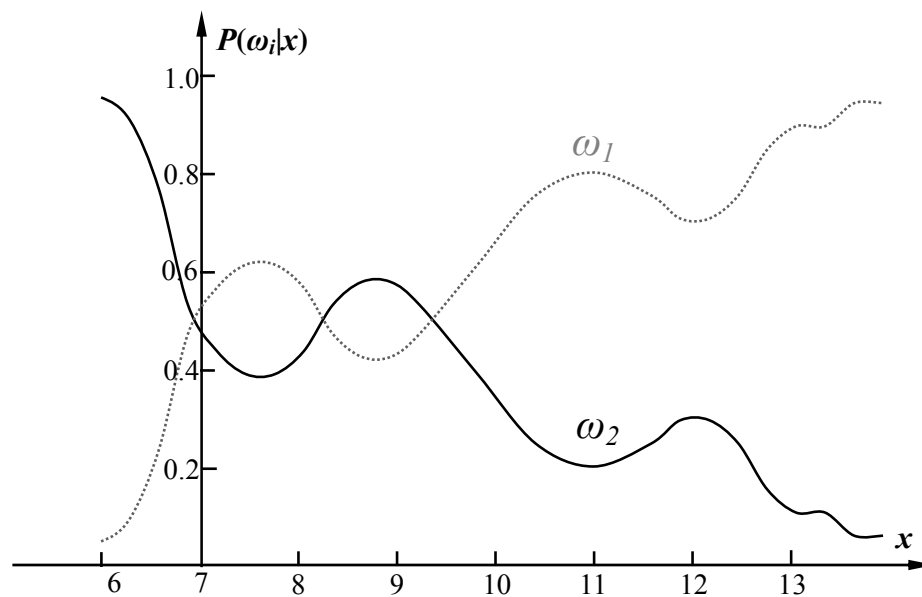


Fig. 17 An example of a two-class partitioning problem based on the corresponding posterior probability $P(\omega_i|x)$ according to a feature vector x .

II.2.2.3 Artificial Neural Network

The artificial neural network (ANN) was introduced by Warren McCulloch and Walter Pitts in 1943 [83]. It is a powerful data modeling tool inspired from the parallel architecture of the brain and is used to extract and represent the relationship between a set of inputs and a set of desired outputs in order to assist us in making predictions and decisions [84]. The basic architecture of the ANN includes three components: the input layer, the hidden layer and the output layer, as shown in Fig. 18. Note that The ANN can include several hidden layers but only one input layer and one output layer. The input units are linear and merely distribute feature values through multiplicative weights to the hidden units. The activities of units in the hidden layer are determined by the input information and the weights on the connections between the input and the hidden units. In the output layer, a prediction would be produced by

associating the values from the hidden units and the weights on the connections between the hidden and the output units.

Like the human brain, a neural network acquires knowledge through learning. There are two approaches to learn, supervised and unsupervised. In supervised learning, the neural network runs the inputs and compares the resulting outputs against the desired output. Then, learning errors are estimated and propagated back to the network to adjust the weights by an operator. The learning process occurs continually until the weights represent the passes without errors. In unsupervised learning, the neural network is only provided with the inputs, but without the desired outputs. The system adjusts the weights through minimizing a cost function composed of the inputs and the resulting outputs.

ANN is a statistical computer program which can categorize similar testing cases together based on the optimizing properties obtained from the previous training. Kauczor *et al.* [42] used three neural networks to recognize ground-glass opacities on CT images. The first neural network was employed to divide the given image into ground-glass pixels and non-ground-glass pixels by the defined density range. The second and third neural networks were used to detect contrast-rich opaque areas close to high-attenuation structures using contrast as an explicit textural parameter. Their approach achieved sensitivity of 99%, specificity of 83%, positive predictive value of 78%, negative predictive value of 99%, and accuracy of 89%. Uchiyama *et al.* [55] employed the ANN for distinguishing seven different patterns including normal tissue, ground glass opacities, reticular and linear opacities, nodular opacities, honeycombing, emphysema, and consolidation. In their approach, six physical measures including the mean, the standard deviation, air density components, nodular components, line components and multilocular components, were exploited to evaluate each ROI with a 32x32 pixels size. The sensitivity of the approach on their database for six abnormal patterns was 99.2% for ground glass opacities, 100% for reticular and linear opacities, 88.0% for nodular opacities, 100% for honeycombing, 95.8 for emphysema, and 100% for consolidation.

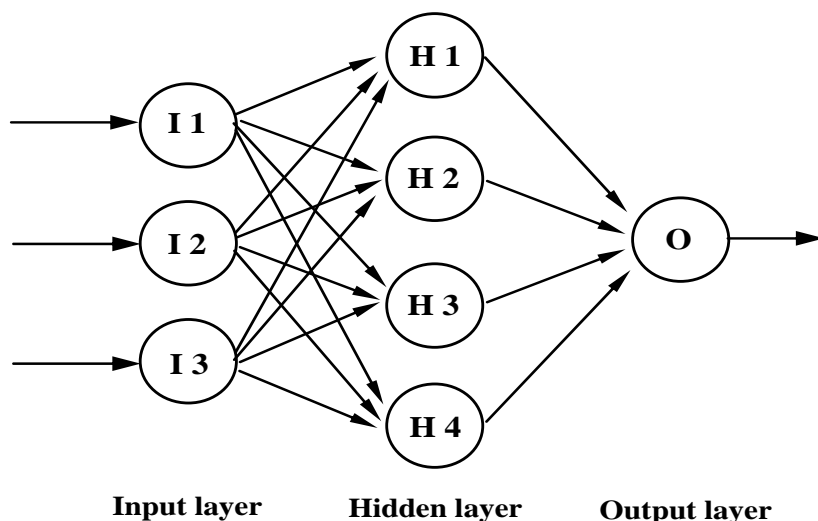


Fig. 18 A basic three-layer neural network.

II.2.2.4 Support Vector Machine

The support vector machine (SVM) invented by Vapnik [85] is a concept in computer science for a set of related supervised learning methods used for classification and regression analysis in data analysis and pattern recognition. Generally, there are many hyper-planes that might separate a set of points into two categories. The SVM selects the best one which is with the maximum margin. Note that the maximum-margin means the distance from the hyper-plane to the nearest point on each side is maximized. Fig. 19 illustrates such concept of the SVM. A set of points is separated into two categories, V_1 and V_2 , by the maximum-margin hyper-plane. However, most classification tasks require a non-linear hyper-plane (curve) for a full separation, as shown in the left side of Fig. 20. The SVM maps points into a higher dimension space through an appropriate non-linear mapping function (the kernel function) which is produced from training data. In this space, the points are rearranged and thus the maximum-margin hyper-plane can be found instead of the curve for a full separation, as shown in the right side of Fig. 20.

The SVM provides a non-linear mapping to model non-linear relationship of the testing data in a high dimensional feature space and then performs classification by constructing a hyper-plane that optimally categorize the data into two groups. Kakar *et al.* [86] exploited fuzzy C -means clustering [87, 88] and the Gabor filter [89] to segment the lung volume and extract texture features, and then subjected the results to a SVM classifier for recognition of lesions and lung fields in training and testing. For segmentation, the accuracy of delineation was 94.06%, 94.32% and 89.04% for left lung, right lung, and lesions respectively, by comparing with the delineation results of the expert radiologist. Korfiatis *et al.* [90] used wavelet decomposition for lung field segmentation and performed a discrimination of

interstitial lung disease patterns as honeycombing, reticulation and ground glass by SVM classification associating 3-D co-occurrence features. The accuracy of their classification system for normal tissue, reticular, honeycombing, and ground glass was $89\% \pm 2\%$, $72\% \pm 5\%$, $71\% \pm 3\%$ and $70\% \pm 4\%$, respectively. In [91], a CAD system was proposed to detect both solid nodules and ground-glass opacity nodules. In the system, the combination of local shape information and local intensity dispersion information was used to express the initial nodule candidates. After segmenting potential nodule objects, rule-based filtering and a weighted SVM classification were respectively employed to remove easily dismissible non-nodule objects and reduce the number of false positive (FP) objects. Overall, the average detection rate is 90.2% with approximate 8.2 FPs/scan.

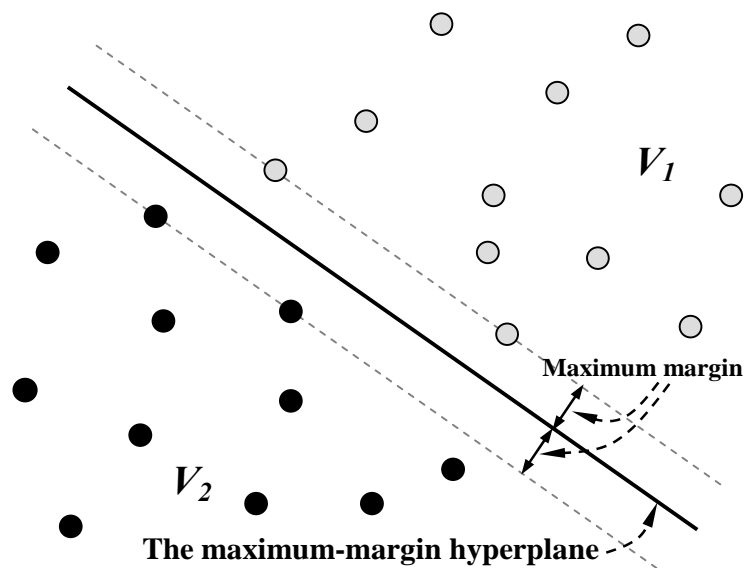


Fig. 19 The concept of support vector machines.

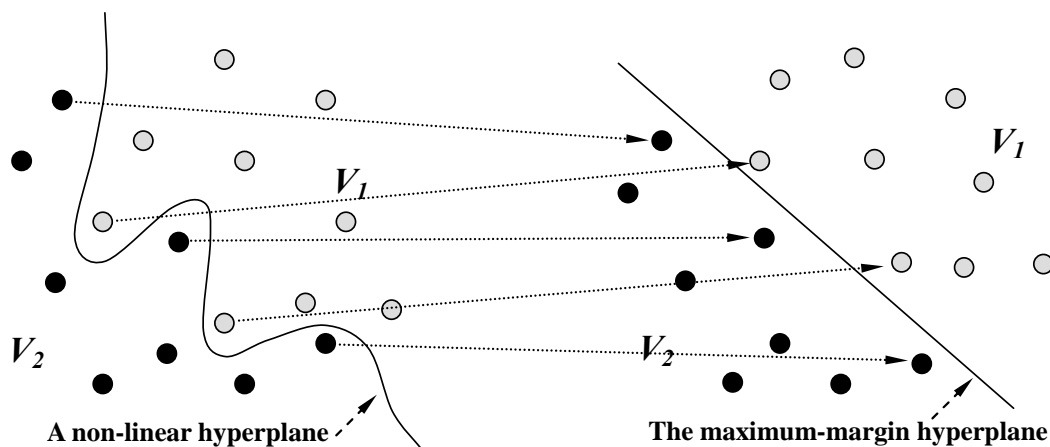


Fig. 20 A non-linear classification (left side) can be transformed as a linear classification (right side) by mapping the points into a higher dimension space.

II.2.2.5 Logistic Regression

The goal of the logistic regression model is to find a best fitting and most parsimonious function to describe the relationship between an outcome (dependent or response variable), and a set of independent (predictor or explanatory) variables [92]. The outcome variable in logistic regression is binary (“1” and “0”) or dichotomous (“yes” and “no”), that is, the dependent variable can be the value 1 with a positive probability p , or the value 0 with a negative probability $(1-p)$. The logistic regression model is defined by

$$z = \log\left(\frac{p}{1-p}\right) = \alpha + \sum_{i=1}^k \beta_i X_i, \quad (2.10)$$

where α is an “intercept” and β_i is a regression coefficient of an independent variable X_i . Note that significance and contribution of each independent variable X_i is reflected on the magnitude of the corresponding coefficient β_i . Hence, the probability p derived from z is given by

$$p = f(z) = \frac{e^z}{e^z + 1} = \frac{1}{1 + e^{-z}}. \quad (2.11)$$

The relationship between the function $f(z)$ and the value z is expressed in an S -shape curve, as shown in Fig. 21.

The likelihood ratio test is a statistical measurement used to evaluate the significance of the difference between the likelihoods of two models, one of which (the full model) is a special case of the other (the restricted model). Note that, the full model is composed of all coefficients (β_i), and the restricted model is obtained when one or more coefficients in the full model are restricted to be zero. In logistic regression, the likelihood ratio test is employed to exclude those variables having no predictive ability or high correlation with other variables from a logistic regression model. It can be roughly divided into two approaches, forward and backward. The forward regression model starts with no independent variable at the beginning, and adds one significant variable at a time until variables outside the regression model are insignificant in statistical contribution. Inversely, in the backward approach, all independent variables are put into the regression model at the beginning, and then the variables with the least contribution would be removed at a time. This process is stopped while the remained variables are all significant in statistical contribution.

The logistic regression model is widely applied in computer science. In Data mining, Arshadi *et al.* [93] combined a case-based reasoning classifier with spectral clustering and logistic regression in order to enhance accuracy for class discovery in molecular biology. Spectral clustering was applied to cluster the dataset into several groups and logistic regression model was used to exclude redundant and irrelevant features of each cluster. In their experiment, the prediction accuracies of two ovarian mass spectrometry data sets were

improved from 80% to 93% and from 90% to 98.4%. In medical image analysis, Schluchter *et al.* [94] used logistic regression to estimate the ability of the approaches to discriminate between patients with cystic fibrosis at the extremes of phenotype in order to evaluate quantification approaches of pulmonary disease severity. Recently, Washko *et al.* [95] employed regression analysis to evaluate the relationship between interstitial lung abnormalities and measurements of total lung capacity and emphysema. In their approach, the linear and logistic regression models were respectively used for continuous and binary analyses which included the variables for age, sex, body-mass index, pack-years of smoking, smoking status. The experiment result showed that interstitial lung abnormalities were associated with the average reduced total lung capacity of -0.444 liters, and the average lower percentage of emphysema defined by lung-attenuation thresholds of -950 HU (-3%) and -910 HU (-10%).

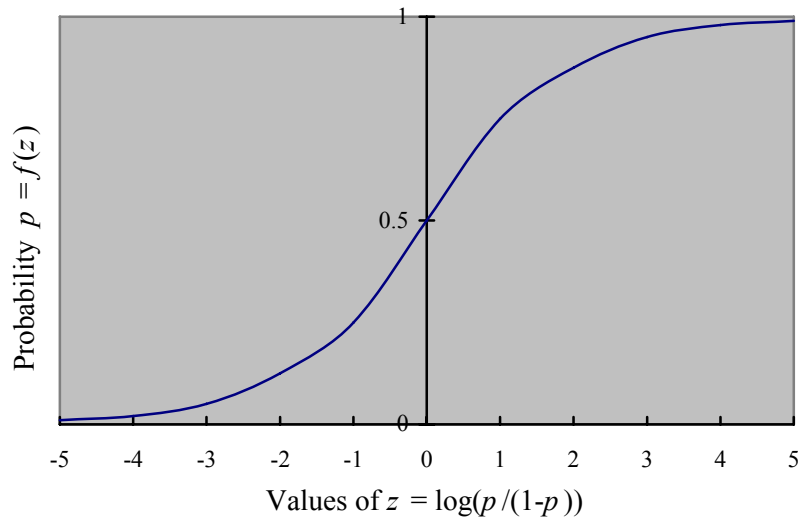


Fig. 21 The logistic function with the probability p on the vertical axis and the variable z on horizontal axis.

II.2.2.6 Fuzzy System

Fuzzy set theory [96-98] was introduced by L. A. Zadeh, Professor of computer science at the University of California in Berkeley. It provides the membership function operating over the range of real numbers $[0, 1]$ instead of the conventional elements of binary logic, such as 0/1, yes/no, and true/false. Hence, the fuzzy set theory is considered as a major tool in the information engineering applied to bridge the gap between human-originated formalized knowledge and numerical data.

The fuzzy system is a knowledge-based system and consists of the fuzzy IF-THEN rules. The fuzzy IF-THEN rules induced from human experts or based on domain knowledge

are IF-THEN statements in which some words are used to characterize a continuous membership function. According to different rule principles, fuzzy systems are divided into three types, the pure fuzzy system, the Takagi-Sugeno-Kang (TSK) fuzzy system [99, 100], and the fuzzy system with fuzzification and defuzzification [101].

A pure fuzzy system is composed of a fuzzy inference unit combined with a fuzzy rule base, which is the collection of fuzzy IF-THEN rules. The basic architecture of the pure fuzzy system is shown in Fig. 22. Suppose the death rate has sharp increase in people with 65-75 years old. In the pure fuzzy system, fuzzy IF-THEN rules are represented in the following form:

IF the age of a person is within 65-75 years old
 THEN with high death rate

With the fuzzy rule, the fuzzy inference unit maps the fuzzy set from the input space U to the output space V . The main problem of the pure fuzzy system is that its inputs and outputs are fuzzy sets, which are represented by words in natural languages, rather than real-valued variables used in engineering systems.

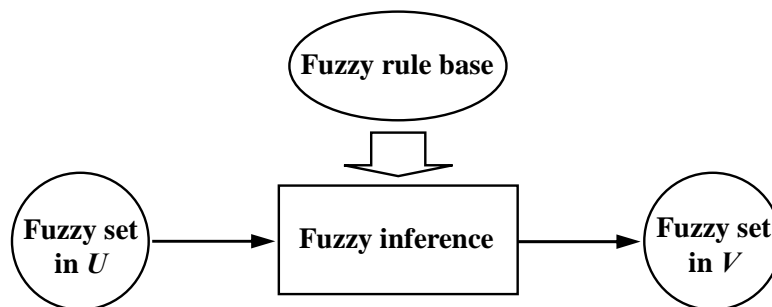


Fig. 22 The architecture of a pure fuzzy system.

A TSK fuzzy system is proposed to solve the problem of the pure fuzzy system. The basic architecture of the TSK fuzzy system is shown in Fig. 23. In the TSK system, the form of fuzzy rules is represented in a mathematical formulation as

IF a person is x years old, and x is within 65-75
 THEN the death rate of the person is $y = cx$

where c is a constant. This change makes inputs and outputs to be real-valued variables and the fuzzy inference unit in the TSK system is a weighted average of the values in the THEN parts of fuzzy rules. However, the TSK system has two problems; that is, the lack of representing human knowledge and the difficulty of applying different principles in fuzzy logic.

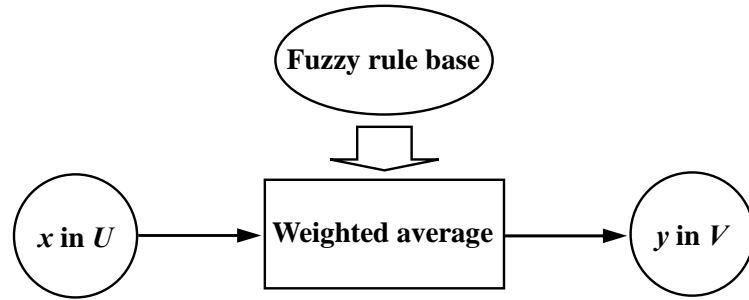


Fig. 23 The architecture of a Takagi-Sugeno-Kang fuzzy system.

A fuzzy system with fuzzifier and defuzzifier transforms input real-valued variables into a fuzzy set by using a fuzzifier, and the output of this system is transformed from a fuzzy set into real-valued variables by using a defuzzifier. The basic architecture of the fuzzy system with fuzzifier and defuzzifier is shown in Fig. 24. Under this architecture, inputs and outputs are represented by real-valued variables so that it is easier to perform analysis in mathematical functions; on the other hand, the human knowledge can be constructed in engineering applications.

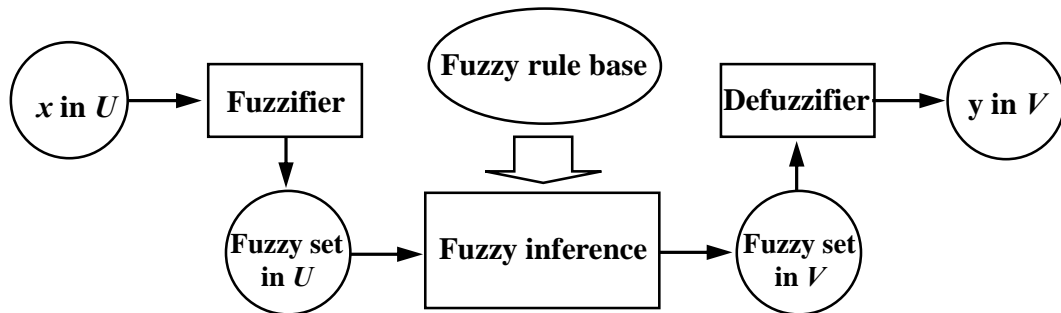


Fig. 24 The architecture of a fuzzy system with fuzzifier and defuzzifier.

In medical image analysis, the fuzzy logic systems were applied in several applications. In order to automatically segment the lobar fissures, Zhang *et al.* [101] employed a fuzzy reasoning system to analyze information from three sources: the image intensity, an anatomic smoothness constraint, and the atlas-based search initialization. Their approach was tested on 22 volumetric thin-slice CT scans from 12 subjects, and the root mean square error between the automatically and manually segmented results achieved 1.96 ± 0.71 mm. Ahmed *et al.* [102] presented a novel algorithm for segmentation of magnetic resonance imaging (MRI) data and estimation of intensity heterogeneities using fuzzy logic analysis. Their algorithm is formulated by modifying the objective function of the standard fuzzy *C*-means algorithm [87, 88] to compensate for such heterogeneities and to allow the labeling of a pixel to be influenced by the labels in its immediate neighborhood. The segmentation accuracies of their

approach applied respectively on simulated MRI images with three signal-to-noise ratios, 13 db, 10 db, and 8 db, were 99.25%, 97.3%, and 93.7%. In [103], two types of fuzzy rules, Mamdani and TSK, were used for lung nodule classification. By using fuzzy rules, the CAD system can deal with uncertainty in input data, which is inherent problem in an image-based practice of medicine. The performance of two fuzzy logic systems without training was evaluated by accuracy (Mamdani: 67.2%, TSK: 77.4%), sensitivity (Mamdani: 67.9%, TSK: 75.6%) and specificity (Mamdani: 65.9%, TSK: 66.1%). Moreover, after training, the performance of the TSK system achieved 98.7% (accuracy), 96.7% (sensitivity) and 93.3% (specificity).

II.3 Validation Approaches

Sometimes, although accuracy of a CAD system is quite high, reliability and sensitivity of the system is weak due to a small or specific testing dataset. Hence, validation is necessary to evaluate the classification performance. In this section, we briefly describe three validation methods including experts, kappa statistic, and receiver operating characteristic curve.

- The validation performed by **radiologist expert** is the primary and simplest way to evaluate the testing results. The expert manually performs the segmentation and classification (labeling) of the testing data. Then, comparison is performed to evaluate difference between the diagnosis result and the result of the CAD system. Even now, the radiologist expert has still an important role to offer the preliminary training result and the evaluation of a CAD system. However, lung disease analysis is generally based on subjective evaluation of CT images, leading to high inter-observer but also intra-observer variability. Therefore, the development of reliable and reproducible validation methods is necessary.
- **Kappa statistic** [104] is a common method in assessing the agreement of two or more observers evaluating the same data for assignment to categories. For example, in medical study, kappa statistic is used to assess the agreement of radiologist analysis (rater 1) and computer analysis (rater 2) using the same X-ray data to label a growth malignancy (M) or benignancy (B). The probabilities (Pr) of the agreement of two raters are as follows:

	Rater 2 (M)	Rater 2 (B)	Total
Rater 1 (M)	Pr_{11}	Pr_{12}	Pr_3
Rater 1 (B)	Pr_{21}	Pr_{22}	Pr_4
Total	Pr_1	Pr_2	

Then, the value of kappa statistic, k , is defined as

$$k = \frac{P_o - P_e}{1 - P_e} \quad (2.12)$$

where $P_o = Pr_{11} + Pr_{22}$, and $P_e = Pr_1 \times Pr_3 + Pr_2 \times Pr_4$. The value k represents difference between the observed probability of malignancy (P_o) and the probability of malignancy associated with the assumption of an extremely bad case (P_e). Note that the maximum value for kappa statistic is 1. In kappa statistic, the benchmarks to interpreting k values are listed in Table 1.

Table 1 The interpretations of k values in Kappa statistic.

k value	Interpretation
0.00-0.20	slight
0.21-0.40	Fair
0.41-0.60	Moderate
0.61-0.80	Substantial
0.81-1.00	Almost perfect

- The performance of the CAD system is evaluated by five performance indices: accuracy, sensitivity, specificity, positive predictive value (PPV), and negative predictive value (NPV). These performance indices are defined by

$$\text{Accuracy} = (TP + TN) / (TP + TN + FP + FN) \quad (2.13)$$

$$\text{Sensitivity} = TP / (TP + FN) \quad (2.14)$$

$$\text{Specificity} = TN / (TN + FP) \quad (2.15)$$

$$\text{PPV} = TP / (TP + FP), \text{ and} \quad (2.16)$$

$$\text{NPV} = TN / (TN + FN) \quad (2.17)$$

where the true positive rate (TP) represents percentage of correctly classified positive cases, the true negative rate (TN) represents percentage of correctly classified negative cases, the false positive rate (FP) represents percentage of incorrectly classified positive cases, and the false negative rate (FN) represents percentage of incorrectly classified negative cases.

The **receiver operating characteristic** (ROC) curve [105] is a graphical plot of sensitivity against $(1 - \text{specificity})$, i.e. a plot of the proportion of TP versus the proportion of FP. From the computer science point of view, ROC analysis can be used as an evaluation tool for discrimination of effects among different methods. The overall performance of diagnostic results can be measured by the total area (A_z) under the ROC curve. Intuitively, the area is in the interval $[0.5, 1]$, and a large area indicates a better performance.

Sometimes, ROC analysis is also used to compare the performance of two methods applied on the same dataset. Note that it is important to consider the correlation between areas of ROC curves of two methods. In such case, the z -test is used to evaluate differences between the areas for which the correlation is counted, and is defined as

$$z = \frac{A_{z1} - A_{z2}}{\sqrt{SE_1^2 + SE_2^2 - 2rSE_1SE_2}} \quad (2.18)$$

where A_{z1} and A_{z2} are the two areas, SE_1 and SE_2 are the corresponding standard errors, and r is the quantity representing the correlation between the two areas.

II.4 Summary

In the state of the art, the techniques for lung disease classification are introduced in three stages: lung region segmentation, lung partitioning, and classification. Several conclusions can be resumed and addressed as follows.

In the case of lung region segmentation, optimal thresholding, region-growing, and edge-tracking are exploited to identify the points within the lung parenchyma based on the gray-level contrast between lung parenchyma and the surrounding tissues. Each of them extracts the lung regions in a CT image in very short time. However, these methods easily fail on the scans with pathological lungs which include dense regions. Such scans occur frequently in clinical practice and are the aim of the lung CAD system. Furthermore, the region-growing and edge-tracking approaches are not fully automatic methods due to the user-interactive seed point.

In the case of lung partitioning, ROI setting is a basic method to provide a simple way to partition the lung region by a grid of square regions. In this approach, the use of regions is with a fixed size so that the shape is insensible to the boundary between different tissues inside the lung region. This may cause serious consequences for performance of the following analysis. Such problem can be overcome by using the watershed transform or region-merging algorithms which partition the lung region based on photometric properties, gray-level and texture. However, oversegmentation is a well-known drawback in watershed segmentation. Thus, watershed transform should be combined with other approaches, such as thresholding markers [106] and gradient map construction [107], for reducing the oversegmentation. High computation time is one of the disadvantages of region-merging. The other one is the parameterization problem because there is no functional relationship with the number of output regions and with their sizes. Users need to find the appropriate segmentation level by a trial, and require priori knowledge for constraining the size and shape of the region.

Table 2 is a summarized comparison of classifiers that are mentioned in Section II.2.2 with respect to four criteria: time, training data requirement, accuracy, and n -class classification. The Bayesian classifier is easy to implement and requires a small amount of training data to estimate the parameters for classification based on the independent variable assumption. However, the Bayesian classifier is limited with dependent variables which

usually exist in practical cases. The ANN is used as a function approximation mechanism with a simple architecture. The weights of the hidden layer are adjusted through supervised/unsupervised learning from the observed data so that training data requirement is not too high. Although its accuracy is high, it only deals with the linearly separable problem of two classes. The SVM can avoid the difficulty of the non-linear separation by mapping the two-class variables in the higher feature space, and is with low training data requirement. However, the computation complexity is high, the selection of the kernel function parameters is difficult, and it lacks of multi-classification possibility. Like SVM, logistic regression also can solve the non-linear separation problem. Additionally, it has easier clinical inferences than ANN and SVM duo to the log odds interpreted as the relative increase or decrease in the probability of an outcome. Unfortunately, logistic regression requires much data to achieve a stable and meaningful result (high accuracy) so that the computation complexity is quite high. The main advantage of fuzzy logic analysis is the use of vague linguistic terms in the rules. Such rules allow the analysis to offer the mixed classification which is closer to the human thinking mode. The difficulty is to establish the fuzzy rule base and to combine the outputs of the rules.

Table 2 Summarized comparison of the different classifiers.

Classifiers	Criteria			
	Time complexity	Training data Requirement	Accuracy	<i>n</i> -class Classification
Baysian	Low	Low	Medium	Yes
ANN	High	Medium	High	No
SVM	High	Medium	Medium	No
Logistic Regression	High	High	Low	No
Fuzzy Logic	Medium	Medium	High	Yes

There are many CAD systems proposed for the lung disease analysis. We summarized them into four categories and the comparison between them is listed in Table 3. The point-based analysis was used to estimate the severity of the diseased lung by the ratio of the lung volume selected by a defined threshold value to the total lung volume. The analysis is very simple with low time complexity, but it cannot discriminate between several pathologies of lung parenchyma occurring at the same time. The approaches including lung segmentation and classification can overcome this drawback by applying classification on each point in the lung region. However, such methods are weak in accuracy and robustness. When pathological targets appear locally in the lung, the methods might fail due to insufficient gray-level and texture information extracted from the given point and its neighborhood. In order to obtain the

locally gray-level and texture information, lung region partitioning is added to the CAD system for separation of lung region. Overall, the 2-D/3-D CAD system can classify the partitioning regions into normal or one of several pathologies, and has higher accuracy and robustness. Nevertheless, the 2-D system is weak in specificity because the system analyzing the lung region slice by slice is insufficient in the spatial information and volumetric statistics. The 3-D system has high performance both in sensitivity and specificity using the completely 3-D local and spatial information, but its time complexity is usually much higher than other categories of approaches. Furthermore, both of 2-D and 3-D analysis are usually semi-automatic because an initial seed point is required in the beginning of lung segmentation, and ROIs setting.

Table 3 Summarized comparison of the different kinds of the analysis systems.

Approach	Criteria				
	Pathology discrimination	Sensitivity	Specificity	Robustness	Time complexity
Pointwise (pixel/voxel-based) analysis	No	Medium	Low	Low	Low
Lung segmentation + Classification	Yes	Medium	Low	Low	Low
2-D + Lung segmentation + Lung partitioning + Classification	Yes	High	Medium	High	Medium
3-D + Lung segmentation + Lung partitioning + Classification	Yes	High	High	High	High

In conclusion, based on the identified drawbacks in the state of the art, two key points have to be specifically addressed in the development of new lung CAD systems: the automation of the solution and the acquisition of more complete photometric information. Hence, in order to overcome the limitations of each discussed category of methods, a new approach is proposed in Chapter III. Considering the reliability and robustness criteria, we situate the proposed approach in the 3-D case, according to the system architecture including lung segmentation, lung region partitioning, and classification. In our approach, a multi-resolution decomposition scheme is proposed to segment and partition lung regions automatically. The resulting decomposition pyramid is investigated based on a hierarchic tree

structure relating the lung regions at different resolution levels. Several features including the gray-level information and the spatial connectivity information are computed for each region and associated with the tree structure. Then, because of its flexibility, the fuzzy logic analysis is used to implement the mixed classification. Finally, a spatial partitioning approach is presented for upgrading the multi-resolution decomposition scheme, and the classification result is represented according to the radiologist's investigation criteria.

Chapter III

Multi-resolution Approach for Characterization of Lung Diseases

As concluded in Chapter II, the development of a new CAD system for lung pathology detection should focus on two aspects:

- first, the automation of the approach allowing the analysis of large amount of patient image data and thus releasing the interaction burden for the clinician and,
- second, the ability to provide new discriminative features computed from the CT image data, exploitable by a classification system. We recall that the parenchyma patterns targeted by the objective CAD system concern normal pulmonary tissue (N), emphysema (EM), fibrosis/honeycombing (FHC), and ground glass (GDG).

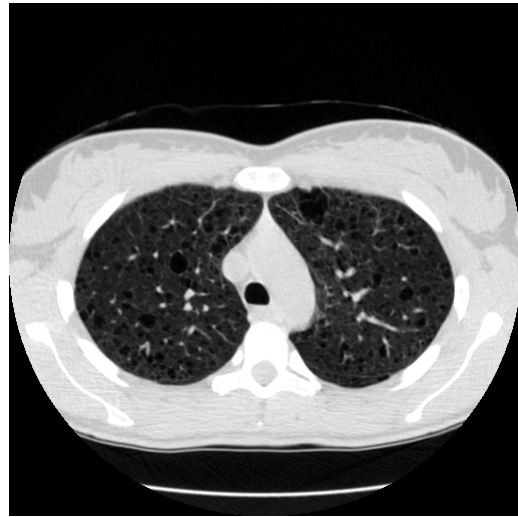
The detection of such patterns closely relies on the analysis of their tissue density as captured in the CT data. For emphysema and fibrosis, the common characteristics refers to the presence of low-attenuated regions $[-1000, -950]$ HU / $[0, 10]$ GL² due to the tissue destruction, while ground glass is distinguished by medium-high intensity $[-650, -500]$ HU / $[75, 105]$ GL, superior to the normal tissue $[-920, -850]$ HU / $[16, 35]$ GL. The idea exploited by the proposed approach is to detect EM and FHC by performing an analysis of the low-attenuated regions and to tackle the GDG on the remaining zones. Such analysis will rely on a set of image features specific to each class of pathology which will be identified in the CT data. They refer to size, clustering and gray-level distribution, both inside and around the patterns. The considered features are summarized below:

- the low-intensity patterns in normal tissue have very small sizes and are normally distributed, Fig. 25 (a).
- in EM, the size of the low-intensity patterns is large and their border generally shows intensities similar with normal tissue, Fig. 25 (b). Moreover, the border intensity depends on the EM spatial location in the lung and may increase when the pattern is adjacent to lung fissure or thorax cage, Fig. 25 (c). Note that an inflammatory condition can also induce an increase of EM border intensity, Fig. 25 (d).
- the FHC low-intensity patterns are smaller in size than those of EM, with high-intensity borders $[-780, -680]$ HU / $[46, 68]$ GL known as reticulations, and usually cluster together, Fig. 25 (e).
- GDG is defined as hazy increased attenuation within the normal region, Fig. 25 (f).

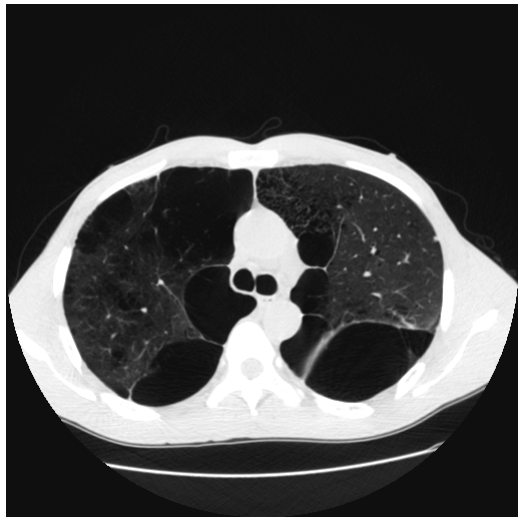
² GL refers to the gray-level value in the grayscale range $[0, 255]$ considered for a CT “lung” window, $[-1000, 200]$ HU



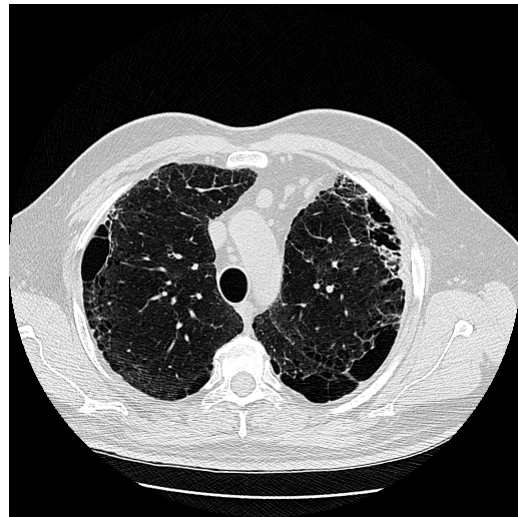
(a) N



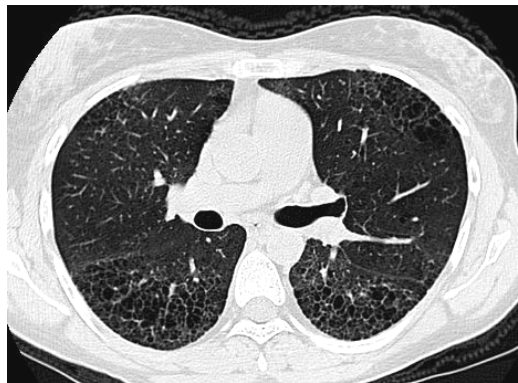
(b) EM



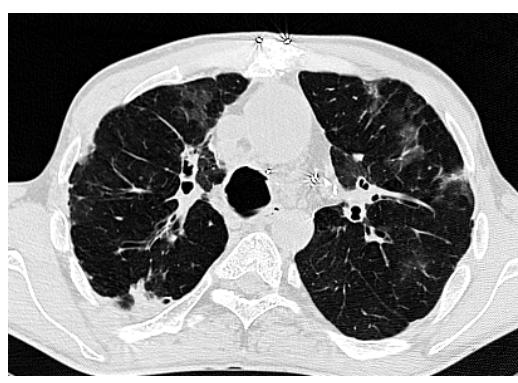
(c) EM



(d) EM + F



(e) FHC



(f) GDG

Fig. 25 Image features of different physio-pathological lung patterns: (a) normal lung, (b) centrilobular emphysema, (c) panacinar emphysema, (d) distal acinar emphysema coupled with fibrosis, (e) fibrosis-honeycombing, (f) ground glass.

The analysis of the size property is addressed via a multi-resolution decomposition approach of the lung volume relief. It allows the identification (segmentation) of low-density patterns according to their sizes and also involves a local gray-scale analysis of each such pattern and its environment. Note that the patterns extracted at different resolution levels may not be disjoint and this property will be exploited to detect pattern clustering. In this respect, the resulting multi-resolution decomposition of the low-density patterns will be further on described and analyzed by means of a hierarchic tree graph structure, where a node is associated to a given pattern at the given resolution level and the tree vertices correspond to the spatial connectivity between patterns at different resolution levels. The analysis of the neighborhood of each node in such a tree structure (parent - child - sibling) will automatically provide the clustering information. The decision step in the final classification will exploit the multi-valued features of the multi-resolution lung patterns (size, gray-level distribution, clustering, ...) and will be implemented by means of a fuzzy logic reasoning.

The developed method can be classed in the third category of methods described in the state of the art, Chapter II, which perform a fully 3-D analysis and successively segment the lung field, partition the lungs into regions and class them as normal or pathologic. In order to ensure a higher robustness with respect to the CT acquisition parameters, an image pre-processing/enhancement step can be applied, as discussed in Section III.1. The lung segmentation (Section III.2) has in our case two objectives: first, limiting the volume of the processed data and second, providing information on the high-density regions such as fibrosis reticulations occurring at the lung periphery and which may be disregarded by the multi-resolution analysis focusing on the low-attenuated patterns. Section III.3 presents the principle of lung region partitioning based on the multi-resolution decomposition scheme, while the attribute description and the fuzzy logic-based classification are respectively discussed in Sections III.4 and III.5. The detection scheme is improved by introducing an additional spatial partitioning of the multi-resolution decomposition of the lung relief, the results being discussed in the Section III.6. The global flowchart of the proposed approach is illustrated in Fig. 26.

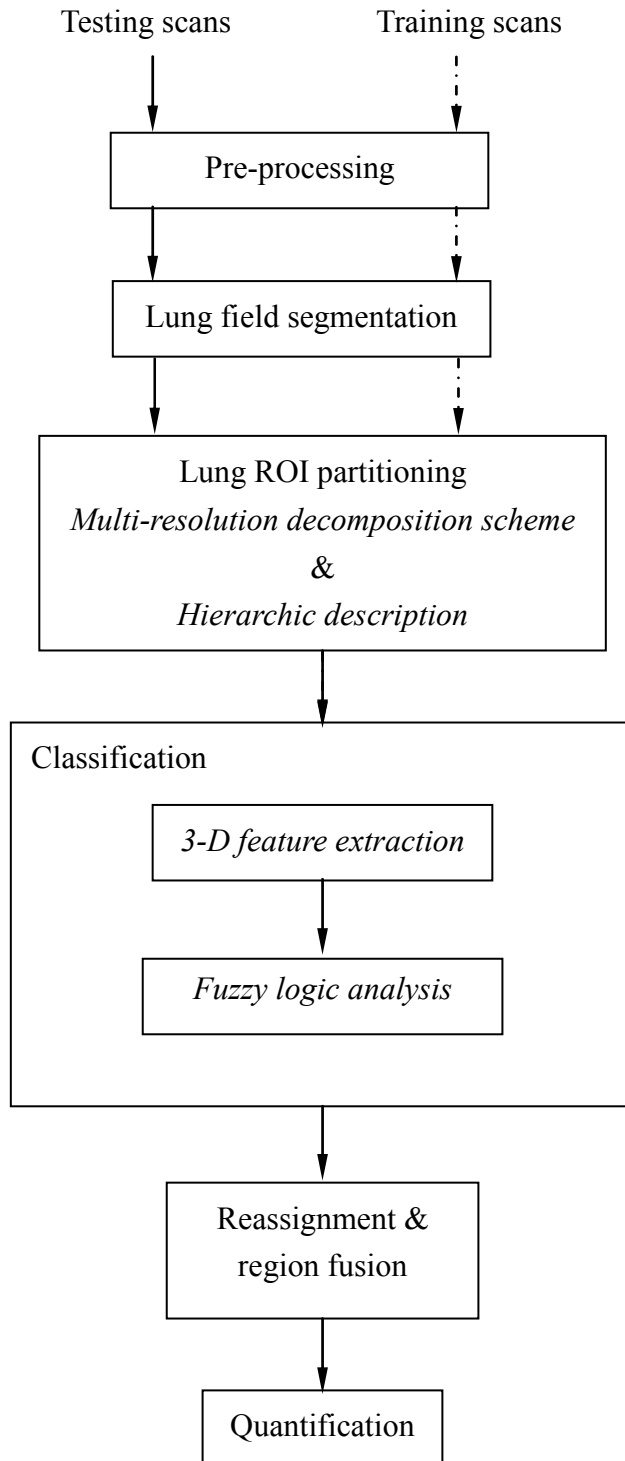


Fig. 26 The global flowchart of the proposed approach.

III.1 Pre-processing

Generally, the first problem for a CAD system is how to enhance image quality in terms of contrast and boundary delineation between different patterns. According to the MSCCT acquisition protocol used, several filters may be considered here. We shall briefly discuss in the following only the anisotropic diffusion filter and the stick operator as potential pre-processing approaches to respectively remove noise and strengthen the gradient on the patterns boundary. Other pre-processing techniques remain nevertheless conceivable, such as the classic Gaussian smoothing filter.

III.1.1 Anisotropic Diffusion Operator

Traditionally, the medical image always has strong speckle noise because of the wave interference occurrence inherent in any coherent imaging process. The anisotropic diffusion filter offers a good compromise in reducing speckle noise while preserving boundary information.

Perona *et al.* [108] used the local image gradient to control anisotropic diffusion and modified the classical isotropic diffusion equation into an anisotropic diffusion equation, given by

$$\frac{\partial I(x, y, t)}{\partial t} = \text{div} \left[g(\|\nabla I\|) \cdot \nabla I \right] \quad (3.1)$$

where $\|\nabla I\|$ is the gradient magnitude, div is the divergence operator, $\|\ \ \|$ denotes the magnitude, and $g(\|\nabla I\|)$ is an edge-stopping function. This function is chosen to satisfy $g(x) \rightarrow 0$ when $x \rightarrow \infty$ and should be monotonically decreasing so that the diffusion decreases as the gradient strength increases, and it stops across edges. Fig. 27 shows results produced by applying the anisotropic filter to CT images with emphysema and fibrosis, respectively.

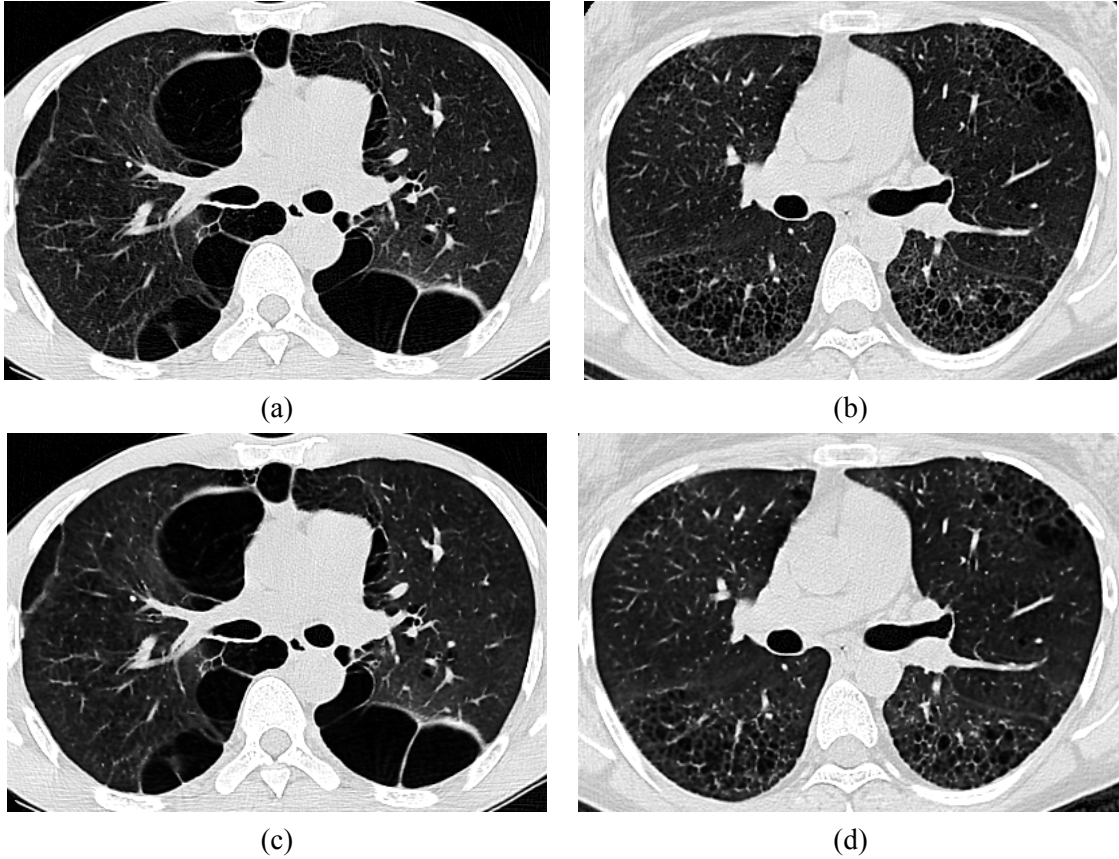


Fig. 27 The results (c) and (d), showing only the lung field, were produced by applying the anisotropic diffusion filter to original CT images with (a) emphysema and (b) fibrosis, respectively.

III.1.2 Stick Operator

The stick method is used to enhance the boundary of the reticulation patterns which have different spatial directions. Although the conventional stick algorithm is often applied to 2-D images, the extension of the stick from 2-D to 3-D could be employed to enhance the boundary information which is between image slices. Table 4 shows 3 different symmetric templates of the stick mask with size = 7. Note that, in coordinate (i, j, k) , the middle portion “3” means that 3 successive points form a straight path in axis i, j , or k . Based on such templates, 3 types of stick masks can be represented by (1-1-1-1-1-1-1), (1-1-3-1-1), and (1-5-1), and the number of forms for each type of mask is 7, 12, and 12, as listed in Table 5. Therefore, a given point on a line (size = 7) in an image would match with one of 31 stick masks with size = 7. Fig. 28 shows two samples of 3 types of the stick mask with size = 7. The stick operator is defined as

$$s = \max_{n=1}^{31} \left(\frac{m_n(I(i, j, k))}{7} \right) \quad (3.2)$$

$$m_n(I(i, j, k)) = \sum_{a=-3}^3 \sum_{b=-3}^3 \sum_{c=-3}^3 I(i+a, j+b, k+c) \times B_n(a, b, c), \quad (3.3)$$

where $I(i, j, k)$ is the intensity of central voxel in the $7 \times 7 \times 7$ reference region, $m_n(\cdot)$ is the result intensity after applying n -th stick mask, $B_n(\cdot)$ is the n -th stick mask, the value of black voxels is 1 and the value of other voxels are 0 in the masks, and $\max(\cdot)$ is the maximum intensity among the results after performing the 31 stick masks. Fig. 29 (a) and (b) respectively show the results produced by applying the stick detection to the CT images with emphysema and fibrosis, which had been processed by the anisotropic diffusion filter.

Table 4 The three symmetric templates of the stick mask with size = 7.

mask size	Left portion	Middle portion	Right portion
7	1, 1, 1	1	1, 1, 1
	1, 1	3	1, 1
	1	5	1

Table 5 Three types of the stick mask with size = 7 and the number of forms.

mask size	types of the stick mask	The number of forms
7	a(1-1-1-1-1-1-1)	7
	b(1-1-3-1-1)	12
	c(1-5-1)	12

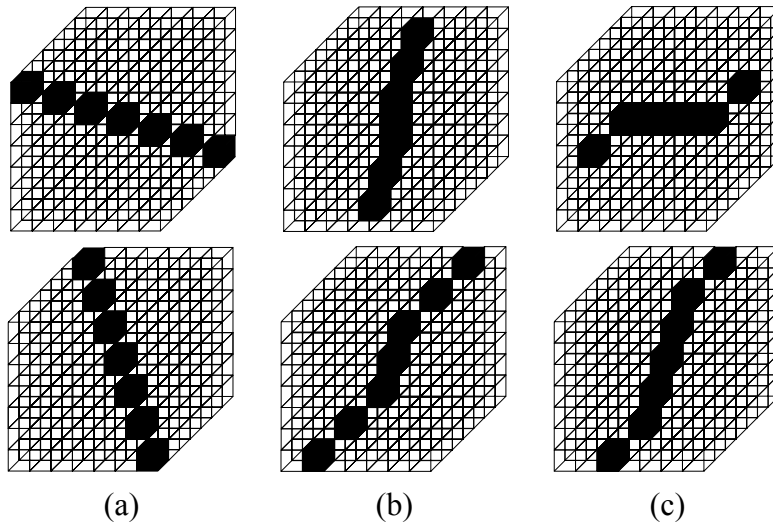


Fig. 28 Sample forms of the stick mask with size = 7 for (a) the category a, (b) the category b, and (c) the category c in Table 5.

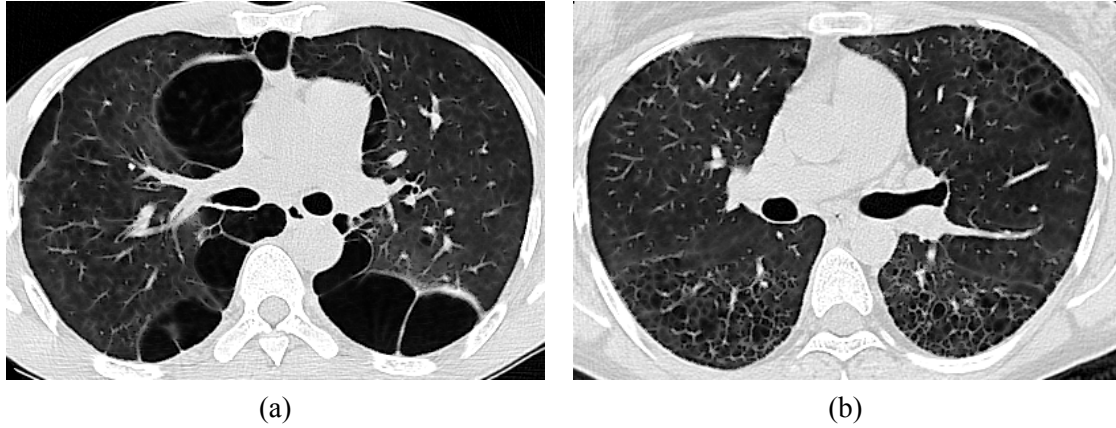


Fig. 29 The results produced by applying the stick detection to CT images of Fig. 27 with (a) emphysema and (b) fibrosis.

III.2 Lung field segmentation

The purpose of this step is to provide a mask of the lung field including the high intensity regions, such as pulmonary vessels and fibrosis reticulations, but also the large airways connecting the lungs. The lung segmentation procedure here developed relies on a set of standard and geodesic 3-D mathematical morphology operators which are first reminded in Section III.2.1 for the sake of completeness, the segmentation algorithm being detailed in Section III.2.2.

III.2.1 Definitions

Consider $f: R^n \rightarrow R$ a discrete function of compact support and $D \subset R^n$ a structuring element (SE) and D_S its symmetric with respect to its origin, $D_S(x) = D(-x)$. The following morphological operators are defined [126]:

— Erosion

The erosion of the function f by the SE D is defined as

$$\forall x \in \text{supp}(f), [e^D(f)](x) = (f \ominus D_S)(x) = \bigwedge_{\xi \in D} f(x + \xi), \quad (3.4)$$

where \bigwedge denotes the infimum operator and \ominus the Minkowski subtraction [127]. Fig. 30 illustrates the morphological erosion in the one-dimensional (1-D) case.

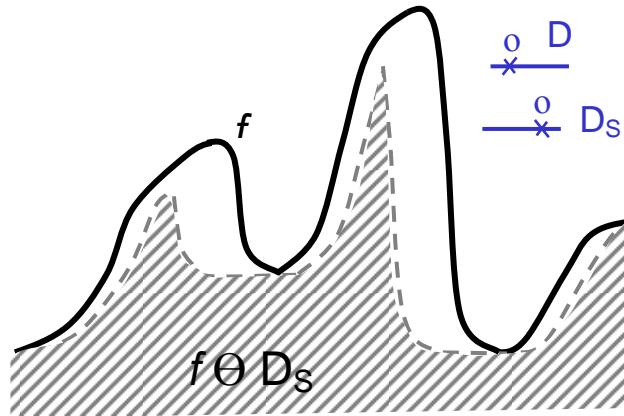


Fig. 30 Illustration of the morphological erosion operation of a 1-D function f by a structuring element D .

From an intuitive point of view, the erosion operator “shrinks” the “relief” of the function so that “hills” shapes become thinner and valleys are enlarged by plateau creation.

– **Dilation**

The dilation of the function f by a SE D is defined as

$$\forall x \in \text{supp}(f), \quad [\delta^D(f)](x) = (f \oplus D_s)(x) = \bigvee_{\xi \in D} f(x - \xi) = \bigvee_{\xi \in D_s} f(x + \xi), \quad (3.5)$$

where \bigvee denotes the supremum operation and \oplus the Minkowski addition [127]. Fig. 31 illustrates the morphological dilation operator in a 1-D example.

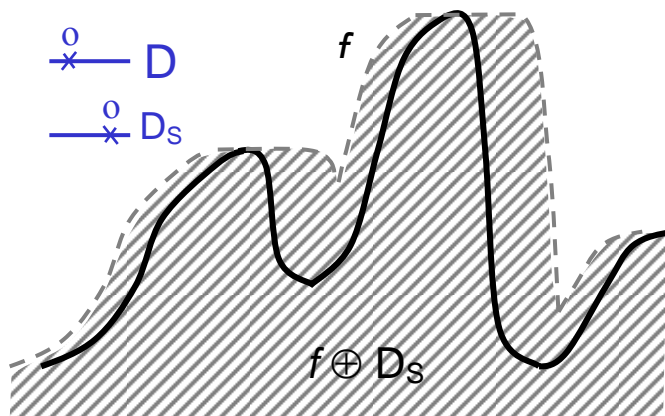


Fig. 31 Illustration of the morphological dilation operation of a 1-D function f by a structuring element D .

From an intuitive point of view, the effect of the dilation operator is to enlarge boundaries of “hills” in the “relief” by plateau creation and “shrink” or “fill in” the “basins”.

– **Opening**

The translation-invariant opening of the function f by a structuring element D is defined as the successive erosion-dilation of f by D (Fig. 32):

$$\forall x \in \text{supp}(f), (f \circ D)(x) = (f \ominus D_S) \oplus D. \quad (3.6)$$

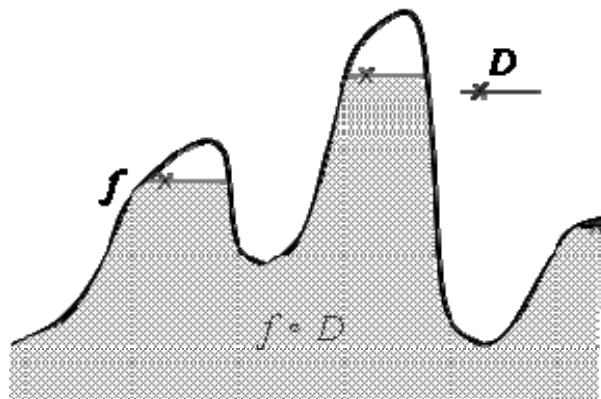


Fig. 32 Illustration of the morphological opening operation of the 1-D relief f by a structuring element D .

From an intuitive point of view, the opening operator “grinds” the “hills” and “protrusions” in the “relief” of the function so that the tops of “hills” become flatter, and the surface of the “relief” becomes smoother.

– **Closing**

The translation-invariant closing of the function f by a SE D is defined as the successive dilation-erosion of f by D (Fig. 33)

$$\forall x \in \text{supp}(f), (f \bullet D)(x) = (f \oplus D_S) \ominus D. \quad (3.7)$$

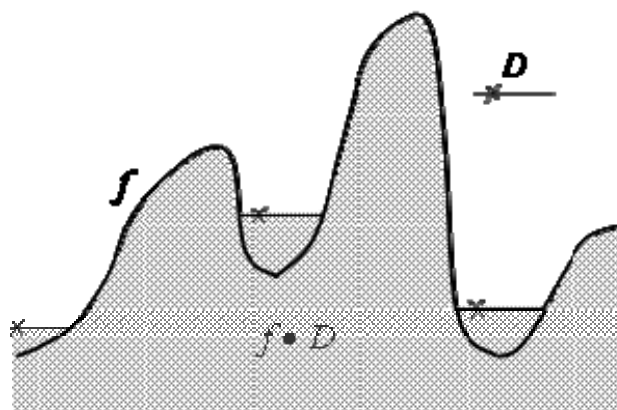


Fig. 33 Illustration of the morphological closing operation of the 1-D relief f by a structuring element D .

From an intuitive point of view, the closing operator “fills in” the “basins” and the narrow “gulfs” in the “relief” f so that the bottoms of the “basins” become flatter and the surface of the “relief” becomes smoother.

– **Grayscale reconstruction by dilation/erosion**

Let $f, g: R^n \rightarrow R$ and $f \geq g$. The geodesic reconstruction by dilation of f by g is defined as [128]:

$$\rho_f^\delta(g) = \delta_f^{(\infty)}(g), \quad (3.8)$$

with

$$\begin{aligned} \delta_f^{(1)}(g) &= (g \oplus H) \wedge f \\ \delta_f^{(n)}(g) &= \delta_f^{(1)}(\delta_f^{(n-1)}(g)) \end{aligned} \quad (3.9)$$

where H is a unit SE and $\delta_f^{(1)}(g)$ is the geodesic elementary dilation of g in f . Fig. 34 (a) illustrates the reconstruction by dilation of f by g on a 1-D example. Note that the reconstruction by dilation of f by g reconstructs only the “hills” of f marked by the regional maxima of g and imposes plateaus at the level of g maxima.

Let $f, g: R^n \rightarrow R$ and $f \leq g$. The geodesic reconstruction by erosion of f by g is defined as [128]:

$$\rho_f^\varepsilon(g) = \varepsilon_f^{(\infty)}(g), \quad (3.10)$$

with

$$\begin{aligned} \varepsilon_f^{(1)}(g) &= (g \ominus H) \vee f \\ \varepsilon_f^{(n)}(g) &= \varepsilon_f^{(1)}(\varepsilon_f^{(n-1)}(g)) \end{aligned} \quad (3.11)$$

where $\varepsilon_f^{(1)}(g)$ is the geodesic elementary erosion of g in f . Fig. 34 (b) illustrates the reconstruction by erosion of f by g on a 1-D example. Note that the reconstruction by erosion of f by g fills in the “basins” of the relief f by creating plateaus at most at the level of the local minima of g .

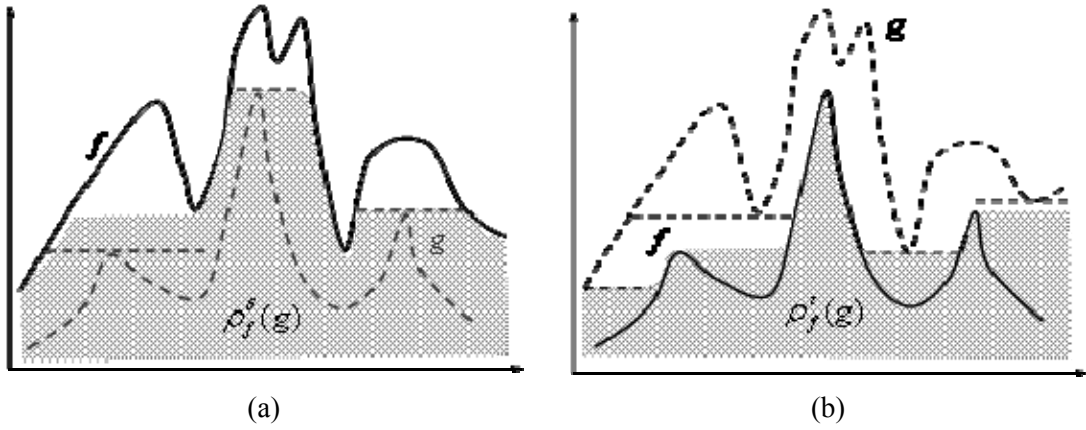


Fig. 34 Illustration of the morphological reconstruction by (a) dilation and (b) erosion of f by g on a 1-D example.

— **Connection cost**

Let $f: R^n \rightarrow R$ a function of connected support and upper-bounded, and $\lambda \in R$ a value of f . The threshold $X_{f,\lambda}$ of at level λ is defined as

$$(f, \lambda) \rightarrow X_{f,\lambda} = \{x \in \text{supp}(f), f(x) \leq \lambda\}. \quad (3.12)$$

The connection cost $C_f(x, y)$ [109] of two points $x, y \in R^n$ on f can be defined as

$$C_f(x, y) = \begin{cases} \wedge \{\lambda \in R / \delta_{f,\lambda}(x, y) < +\infty\} & \text{if } x \neq y \\ -\infty & \text{if } x = y \end{cases}, \quad (3.13)$$

where $\delta_{f,\lambda}$ is the geodesic distance relative to the threshold of f at level λ . Fig. 35 (a) illustrates concept of the connection cost of two points, x and y . If $Y \subset \text{supp}(f)$ denotes a non-empty subset, the connection cost of a point x with respect to Y can be defined as

$$C_f(x, Y) = \begin{cases} \wedge \{\lambda \in R / \delta_{f,\lambda}(x, Y) < +\infty\} & \text{if } x \notin Y \\ -\infty & \text{otherwise} \end{cases}. \quad (3.14)$$

Note that $C_f(x, Y)$ fills in all basins associated with the regional minima of f , except those located on the support of Y . The illustration of the connection cost with respect to Y is shown in Fig. 35 (b).

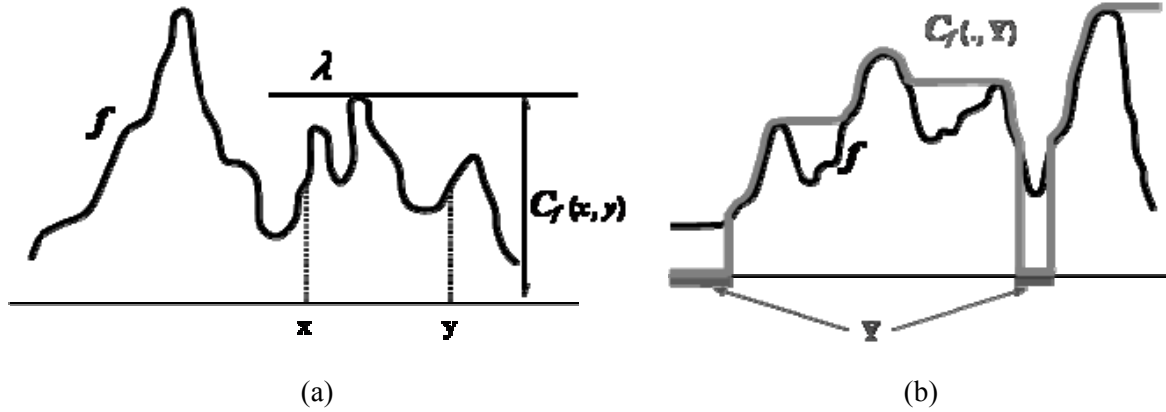


Fig. 35 Illustration of the connection cost in a 1-D case. (a) Connection cost of two points x and y , and (b) connection cost with respect to a non-empty subset Y .

In medical imaging applications, setting up the $C_f(x, Y)$ at $-\infty$ for all $x \in Y$ is constraining as the original f -intensities are removed. A slightly modified version of $C_f(x, Y)$ which is used in our approach processes the f values for $x \in Y$ and is defined as

$$C_f(x, Y) = \begin{cases} \wedge \{ \lambda \in R / \delta_{f, \lambda}(x, Y) < +\infty \} & \text{if } x \notin Y \\ f(x) & \text{otherwise} \end{cases} \quad (3.15)$$

The implementation of the modified version of the $C_f(x, Y)$ can thus be achieved by using the grayscale reconstruction by erosion:

$$C_f(., Y) = \rho_f^e(g_Y), \quad (3.16)$$

with

$$g_Y(x) = \begin{cases} +\infty & \text{if } x \notin Y \\ f(x) & \text{otherwise} \end{cases} \quad (3.17)$$

III.2.2 Segmentation of the lung mask with discrimination of large airways and high density structures

Basically, we can roughly use three threshold values to divide the lung parenchyma tissue grayscale range in low-density $[0, LD]$, medium-density $(LD, HD]$ and high-density $(HD, 255]$ values, where $LD = 10$, $MD = 65$, $HD = 100$. As the lung parenchyma is a mixture of airspaces and dense structures (vessels, bronchi, reticular patterns), the lung texture shows a large point-value variation, which increases in the presence of pathology or at smaller inflation volume (expiration).

Therefore, a lung segmentation procedure based on a low-value thresholding is not robust in the general case. Here, we exploit instead the fact that the lung field is enclosed by the thorax cage, of high and homogeneous intensity values, which allows an easy segmentation of the lung low-density regions by using the grayscale reconstruction by erosion

operator.

If $f: N^3 \rightarrow Z$ denotes the original 3-D image, a reference function g_{HD} is defined as:

$$g_{HD}(x) = \begin{cases} \vee (f(x), HD) & \text{if } x \notin \partial f \\ f(x) & \text{otherwise} \end{cases}, \quad (3.18)$$

where HD denotes the previous grayscale (or the Hounsfield unit) value assigned to high density regions in the lung and ∂f the border of the original volume data, the support of f , $\text{supp}(f)$.

By applying the operator of grayscale reconstruction by erosion of f with respect to g_{HD} , $\rho_f^e(g_{HD})$, the lung field is “filled in” up to the HD level and can be segmented by subtracting the original relief f (and binarizing the result). Note that other patterns outside the lungs can also be extracted by this procedure; however, the lung field connected by the large airways represents the largest 3-D connected component and can be easily isolated by means of a 3-D labeling operator, leading to the lung field subset, further denoted by f_L . Fig. 36 illustrates these steps on an axial cross-section image, while the 3-D segmentation result is shown in the coronal projection in Fig. 38 (a). Trachea and the main bronchi are furthermore assigned a different label from the lungs, L_{aw} , Fig. 38. In order to avoid affecting the shape of the lungs, the relabeling procedure should act locally, starting from a seed selected inside (at the top of) the trachea. While 2-D approaches dedicated to trachea and main bronchi detection have already been proposed in the literature [107], the success of a slice-by-slice detection may be subject to the anatomic variability concerning the airway morphology at the level of the hilum.

We have thus developed a robust 3-D procedure to detect the trachea and the main bronchi by directly “filling-in” these regions with the same value as the new assigned label (constrained region growing approach). Note that in f_L , the grayscale value corresponding to the lungs and airways is 255, whereas the other regions have a 0 value. The large airways labeling procedure on f_L performs as follows and is schematically illustrated in Fig. 37.

1. The trachea section is automatically detected on the first axial original image in the 3-D MSCT data [110], a seed s defined at its center and the radius r_t of the maximal inscribed disk computed.

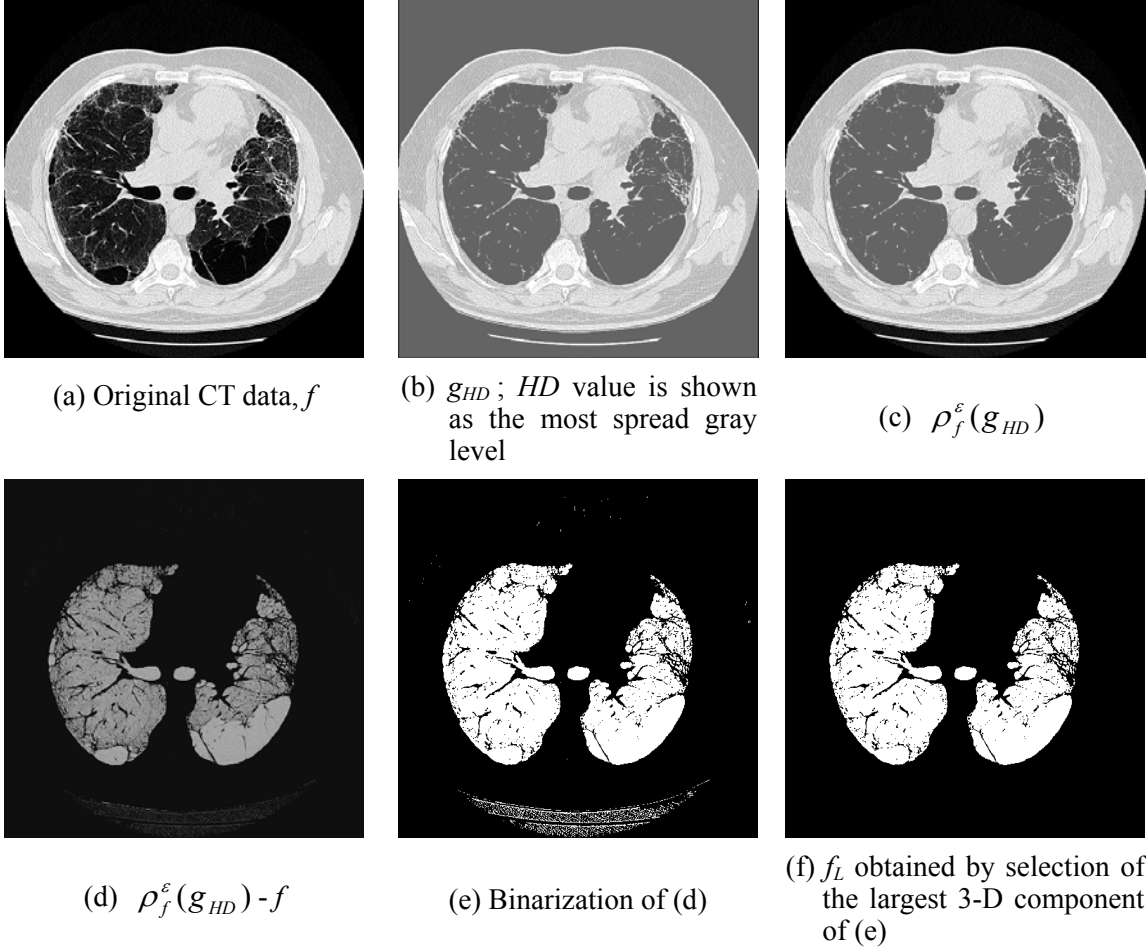


Fig. 36 Lung field segmentation algorithm illustrated on an axial image (case of emphysema-fibrosis). Note that the f_L subset in (f) comes from a single 3-D connected component.

2. The 3-D geodesic distance function with respect to the seed s and inside the 255-value subset f_L is computed, and further on denoted by $d_{f_L}(s)$.
3. A spherical structuring element $SE(r_s)$ of radius r_s is defined, Fig. 37 (a), and a constrained region growing procedure inside f_L is performed starting from the seed s . The region growing acts in f_L and builds up a subset T , Fig. 37 (b), by aggregating points \mathbf{x} which respect the following conditions:
 - the structuring element centered at \mathbf{x} , $SE(r_s)(\mathbf{x})$, should be inscribed in the 255-value subset of f_L , $SE(r_s)(\mathbf{x}) \subset f_L$,
 - the radius of the structuring element, r_s , increases with the distance to s :
$$r_s(\mathbf{x}) = \min(r_t/2, r_t/4 + 0.01 d_{f_L}(s)(\mathbf{x})), \quad (3.19)$$
in order to limit the propagation inside the main airways,
 - the region growing stops if $d_{f_L}(s)(\mathbf{x}) > d_{max} = 200 r_t$ to guarantee a limited penetration inside the lungs in the case of pathological airways (which do not taper in distality). The d_{max} value is here established based on heuristic tests performed on a large database (96 cases) of MSCT images from a COPD study [129].

4. Finally, for each point x of the T subset, and for all its neighbors $y \in SE(r_t)(x)$, we set $f_L(y) = L_{aw}$ if $d_{f_L}(s)(y) < d_{max}$, Fig. 37 (c). In this way, the airways are relabeled irrespective to their shape irregularities, while the surface of the lungs (even closer than r_t to the airways) is not affected, Fig. 37 (d). The result, denoted by $f_{L_{aw}}$, is illustrated in Fig. 38.

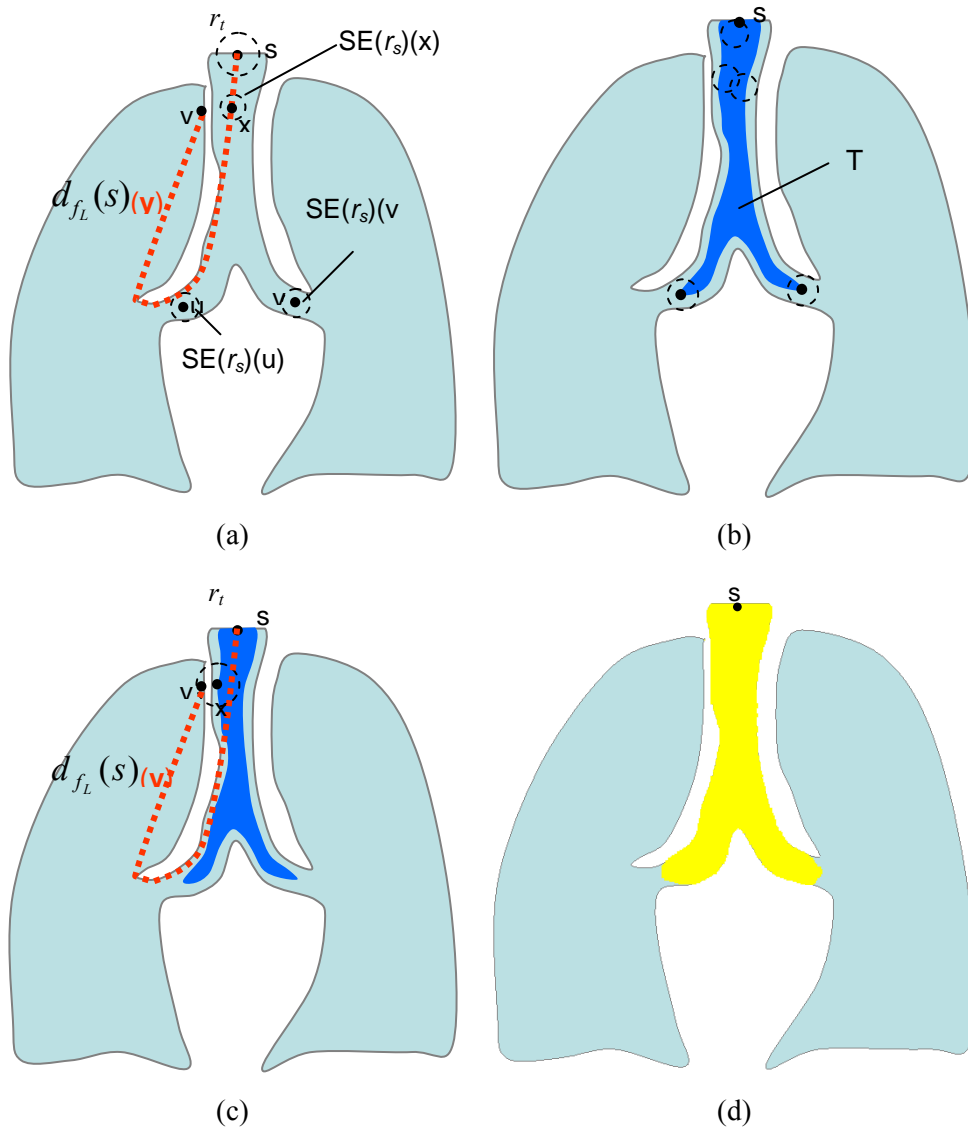
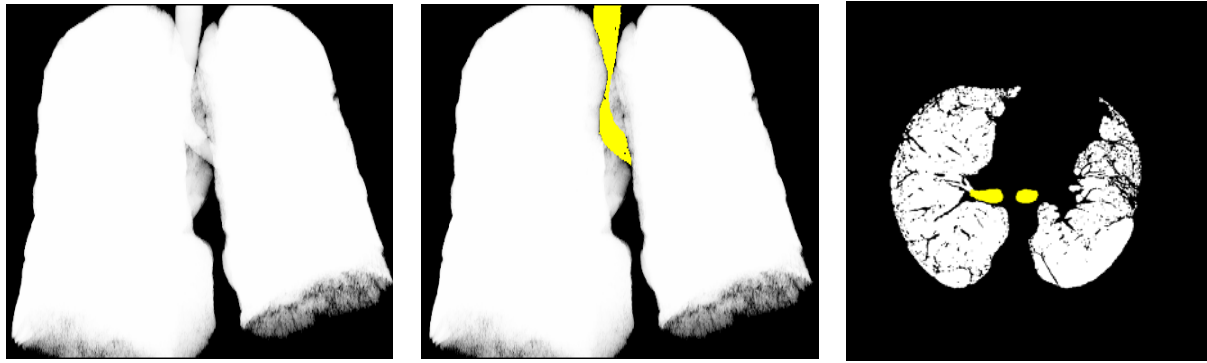


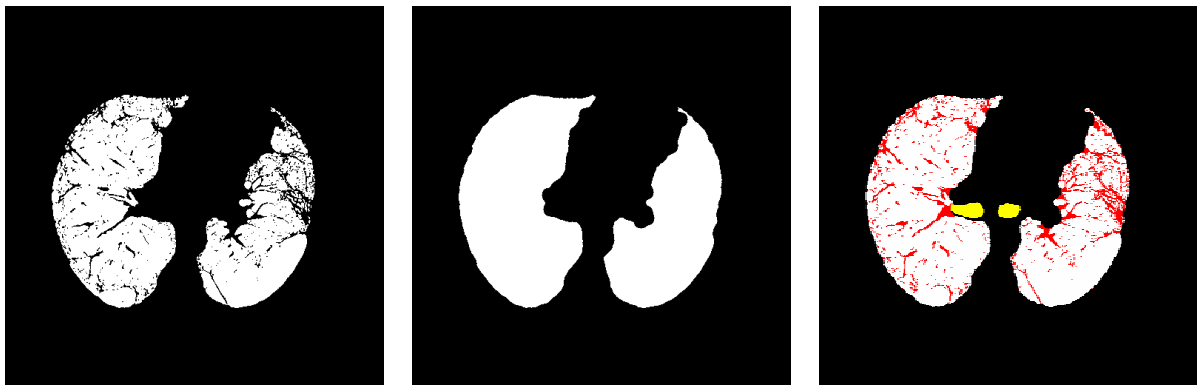
Fig. 37 Principle of airway relabeling: (a) definition of the structuring elements according to the size of the trachea cross-section (at s) and the geodesic distance with respect to s , $d_{f_L}(s)$; (b) constrained region growing resulting in the T subset; (c) local relabeling of each region in the T neighborhood, constrained by the geodesic distance value – which avoids affecting lung regions; (d) relabeled airways.



(a) f_L (b) f_{Law} (c) f_{Law} , axial image

Fig. 38 Large airways relabeling result, f_{Law} . Coronal projection and axial views.

Note that, the lung mask as extracted in f_{Law} contains holes corresponding to high opacities in the lung parenchyma (blood vessels, bronchus walls, fibrosis reticulations). In order to include these high intensities into the lung mask with a specific label L_{HD} , a lung shape filtering is performed as follows. A morphological closing with a $SE(r_s)$ is applied separately to each lung (ignoring the airway label), followed by a 3-D hole-filling operator performing in 6-connectivity, Fig. 39. The final lung mask, denoted by f_{LawHD} , is used to select the region from the original 3-D MSCT data which is further on taken into account for the lung partitioning into ROIs via a multi-resolution decomposition scheme.



(a) (b) (c)

Fig. 39 Inclusion of high-density regions into the lung mask (illustration on an axial image): (a) lung mask without the airway label, (b) lung field obtained by morphological closing and hole-filling, (c) final lung mask including the large airways (yellow) and high density regions (red).

III.3 Multi-resolution Decomposition Scheme

The multi-resolution analysis aims to provide the characteristics of the parenchyma texture at different scales. While several multi-resolution pyramids can be used, such as Gaussian, Laplacian, granulometry, etc., our objective was to preserve the shape of the

structures across the scales. The analysis is focused on the detection and extraction of the low-intensity regions at several resolutions based on a controlled flooding scheme. In this way, the lung region is decomposed in patterns corresponding to catchment basins of increasing width among which the EM and FHC low-intensity regions are selected.

A structured and simplified relief (pyramid) of the lung parenchyma is thus obtained, which can be analyzed by means of graph inference. The multi-resolution description scheme relies on a 3-D morphological filter—the flood size-drain leveling (FSD)³ [111]—which is sequentially used in conjunction with other morphological operators and is described in detail in the following.

III.3.1 Flood size-drain leveling

The flood size-drain leveling (FSD) is a morphological filter derived from the previous operators which has the property to “flood” the relief basins according to a size criterion. Let FSD be denoted as FD_f^m , where f represents the grayscale function $f: X \subset R^n \rightarrow R$, and m is the filter size.

The FSD principle consists of flooding a relief f up to a draining level imposed by a constraint related to the size of the basins of f . This procedure can be defined by means of the grayscale reconstruction by the erosion operator as:

$$FD_f^m = \rho_f^\varepsilon(h_m) = \varepsilon_f^\infty(h_m) \quad (3.20)$$

where $\rho_f^\varepsilon(h)$ represents the grayscale reconstruction by erosion of f by h , and h_m denotes the draining constraint function.

If a specific draining constraint is desired on a given subset $Y \subset \text{supp}(f)$, the h function becomes

$$h_{m,Y} = (f \bullet D_m) \wedge g_Y \quad (3.21)$$

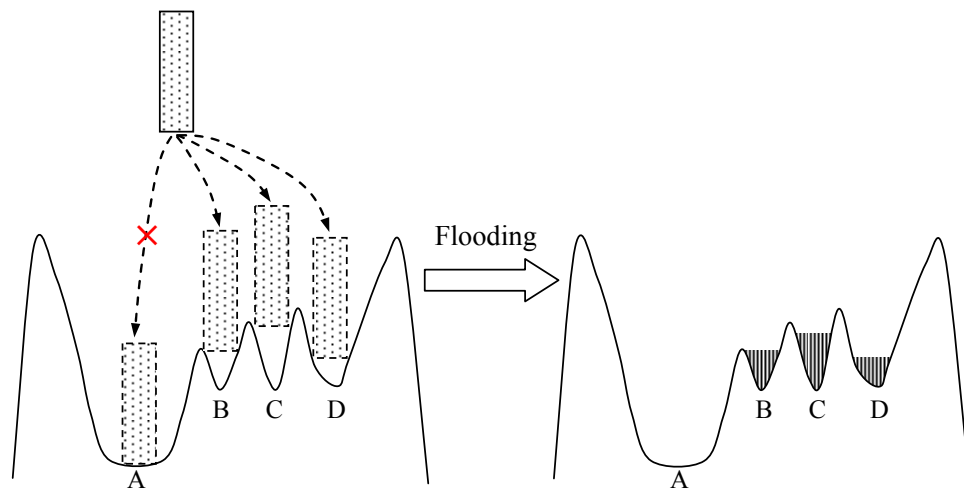
where D_m denotes the disk SE of radius m (defined in the axial plane) and g_Y is given by eq. (3.17). The general formulation of the FSD filter becomes:

$$FD_f^m(\cdot, Y) = \rho_f^\varepsilon(h_{m,Y}). \quad (3.22)$$

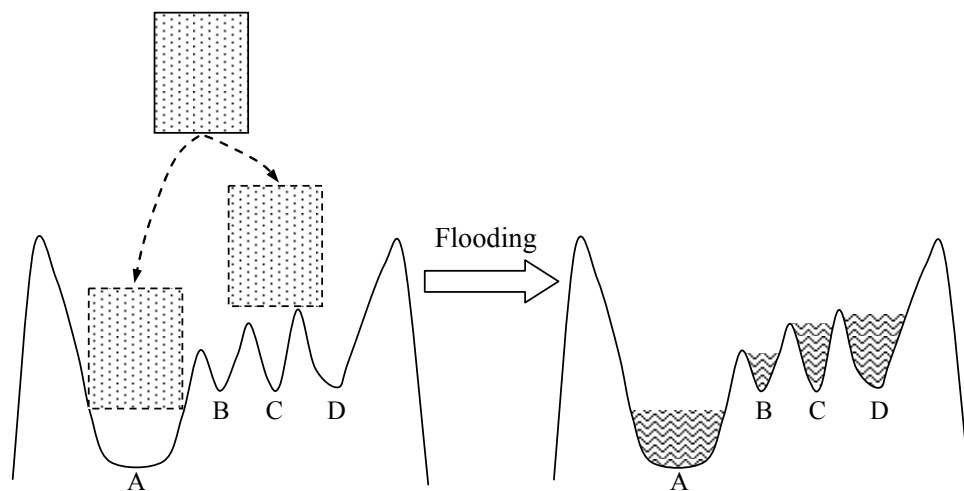
From an intuitive point of view, the FSD “fills in” a given region of f if the region satisfies two conditions: it should be basin-like on the relief f and its size has to be smaller than the current size of the FSD filter. Namely, if a draining pipe can be put into a basin and stopped by the wall of the basin, or if the size of the pipe is larger than the basin size, the basin is flooded until water touches the bottom of the pipe; otherwise, if the size of the pipe is smaller than the basin one, the basin is not flooded. Fig. 40 illustrates the flooding concept of the FSD

³ this filter was previously introduced under the name of *sup-constraint connection cost*

filter. In Fig. 40 (a), a pipe with size $m = m_1$ checks basins with different sizes. The size of the basin A is large, so that the pipe penetrates until the bottom of the basin A. For basins B, C, and D, the size of the pipe is large enough to be locked by the walls of the basins. So, the basins B, C, and D were flooded, as shown at the right of Fig. 40 (a). Note that the heights of water in the basins are according to where the pipe was stopped. In Fig. 40 (b), the size of the pipe is m_2 , where $m_2 > m_1$. For the basin A, the pipe is locked at the middle of the wall of the basin, and for the basins B, C, and D, the size of the pipe is larger than the sizes of the basins. Hence, the basin A was flooded until the bottom of the pipe, and the basins B, C, and D were filled in, as shown at the right of Fig. 40 (b).



(a) the filter size $m = m_1$



(b) the filter size $m = m_2$

Fig. 40 The flooding concept of the FSD filter. The flooded basins are drained by a pipe with (a) the size $m = m_1$, and (b) the size $m = m_2$, where $m_1 < m_2$. When the size $m = m_2$, basin A was partially flooded, and basins B, C, and D were completely filled in, as their sizes were smaller than m_2 .

Note that the FSD is a strong morphological filter as it verifies the following conditions. Using the notation $\psi = FD_f^m(\cdot, Y)$, for a given $Y \neq \emptyset$, $m \in R_+^*$:

$$\text{filter} \begin{cases} \text{idempotent: } \psi \circ \psi = FD_\psi^m(\cdot, Y) = \psi \\ \text{increasing: } f \leq g \Rightarrow FD_f^m(\cdot, Y) \leq FD_g^m(\cdot, Y) \end{cases} \quad (3.23)$$

and

$$\text{strongness} \begin{cases} \wedge\text{-filter: } \psi \circ (f \wedge \psi) = \psi \circ f = \psi \\ \vee\text{-filter: } \psi \circ (f \vee \psi) = \psi \circ \psi = \psi \end{cases} \quad (3.24)$$

In addition, the FSD shows two important properties which are exploited in the developed multi-resolution analysis scheme:

$\forall m_1, m_2 \in R_+^*$, $m_1 < m_2$, $f: R^n \rightarrow R$, $Y \subset \text{supp}(f)$, and $Y \neq \emptyset$

– increasing with respect to SE size:

$$FD_f^{m_1}(\cdot, Y) \leq FD_f^{m_2}(\cdot, Y), \text{ and} \quad (3.25)$$

– stacking:

$$\text{if } g = FD_f^{m_1}(\cdot, Y), \text{ then } FD_f^{m_2}(\cdot, Y) = FD_g^{m_2}(\cdot, Y). \quad (3.26)$$

The impact of the size of the SE on the relief “flooding” reaches two extrema as follows:

– no “flooding”:

$$m = 0 \Rightarrow FD_f^m(\cdot, Y) = f \quad (3.27)$$

– full “flooding”:

$$m = \infty \Rightarrow FD_f^m(\cdot, Y) = C_f(\cdot, Y) \quad (3.28)$$

Note that, throughout the “flooding” process, the FSD operator preserves the contours of the basins in the relief f , unless they are completely flooded in a larger basin. This property is illustrated in Fig. 41, where the FSD operator is compared with the morphological closing with the same SE.

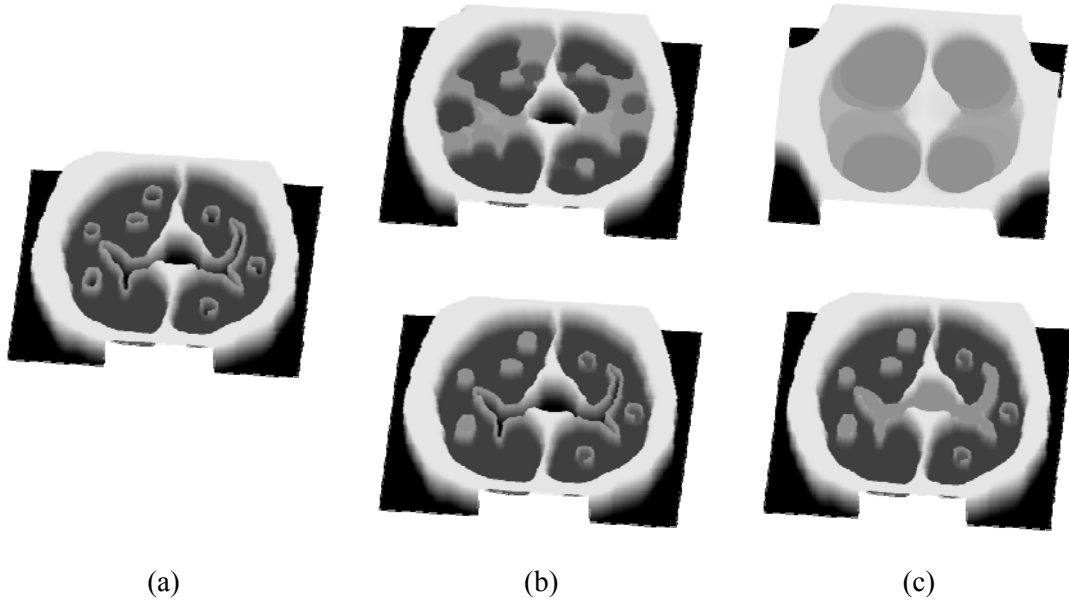


Fig. 41 Illustration of the structure contour preservation by the FSD. (a) Image interpretation in terms of topographic relief f , (b) $f \bullet D_m$ (top) and FD_f^m (bottom) with the size $m = m_1$, and (c) same as (b) for the size $m = m_2$, where $m_1 < m_2$.

III.3.2 The Multi-resolution Decomposition Approach

The multi-resolution approach proposed for the analysis of the parenchyma tissue exploits the FSD filter in the following manner. By progressively increasing the size of the FSD structuring element which defines the resolution level of the analysis, an incremental flooding of the image relief is achieved, according to the size of the basins in the relief.

The relief information extracted at each level is related to the regions affected by the flooding with respect to the previous level. The stacking property of the FSD, as defined in eq. (3.26), is here exploited for the analysis at a given level of resolution.

In order to illustrate the developed approach, let us consider a representation of the lung tissue intensity in a CT image as a topographic “relief”, f , which is composed of thorax cage, vessels, airways, normal tissue, emphysema, fibrosis and ground glass. Fig. 42 shows such a 1-D representation, where the ordinate denotes the gray-level intensity. Here, a “hill” stands for a blood vessel or an airway wall, a “basin” represents the different low-density patterns, such as alveolar, bronchial or destroyed patterns within emphysema and fibrosis, and clustered “holes” on a plateau represents destroyed patterns with ground glass. Gray-levels of voxels within a blood vessel, an airway wall, and a ground glass pattern, are larger than in voxels within emphysema and fibrosis, and the gray-level range of normal tissue is comprised between emphysema and ground glass patterns.

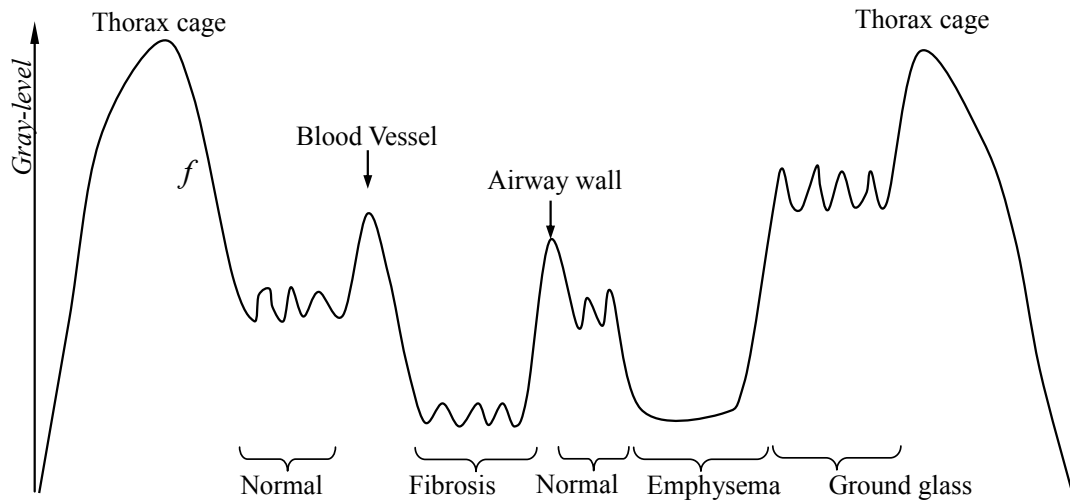


Fig. 42 Representation of normal and pathological tissues in 1-D domain (solid line) as a topographical “relief” f .

By applying the FSD filter FD_f^m with an increasing size m , all local basins of f are progressively flooded, as shown in Fig. 43 (a)-(d), where m takes successively the values $m_0 < m_1 < m_2 < m_3$.

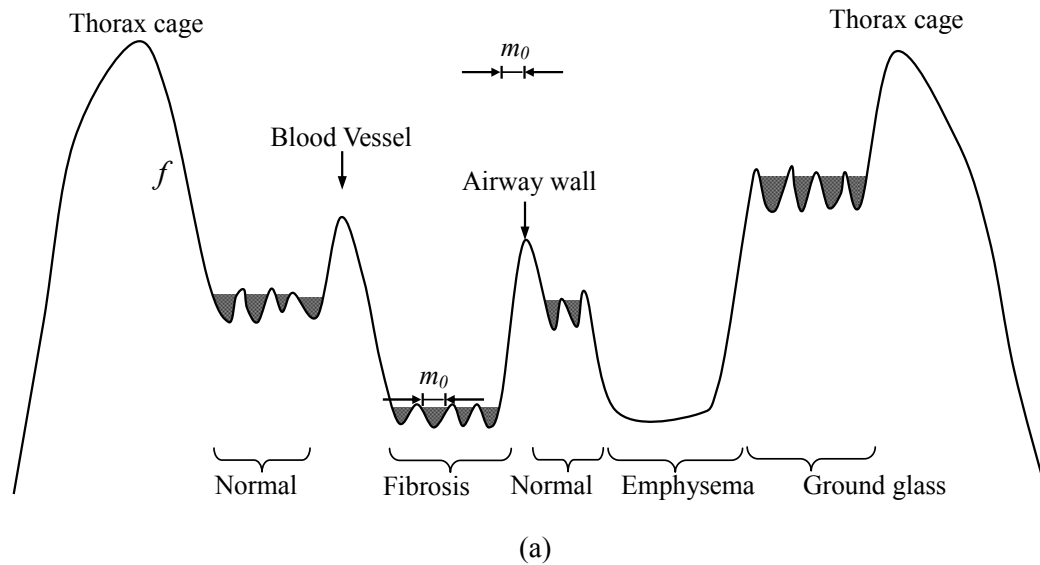
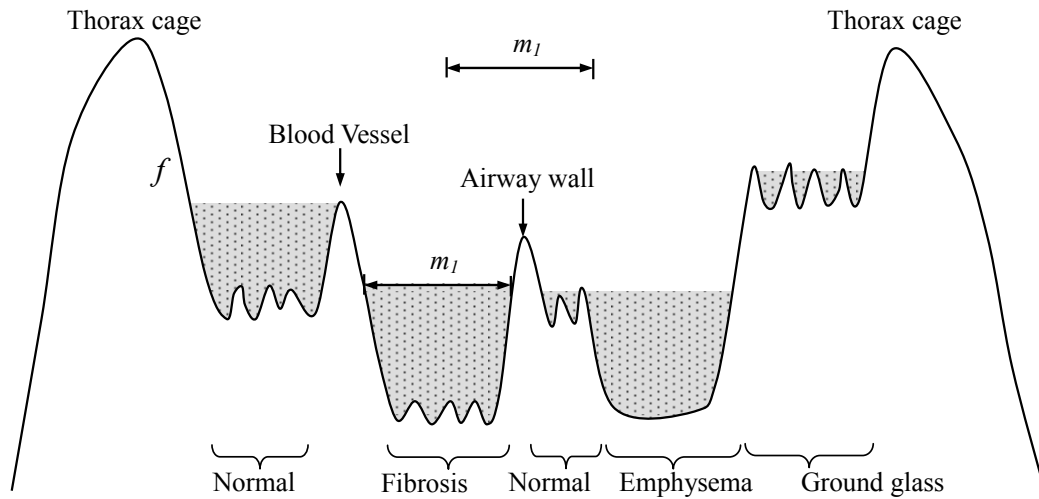
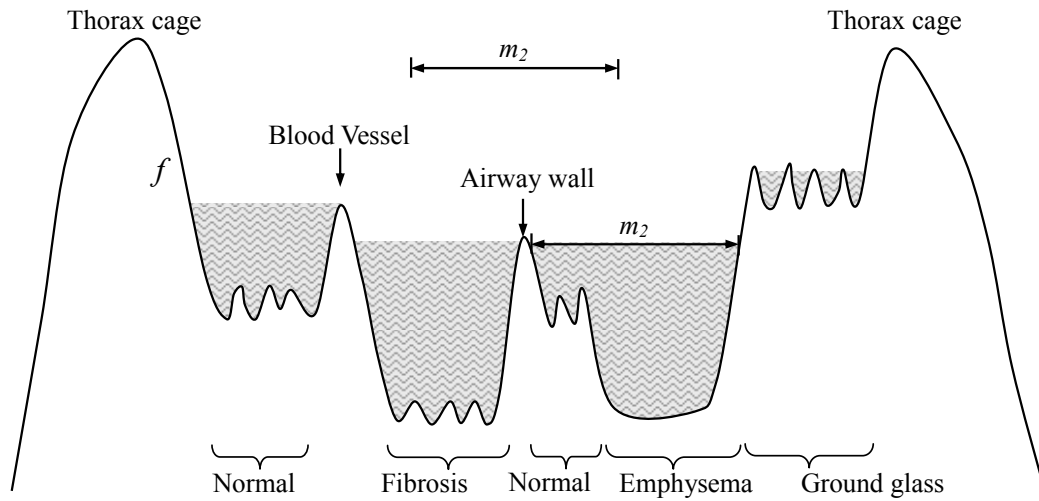


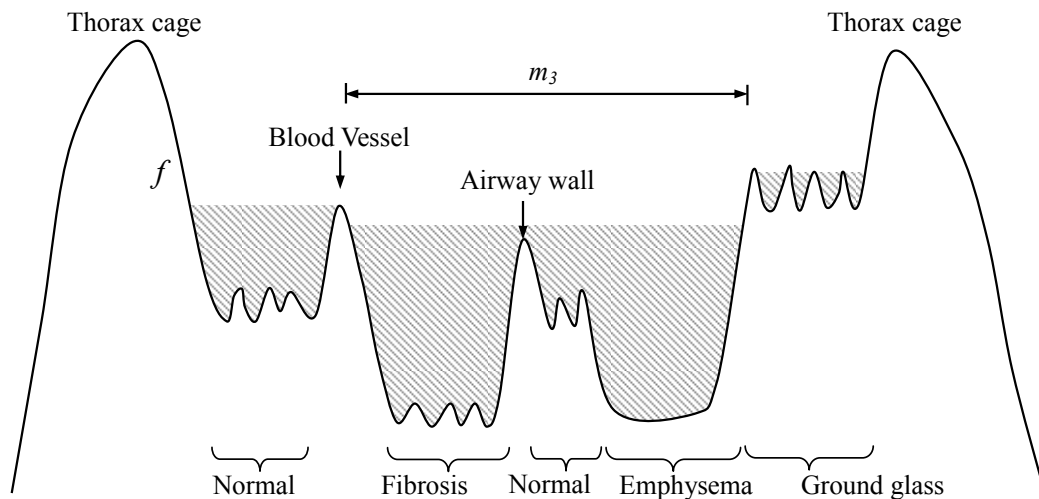
Fig. 43 On a topographical “relief” f , the effect of the FD_f^m filtering with (a) $m = m_0$, (b) $m = m_1$, (c) $m = m_2$, and (d) $m = m_3$, where $m_0 < m_1 < m_2 < m_3$.



(b)



(c)



(d)

Fig. 43 (Continued). On a topographical “relief” f , the effect of the FD_f^m filtering with (a) $m = m_0$, (b) $m = m_1$, (c) $m = m_2$, and (d) $m = m_3$, where $m_0 < m_1 < m_2 < m_3$.

During the relief flooding, the multi-resolution analysis consists of detecting the lung patterns affected at each resolution level. If l denotes a resolution level and m_l denotes the associated size of the FSD filter, the lung pattern P_l detected at level l is given by:

$$P_l = \bigcup_{x \in \text{supp}(f)} \{x \mid FD_f^{m_l}(x) - FD_f^{m_{l-1}}(x) > 0\} \quad (3.29)$$

The union of these patterns $P_l, l = \overline{0, m_l}$, forms a lung parenchyma decomposition into low-density regions. Fig. 44 illustrates the decomposition of the lung relief of Fig. 43 for 4 levels of resolutions.

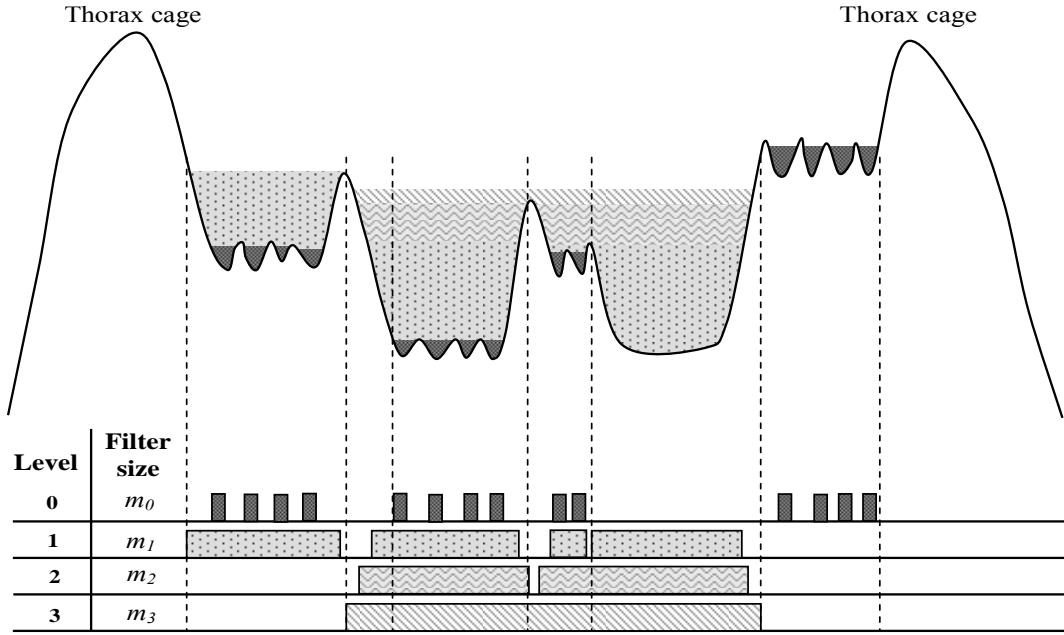


Fig. 44 Multi-resolution decomposition (bottom) of the schematic lung “relief” f by successive FD_f^m filtering with increasing size m (top).

Another decomposition example of a 2-D lung relief is shown in Fig. 46 for 7 levels of resolution. Note that the stacking property of the FSD filter guarantees that:

$$P_{l-1} \subseteq P_l, \text{ if } P_{l-1} \cap P_l \neq \emptyset \quad (3.30)$$

where $m_{l-1} < m_l$, cf. eq. (3.29). Based on the property of eq. (3.30), a decomposition pyramid D_f of the relief f can be built-up by associating to each pattern P_l a decreasing gray-level G_l with respect to the increasing resolution level l :

$$\forall x \in P_l, \quad G_l(x) = L - l \quad (3.31)$$

where L denotes the maximum gray-level of the f intensity range. The decomposition pyramid is defined as:

$$D_f(x) = \bigvee_{l \in [0, l_{\max}]} G_l(x). \quad (3.32)$$

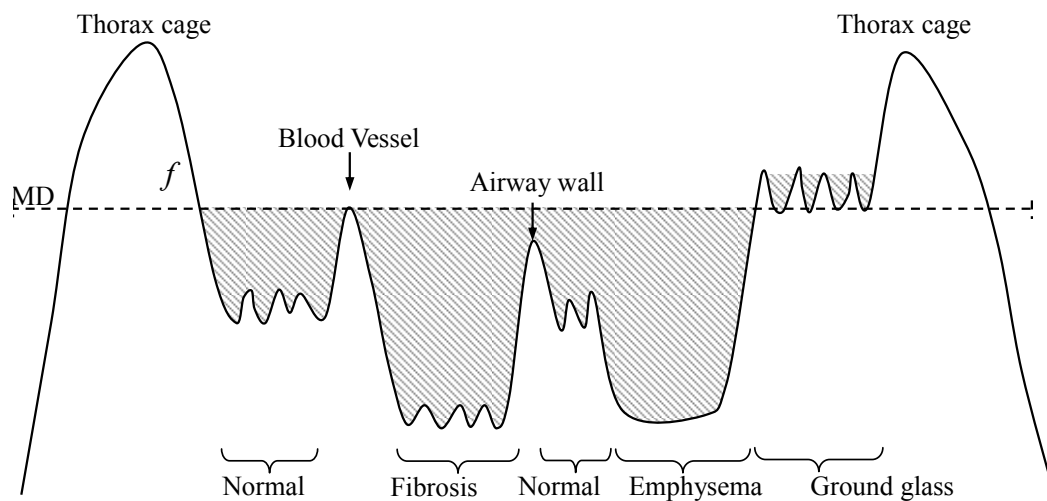
Note that, according to the choice of the number of decomposition levels l_{\max} , the “flooding” effect of the FD_f^m filter $m = m_{l_{\max}}$ might not be total for the lung field. In order to guarantee

a level of flooding at least as high as the medium density (MD), an additional flooding step is considered such as applied in the lung segmentation approach (Section III.2.2), Fig. 45 (a). This final step called MD-leveling will provide the largest pattern P_b , $b = l_{max}+1$, in the decomposition pyramid as:

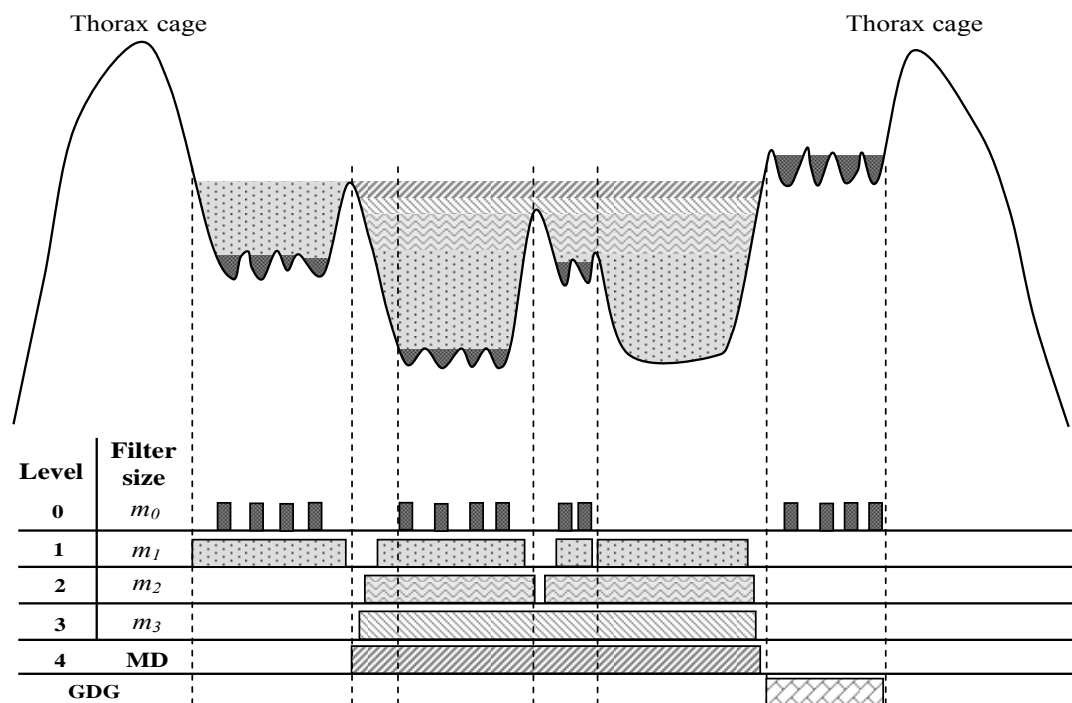
$$P_b = \bigcup_{x \in \text{supp}(f)} \{x \mid \rho_f^{\varepsilon_l}(g_{MD}(x)) - FD_f^{m_{l-1}}(x) > 0\} \quad (3.33)$$

where $\rho_f^{\varepsilon}(g)$ denotes the grayscale reconstruction by erosion and g_{MD} is given by eq. (3.18) by replacing HD with MD. The decomposition pyramid is thus updated according to eq. (3.31) and (3.32) for $l \in [0, l_{max} + 1]$.

As the multi-resolution procedure targets mostly low-density regions, ground glass patterns may not be present in the decomposition pyramid. In order to include also this kind of tissue in the analysis, the potential GDG regions will be associated with the flooded relief zones of the lung field, Fig. 45 (a), having the intensity between MD and HD values. GDG regions will be added at the "base" level in the decomposition pyramid, as shown in Fig. 45 (b). The resulting decomposition pyramid for the example of Fig. 45 is illustrated in Fig. 47.

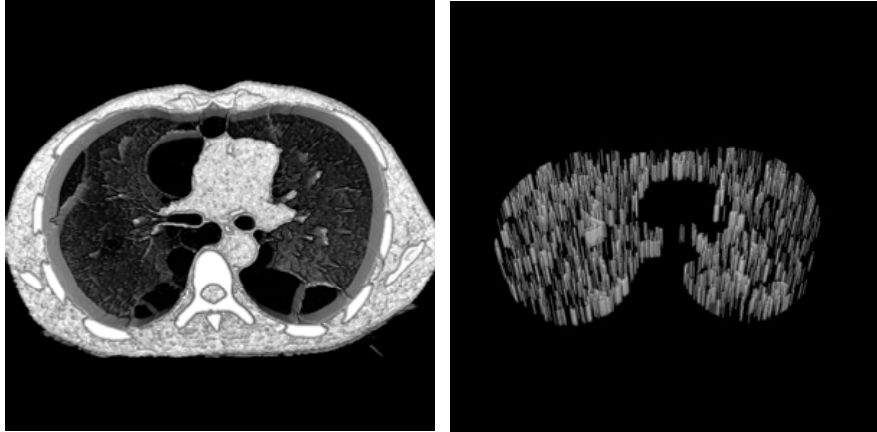


(a)

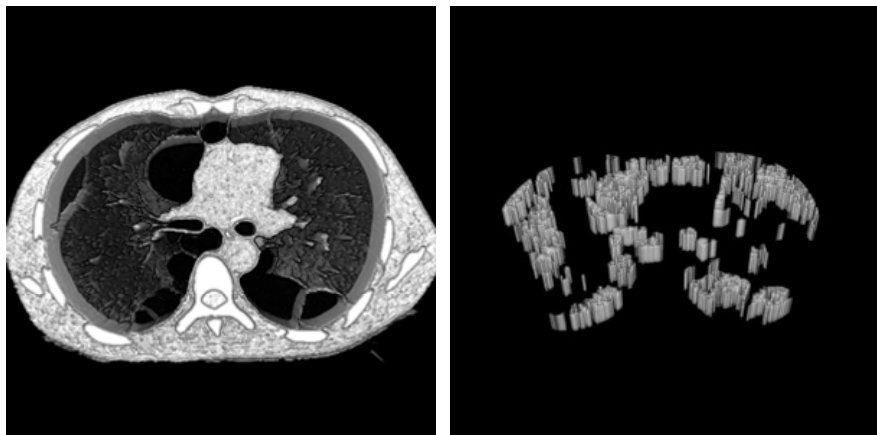


(b)

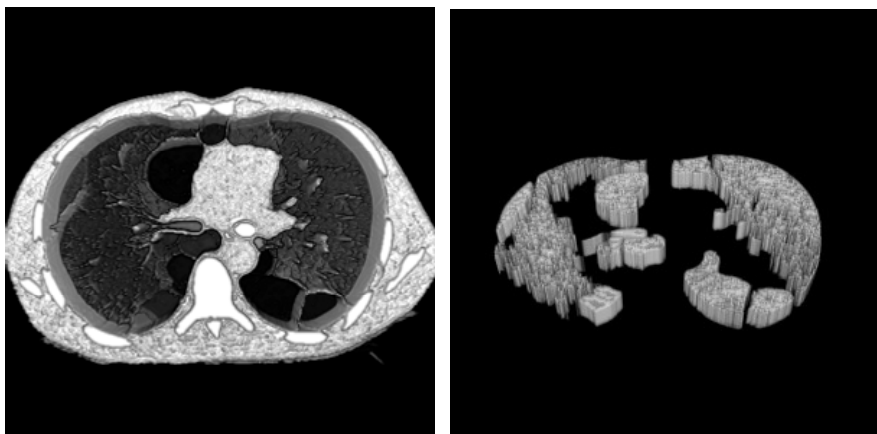
Fig. 45 (a) The MD-leveling result for Fig. 42, and (b) the resulting decomposition updated from Fig. 44 and including the GDG level.



(a) level 1

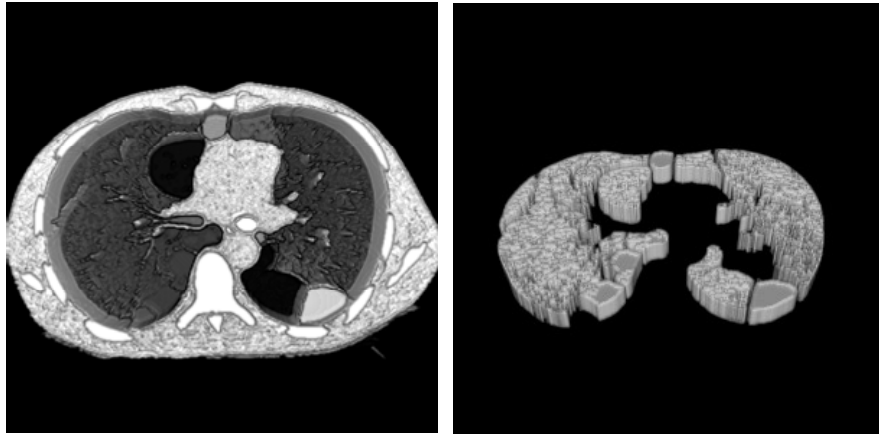


(b) level 2

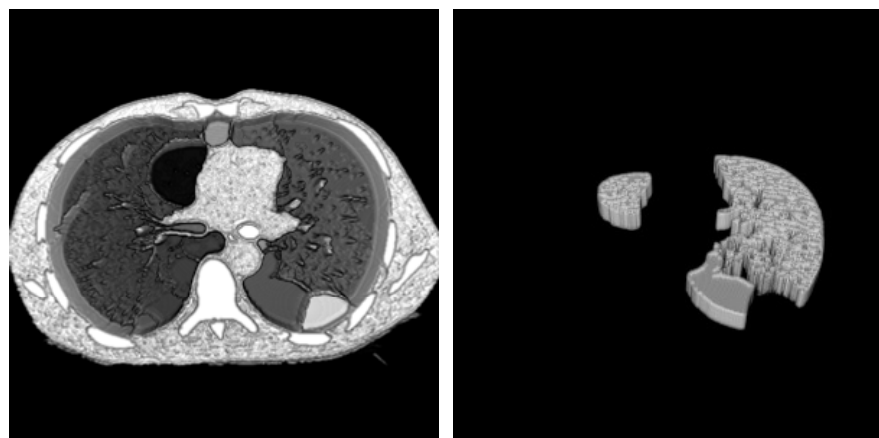


(c) level 3

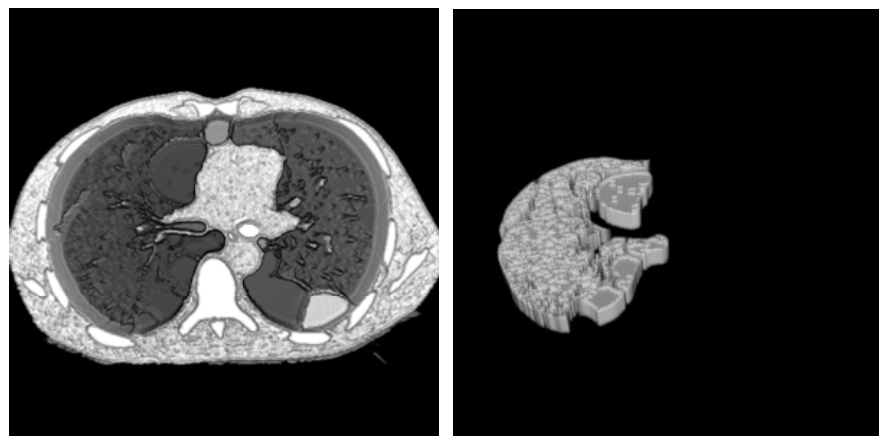
Fig. 46 The result of multi-resolution decomposition for 2-D lung relief by using 7 levels of resolutions. Note that the left side images show the flooded relief at each level and the right side ones show the corresponding patterns extracted at each level. The final levels corresponding to the MD leveling and GDG are not shown.



(d) level 4

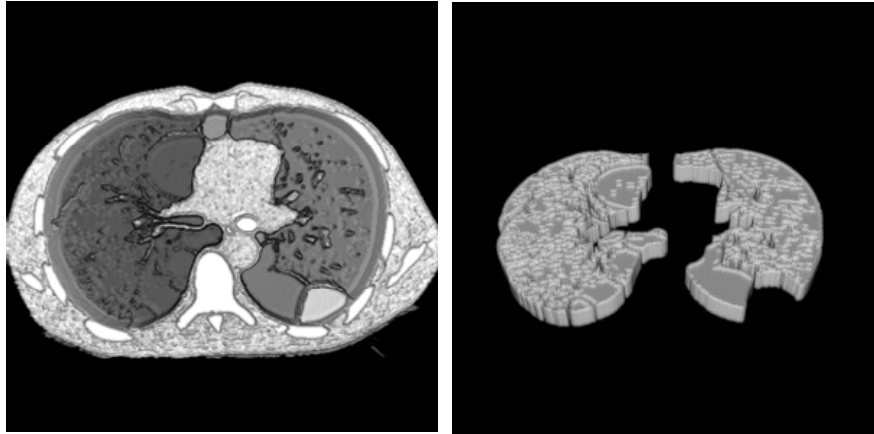


(e) level 5



(f) level 6

Fig. 46 (Continued). The result of multi-resolution decomposition for 2-D lung relief by using 7 levels of resolutions. Note that the left side images show the flooded relief at each level and the right side ones show the corresponding patterns extracted at each level. The final levels corresponding to the MD leveling and GDG are not shown.



(g) level 7

Fig. 46 (Continued). The result of multi-resolution decomposition for 2-D lung relief by using 7 levels of resolutions. Note that the left side images show the flooded relief at each level and the right side ones show the corresponding patterns extracted at each level. The final levels corresponding to the MD leveling and GDG are not shown.

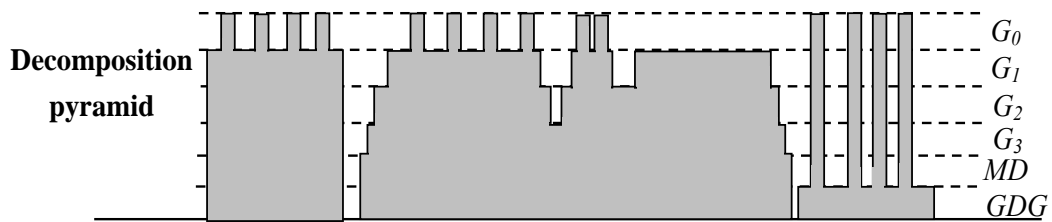


Fig. 47 The result of decomposition pyramid for the example of Fig. 45.

III.4 Hierarchic Description

In the multi-resolution decomposition scheme, a lung volume is decomposed into patterns with an increasing size m at successive levels. For each pattern, properties of the size and gray-level distribution are analyzed and extracted as criteria for classification. In addition, in order to check the existence of clustering of low-density patterns, we have to cross-analyze patterns of different resolution levels. Such cross-analysis relies on the spatial connectivity existing between patterns of different resolution levels, which can be described by a graph structure built up from the lung decomposition pyramid. In this section, we present the construction of such a description graph structure which has a tree topology due to the stacking property of the FSD-based lung relief decomposition.

III.4.1 Definition

In graph theory, a tree is an undirected simple graph that should satisfy the following conditions:

- A tree is connected and acyclic.
- If any edge is added to a tree, a cycle is form.
- If an edge is removed from a tree, the tree is separated into two partitions.
- Any two vertices in a tree are connected by a unique simple path.

If a vertex is designated as a “root”, the vertex has no superior and the edges have a natural orientation away from the root in the tree. In such rooted tree structure, a hierarchy can be inferred and represented in a graphical form. The components and the relationships introduced by a hierarchic tree structure T are briefly described in the following.

– Node and branch

In T , the components representing vertices are called “nodes”, and the “links” between nodes are called “branches”. Two nodes are called “adjacent” if the graph does not admit the insertion of an intermediary node between them.

– Depth and level

In T , the “depth” of a node V_i is the “length” of the path from the root to V_i with the convention that the length of a branch between adjacent nodes is 1. Also, the set of nodes with the same depth is called a “level” of the tree; that is all the nodes have associated a given level. Note that, by convention, the root has a zero depth.

– Parent, child, and sibling

In T , if there is a branch between the node V_i at level $m - l$, $l > 0$, and the node V_j at level m , the node V_i is the “parent” of the node V_j ; that is the node V_j is the “child” of the node V_i . Note that a node that has no child is called a “leaf”. The “siblings” (“brothers”) are nodes that share the same parent node.

Fig. 48 shows an example of a tree structure. Here, node A is a root at level 0, and the depth of node E is 2. Also, node B is the parent of node E , and node D is a sibling of node E because they are children of node B . Also (A, B) , (B, D) , (A, C) , (B, E) , (E, G) , (E, H) , and (C, F) are adjacent nodes while (C, D) are not adjacent.

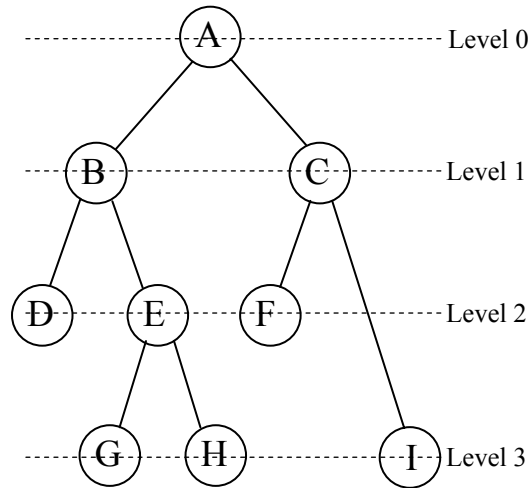


Fig. 48 An example of a tree structure.

III.4.2 Hierarchic Tree Structure

As discussed in Section III.3.2, the lung relief was decomposed into a pyramid of low-density patterns by using the FSD based multi-resolution decomposition scheme (Fig. 47). According to the stacking property of the FSD filter, the decomposition patterns of the pyramid can be represented as nodes of a hierarchic multiple tree structure where branches denote a connectivity relationship between patterns at different resolution levels. Let patterns p_i and p_j respectively denote basins A_i and A_j , as shown in Fig. 49, where the basin A_i is enclosed by the basin A_j in the f relief. In the decomposition pyramid, the pattern p_i is stacked on the pattern p_j , as the basin A_i is flooded by the FSD filter $FD_f^{m_i}$, and the basin A_j is flooded by $FD_f^{m_j}$, where $m_i < m_j$. In addition, patterns on the same resolution level may come from basins of various “altitude”, but in all cases they characterize basins disconnected at that resolution level. In the example of Fig. 49, the patterns circled by a red dotted ellipse and the patterns circled by a blue dotted ellipse are extracted by the filter size m_0 at level 0 and they are close to each other, but they are stacked on different patterns decomposed by the filter size m_1 at level 1. That is because the two pattern (basin) groups are respectively enclosed by different larger basins. Another consequence of the stacking property is that if a pattern p_i at level i is spatially connected with a pattern p_j at level j where $i < j$, then $p_i \subset p_j$. The intersection between patterns p_i and p_j corresponds to the same 3-D spatial location in the lung, which means that such decomposition provides a characterization of the same regions in the lung at different resolution levels. Fig. 50 illustrates the stacking property on the 2-D example of Fig. 46.

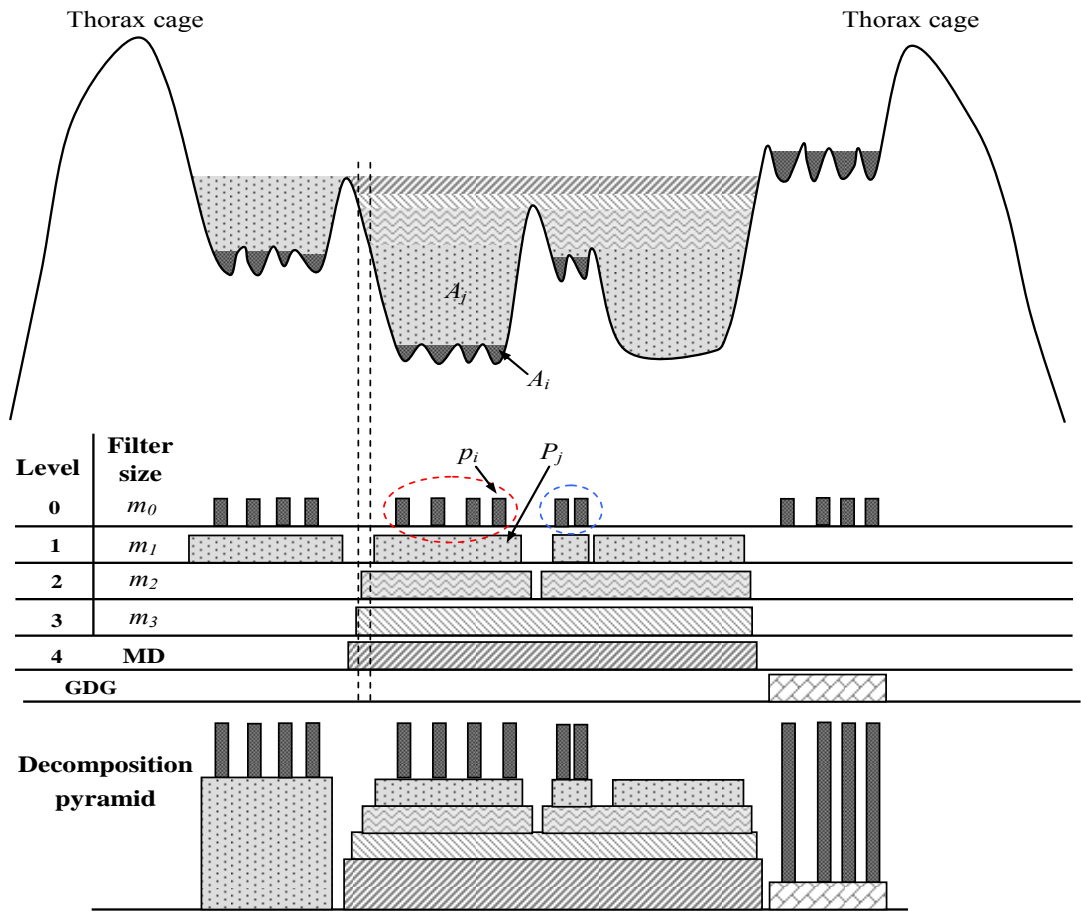


Fig. 49 The decomposition pyramid of low-density regions (basins) in the relief.

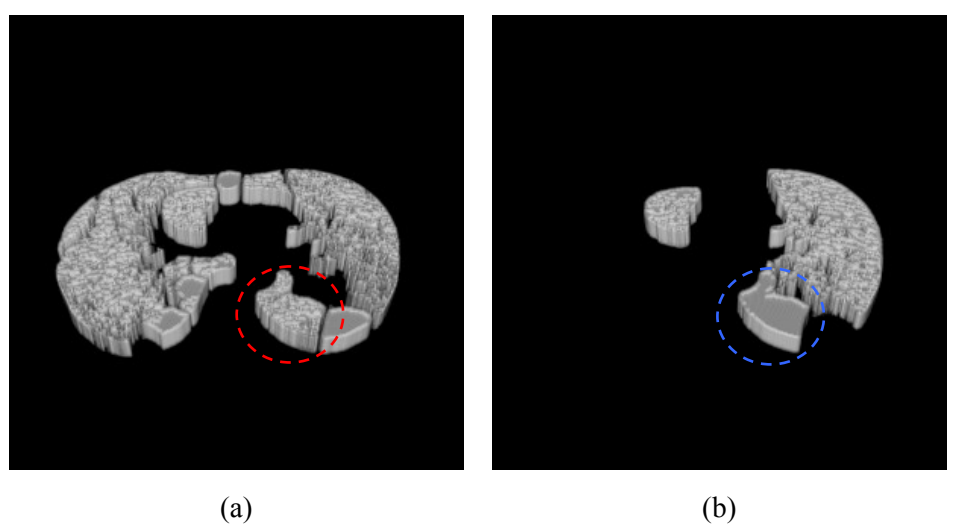


Fig. 50 The decomposition results at (a) level 4 and (b) level 5 in Fig. 46. Note that, in (a), a pattern indicated by a red dotted ellipse is included in a larger pattern indicated by a blue dotted ellipse, as shown in (b).

The hierarchic tree graph structure associates a node t_i with each pattern p_i of the decomposition pyramid P_f . A branch B_{ij} between node t_i and t_j is setup iff the patterns p_i and p_j

associated with t_i and t_j verify $p_i \subseteq p_j$ or $p_j \subseteq p_i$. B_{ij} is a directional branch in the sense parent-child, where the parent node corresponds to the largest pattern among p_i and p_j , that is the one on the higher decomposition level according to the FSD stacking property. The tree structure may be disconnected, consisting of disconnected sub-trees, and thus may have several root nodes. Fig. 51 illustrates the descriptive graph associated with the decomposition pyramid of Fig. 45 (b). Note that tree branches may exist only between nodes at different pyramid levels. Indeed, a graph branch B_{ij} means a spatial connectivity between patterns p_i and p_j , and if p_i and p_j would be at the same decomposition level, they would form a single pattern. Also, the reader should not mix up decomposition level and graph level as defined in Section III.4.1. In our case, these notions are complementary since the 0-decomposition level corresponds to the “leaves” of the descriptive tree graph. In the following, whenever we use the notion of level, it refers to the decomposition level unless specifically mentioned otherwise.

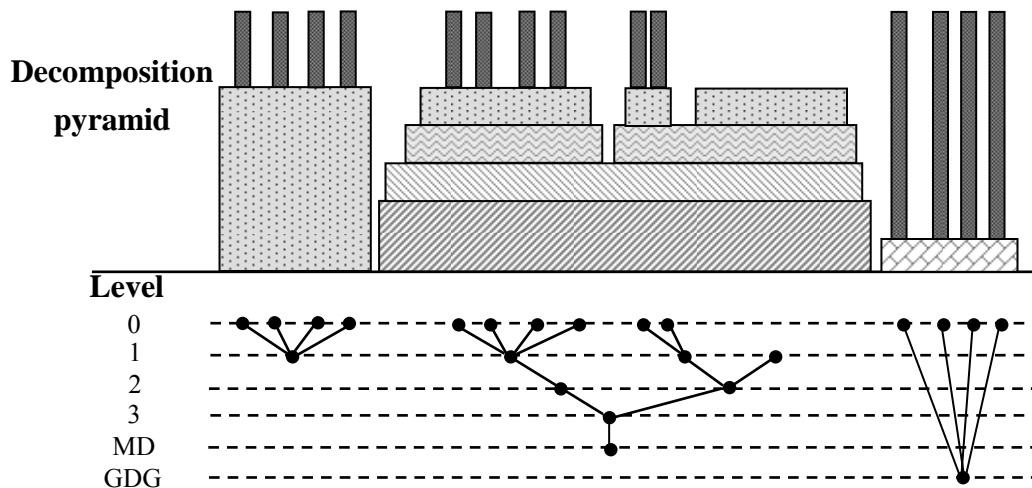


Fig. 51 The hierarchic description of multi-resolution decomposition result in terms of tree structure.

The descriptive tree structure of a decomposition pyramid allows an easy manipulation and analysis of the connectivity properties across different scales and may stress out pattern clustering. Moreover, additional properties related with the represented patterns are included at each node in order to increase the efficacy of the pattern classification over the scales. Such properties are related to the density of the pattern and of its surroundings, but also to its shape and size. They are described in detail in the next section for the classification stage. The implementation of the tree descriptive structure is performed as a binary tree along the relationship parent-child-brother. Namely, a node only “sees” its first “child“ and the “child” points out to its next “brother”, thus establishing a bifurcation of a binary tree. Fig. 52 shows an example of the implementation of a simple tree descriptive structure.

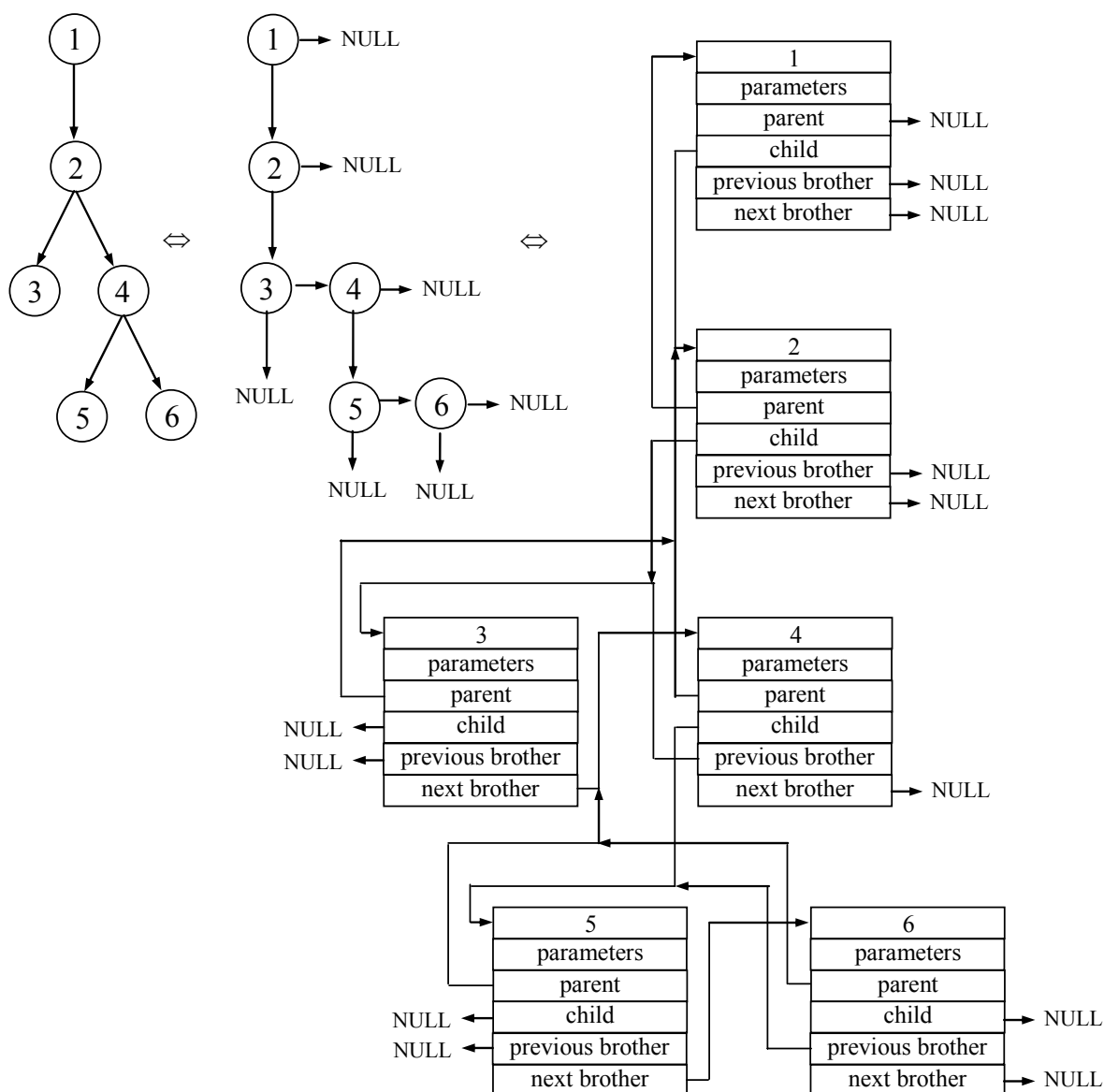


Fig. 52 The implementation of the tree descriptive structure: equivalence with a binary tree.

In order to speed up the navigation inside the tree, the binary structure is enriched at the level of each node with pointers towards the parent and the previous brother. The inclusion of pattern properties at each node requires that the descriptive graph is built at the same time as the decomposition pyramid, as follows.

In the implementation, we suppose that the tree structure T was updated for the levels $i < j$. For each pattern $p_{j,k}$ extracted at level j from the pyramid:

- (1) a new node $t_{j,k}$ is created with a spatial coordinate inside $p_{j,k}$.
- (2) the properties associated to $p_{j,k}$ are computed from the native CT data,
- (3) the node $t_{j,k}$ is included in T as a root node and the link with the existing nodes, if $j \geq 1$, is created as follows:

- a list of root nodes $t_{i,k}$ at levels $i < j$ is obtained from T .
- for each $p_{j,m}$ pattern, if the spatial position of $t_{i,k}$ is inside $p_{j,m}$, the stacking property implies a spatial connectivity between $p_{i,k}$ and $p_{j,m}$, and also $t_{i,k}$ is linked as a child of $t_{j,m}$.

Fig. 53 shows the geometry of a tree descriptive structure at 7 phases of construction (pyramid levels) for a 3-D decomposition of a MSCT thorax data.

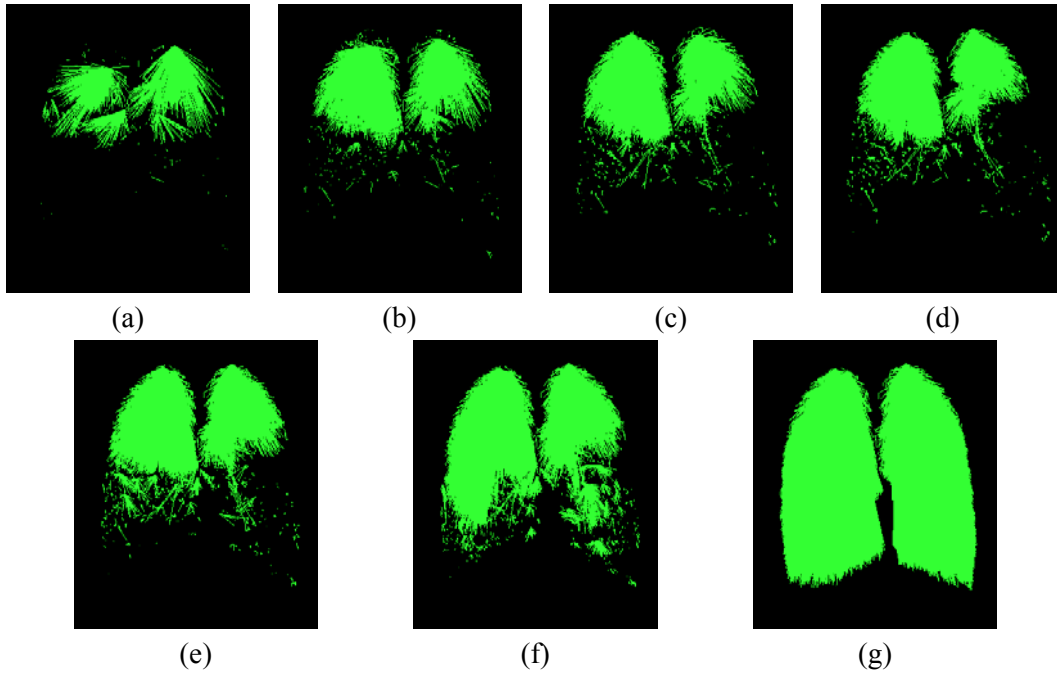


Fig. 53 The geometry of a tree descriptive structure at 7 phases of construction for decomposition of a 3-D MSCT thorax data.

III.5 Fuzzy Classification

Classification [112-119] is widely used to recognize a given object according to analysis of texture features extracted from the region of interest. However, in a lung volume, sometimes, it is difficult to absolutely determine an area associated with a specific pathology. For example, some parts of the area are normal tissue, some parts are emphysema tissue, and the regions between two tissues vary progressively from the normal stage to the emphysema stage. Thus, in this study, fuzzy logic analysis [96, 97] is exploited to strengthen the flexibility and the robustness of the classification. By using fuzzy logic analysis, probabilities for a pattern to be assigned one of the categories normal (N), emphysema (EM), fibrosis/honeycombing (FHC), and ground glass (GDG), can be computed. The developed classification approach based on fuzzy logic analysis is described in the following.

III.5.1 Definition

Generally, fuzzy logic is a form of multi-valued logic derived from fuzzy set theory [96], as mentioned in Section II.2.2.6, and used to handle with the concept of partial truth values between “completely true” and “completely false”; that is, the logic modes are approximate rather than exact. Thus, fuzzy logic has a truth value that ranges between 0 and 1.

Fuzzy logic analysis can be divided into three stages: feature extraction, fuzzy reasoning [120] and relaxation [121, 122]. First, several components of a fuzzy logic system, as shown in Fig. 55, are briefly described in the following.

– **Feature extraction**

For sequential, spatial, or other structured data, feature extraction is to use specific techniques like convolution methods using hand-crafted kernels or syntactic and structural method to encode problem-specific knowledge into the features. For example, in medical imaging, the brightness degree of a region is extracted from a symptom to express the health status of a patient.

– **Fuzzy reasoning**

Fuzzy reasoning [120] is an approximate method to determine an object according to possible imprecise membership functions from a set of possibly imprecise rules of inferences [123, 124]. Here, membership functions and rules of inferences are described respectively as follows.

- A **membership function** is a transfer function that defines how each element in the input set is mapped to a membership value between 0 and 1. Generally, the membership function can be described in a graphical representation, using straight line segments or the Gaussian distribution curve. Two types of the straight line functions are triangular and trapezoidal, and the advantage of the function is simplicity. The Gaussian membership functions also include two types: a simple Gaussian curve and a two-sided composite of two different Gaussian curves. Both of these curves have the advantage of being smooth and nonzero at all elements.
- The **rule of inference** is a scheme establishing syntactic relations between a set of formulas (membership functions) and a result. It is usually concluded from human experiences and knowledge, and used by means of IF-THEN rules. By rules of inference, the probabilities of possible classes, which are analyzed by membership functions are summarized as an assertion.

If two fuzzy sets A and B denote two categories, the membership function ω for the two sets can respectively be denoted as ω_A and ω_B . For an element x of a set X , the probability $\omega_A(x)$ is called the membership degree of x in the fuzzy set A . An example of graphical representation of the membership function for the two sets A and B is shown in Fig. 54, where probability measures of ω_A and ω_B at each point x are represented as a trapezoid distribution along x associated with three thresholds, Th_1 , Th_2 , and Th_3 , indicating the turning points of the function. Thus, the trapezoid distribution for ω_A has monotonic increase from 0 to Th_1 , a plateau level between Th_1 and Th_2 , and monotonic decrease from Th_2 to Th_3 . While $x = x_0$, the probability for ω_A is $\omega_A(x_0)$, and that for ω_B is $\omega_B(x_0)$; it means that by this membership function (the feature), the probability for the object to be the category A is $\omega_A(x_0)$, and that to be category B is $\omega_B(x_0)$.

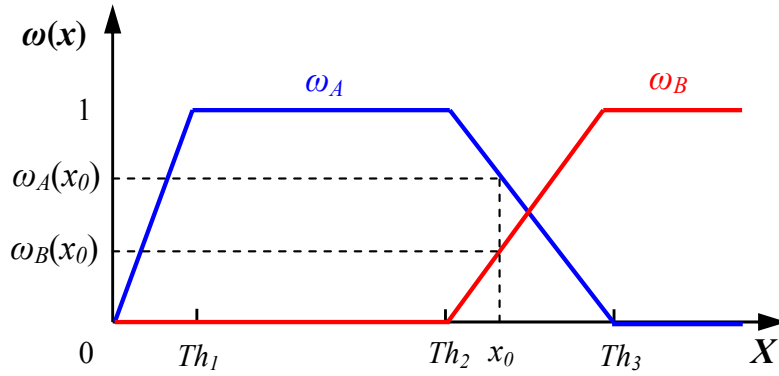


Fig. 54 The illustration of the membership function ω .

Then, an example of rules of inference is defined by:

R: If $\omega_A(x_0) \geq \omega_B(x_0)$
Then the object is category A .

R: If $\omega_A(x_0) < \omega_B(x_0)$
Then the object is category B .

(3.34)

— Relaxation

A relaxation technique [121, 122] is required for determining the attribute of each voxel from the membership function output. In general, a relaxation technique based on an iterative defuzzifier unit is applied to adjust the attribute of a voxel by its neighbors attributes to maintain the similarity among neighboring voxels.

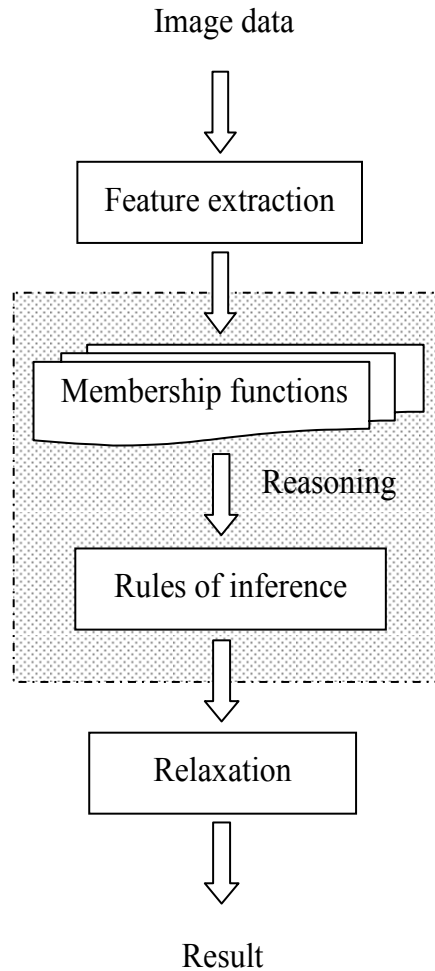


Fig. 55 The flowchart of a fuzzy logic system.

III.5.2 Lung Disease Classification

In the classification stage, the fuzzy logic analysis is exploited to discriminate between the lung patterns enclosed by each ROI for each resolution level in the decomposition pyramid. The analysis is divided into four parts, feature extraction, membership function analysis, rules of inference, and relaxation which are described in the following.

III.5.2.1 Feature extraction

Feature extraction is used to quantify the characteristics of the descriptive tree structure. In this study, 6 features are defined based on the properties mentioned at the beginning of this chapter. Such properties can be separated into two categories: the gray-level information and the spatial connectivity information.

In the gray-level information, we focus on the representation of the voxels on the CT

data which is related to the physical tissue density of the pattern and of its surroundings. Such representation can be characterized by the value and distribution of gray-levels of voxels within the pattern and its neighborhood. Hence, three features, gray-level mean, standard deviation, and external mean, are defined.

The spatial connectivity information is used to express the correlation of patterns across different resolution levels. Such information is related to the pattern clustering, but also to the volume variation and the shape of the pattern from one resolution level to another. Thus, three features, sibling degree, relative volume increase, and spread index are defined.

If p_i denotes the decomposition pattern associated with the node t_i of the descriptive graph and v denotes a voxel within the lung volume, the 6 features for analyzing the pattern are described and defined in the following.

– **Gray-level mean, $\mu(t_i)$**

The gray-level mean is used to represent brightness of a pattern. As mentioned in Chapter I, the pattern with EM or FHC is very dark (low intensity) on the CT image, that is the gray-level of voxels within such pattern are quite low. The GDG pattern is associated with medium-high intensity, and the intensity of the N pattern is between the EM pattern and the GDG pattern. The gray-level mean is computed according to:

$$\mu(t_i) = \frac{1}{Nv} \sum_{k=1}^{Nv} f(v_k), \quad (3.35)$$

where Nv denotes the number of the voxels within the pattern p_i , v_k denotes a voxel within the pattern p_i , and $f(v_k)$ is the gray value of the voxel v_k .

– **Standard deviation, $\sigma(t_i)$**

The standard deviation is used to represent distribution of gray-levels of the voxels within a pattern. In Chapter I, we have discussed about the causes of EM and FHC. Due to tissue destruction, the representation of the pattern in the CT image is like an air sac. Thus, almost all voxels within the pattern are with low intensity so that the gray-level distribution is concentrated around the mean value. The gray level distribution inside the N pattern is rather uniform in a larger range than EM/FHC. The GDG pattern has a similar situation as the N pattern but with a mean value translated to high gray levels and a larger standard deviation. Thus, the standard deviation can be a discriminative feature for these patterns and is computed as:

$$\sigma(t_i) = \sqrt{\frac{1}{Nv} \sum_{k=1}^{Nv} (f(v_k) - \mu_i)^2}, \quad (3.36)$$

where μ_i denotes the gray-level mean of the pattern p_i .

– **External mean, $\mu_{ext}(t_i)$**

The external mean is used to measure brightness of the pattern neighborhood in a given distance (surrounding band). Generally, the FHC pattern is surrounded by high intensity tissue, such as reticulation, so that its surrounding band is brighter than the surrounding band of the EM, N, and GDG pattern. The surrounding band of the EM pattern differs according to the type of emphysema and is distinguished by medium-high intensity, equal or superior to that of the N pattern.

In this study, the range of the surrounding band of the pattern p_i is limited by a sphere. While the center of a sphere moves along the voxels on the boundary of the pattern p_i , a voxel, which is outside the pattern p_i and inside the sphere, is included into the surrounding band of the pattern p_i and denoted as vs . The surrounding band of the pattern inside the lung region is illustrated in Fig. 56 (a). If the given pattern is near by the boundary of the lung region, as shown in Fig. 56 (b), the surrounding band may include voxels inside thorax cage. Such voxels are usually of high intensity and will bias the analysis for the external mean. In order to avoid such situation, the surrounding band will be considered only inside the lung field mask f_{LawDH} extracted as discussed in Section III.2.2. Thus, the external mean is defined as

$$\mu_{ext}(t_i) = \frac{1}{Nvs} \sum_{k=1}^{Nsv} f(vs_k) | vs_k \in f_{LawHD} \quad (3.37)$$

where Nvs denotes the number of voxels in the surrounding band of the pattern p_i .

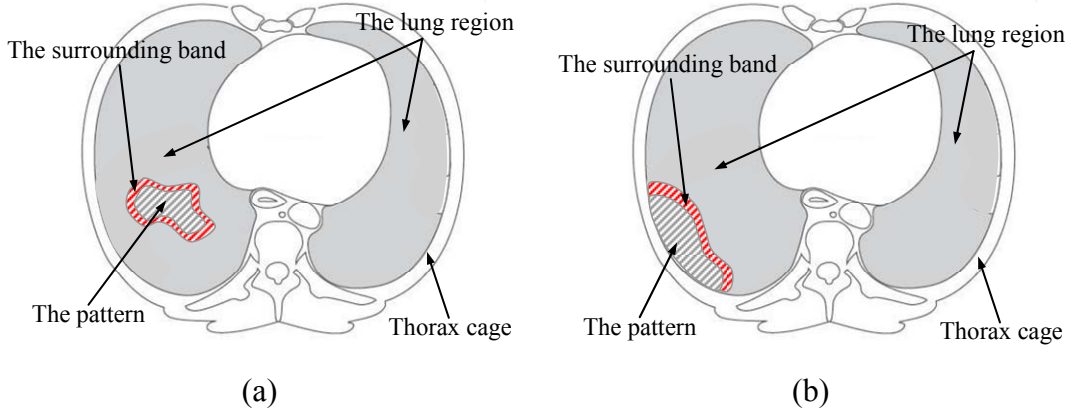


Fig. 56 The surrounding band (the red region) of the pattern (a) inside the lung region, and (b) near by the boundary of the lung region.

– **Sibling degree, $sd(t_i)$**

On the CT image, in FHC, lots of small low-intensity patterns are cluster together so that in the descriptive tree structure the cluster patterns are siblings (brothers) at the same level. In EM, N, and GDG, the number of the low-intensity patterns is less than in FHC. So, the sibling degree is defined as the number of “brothers” of t_i , i.e. the number of nodes at the same level, which have the same “parent” t_i .

$$sd(t_i) = Num_s(t_j) - 1, \quad (3.38)$$

where $Num_s(t_j)$ is the number of children of the node t_j , where t_j is the father of the node t_i .

– **Relative volume increase, $rv(t_i)$**

The volume of the pattern associated with the clustering property may show a sharp increase by comparing to the total volume of its children. So, while the FHC pattern has noticeable increase in volume, the EM pattern has less increase than the FHC pattern, but superior to the N pattern and the GDG pattern.

Based on such concept, the relative volume increase is defined to calculate the ratio of the p_i volume increase with respect to the total volume of its children as

$$rv(t_i) = \frac{vol(p_i) - svol(p_i)}{svol(p_i)}, \quad (3.39)$$

with

$$svol(p_i) = \sum_{k=1}^{Ns} vol(p_{ik}), \quad (3.40)$$

where $vol(p_i)$ is the volume of the pattern p_i , $svol(p_i)$ is the total volume of p_i 's children p_{ik} , and Ns denotes the number of children of the pattern p_i .

– **Spread index, $rvs(t_i)$**

The spread index is to calculate the ratio of the p_i volume increase to the volume of the sphere of diameter equal to the given level size m_l . It provides information on the space spreading of pattern p_i with respect to a reference volume. If the flooding of the valley corresponding to p_i in the lung relief does not expand outside this valley, the spread index is low (indicating a good separation between the pattern and its environment) otherwise, higher values denote cluster formation. The spread index is defined as:

$$rvs(t_i) = \frac{vol(p_i) - svol(p_i)}{Sphe(p_i)} \quad (3.41)$$

with

$$Sphe(p_i) = \frac{4}{3} \times \pi \times r^3, \quad (3.42)$$

where $vol(p_i)$ and $svol(p_i)$ are given in eq. (3.40), and the radius r depends on the p_i level, $r = m_l / 2$.

These features will provide the probabilities of associating a given pattern p_i with a lung tissue category based on the membership functions defined in the following.

II.5.2.2 Membership function

The membership functions, associated with the six features are chosen as trapezoid

distributions due to lower complexity. The trapezoid distribution is set up according to the expected characteristics of each pathological tissue with respect to the selected feature. Each trapezoid distribution can be divided into three zones, such as monotonic increase, a plateau level, and monotonic decrease, controlled by two threshold values. In order to acquire these threshold values, several cases are selected from testing cases for training purposes.

In the training procedure, volumes of interest (VOIs) focusing on different physiopathological tissues of N, EM, FHC, and GDG, were manually selected by an experienced radiologist. The multi-resolution decomposition scheme was applied to each training case, the decomposition pyramid and the hierarchic tree generated, and the 6 features computed and analyzed for each node in each VOI. According to the features analysis of each interesting pathology pattern, the preliminary threshold values for the associated membership function were obtained and further on confirmed by the radiologist expert.

The fuzzy membership functions associated with the six features $\mu(t_i)$, $\sigma(t_i)$, $\mu_{ext}(t_i)$, $sd(t_i)$, $rv(t_i)$, and $rvs(t_i)$ are shown in Fig. 57 (a)-(f), respectively, where P_C^M denotes the probability value of the C class (namely N, EM, FHC and GDG) with respect to the M membership function. In Fig. 57, the probability $P_C^M(x)$ of EM, FHC, N, and GDG is 1 at the plateau of each trapezoid distribution; otherwise, $0 \leq P_C^M(x) < 1$, and for any x

$$\sum_C P_C^M(x) = 1. \quad (3.43)$$

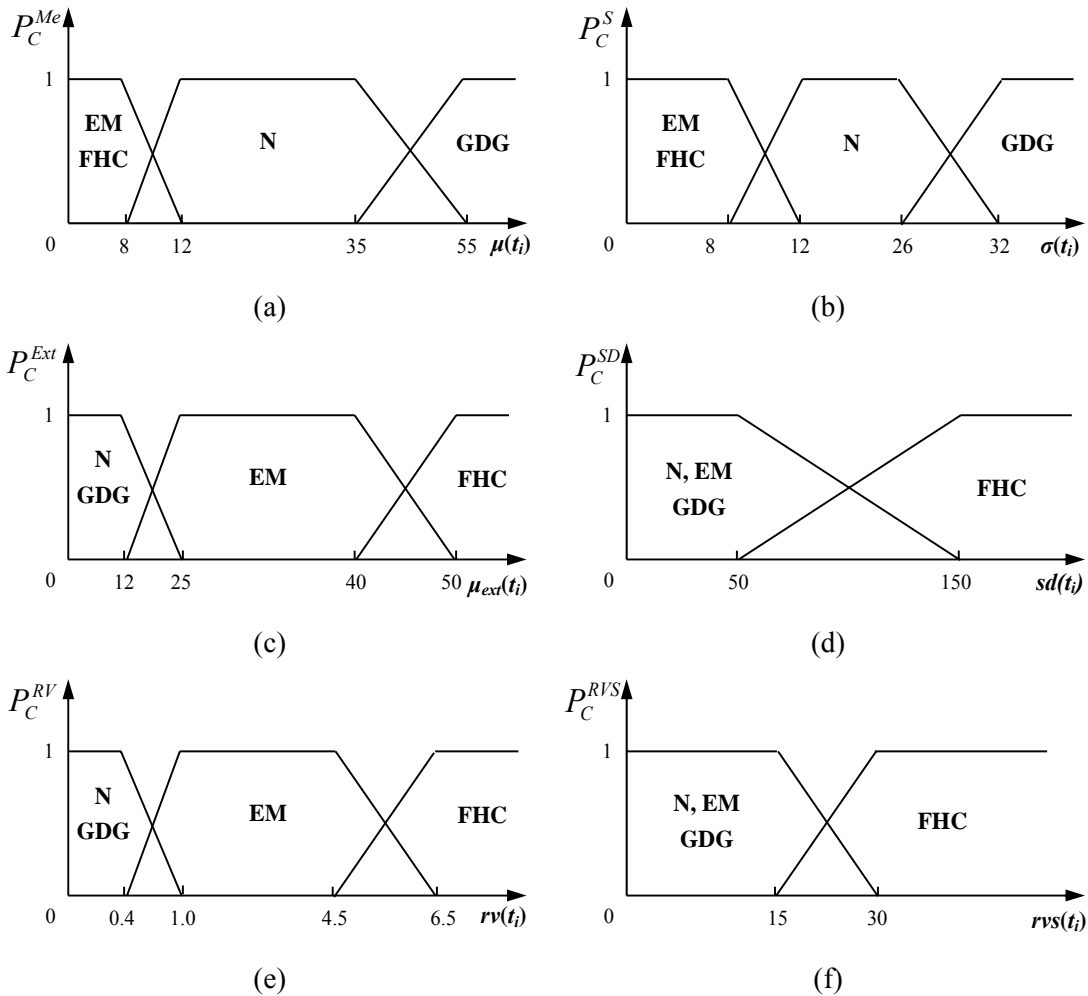


Fig. 57 The fuzzy membership functions with respect to 6 features, (a) the gray-level mean, (b) the standard deviation, (c) the external mean, (d) the sibling degree, (e) the pattern relative volume increase and (f) the spread index. Note that the x -axis represents the computed feature value, and the y -axis represents the corresponding fuzzy analysis probability.

II.5.2.3 Rules of inference

The rules of inference will combine the output of the membership functions to decide the class probability for each of the N, EM, FHC, and GDG possible assignments, and will select the most pertinent assignment. Such classification inference can be divided into two stages. First, the probabilities derived from the 6 features are linearly combined with corresponding weights to obtain the probability of a pathology assignment to each node. The weights are pre-defined according to the confidence associated with the feature. Note that, each node t_i is assigned 4 values $Prob_C(t_i)$, $C \in \{N, EM, FHC, GDG\}$, which express the probability of t_i to be defined as the category C :

$$\begin{aligned}
Prob_C(t_i) = & \alpha_M P_C^{Me}(\mu(t_i)) + \alpha_S P_C^S(\sigma(t_i)) + \alpha_{Ext} P_C^{Ext}(\mu_{ext}(t_i)) + \alpha_{SD} P_C^{SD}(sd(t_i)) \\
& + \alpha_{RV} P_C^{RV}(rv(t_i)) + \alpha_{RVS} P_C^{RVS}(rvs(t_i))
\end{aligned} \quad (3.44)$$

where $\alpha_M + \alpha_S + \alpha_{EM} + \alpha_{SD} + \alpha_{RV} + \alpha_{RVS} = 1$.

Then, in the second stage, two classification thresholds, $T_{category}$ and $T_{decision}$, where $0 < T_{category} < T_{decision} < 1$, are exploited to allow taking into account only the most representative membership probabilities. Let $Prob_{Max}(t_i)$ denotes the maximum probability among the 4 combined probabilities,

$$Prob_{Max}(t_i) = \max\{Prob_C(t_i), C \in \{N, EM, FHC, GDG\}\}. \quad (3.45)$$

A node t_i is assigned the category C , denoted as $Assign_C(t_i) = 1$, if $Prob_C(t_i)$ is satisfying two conditions:

$$Prob_C(t_i) > T_{category}, \quad (3.46)$$

and

$$Prob_C(t_i) / Prob_{Max}(t_i) > T_{decision}; \quad (3.47)$$

otherwise, $Assign_C(t_i) = 0$. Note that these conditions are used to select the highest representative probabilities of association with a given category, and that the selected probabilities are close to each other. Thus, mixed classification of a lung pattern is possible while more than one disease category is satisfying eq. (3.46) and (3.47). Such mixed classification may include N and one of EM or FHC, which is denoted as mild emphysema (MEM) and mild fibrosis/honeycombing (MF), and in addition, mixtures of EM and FHC may occur which is denoted EF. Table 6 presents the 16 mixtures, $MC(k)$, $k=1..16$, of N, EM, FHC, and GDG. The parameters of the scheme including the weights and classification thresholds were chosen as follows:

$$\begin{aligned}
\alpha_M = 0.3, \alpha_S = 0.2, \alpha_{EM} = 0.2, \alpha_{SD} = 0.1, \alpha_{RV} = 0.1, \alpha_{RVS} = 0.1, \\
T_{category} = 0.5 \text{ and } T_{decision} = 0.8.
\end{aligned}$$

III.5.2.4 Relaxation

The relaxation step is performed in order to assign the final class to each voxel of the lung parenchyma. Note that a voxel in the 3-D dataset will correspond to (at most) one pattern at each level of the decomposition pyramid and then, also to several nodes along a hierarchy path in the description tree. As each node along the hierarchy path has a class assigned (cf. Table 6), a final decision should be taken by integrating the information across the levels. Such integration is performed via the "collapse" of the decomposition pyramid, that is, the class assigned to a given voxel at the spatial location x is the class corresponding to the node of highest depth associated with the pattern including x , as illustrated in Fig. 58.

The final classification result is represented as a labeled (color) image, where each label is defined as follows. Let $I_n(C)$ denotes the category index for the 7 classification possibilities considered, which is assigned as $I_n(N) = 0$, $I_n(EM) = 1$, $I_n(FHC) = 2$, $I_n(MEM) = 3$, $I_n(EF) = 4$,

$I_n(\text{MF}) = 5$, and $I_n(\text{GDG}) = 6$. Then, a category look-up table C_Table corresponding to the 16 mixtures $MC(k)$ in Table 6 can be defined as

$$\begin{aligned} C_Table(k) &= \{ I_n(MC(k)) \mid k = 1, 2, 3, \dots, 16 \} \\ &= \{0, 0, 1, 3, 2, 5, 4, 2, 6, 6, 2, 5, 2, 5, 2, 2\}. \end{aligned} \quad (3.48)$$

Thus, a node t_i classed as the k^{th} mixture result is assigned a gray-level CL_Gray by the following equation

$$CL_Gray(k) = 45 + 30 * C_Table(k). \quad (3.49)$$

This leads to the following labels for the parenchyma patterns: N = 45, EM = 75, FHC = 105, MEM = 135, EF = 165, MF = 195, and GDG = 225, which can be color-coded for a more convenient visual investigation. Fig. 59 illustrates the classification results of CT images in the case of emphysema and fibrosis, respectively.

Table 6 16 mixtures of N, EM, FHC, and GDG.

k	$Assign_N(t_i)$	$Assign_{EM}(t_i)$	$Assign_{FHC}(t_i)$	$Assign_{GDG}(t_i)$	Mixt class, $MC(k)$
1	0	0	0	0	N
2	1	0	0	0	N
3	0	1	0	0	EM
4	1	1	0	0	MEM
5	0	0	1	0	FHC
6	1	0	1	0	MF
7	0	1	1	0	EF
8	1	1	1	0	FHC
9	0	0	0	1	GDG
10	1	0	0	1	GDG
11	0	1	0	1	FHC
12	1	1	0	1	MF
13	0	0	1	1	FHC
14	1	0	1	1	MF
15	0	1	1	1	FHC
16	1	1	1	1	FHC

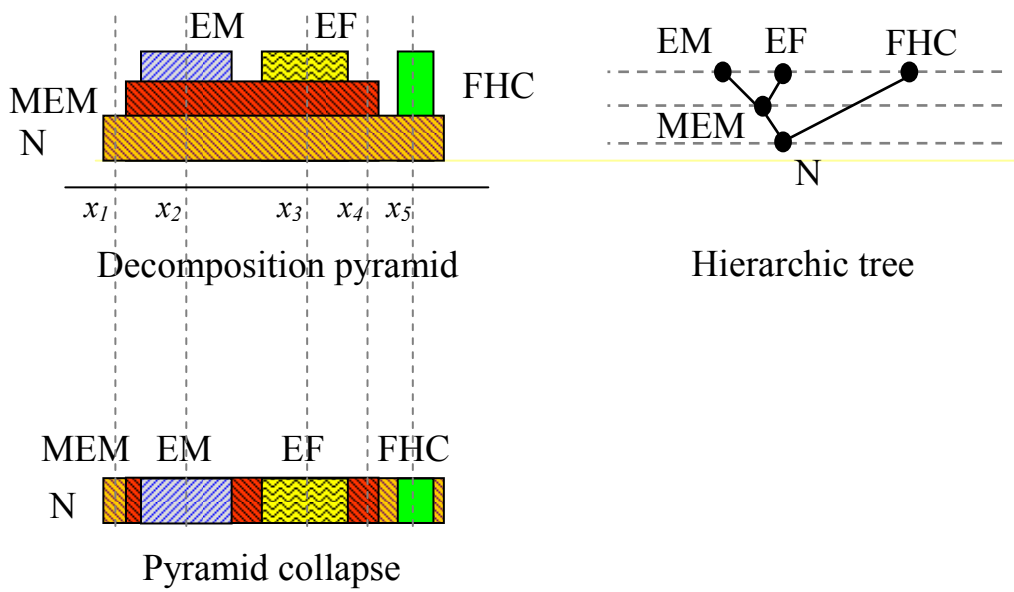


Fig. 58 Example of relaxation process via pyramid collapse. Final classification at spatial locations x_i is given by: $C(x_1) = N$, $C(x_2) = EM$, $C(x_3) = EF$, $C(x_4) = MEM$, $C(x_5) = FHC$.

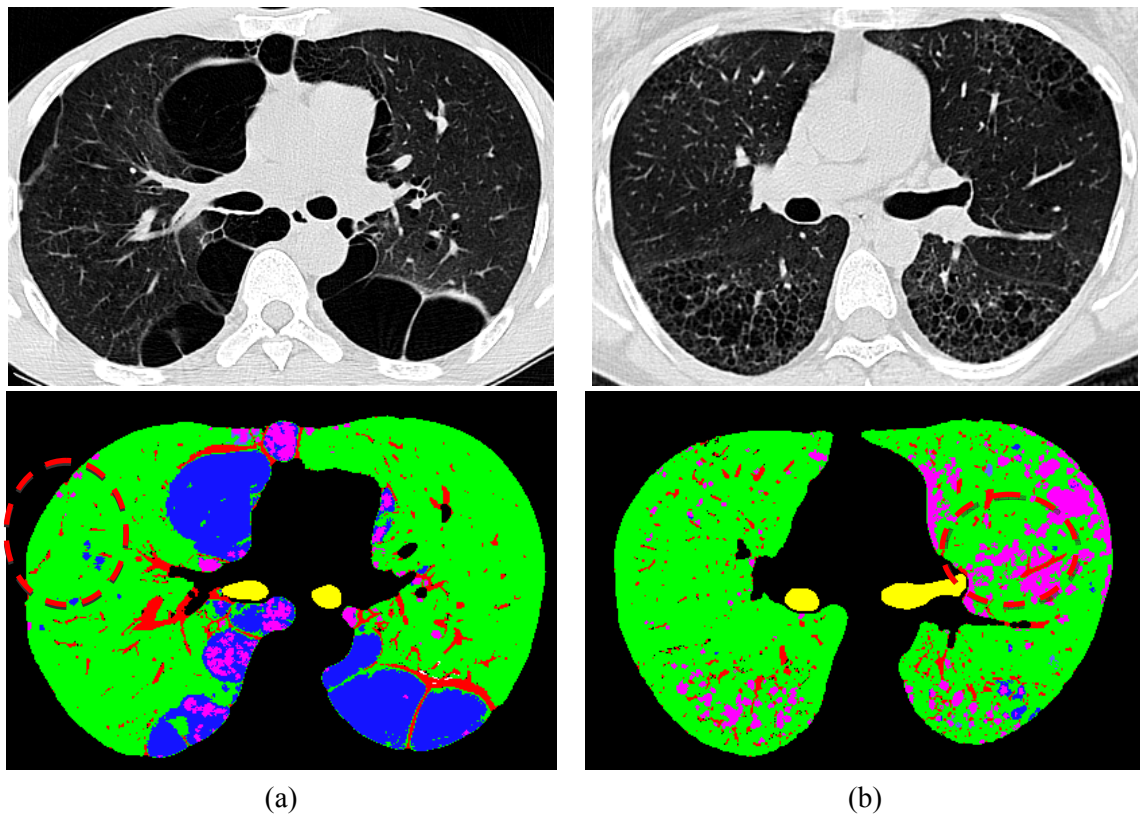


Fig. 59 The classification results (bottom) for CT images (top) with (a) emphysema, and (b) fibrosis. Color code assignment: N ■ MEM ■ EM ■ FHC ■ GDG HD ■.

By visually inspecting the classification result for the examples in Fig. 59, we note that most of the diseased patterns were identified and correctly classed in the right category. However, some regions were missed (N instead of pathologic, Fig. 59 (a) – red circle) or overestimated (pathologic instead normal, Fig. 59 (b) – red circle). Such misclassification is due to the inaccurate separation of the pathologic and normal regions at the same level of resolution in the decomposition pyramid. Namely, during the relief flooding process at a given level, if the "valley" associated with a pathology (EM, FHC) has either locally attenuated walls or is enclosed in a larger valley and immersed during the flooding (Fig. 60), the extracted pathological pattern will be connected to a larger (normal) one. There will be thus a single connected component extracted and the computed features will be biased, leading to misclassification.

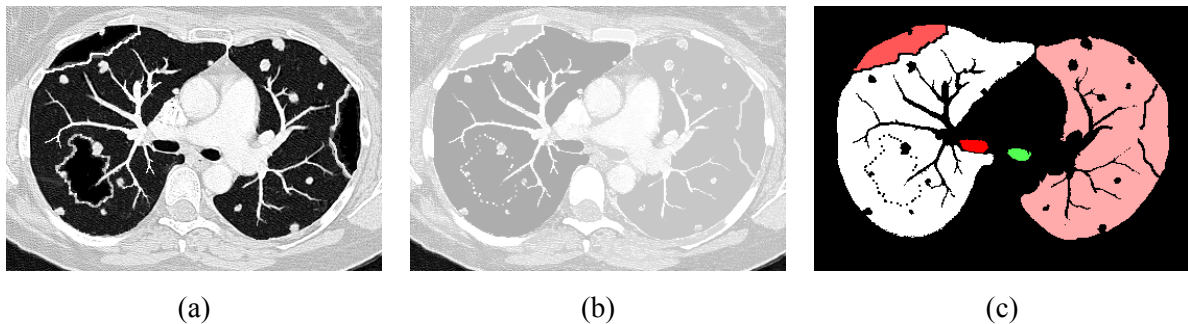


Fig. 60 Example of pattern "overflow" during flooding: (a) simulated lung image including two EM patterns in the right lung, one of continuous high-intensity wall, the other of attenuated intensity wall, and one EM pattern in the left lung of locally attenuated wall (looking like an interruption); (b) the flooding result for a given resolution level; (c) the pattern extracted show that only the first EM region (red) was correctly separated from the normal lung region.

In order to avoid this problem, the region separating pathological and normal tissue should be completely closed and prevent a pattern "overflow" during the flooding. The first requirement may be impaired by the MSCT acquisition protocol (noise, partial volume effect) while the second by the choice of the FSD filter size (or by the number of the decomposition levels). Pre-processing the MSCT data (anisotropic filter, stick operator - Section III.1) may improve some conditions, however, the dependence on the image acquisition protocol remains high, and a robust solution is difficult to find.

To overcome this drawback, we propose combining the multi-resolution decomposition with a spatial partitioning of the lung in ROIs of fixed size and shape over all scales. This will produce smaller patterns at each resolution level and could thus capture local textural properties for a more accurate feature computation. The principle of such combination is described in the following and its benefit investigated with respect to the basic approach.

III.6 Spatial lung partitioning

The objective of spatial lung partitioning is to overcome the “overflow” situation of the multi-resolution decomposition scheme by partitioning the result patterns without interfering with the decomposition process itself. The idea is to define a set of ROIs of fixed shape and size over all scales which will partition the decomposition pyramid in smaller patterns able to capture local textural properties. The partitioning is implemented by two methods, the box partitioning (Section III.6.1), which serves as "proof of concept", and the texture-based partitioning (Section III.6.2), which is case-specific and is adapted to the textural particularity of the lung parenchyma.

III.6.1 Box partitioning

The concept of the box partitioning method is similar to the ROI/VOI setting mentioned in Section II.2.1.1. The box partitioning sets-up a 3-D “grid” in the lung region which will subdivide the patterns extracted at each resolution level in the decomposition pyramid. Since the partitioning is the same for all scales, the stacking property (eq. (3.26) and (3.30)) is preserved and the construction of the hierarchic descriptive tree is not affected. Conversely, the initial tree will be divided in several sub-trees, one per partition box. The selected box size is thus an important parameter, which will be discussed later on. Fig. 61 and Fig. 62 illustrate the concept of the box partitioning in the 1-D relief and the resulting hierarchic tree, respectively. The red dotted lines represent the box ROIs separating the patterns.

Note that the classification process exploiting the decomposition-partitioning procedure performs in the same way as discussed in Section III.5. Fig. 63 and Fig. 64 show few examples of classification with and without box partitioning. The comparison of the two classification results shows that the misclassification pattern, indicated by a circle, has been partitioned into several sub-patterns, and the classification result can be upgraded locally in each sub-pattern. This concludes that the spatial partitioning can overcome the “overflow” problem of the multi-resolution decomposition scheme.

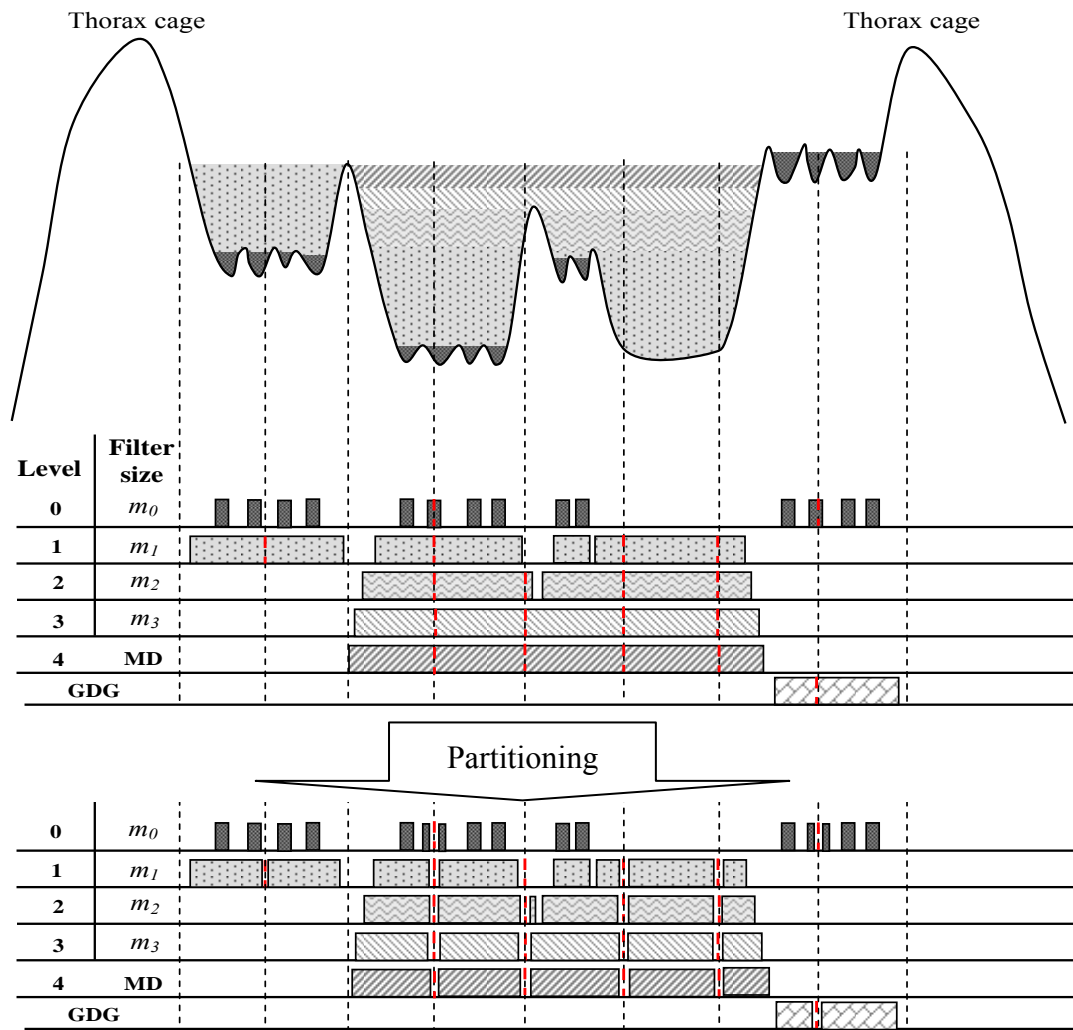


Fig. 61 The box partitioning applied on the decomposition result at each resolution level in the 1-D relief and the modified descriptive tree structure.

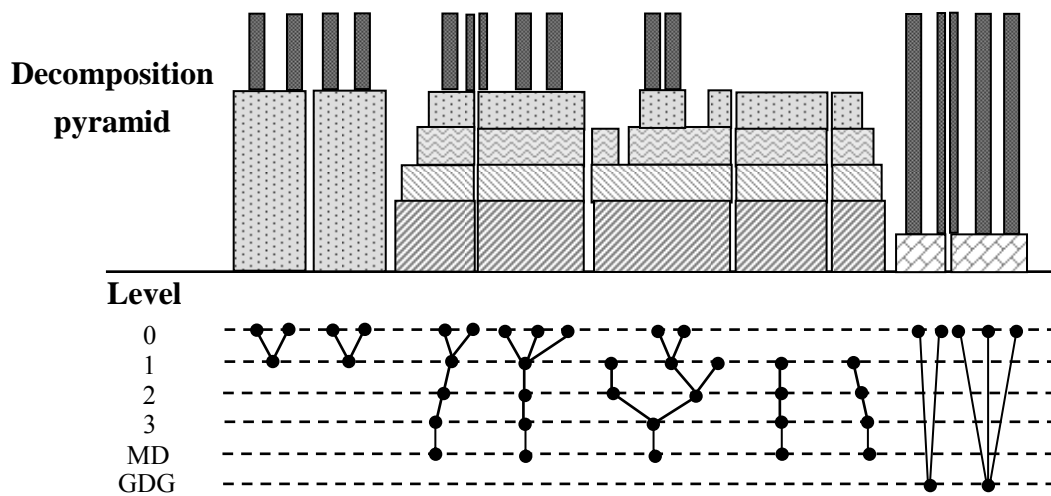
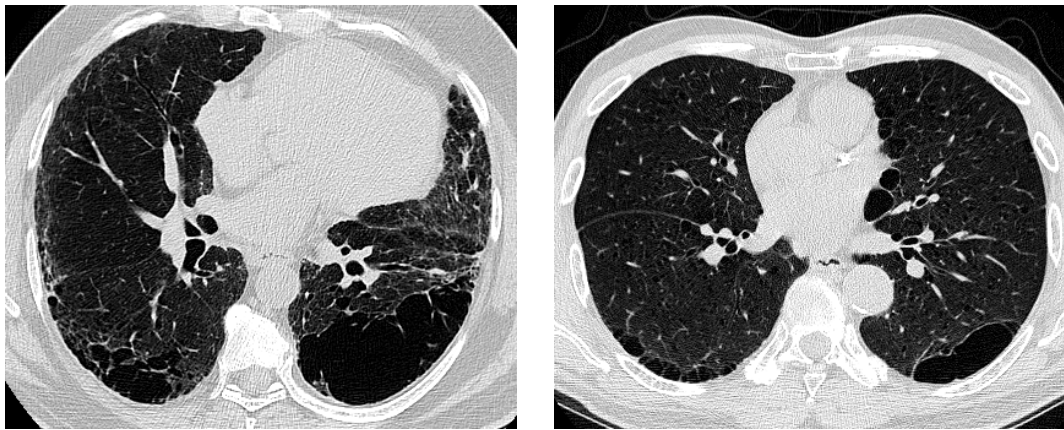
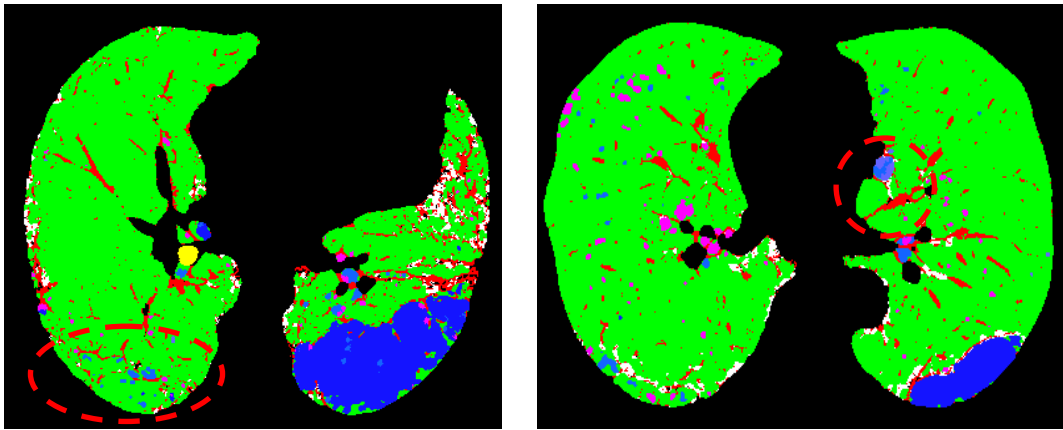


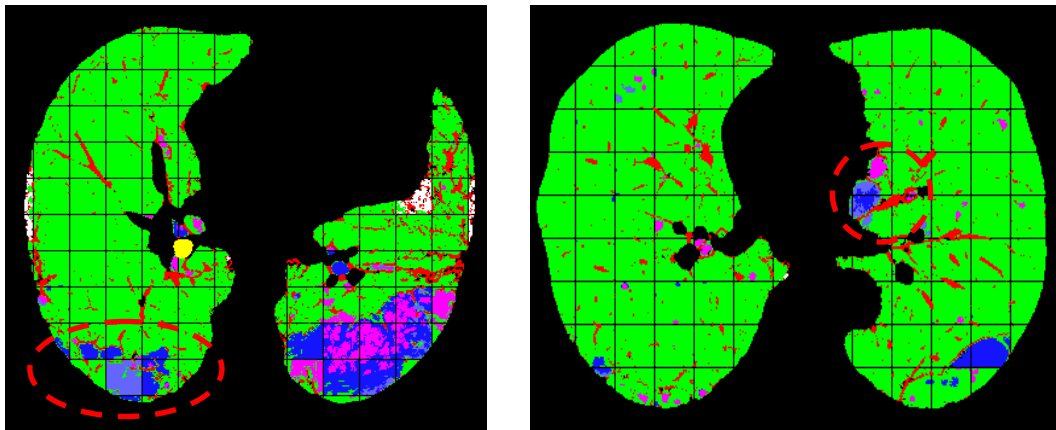
Fig. 62 The hierarchic descriptive tree of the decomposition pyramid ROIs obtained with the box partitioning.



(a)

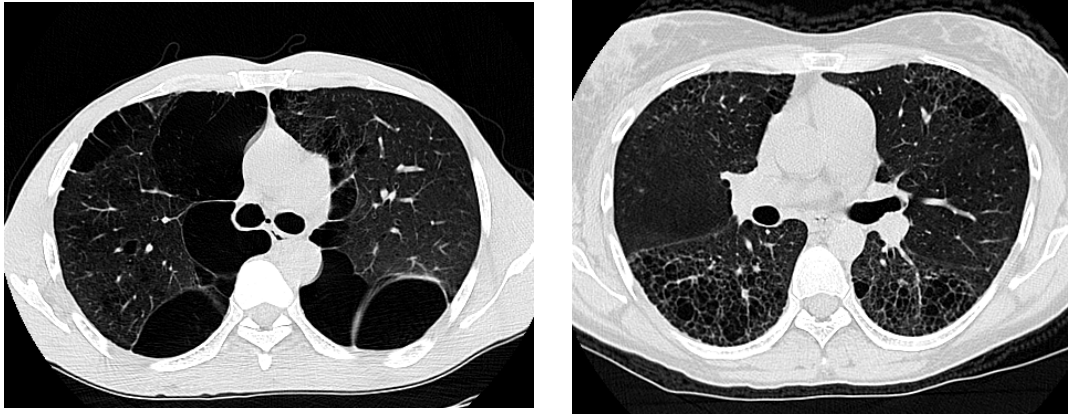


(b)

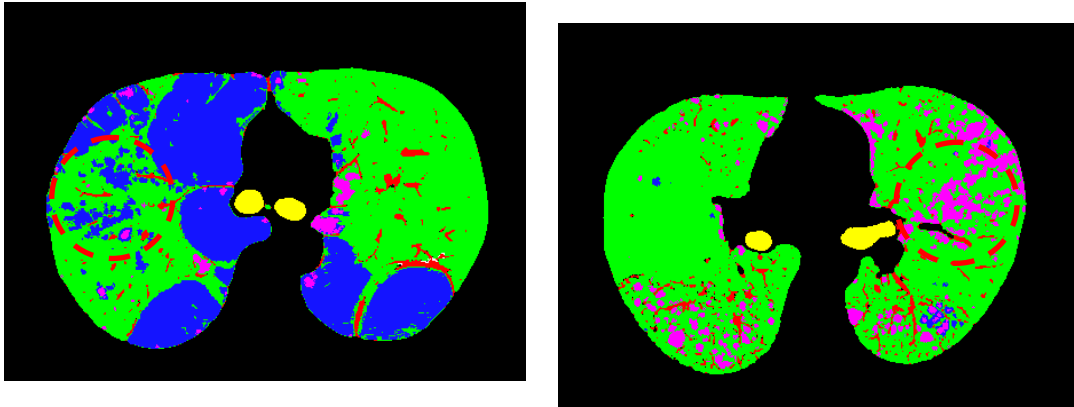


(c)

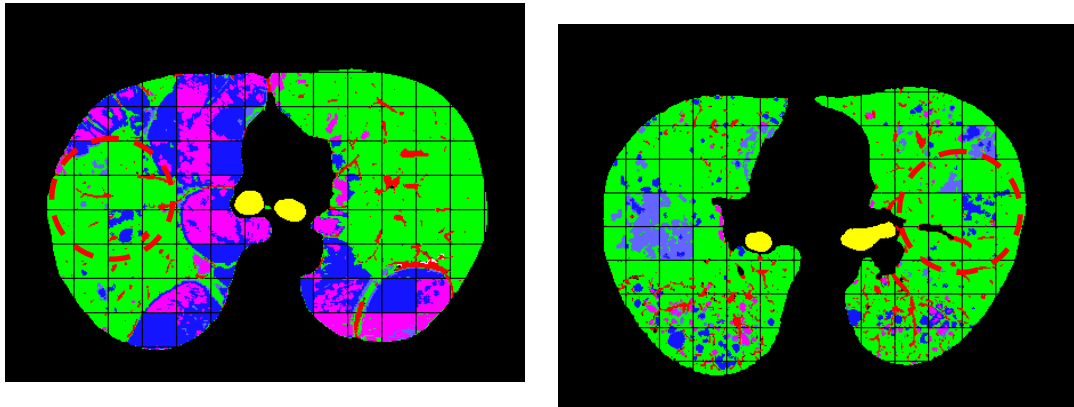
Fig. 63 Example of a classification result illustrated on an axial image of (a) two cases of EM (b) without, and (c) with box partitioning. Color code assignment:
 N MEM EM FHC GDG HD



(a)



(b)



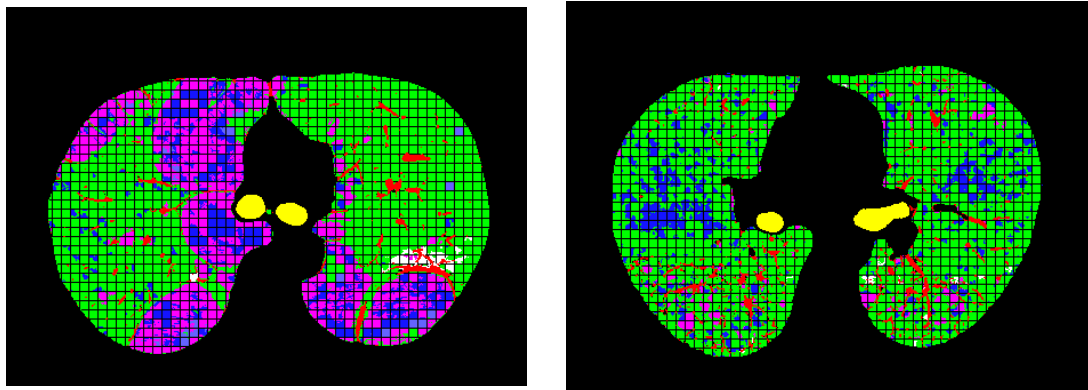
(c)

Fig. 64 Example of a classification result illustrated on an axial image of (a) two cases of EM (left) and FHC (right) (b) without, and (c) with box partitioning. Color code assignment: N ■ MEM ■ EM ■ FHC ■ GDG HD ■.

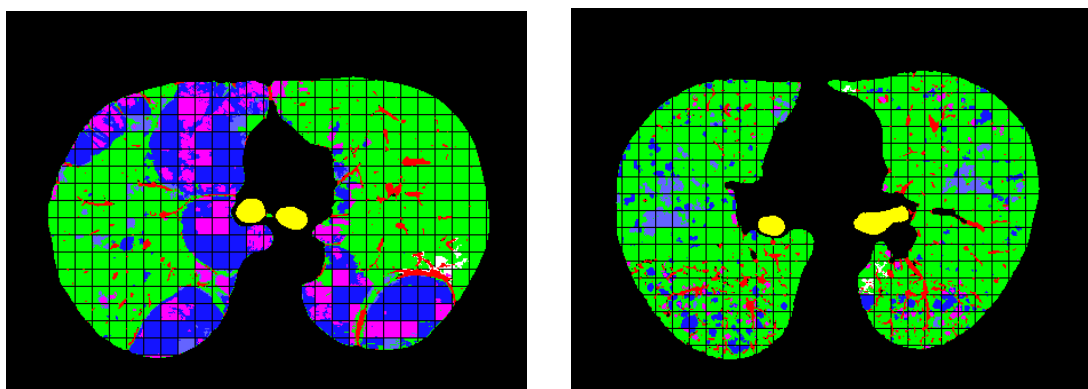
For several regions of the “grid”, however, the classification results are incorrect. This problem is due to the shape of the “grid”. While the box partitioning separates the patterns of the decomposition result at each resolution level using a cube grid of fixed size, the section of each sub-pattern may be not close to the boundary between two tissues. The shape

information and the spatial connectivity information would be distorted. Moreover, the gray-level information is distorted due to the fixed size. For example, a whole pattern such as a fibrosis “hole” might be partitioned into two sub-patterns if crossed by a partitioning line. The important characteristics of the fibrosis, such as external mean, would be computed from the fragmented external region. Therefore, the fuzzy logic analysis is performed based on incorrect feature extraction, which affects the discriminative power of the classification.

The box size used will thus play an important role and the influence of this parameter on the classification result was tested for several values. Fig. 65 shows a comparison between the classification results obtained for cases in Fig. 64 with box partitioning, for five box sizes, namely 8, 15, 30, 45 and 60 units. We notice that the several box sizes perform differently in terms of detection sensitivity and specificity (no obvious box size providing the highest rates in both criteria), which suggests the idea that the partitioning should be adapted to the context (pattern size, density, clustering,...).

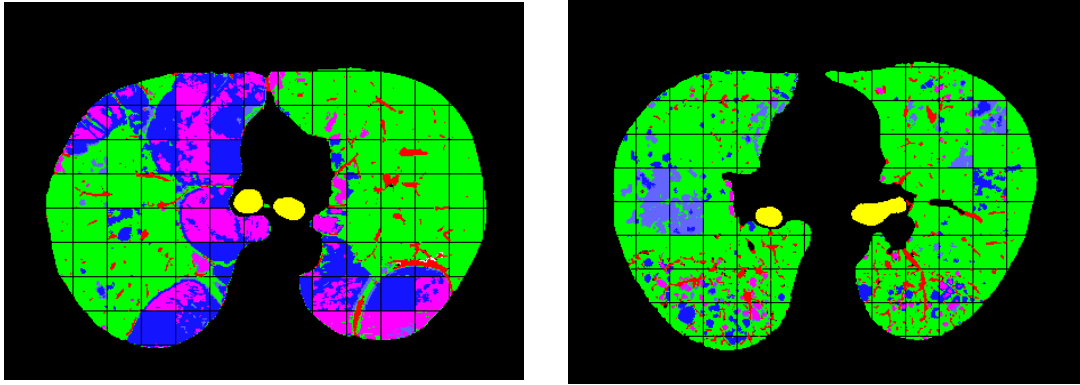


(a) box size = 8

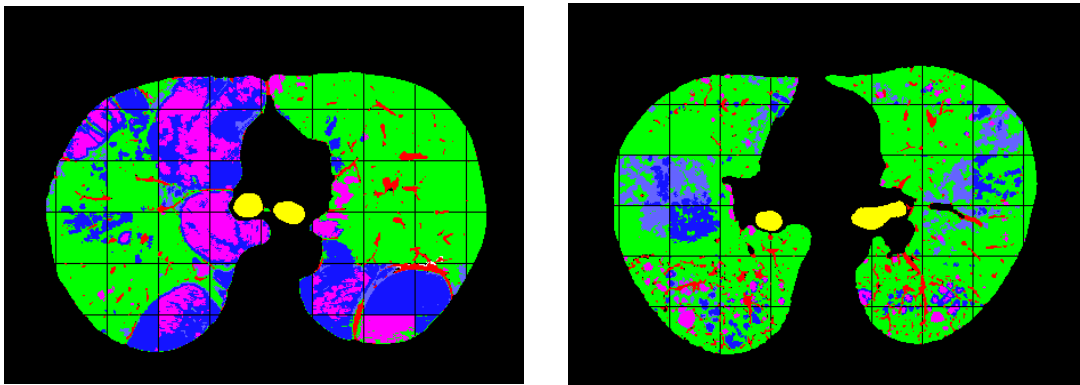


(b) box size = 15

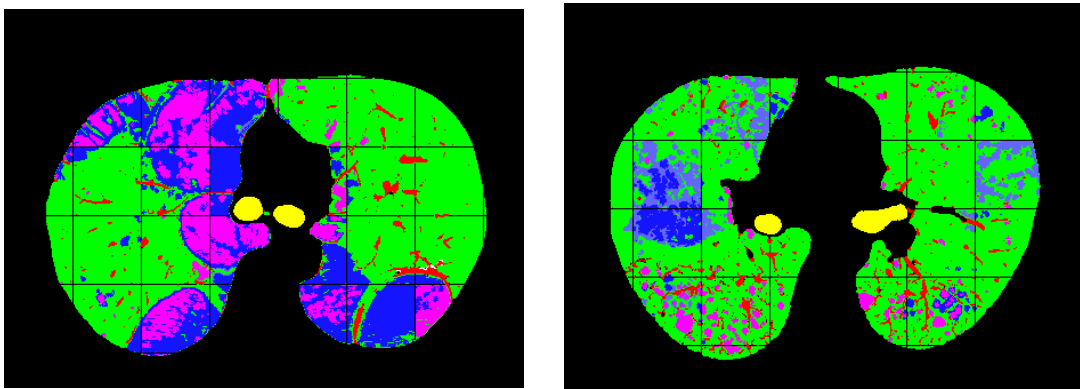
Fig. 65 Comparison of the classification result obtained using box partitioning for different box size = (a) 8, (b) 15, (c) 30, (d) 45, and (e) 60 units, respectively. Color code assignment: N ■ MEM ■ EM ■ FHC ■ GDG HD ■.



(c) box size = 30



(d) box size = 45



(e) box size = 60

Fig. 65 (Continued). Comparison of the classification result obtained using box partitioning for different box size = (a) 8, (b) 15, (c) 30, (d) 45, and (e) 60 units, respectively.

Color code assignment: N ■ MEM ■ EM ■ FHC ■ GDG HD ■.

In order to improve the efficiency of the spatial lung partitioning, a texture-based method is introduced to separate the patterns along the boundary between normal and pathological tissue.

III.6.2 Texture-based partitioning

The shape of a normal/pathological pattern is irregular, and its volume is variable. Thus, the spatial lung partitioning should be non-linear to be close to the border of the pattern. Hence, the idea of texture-based partitioning is to find the boundary between normal tissue and the pathological patterns. Conversely, note that the partitioning does not focus on the boundary between two different pathological patterns. The approach is described in three steps: pathological candidates selection, pathological region extraction, and partitioning line detection.

- The **pathological candidates selection** is exploited to detect the voxels inside the pathological pattern. At the beginning of this chapter, the intensity properties of normal tissue and the pathological pattern in the CT image have been described. The appearance of the pathologies is either in low intensity $[0, LD] = [0, 10]$ GL⁴ (emphysema and fibrosis), or in medium-high intensity range $[MD, HD] = [65, 100]$ GL (ground-glass). Moreover, the voxels along the border of emphysema and fibrosis are with higher intensity $[46, 68]$ GL than those in normal tissue $[16, 35]$ GL. Therefore, the pathological candidates are obtained by means of a double-thresholding selecting the $[0, LD]$ and $[MD, HD]$ intervals, Fig. 66 (b).
- The objective of **pathological region extraction** is to find a space containing the pathological patterns. If the pathological candidates are the individual voxels or small patterns, they might be considered as “noise”. Thus, first, a morphological erosion operation (of unit size) removes the small patterns. Then, the result is dilated (SE size = 4) in order to create a space which completely contains the corresponding pathological patterns.
- Finally, the **partitioning line** between the presumed pathological and normal tissue is extracted using an edge detection operator. This boundary would be used as the partitioning line to separate the decomposition pyramid. Fig. 66 (c) and (d) show the extracted partitioning lines for the CT image in Fig. 66 (a).

Fig. 67 and Fig. 68 illustrate the result of lung parenchyma classification for the examples in Fig. 63 and Fig. 64, respectively, using the texture-based partitioning. Note that the false positive and the missed patterns either without partitioning or using a box-partitioning are now correctly classed. An additional post-processing step can be applied here to remove small-size pathological patterns which can be considered as noise (Fig. 68 (b)).

⁴ GL refers to the gray level value in the grayscale range $[0, 255]$ considered for a CT “lung” window, $[-1000, 200]$ HU

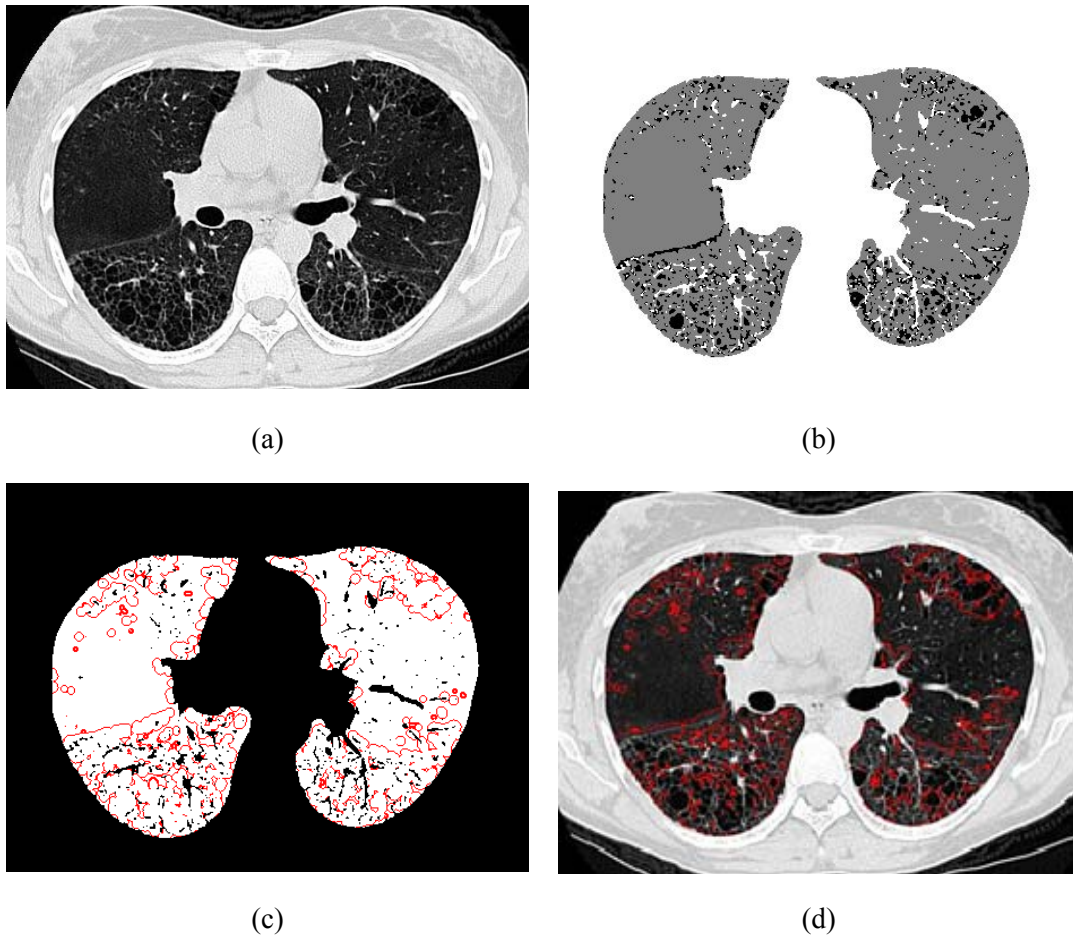


Fig. 66 An example of texture-based partitioning: (a) an original image with fibrosis, (b) the selected pathological candidates (black = [0, LD], white = [MD, HD], gray = normal), and the detected partition boundary (red color) shown on the binary lung mask (c), and superimposed on the original image (d).

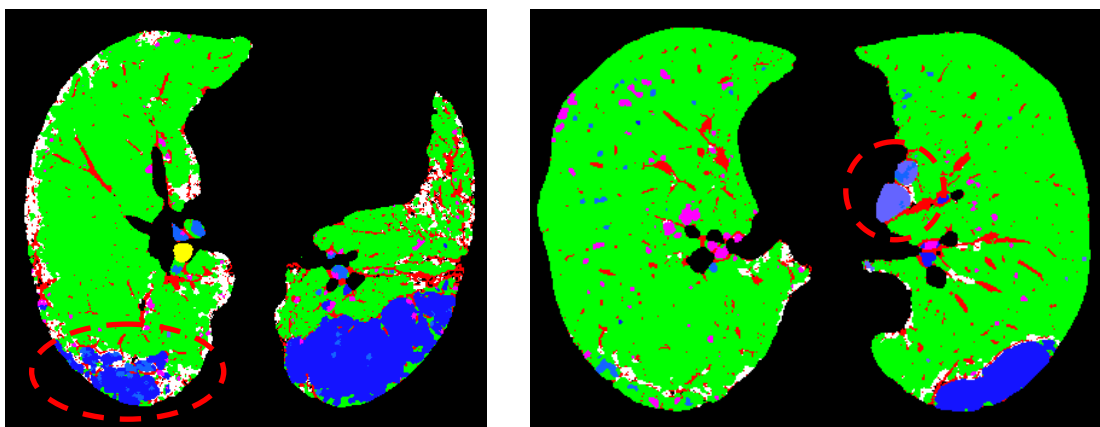


Fig. 67 Classification result using texture-based partitioning for the examples in Fig. 63.

Color code assignment: N ■ MEM ■ EM ■ FHC ■ GDG HD ■.

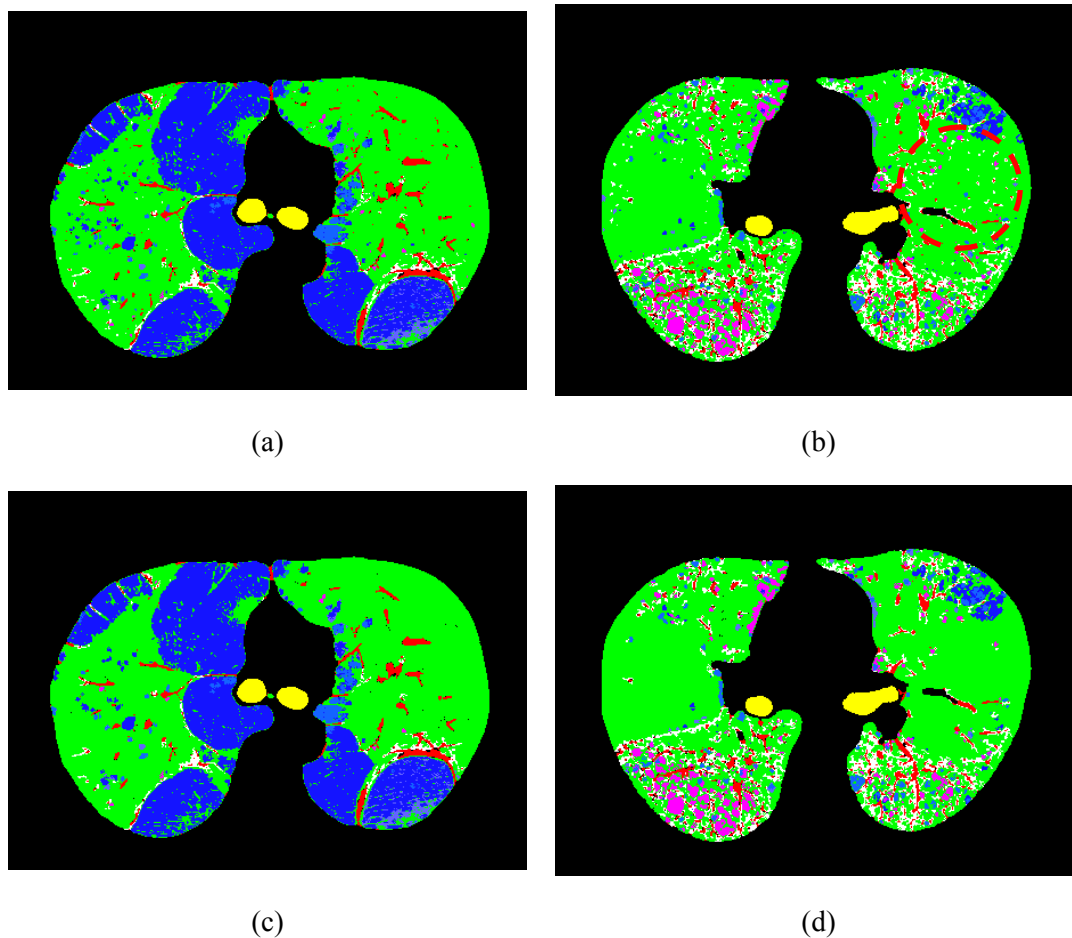


Fig. 68 Classification result using texture-based partitioning for the examples in Fig. 64.

Bottom row: removal of small-size pathological patterns. Color code assignment:

N MEM EM FHC GDG HD

We note that a better sensitivity is achieved for the pathological targets with respect to the previous methods, both in terms of low-density pattern detection and ground-glass like regions. Higher specificity seems also to be reached, especially when very small disease patterns are ignored (reassigned as normal tissue).

This result comforts us in choosing the multi-resolution decomposition and texture-based partitioning as the final approach for lung parenchyma investigation. The global flowchart of the proposed approach is now summarized in Fig. 69, where the lung segmentation step is performed before the pre-processing in order to decrease the computational load.

III.7 Conclusion

This chapter presented an original method developed for lung disease detection and classification based on a relief decomposition-partitioning procedure involving a hierarchic

tree description on which a fuzzy logic reasoning is built up.

The method performances in terms of sensitivity/specificity are analyzed in Chapter IV according to the selected parameters and the CT acquisition protocol. A comparison with an interactive pathology delineation performed by a radiologist expert validates our approach from a subjective point of view. Several investigations on clinical cases are also discussed and illustrated both in axial cross-section and in 3-D volume rendering.

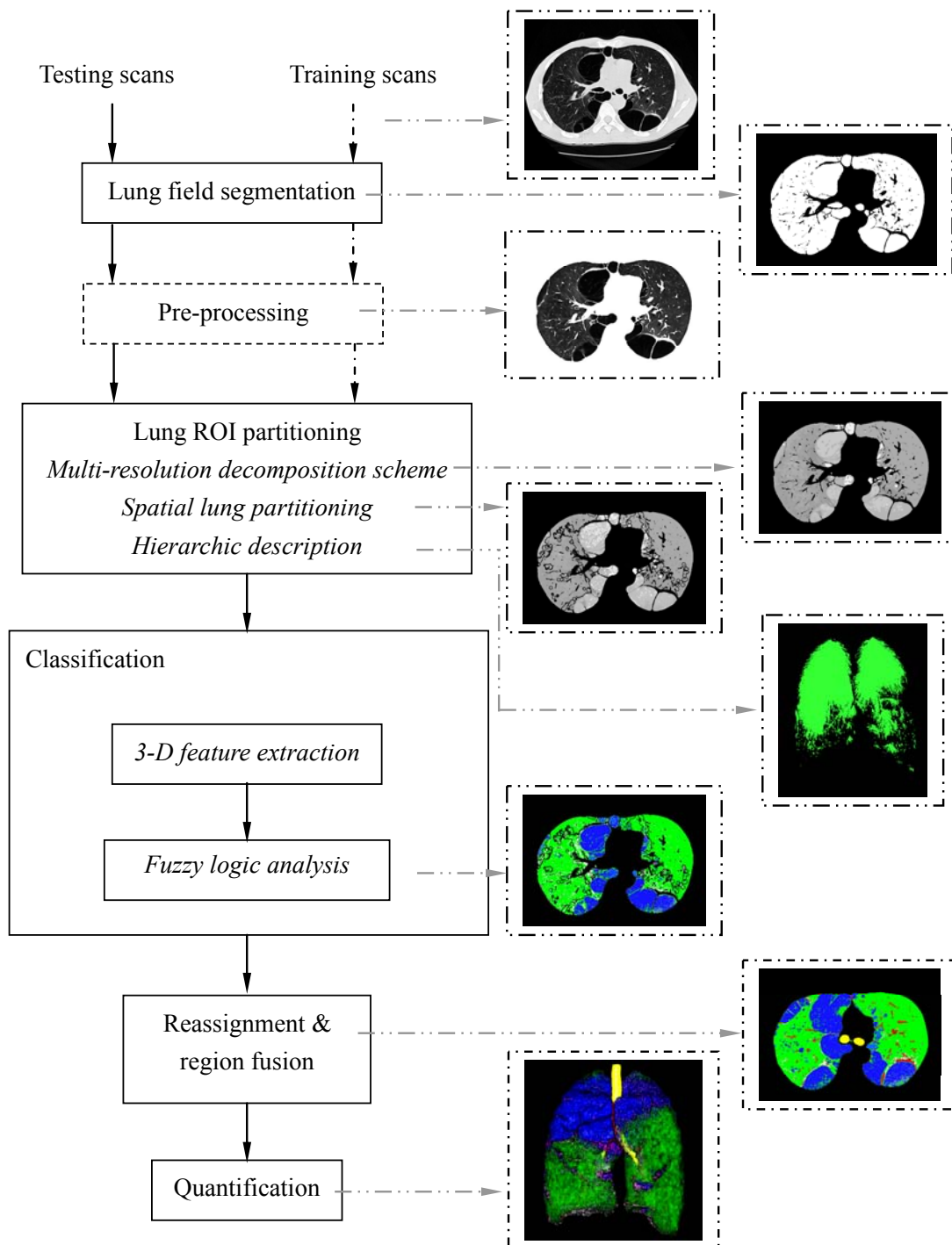


Fig. 69 The final flowchart of the developed approach.

Chapter IV

Clinical assessment

The performance evaluation of the developed approach is here presented in terms of sensitivity and specificity analysis with respect to the method parameter setup, CT acquisition protocol and a comparison with manual pathology selection performed by an independent radiologist expert. The difficulty of such analysis is related to the absence of a (quantitative) ground truth, a large variability among radiologists having been noticed. For this reason, our study with respect to the parameter setup and CT protocol will rely on a visual comparison of the results, either at the same axial level in the thorax, when the same dataset or the same patient is involved, or at the level where the pathology is present, if several cases are cross-analyzed for the same type of pathology.

The evaluation database covered a large variability in terms of pathology type and distribution, and CT acquisition protocol employed in clinical routine. In the following, we shall illustrate the analysis results on representative cases selected from our database.

IV.1 Influence of the method parameter setup

The only user-tunable parameter with potentially high impact on the result is the number of resolution levels, N_{RL} , used in the multi-resolution decomposition analysis. This parameter will condition the size of the low-density structures that can be captured at a given resolution level. The larger N_{RL} , the smaller the size increase of the selected structures between successive levels of decomposition. Low N_{RL} values will increase the risk of pattern clustering (and then of misclassification), while high N_{RL} will introduce more redundancy in the associated hierarchic tree structure leading to a smoother transition over scales of the $r\nu$ and $r\nu s$ features (see Section III.5.2). Note also that the computation time increases linearly with N_{RL} , so smaller N_{RL} values will be preferred.

Fig. 70 and Fig. 71 show a sample of axial images taken at two locations from the classification of three CT scans with emphysema, fibrosis and ground-glass, using 5, 8, 12, 15 and 20 resolution levels in the decomposition, corresponding to an increase in the FSD filter size between successive levels of 27, 16, 10, 8 and 6 points, respectively.

We note that small N_{RL} values tend to overestimate the pathology distribution for EM and MEM cases and miss GDG patterns, while larger N_{RL} values might miss small-size disease patterns. Interestingly, for the FHC case with $N_{RL} = 15$, we note the presence of a FHC region in the middle part of the left lung (circle) which is not present for $N_{RL} = 12$ and $N_{RL} = 20$, and which

is classified as MEM for $N_{RL} = 5$ and $N_{RL} = 8$. This could suggest a potentially unstable behavior for large N_{RL} .

Base on these considerations, we choose as parameter value $N_{RL} = 12$ which seems to offer the best comparison between sensitivity and specificity, with a moderate computational cost.

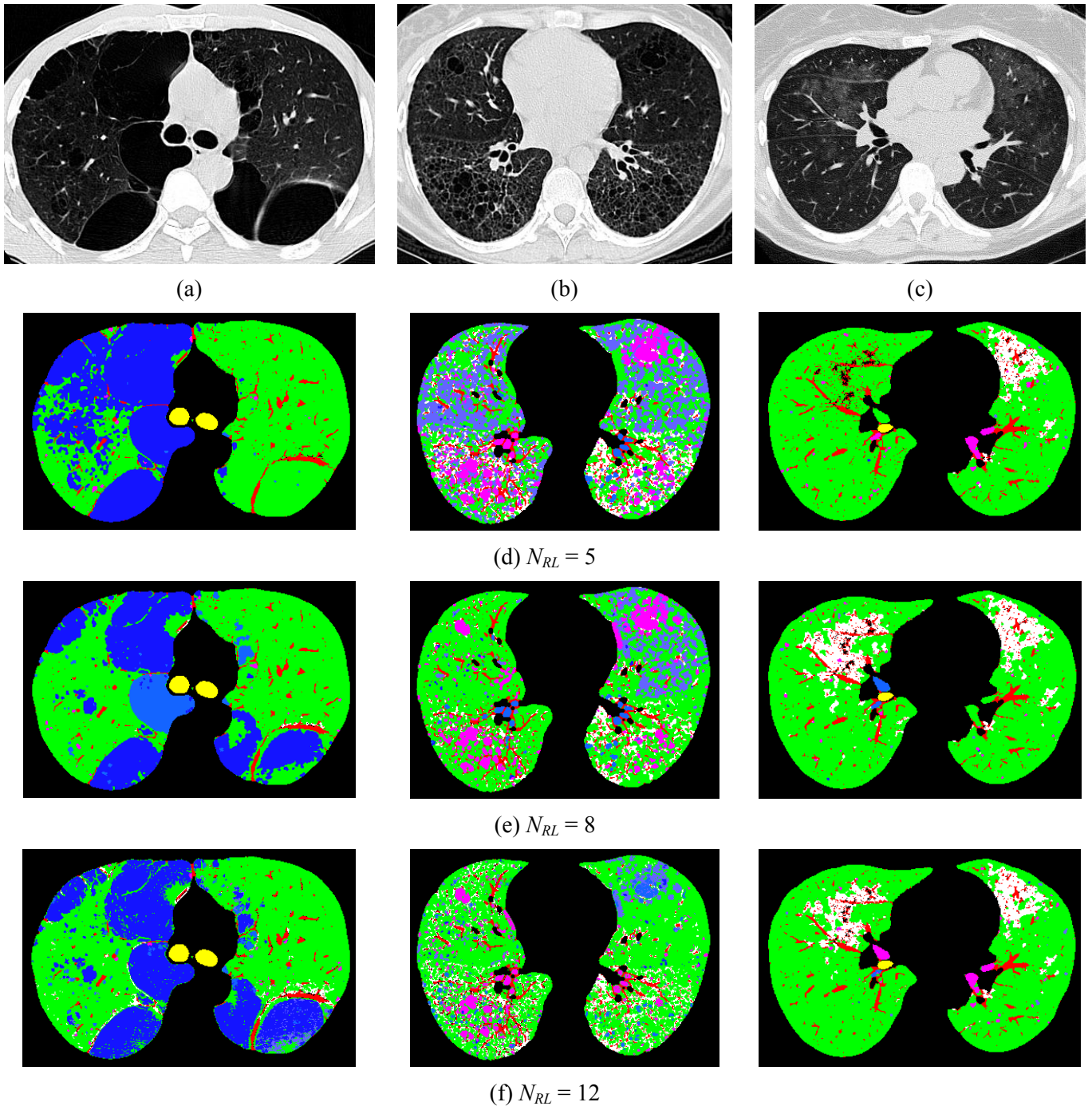
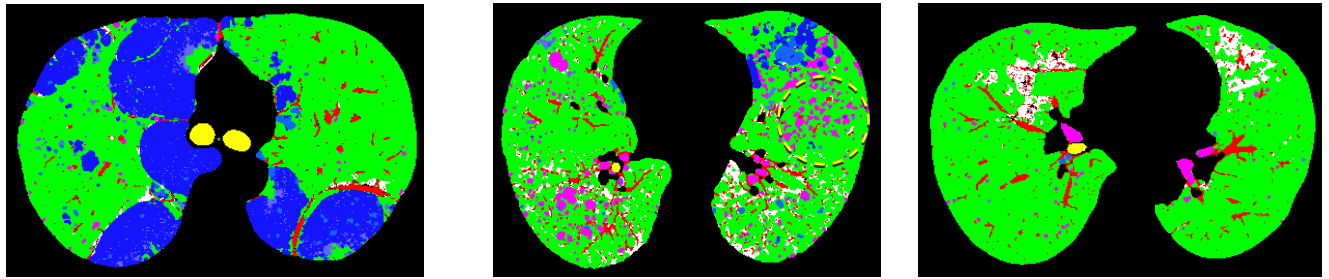
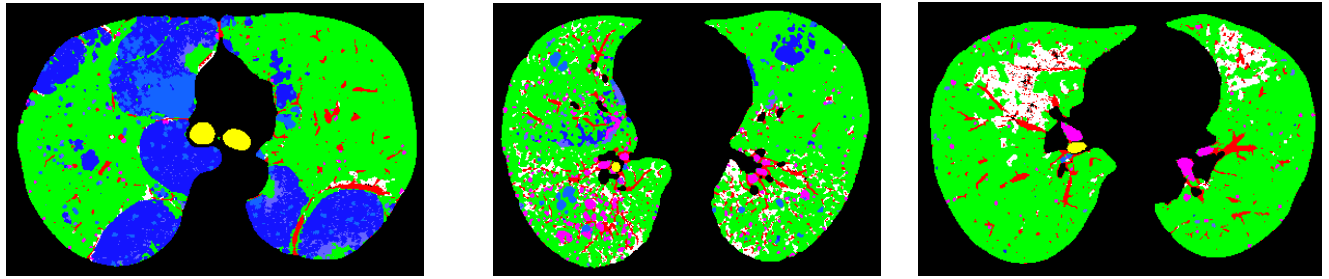


Fig. 70 The original CT images with (a) emphysema, (b) fibrosis, and (c) ground-glass were analyzed with (d) 5, (e) 8, (f) 12, (g) 15, and (h) 20 resolution levels. First selected axial level. Color code assignment: N MEM EM FHC GDG HD.



(g) $N_{RL} = 15$



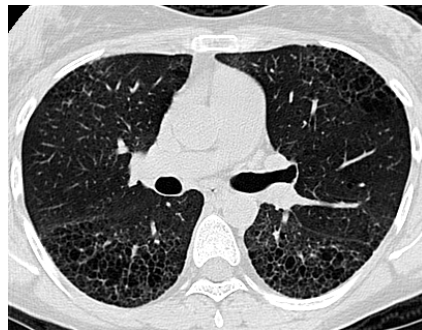
(h) $N_{RL} = 20$

Fig. 70 (Continued). The original CT images with (a) emphysema, (b) fibrosis, and (c) ground-glass were analyzed with (d) 5, (e) 8, (f) 12, (g) 15, and (h) 20 resolution levels. First selected axial level. Color code assignment:

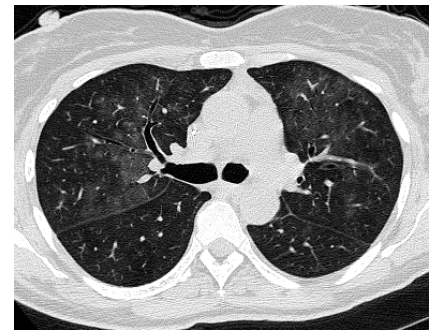
N  MEM  EM  FHC  GDG  HD 



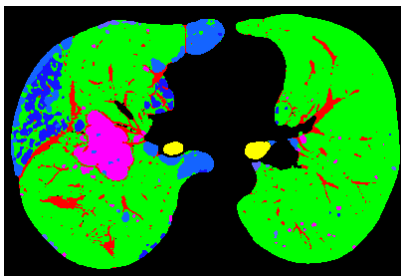
(a)









(b)



(c)



(d) $N_{RL} = 5$

Fig. 71 The original CT images with (a) emphysema, (b) fibrosis, and (c) ground-glass were analyzed with (d) 5, (e) 8, (f) 12, (g) 15, and (h) 20 resolution levels. Second selected axial level. Color code assignment: N  MEM  EM  FHC  GDG  HD 

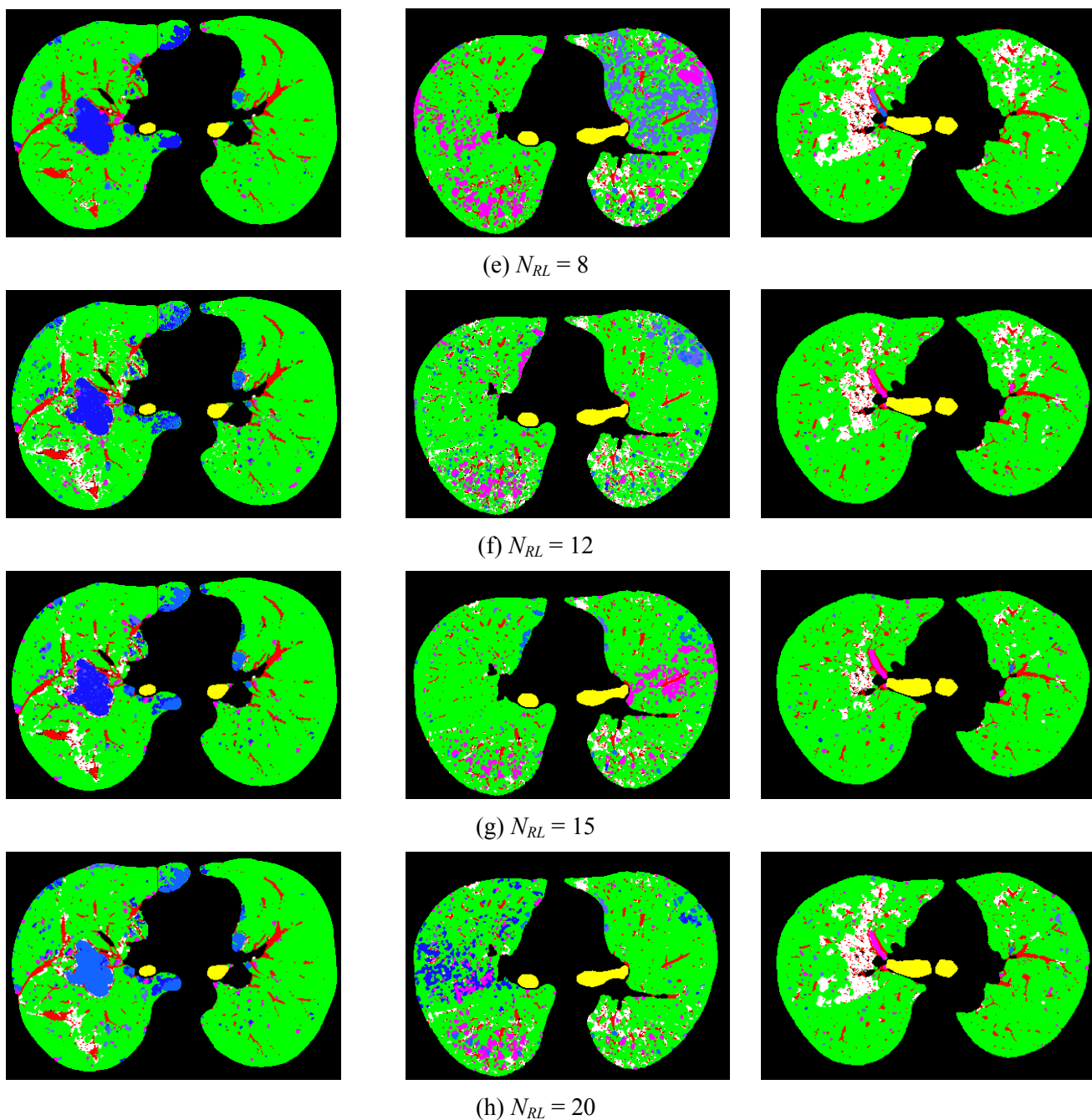


Fig. 71 (Continued). The original CT images with (a) emphysema, (b) fibrosis, and (c) ground-glass were analyzed with (d) 5, (e) 8, (f) 12, (g) 15, and (h) 20 resolution levels. Second selected axial level. Color code assignment:

N MEM EM FHC GDG HD

IV.2 Influence of the CT acquisition protocol

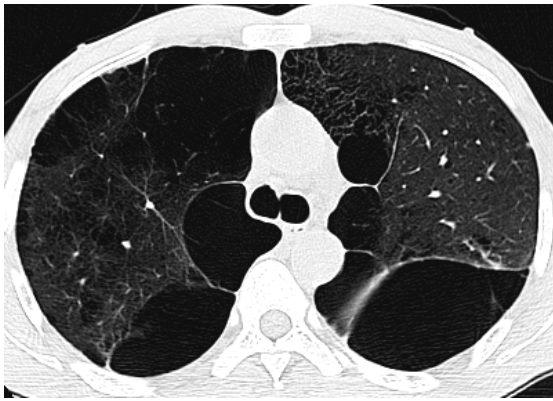
The patient cohort collected for this study consisted of 30 patients suspected of infiltrative lung diseases, including 13 emphysema, 14 fibrosis/honeycombing and 3 ground-glass cases. The CT acquisition was performed at full inspiration using the General Electric Light Speed scanner, with 16 or 64 detector rows. The X-ray beam collimation was of 1.25 mm in most of cases, with few exceptions of larger collimation (up to 3 mm) which will be discussed later on. The radiation dose was normal, varying from 278 to 433 mAs, so no assessment with respect to this parameter was possible. The reconstruction matrix was the usual 512x512 pixels, leading to an axial image resolution between 0.543 and 0.846 mm/pixel. The longitudinal sampling interval varies with the X-ray beam collimation between 1 mm and 1.5 mm.

Three reconstruction kernels were used for evaluation: “STANDARD” (low frequency), “LUNG” (medium-high frequency) and “BONEPLUS” (high frequency). All the scans were acquired in DICOM standard and converted into gray-scale according to the "lung" display window settings: window center = -600 HU, window width = 1600 HU. The influence of the CT acquisition protocol will be further on assessed with respect to the reconstruction kernel and collimation.

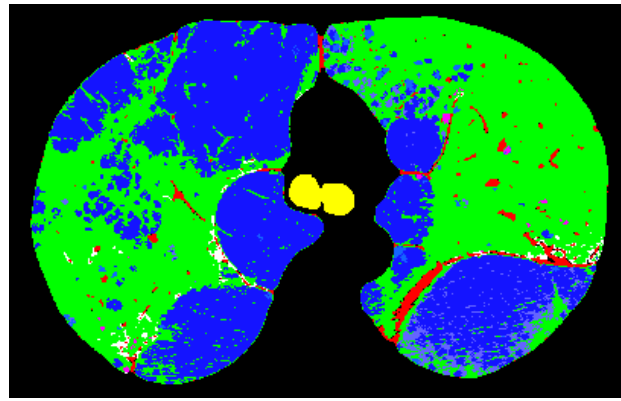
IV.2.1 Impact of the reconstruction kernel

Fig. 72-Fig. 74 illustrate a comparative analysis of the classification results for cases of emphysema, fibrosis and ground-glass, respectively, acquired with the three mentioned reconstruction kernels, for the same X-ray beam collimation (1.25 mm). Note that, when CT reconstructions with all these kernels were not available for the same patient, another subject having the same pathology was included in the comparison.

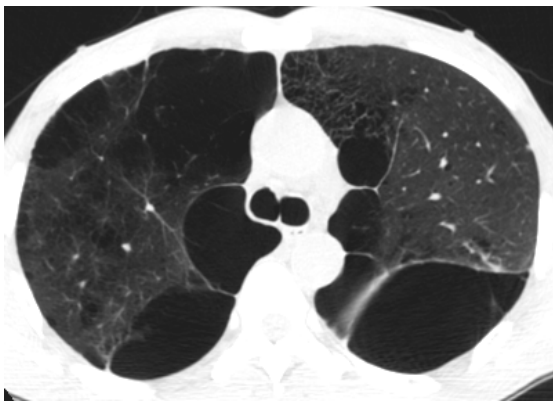
As a general trend, we note that CT protocols using the “STANDARD” kernel induce an overestimation of the pathology in the lung with the appearance in most cases of EM or MEM patterns (but also GDG, Fig. 72 (d) - left lung) which do not occur for the same (or similar) cases reconstructed using the “LUNG” or “BONEPLUS” kernels. This effect is due to the blurring induced by the low-pass frequency filtering which will bias the features related with gray-scale information. Consequently, the reconstruction kernel in the CT protocol should avoid the “STANDARD” filter (or other low-pass frequency kernel).



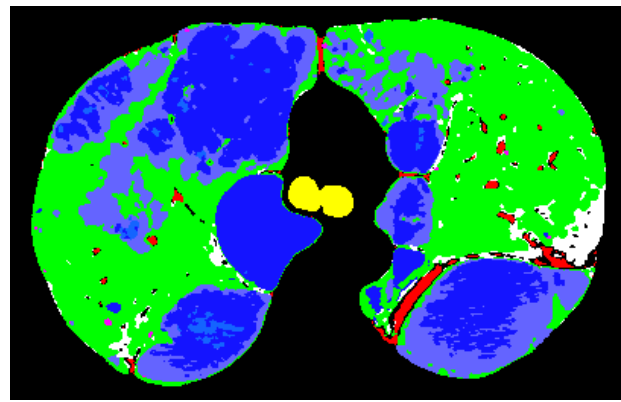
(a)



(b)



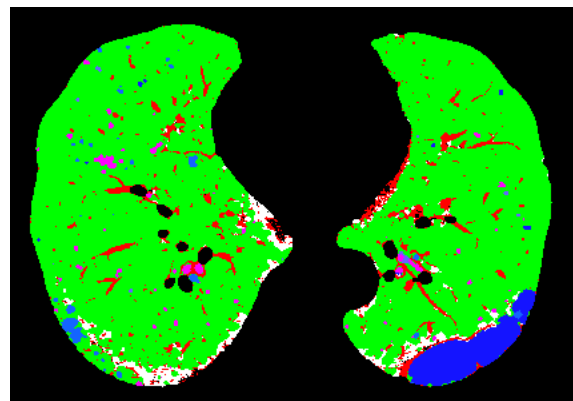
(c)



(d)



(e)

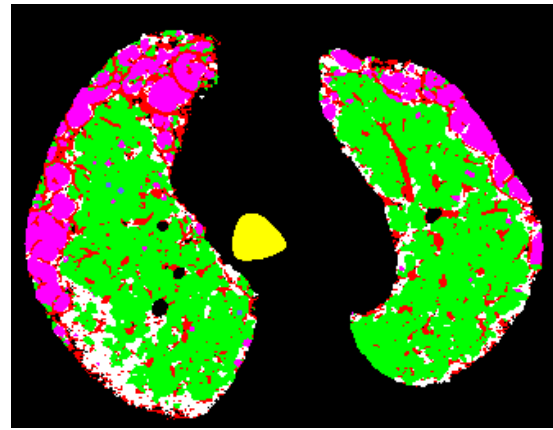


(f)

Fig. 72 Emphysema cases acquired with the (a) “LUNG”, (c) “STANDARD”, and (e) “BONEPLUS” filters, and (b), (d), (f) the corresponding classification results, respectively. Color code assignment: N ■ MEM ■ EM ■ FHC ■ GDG HD ■.



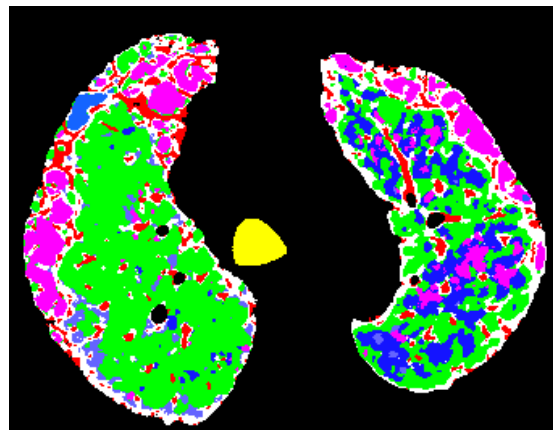
(a)



(b)



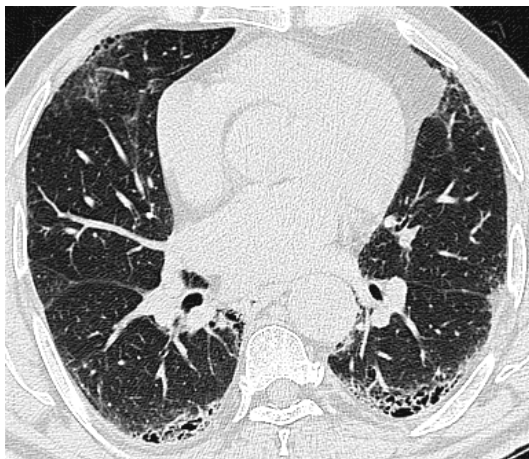
(c)



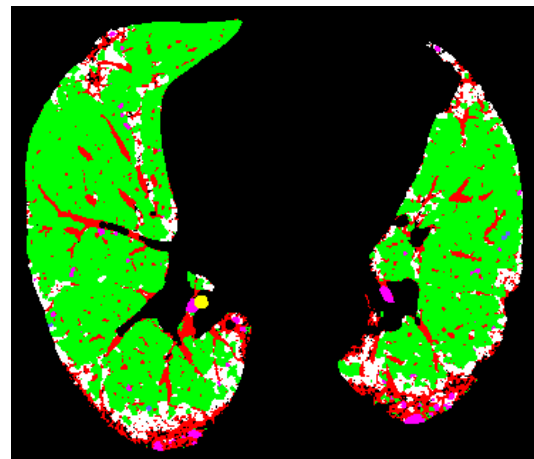
(d)

Fig. 73 The fibrosis cases acquired with the (a) “LUNG” and (c) “STANDARD” filters, and (b), (d), the corresponding classification results, respectively. Color code assignment:

N MEM EM FHC GDG HD .



(a)



(b)

Fig. 74 The ground-glass cases acquired with the (a) “LUNG”, (c) “STANDARD”, and (e) “BONEPLUS” filters, and (b), (d), (f) the corresponding classification results, respectively. Color code assignment:

N MEM EM FHC GDG HD .

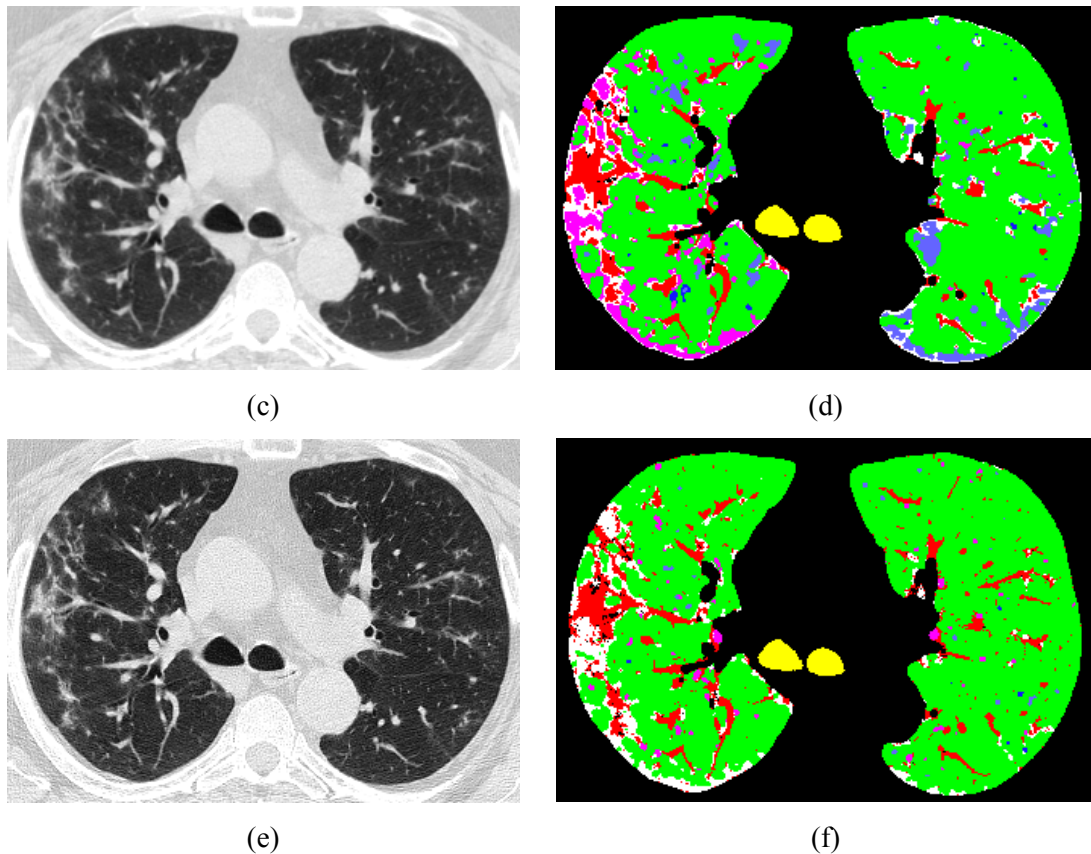


Fig. 74 (Continued). The ground-glass cases acquired with the (a) “LUNG”, (c) “STANDARD”, and (e) “BONEPLUS” filters, and (b), (d), (f) the corresponding classification results, respectively. Color code assignment: N MEM EM FHC GDG HD

IV.2.2 Impact of the X-ray beam collimation

The collimation of the X-ray beam will affect the longitudinal resolution of the 3-D image data and will also produce a visual blurring via the partial volume effect. A similar behaviour for large collimations is thus expected as in the case of the “STANDARD” kernel previously discussed. Fig. 75 shows a comparison between lung texture classifications obtained in the same patient for two acquisitions (longitudinal follow-up) with 0.625 mm and 1.25 mm collimation, respectively, and the “LUNG” kernel. When cross-checking similar axial locations, we note a slightly higher sensitivity in pathological pattern detection for thinner collimations, which is also due to the image resolution itself (allowing also a better visual detection too). However, both collimation values are acceptable for such texture analysis, the most currently used in clinical routine being the 1.25 mm.

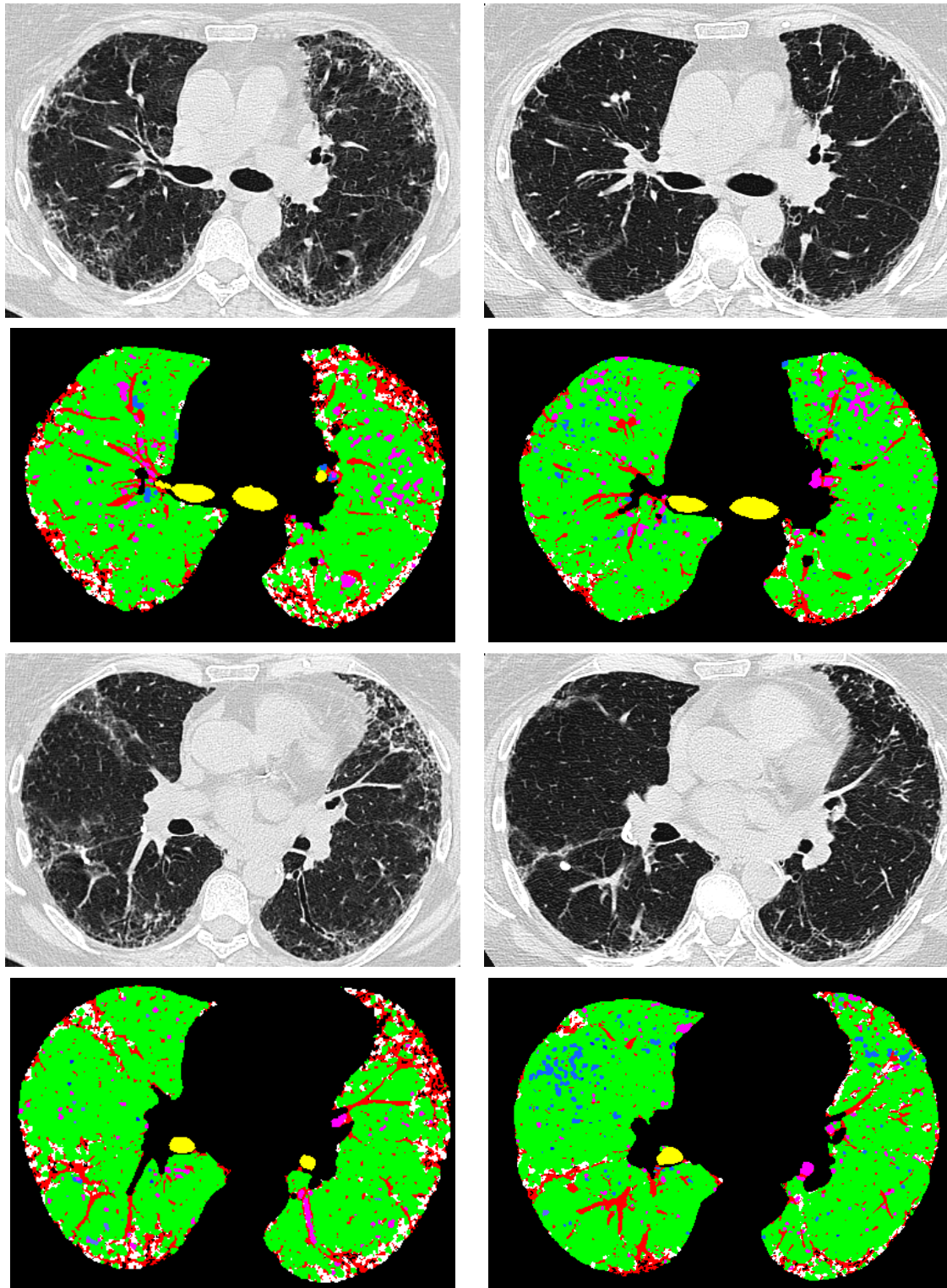


Fig. 75 Original CT images (same patient from a follow-up study) and the corresponding classification results, for acquisitions with 0.625 mm (left column) and 1.25 mm (right column) collimation. Note that the "LUNG" filter was used in both cases. Color code assignment: N MEM EM FHC GDG HD

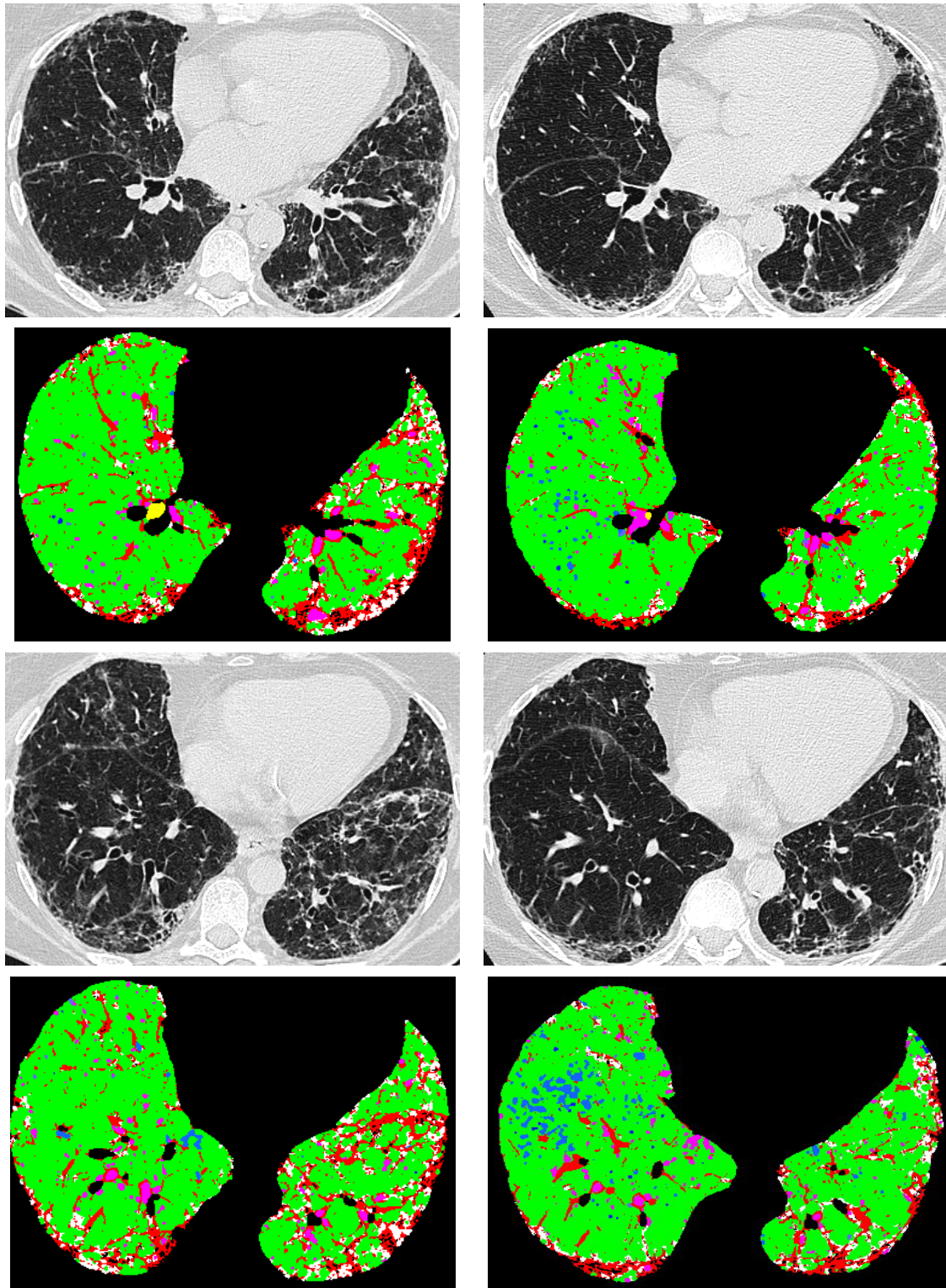


Fig. 75 (Continued). Original CT images and the corresponding classification results, for acquisitions with 0.625 mm (left column) and 1.25 mm (right column) collimation. Note that the "LUNG" filter was used in both cases. Color code assignment:

N MEM EM FHC GDG HD

Fig. 76 illustrates the effect of large (3 mm) versus thin (1.25 mm) collimation acquisitions (using the "BONEPLUS" kernel). The partial volume effect is much more important in this case and the pathology overestimation is extended to the whole lung. Such result was however expected since the classification features tune-up was not performed on large collimations, which are of reduced clinical interest for an accurate quantification. The recommended CT collimation for the developed CAD system is thus 1.25 mm or less.

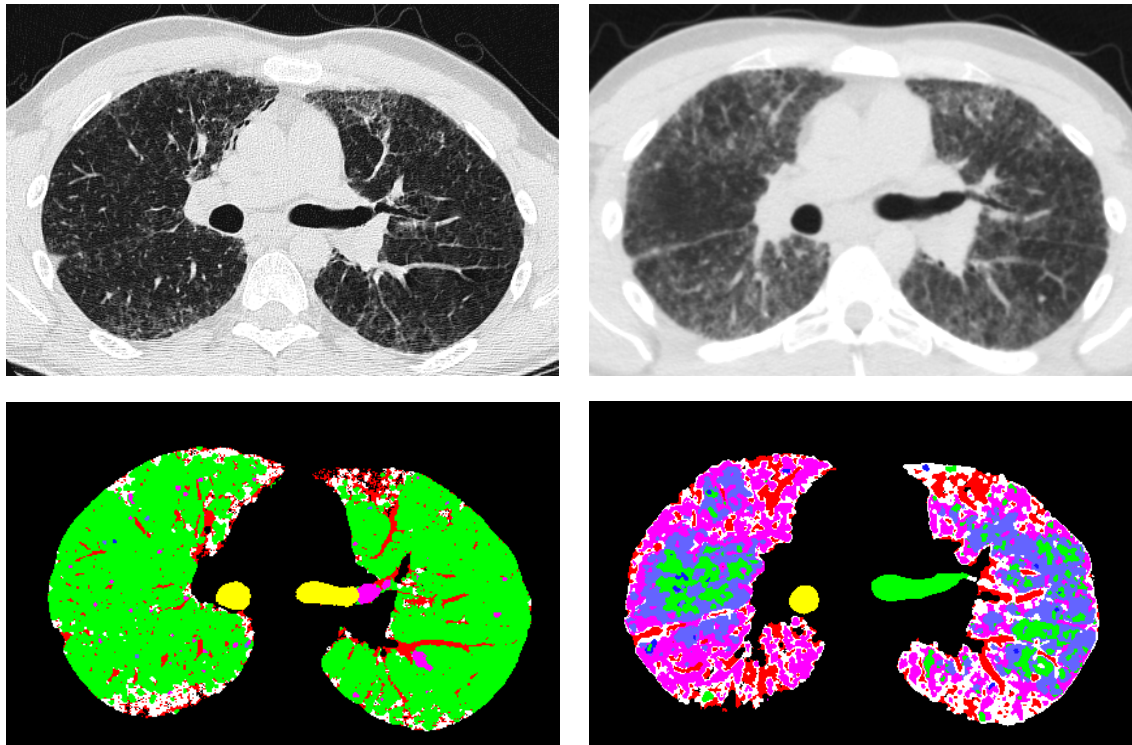


Fig. 76 Original CT images (same patient) and the corresponding classification results, for acquisitions with 1.25 mm (left column) and 3 mm (right column) collimation. Note that the "BONEPLUS" filter was used in both cases. Color code assignment:

N ■ MEM ■ EM ■ FHC ■ GDG HD ■

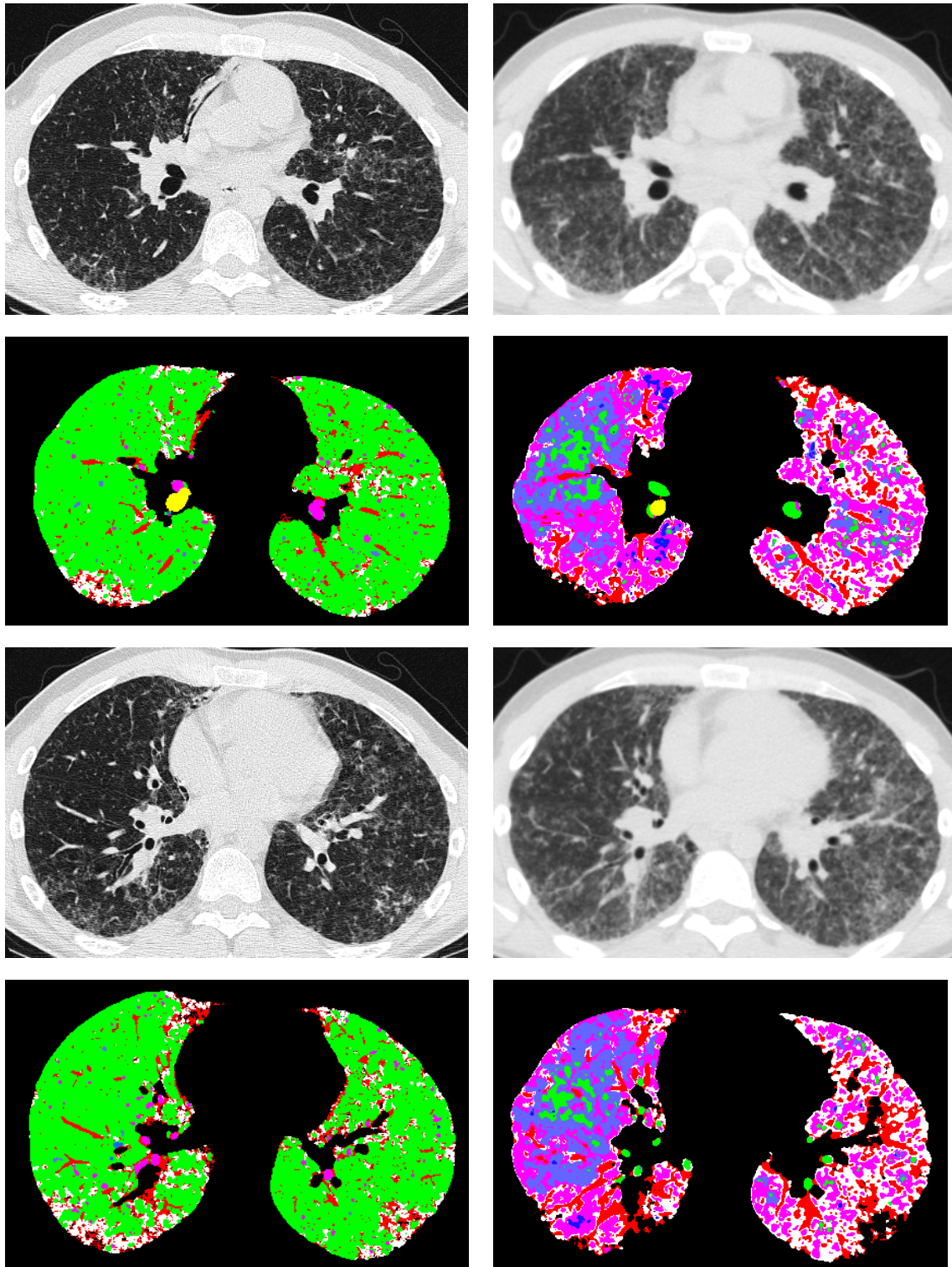


Fig. 76 (Continued). Original CT images and the corresponding classification results, for acquisitions with 1.25 mm (left column) and 3 mm (right column) collimation. Note that the "BONEPLUS" filter was used in both cases. Color code assignment:

■ N
 ■ MEM
 ■ EM
 ■ FHC
 ■ GDG
 HD
■

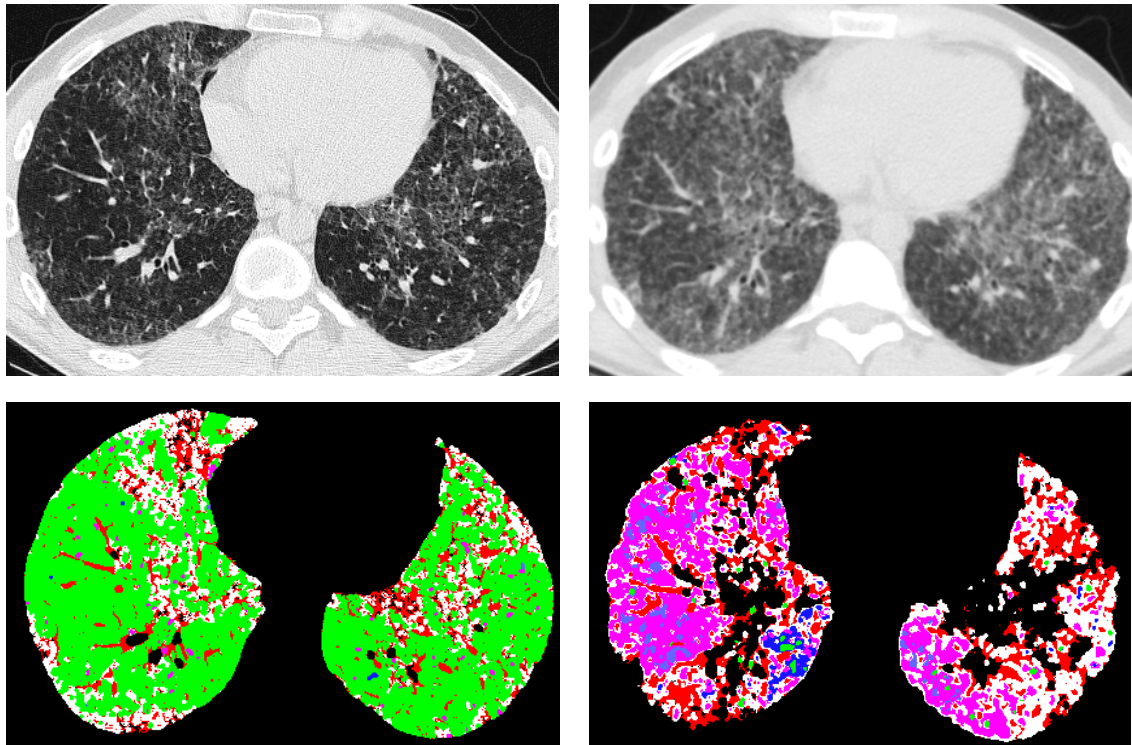


Fig. 76 (Continued). Original CT images and the corresponding classification results, for acquisitions with 1.25 mm (left column) and 3 mm (right column) collimation. Note that the "BONEPLUS" filter was used in both cases. Color code assignment:

N ■ MEM ■ EM ■ FHC ■ GDG HD ■

IV.3 Radiologist expert versus the CAD system

The one of the validation methods for reliability evaluation is to compare the CAD experiment result with the ground truth. In our study, the ground truth was performed by manually margin drawing (by the radiologist expert) and regional coloring (by the computer) of 9 scans from 27/01/2010 to 05/05/2010. Because the development of the ground truth database revealed to be a tedious and time consuming task, the expert selected only a subset of CT images (one for 3-4 images). Therefore, the CAD assessment was performed in 2-D, over the selected images, not for the whole 3-D volume. Additionally, if two pathological targets were adjacent in an image, the expert drew a larger margin of the region involving these two targets, which may also include "normal" tissue. Conversely, the CAD system focuses on individual lung patterns detection and classification, so that different pathological targets are not merged together. Hence, the comparison with the ground truth was here based on the visual aspects only, and did not consider further quantitative evaluation.

Fig. 77 shows a case with emphysema and fibrosis included in the ground truth validation, which is acquired using the "LUNG" filter and 1.25 mm X-ray beam collimation. In this example, the apical regions of the lungs are with a large amount of emphysema, and

the basal regions show few fibrosis patterns. In the first two rows, the comparison shows a high accuracy of our CAD system in pathological region detection comparing to the ground truth, but the target was classed as fibrosis, not emphysema as in the ground truth. This is due to the high-intensity border of the emphysema pattern in this subject, which is one of the texture characteristics of fibrosis. In the fourth row, each fibrosis pattern of the ground truth was detected in the classification result. The patterns marked by red circles were not drawn in the ground truth, but detected and classed as HD and GDG patterns in the CAD system. In visual aspect, these patterns look like pathological targets with high intensity. Hence, these “misclassifications” might be due to the oversights of the expert.

Fig. 78 shows another case with fibrosis included in the validation, which was acquired using the “LUNG” filter with 0.625 mm collimation. In this example, the appearance of fibrosis is in terms of a large amount of reticulations and hazy opacities (similar to GDG) so that such patterns were classified as GDG and HD in the CAD classification result. In the third and fourth rows, most of the pathological regions drawn in the ground truth were detected in the classification results. The areas of these regions in the classification results are smaller than the corresponding areas in the ground truth. Such situation is more obvious in the comparison of the fifth row. Its explanation is that the reasoning modes of the radiologist expert and of the CAD system are different. From the radiologist viewpoint, the selected region should include all the pathological zones which are adjacent so that larger margins of the pathological regions would be drawn, which might include “normal” zones. In classification, however, the CAD system focuses on each texture type. During the analysis, different tissues would be separated (by the multi-resolution decomposition scheme) based on the gray value and texture information, and then, would be classed as normal tissue and pathologies, respectively. Therefore, the “normal”-looking zones would be discriminated from the pathology margin, even though they were surrounded by the pathologies.

In Fig. 79, we show a different case with the same pathological condition, which was acquired using the "BONPLUS" filter and 1.25 mm collimation. In the classification result of the second and fifth rows, regions in the left lung were classed as normal tissue, but were included in the pathology region by the radiologist expert. Note however that the visual aspect of such regions looks “normal” in terms of lung texture.

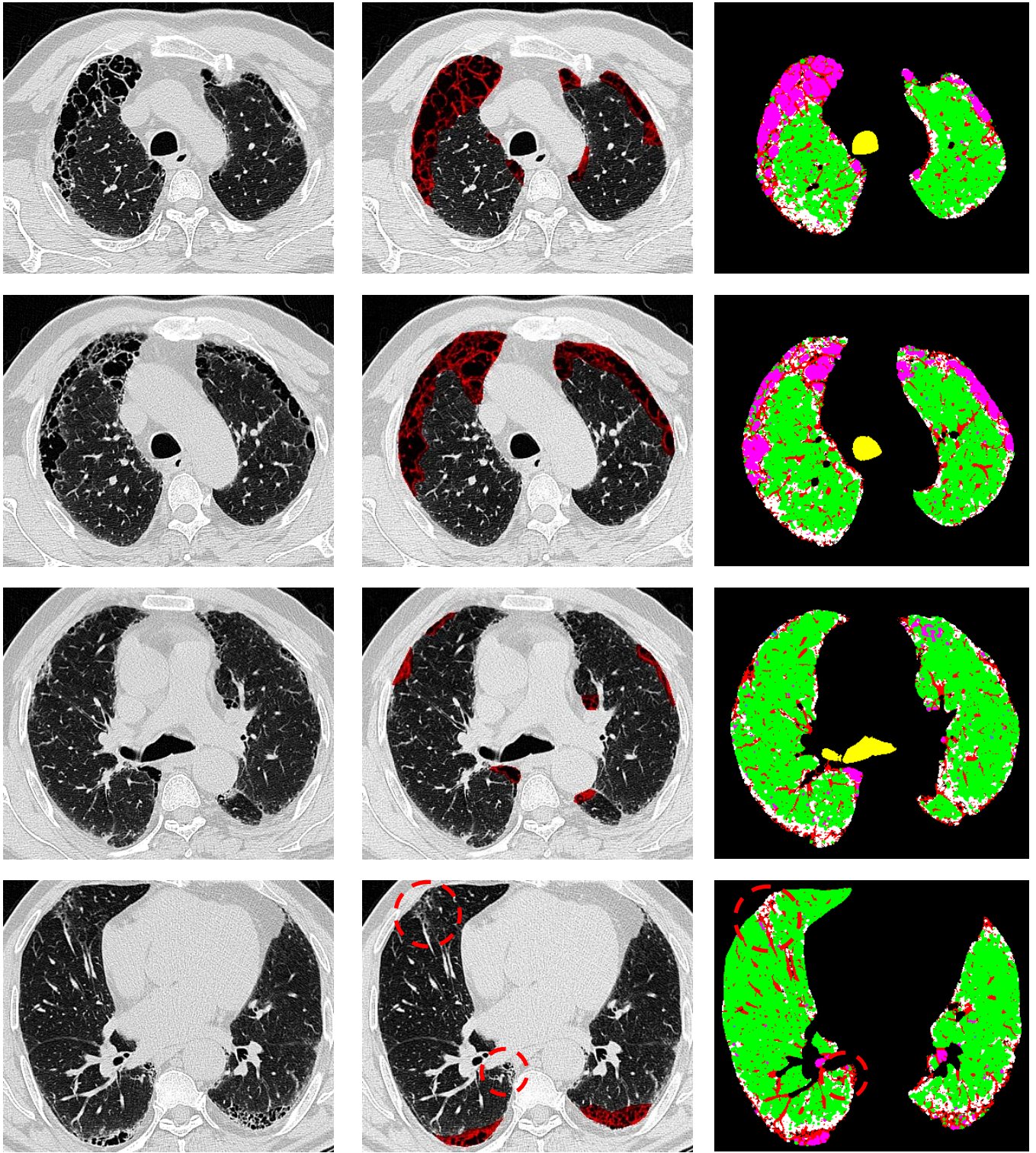


Fig. 77 The comparison between original CT images (left column), the corresponding ground truth (middle column), and classification results (right column). Note that the "LUNG" filter and 1.25 mm collimation was used in this case. Color code assignment: N ■ MEM ■ EM ■ FHC ■ GDG HD ■.



Fig. 77 (Continued). The comparison between original CT images (left column), the corresponding ground truth (middle column), and classification results (right column). Note that the "LUNG" filter and 1.25 mm collimation was used in this case. Color code assignment: N ■ MEM ■ EM ■ FHC ■ GDG HD ■.

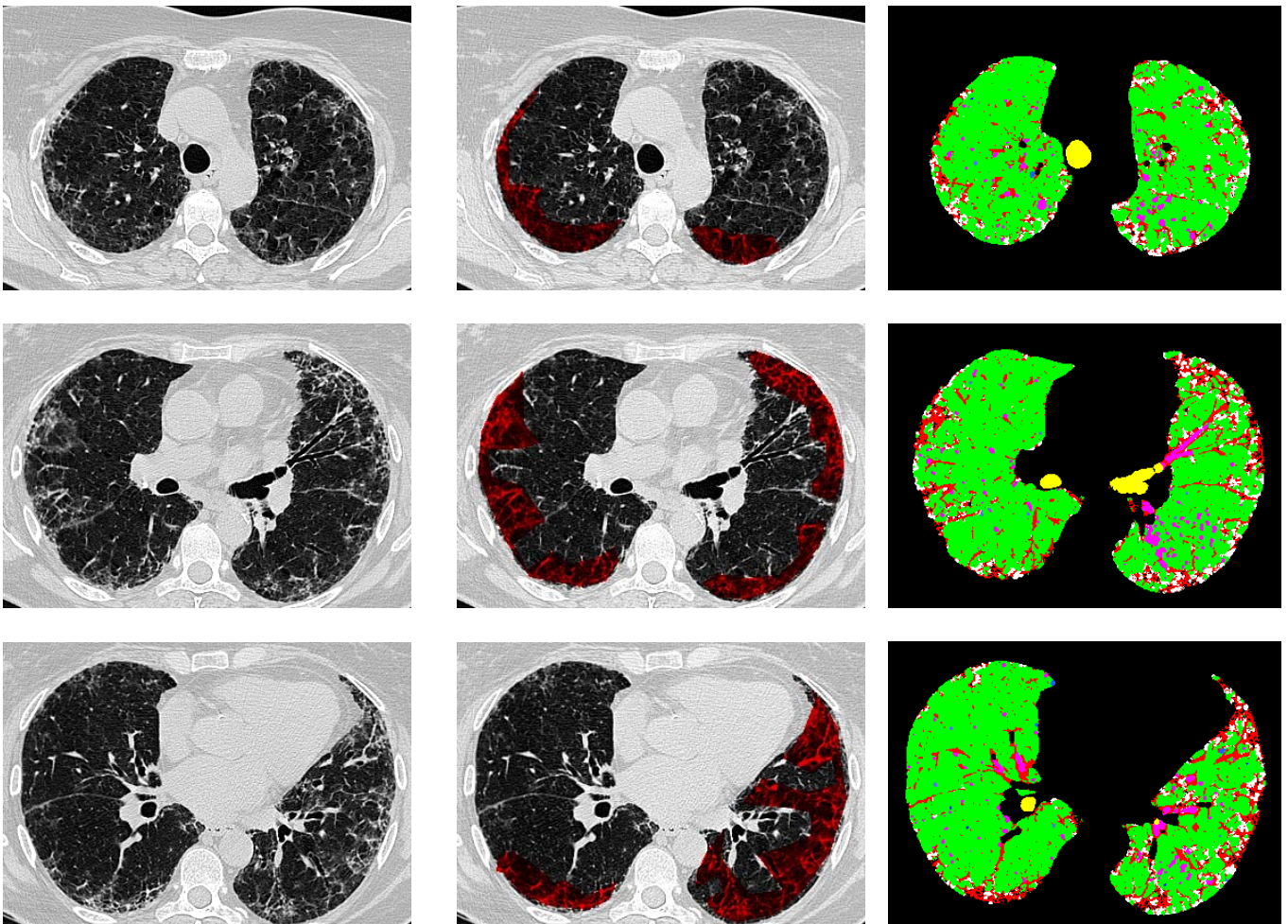


Fig. 78 The comparison between original CT images (left column), the corresponding ground truth (middle column), and classification results (right column). Note that the "LUNG" filter and 0.625 mm collimation was used in this case. Color code assignment: N ■ MEM ■ EM ■ FHC ■ GDG HD ■.

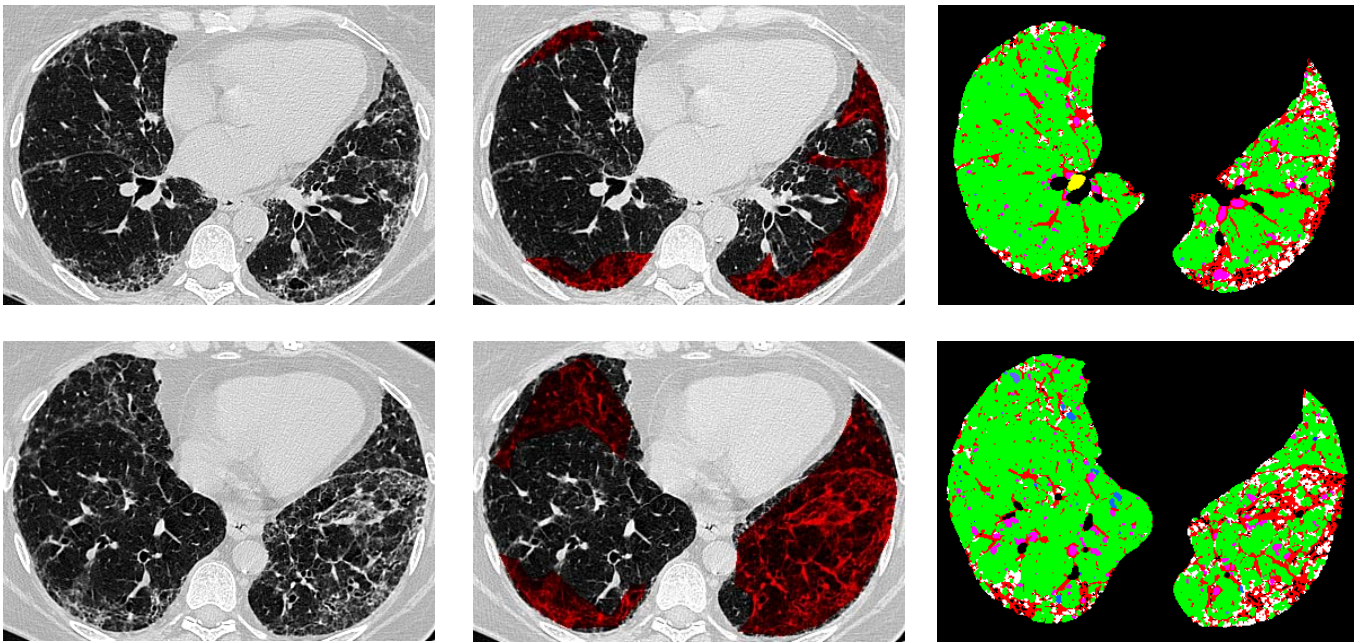


Fig. 78 (Continued). The comparison between original CT images (left column), the corresponding ground truth (middle column), and classification results (right column). Note that the "LUNG" filter and 0.625 mm collimation was used in this case. Color code assignment: N ■ MEM ■ EM ■ FHC ■ GDG HD ■.

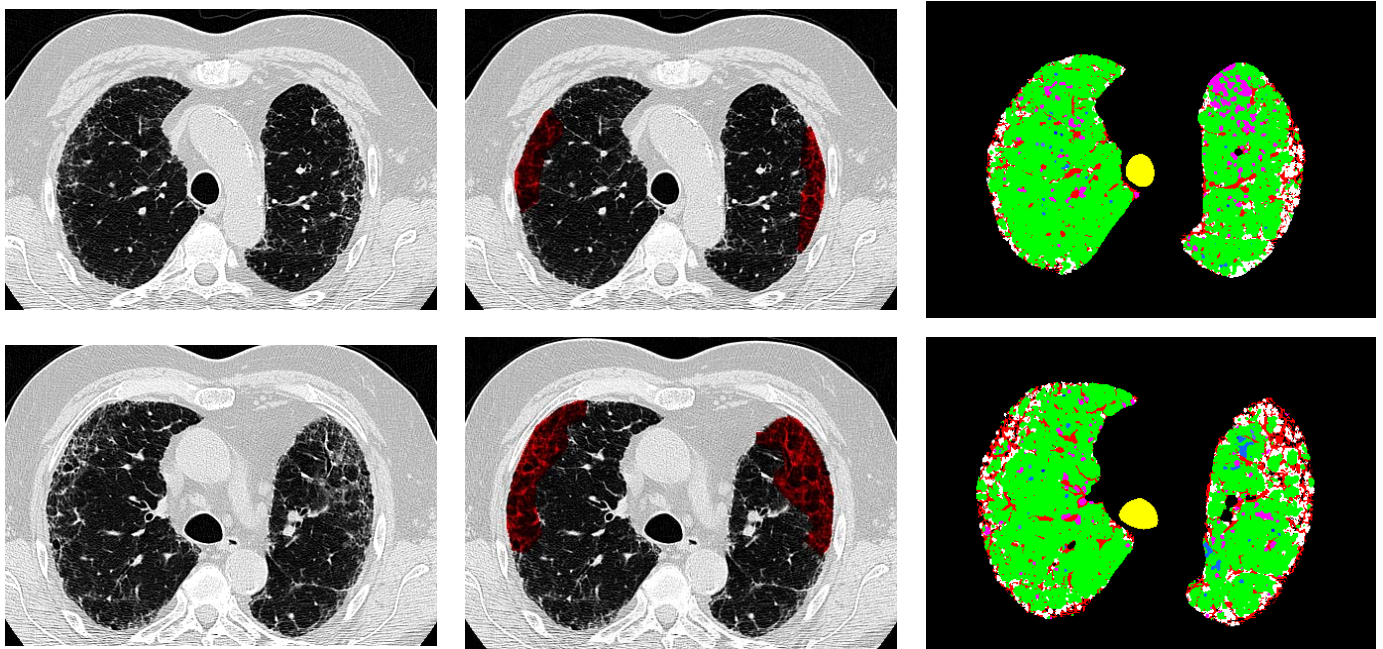


Fig. 79 The comparison between original CT images (left column), the corresponding ground truth (middle column), and classification results (right column). Note that the "BONEPLUS" filter and 1.25 mm collimation was used in this case. Color code assignment: N ■ MEM ■ EM ■ FHC ■ GDG HD ■.

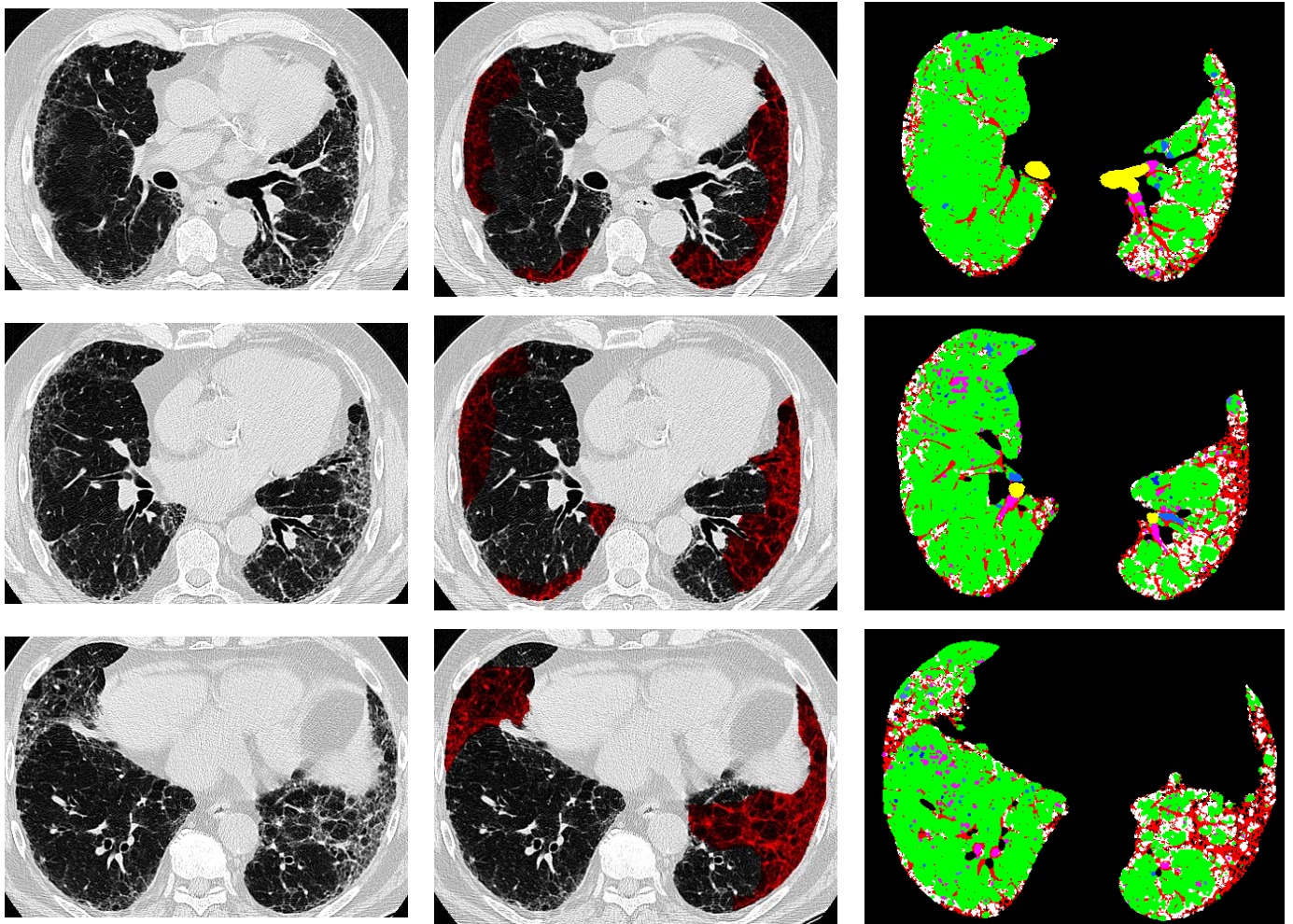


Fig. 79 (Continued). The comparison between original CT images (left column), the corresponding ground truth (middle column), and classification results (right column). Note that the "BONEPLUS" filter and 1.25 mm collimation was used in this case. Color code assignment: **N** ■ **MEM** ■ **EM** ■ **FHC** ■ **GDG** **HD** ■.

We also investigated few normal cases, such as in Fig. 80 and Fig. 81. Since these cases were acquired using a different CT scanner (SIEMENS), they were not included into the testing dataset (30 patients), being used instead for comparison with pathological cases in order to evaluate the specificity of the CAD system. In Fig. 80 and Fig. 81, although most lung regions were classed as normal tissue in the right columns (the classification results of the CAD system), there were still some overestimations. This is due to the different representation of lung tissues on the CT images acquired using other CT protocols. The CAD system result was slightly biased by the scanner type "SIEMENS" with the associated protocol ("B30f" and "B46f" reconstruction kernel, 0.75 mm collimation). For example, in comparison with the representation of the normal tissue on the original CT images in Fig. 79, the representation of normal tissue in Fig. 81 is darker. So, some normal regions were classed

as MEM (overestimation) in the first and second rows in Fig. 81. Note that, in the third row of Fig. 80, the region with slight fibrosis was missed by radiologist, but detected and classed as HD in the CAD classification result.

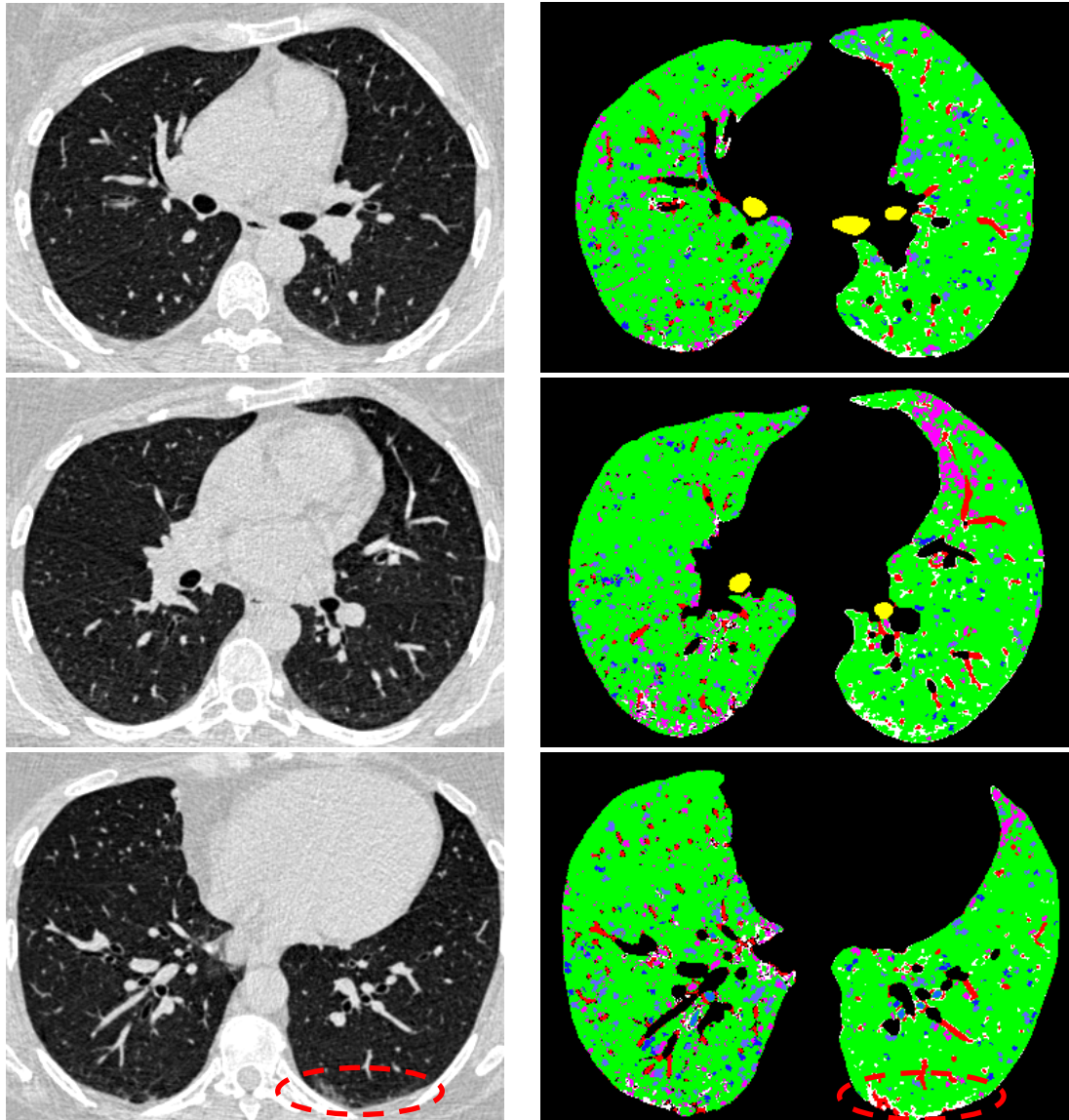


Fig. 80 The comparison between original CT images with normal tissue (left column), and classification results (right column). Note that the data was acquired using a “SIEMENS” machine with the "B30f" reconstruction kernel and 0.75 mm collimation.

Color code assignment: N ■ MEM ■ EM ■ FHC ■ GDG HD ■

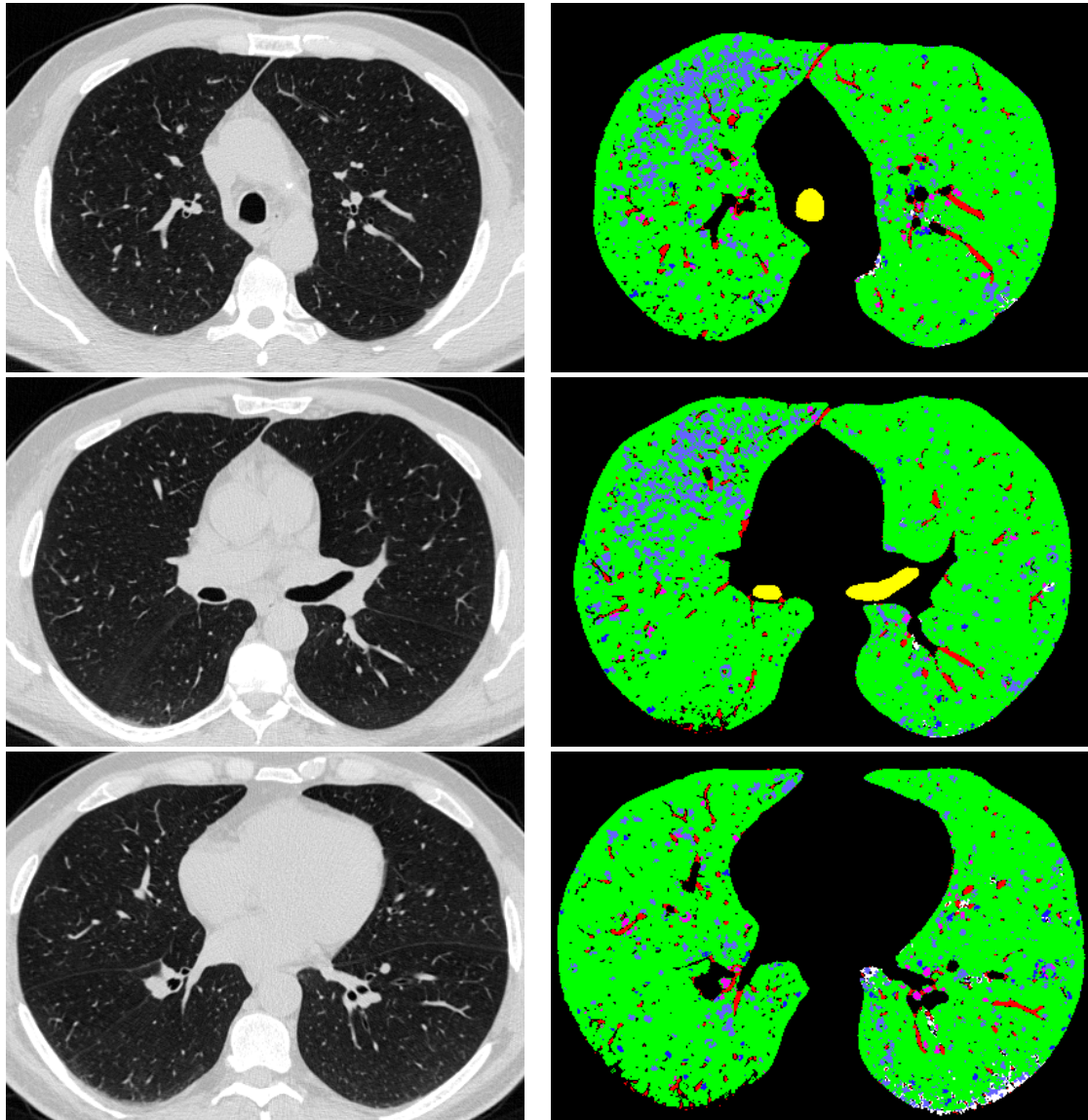


Fig. 81 The comparison between original CT images with normal tissue (left column), and classification results (right column). Note that the data was acquired using a “SIEMENS” machine with the "B46f" reconstruction kernel and 0.75 mm collimation.
 Color code assignment: N MEM EM FHC GDG HD

IV.4 Longitudinal follow-up studies

The interest of a CAD system for lung disease quantification is also expressed in terms of patient follow-up ability that it offers. We have tested the developed approach on some follow-up cases available in our database which will be discussed and illustrated in the following.

The key requirement in longitudinal follow-up is the use of the same CT acquisition and clinical protocols over time. In addition, axial slice-by-slice comparisons are also conditioned by the same patient tilt with respect to the longitudinal scanner axis, which is

almost impossible to guarantee. Thus, the follow-up investigation should be performed in the 3-D space and be based on volumetric quantifications.

The examples that we shall discuss below do not fulfill all these requirements, however they underline the possibility of a 3-D quantitative follow-up of the patient, based on the proposed approach.

Fig. 82 depicts a follow-up analysis at 13 months interval for a subject with fibrosis. In this example, the fibrosis patterns show a large amount of reticulations and hazy opacities similar with ground-glass, while airspaces are practically absent. Consequently, in this type of fibrosis, the classification result shows HD and GDG patterns. Note that the protocol requirements are not respected here, the second acquisition being performed at different lung capacity and using contrast agent injection for complementary investigations. Consequently, the vascular structures are accentuated and we notice more HD/GDG patterns together with a global contrast increase in the image. The impact of the contrast agent on the HD/GDG opacities is not known and is difficult to state if the increase in HD/GDG pattern distribution in the second acquisition is due to the contrast agent or to the pathology itself. Note also that medium-small airways (which can not be extracted by the approach described in Section III.2) are logically classed as FHC since they show the same features. This misclassification can be solved by using a dedicated approach for airways segmentation [125] which is out of the scope of this research.

Another difficulty in the pathology assessment is introduced by the (small size) high-density regions which are detected during the lung mask segmentation (Section III.2). Such patterns may correspond both to fibrosis reticulations and lung vessels which are often locally connected. According to the radiologist definition, the classification of the fibrosis regions should include both low-density patterns and the surrounding reticulations, while avoiding the lung vessels at the periphery of the pathological patterns. To date, the separation of lung vessels from fibrosis reticulations was tackled via morphologic operations but is not completely solved for small-size HD structures (recall that the large vessels are removed from the lung mask).

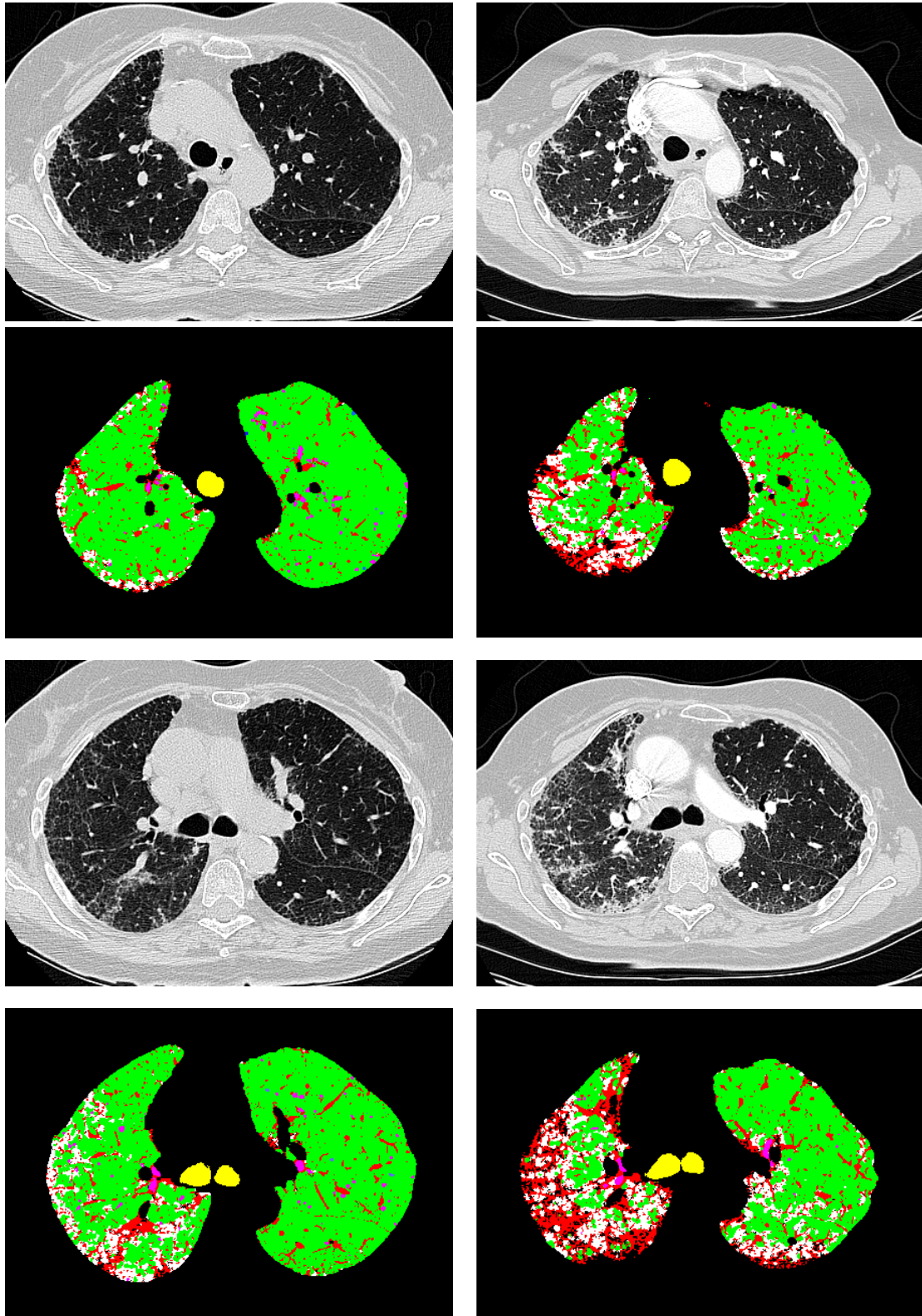


Fig. 82 Example of a follow-up investigation of a GDG case: left column - first examination, right column - 13 months later (exam using contrast agent injection for vascular structures). Both exams use 1.25 mm collimation and the “LUNG” kernel. Color code assignment: N MEM EM FHC GDG HD

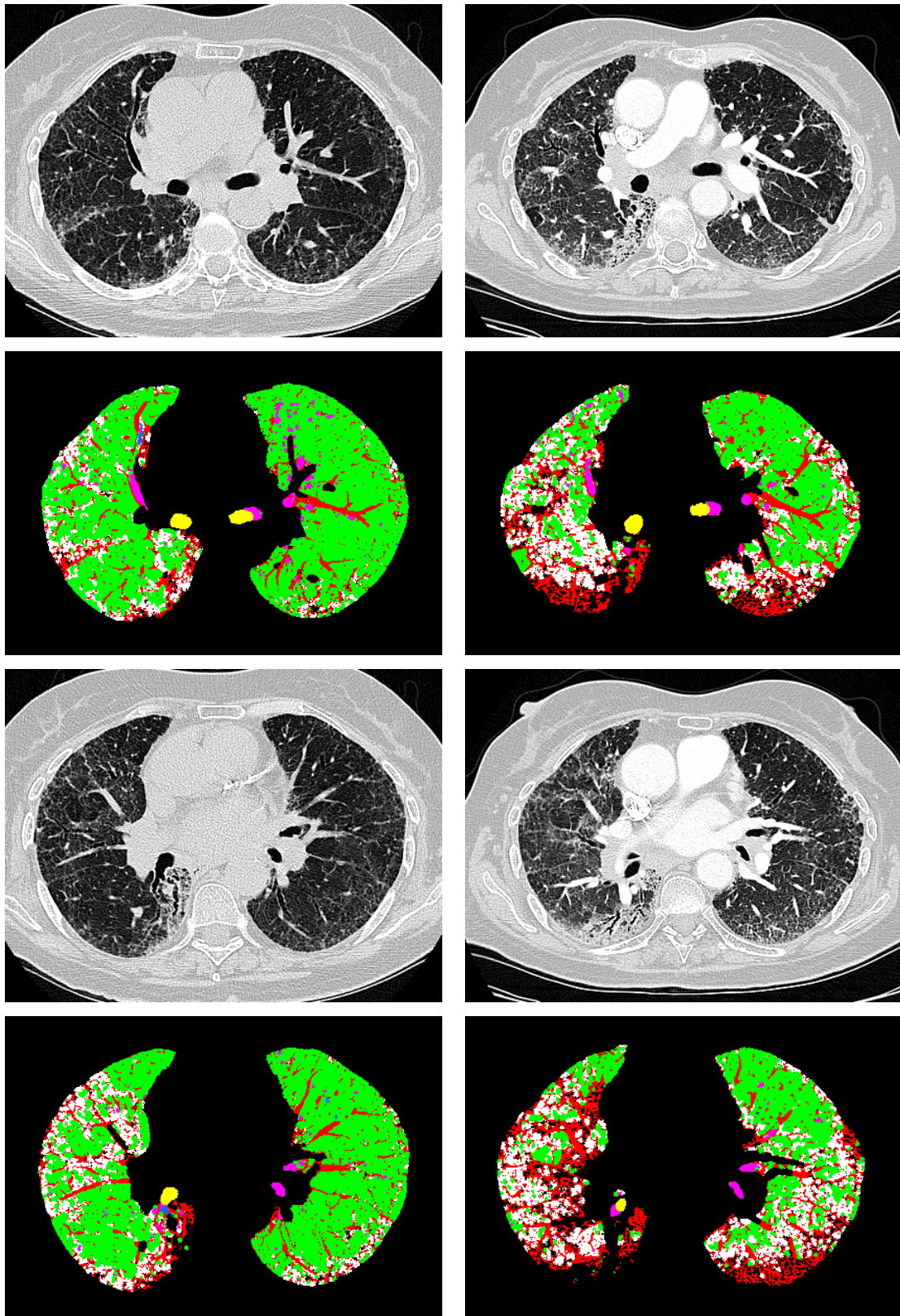
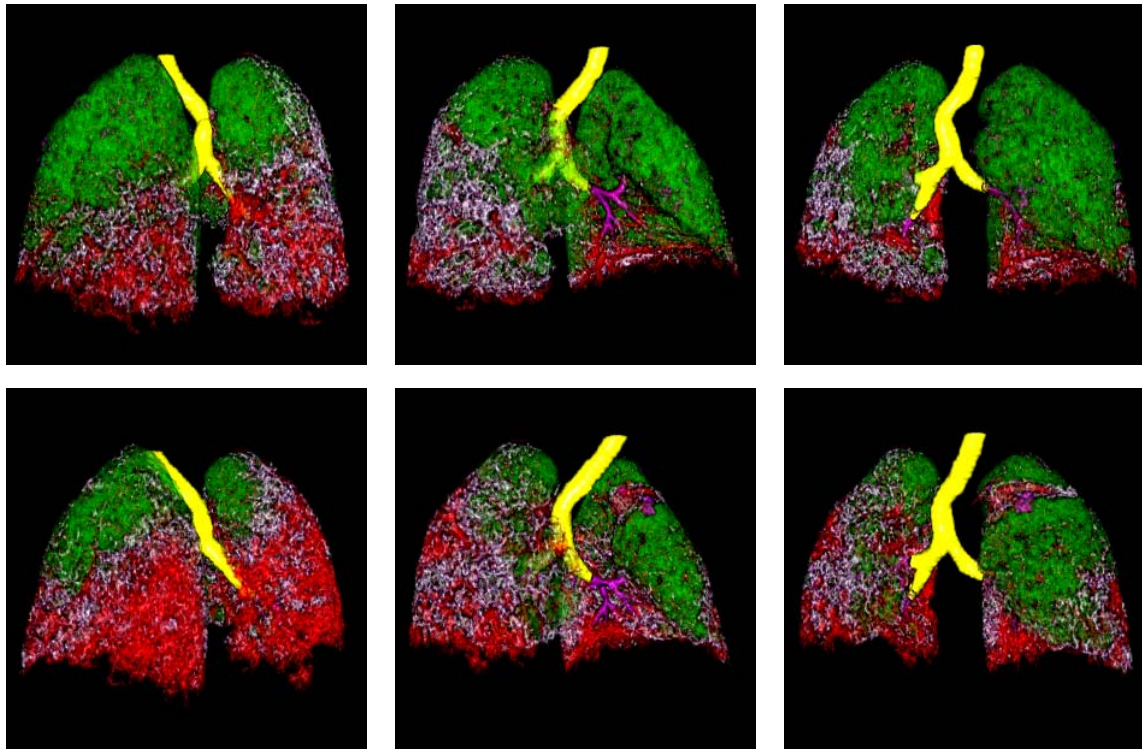


Fig. 82 (Continued). Example of a follow-up investigation of a GDG case: left column - first examination, right column - 13 months later (exam using contrast agent injection for vascular structures). Both exams use 1.25 mm collimation and the “LUNG” kernel.

Color code assignment: N ■ MEM ■ EM ■ FHC ■ GDG HD ■.

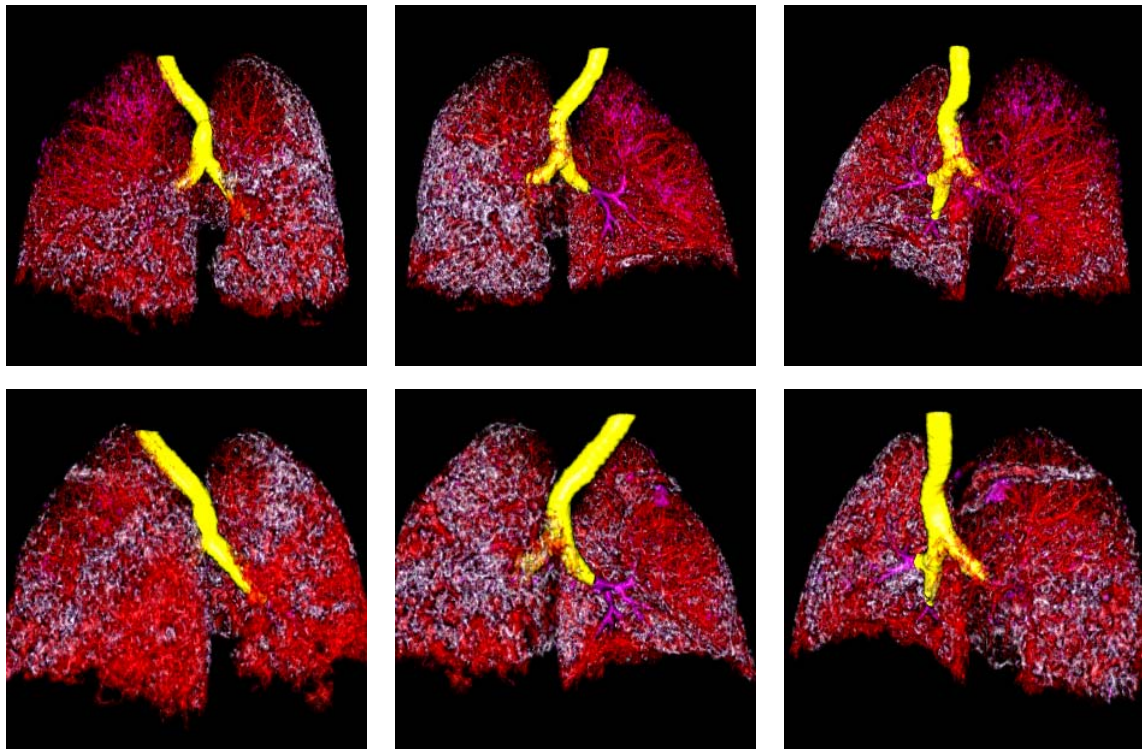
In addition, if high opacities are present at the lung periphery covering a large region (this phenomenon is accentuated for contrast agent injection CT scans) as shown in Fig. 82 right bottom rows, the lung region in this area is not segmented and the pathologic patterns are missed in the classification. Such problem could be solved by adapting the lung mask detection and the classification approach to contrast agent-based acquisitions (for example working on different window settings for lung region detection and the classification).

The developed CAD system should enable a volumetric analysis for patient follow-up, based on 3-D volume rendering representations as illustrated in Fig. 83. Such visualization better underlines the mix-up between lung vessels and fibrosis reticulations which limit the quantification capability of the approach for FHC and GDG patterns. Further developments are needed in order to separate the vascular and non-vascular HD structures in the pathologic lungs.



(a) Illustration of all textural patterns.

Fig. 83 Follow-up analysis for the case in Fig. 82 illustrated using three views obtained with 3-D volume rendering. Top: baseline, bottom: second acquisition. Color code assignment: N ■ MEM ■ EM ■ FHC ■ GDG HD ■.



(b) Illustration of the FHC, GDG and HD patterns only.

Fig. 83 (Continued). Follow-up analysis for the case in Fig. 82 illustrated using three views obtained with 3-D volume rendering. Top: baseline, bottom: second acquisition.

Color code assignment: N ■ MEM ■ EM ■ FHC ■ GDG HD ■.

Fig. 84 shows another follow-up investigation of a subject with fibrosis, performed at 8 months and 5 months intervals, respectively, using 1.25 mm collimation, the “BONEPLUS” (baseline) and the “LUNG” (2nd and 3rd checkup) kernels. The lung capacity is not controlled in this study, neither, but the second and third acquisitions show similar lung volumes. The same remarks as for example in Fig. 83 are also valid here, however the confidence of the findings is increased since the CT protocols are similar and no contrast agent is used. The follow-up analysis shows in this case an alteration of the pathologic status. Fig. 85 illustrates such comparative analysis based on 3-D volume rendering which reinforce the diagnosis confidence.

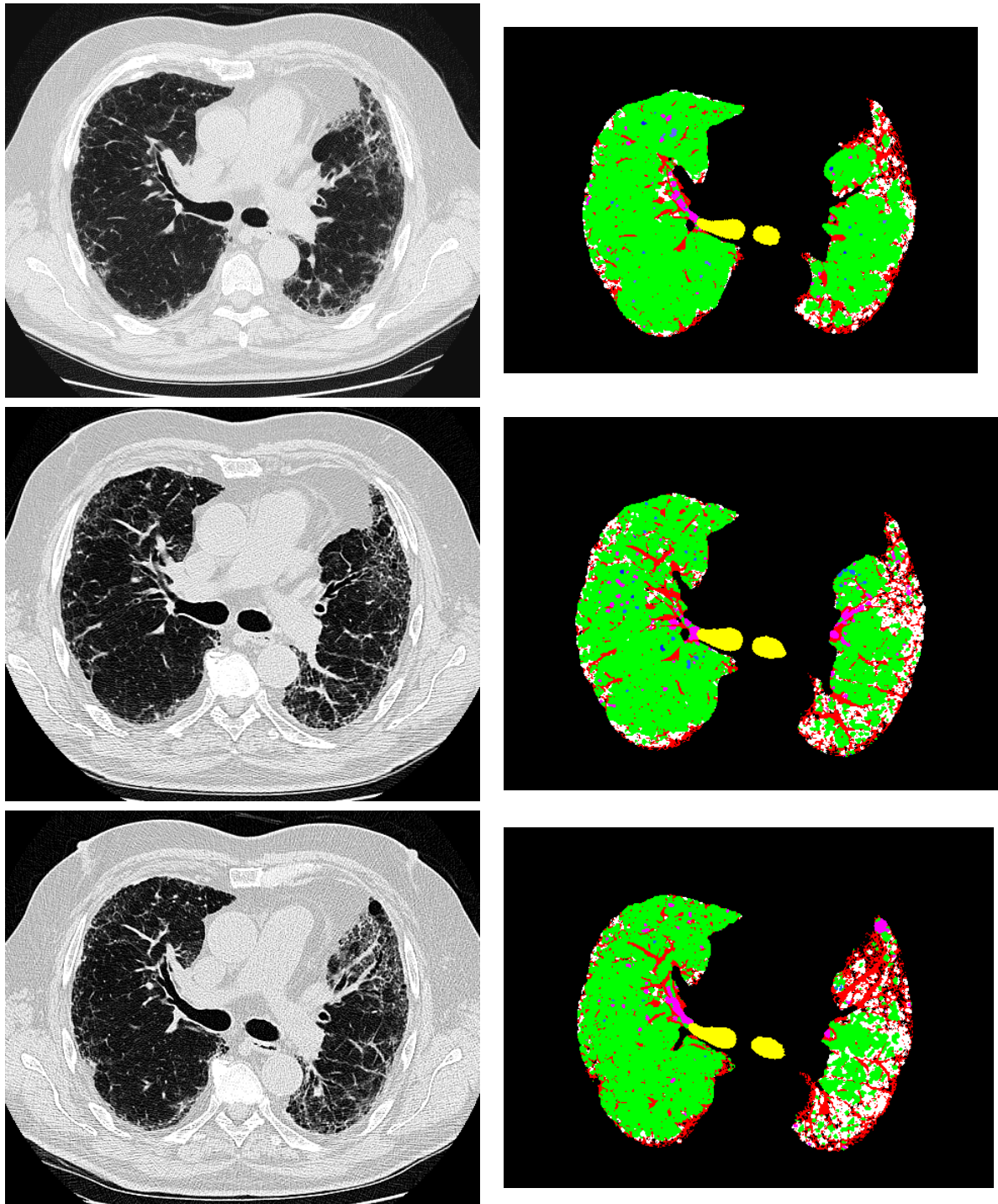


Fig. 84 Example of a follow-up investigation of a fibrosis case at 8 months (middle row) and 5 months (bottom row) interval, respectively. The baseline acquisition (top row) is performed with the “BONEPLUS” kernel, while the following ones use the “LUNG” kernel. All exams use 1.25 mm collimation. Color code assignment:

N ■ MEM ■ EM ■ FHC ■ GDG HD ■

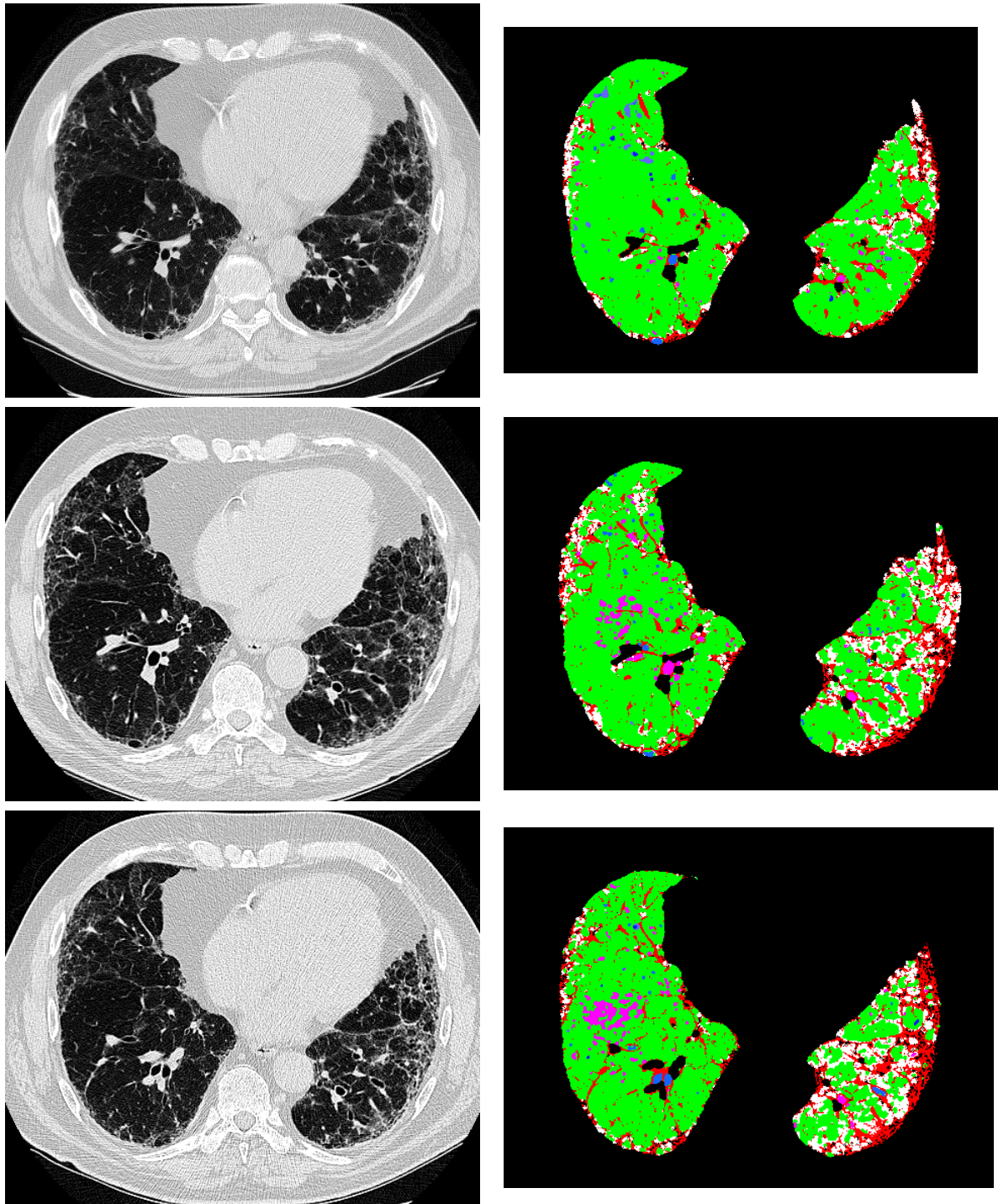
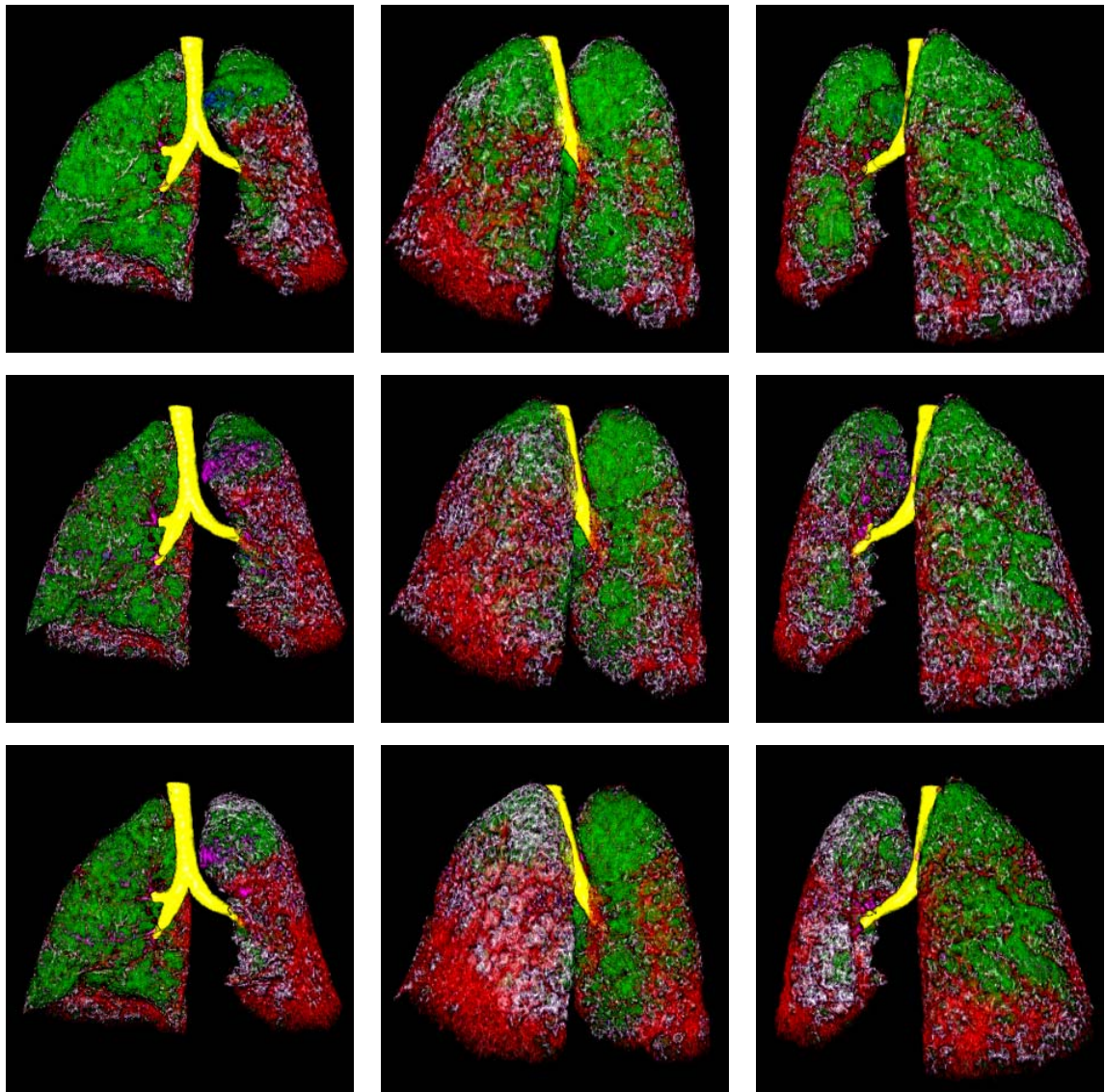
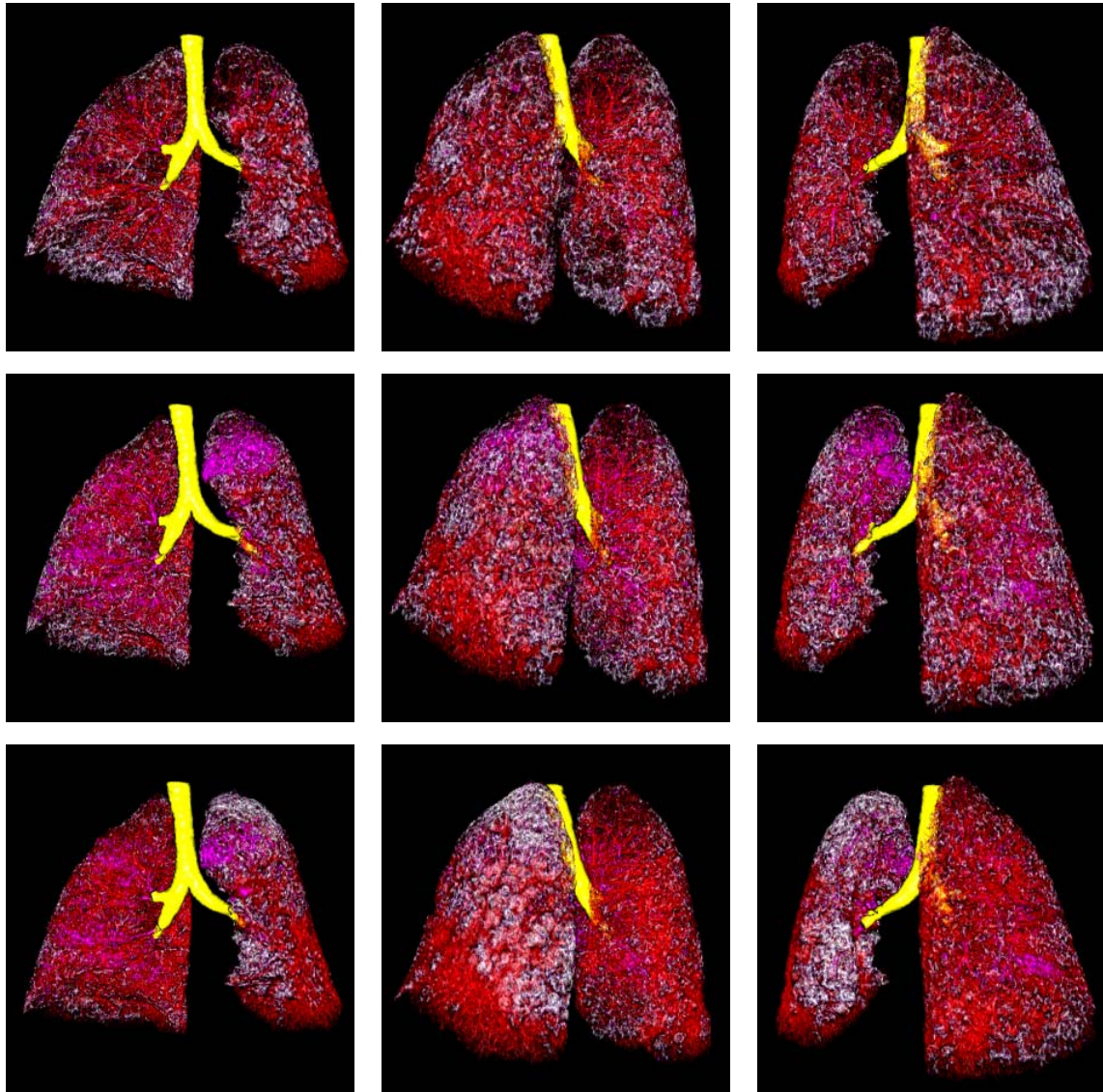


Fig. 84 (Continued). Example of a follow-up investigation of a fibrosis case at 8 months (middle row) and 5 months (bottom row) interval, respectively. The baseline acquisition (top row) is performed with the “BONEPLUS” kernel, while the following ones use the “LUNG” kernel. All exams use 1.25 mm collimation. Color code assignment: N ■ MEM ■ EM ■ FHC ■ GDG HD ■



(a) Illustration of all textural patterns.

Fig. 85 Follow-up analysis for the case in Fig. 84 illustrated using three views obtained with 3-D volume rendering. Top: baseline, middle: second acquisition, bottom: third acquisition. Color code assignment: N ■ MEM ■ EM ■ FHC ■ GDG HD ■.



(b) Illustration of the FHC, GDG and HD patterns only.

Fig. 85 (Continued). Follow-up analysis for the case in Fig. 84 illustrated using three views obtained with 3-D volume rendering. Top: baseline, middle: second acquisition, bottom: third acquisition. Color code assignment:

■ MEM
 ■ EM
 ■ FHC
 ■ GDG
 HD
 ■

IV.5 Concluding remarks

The preliminary evaluation of the developed CAD system allows defining some specifications related with the recommendation values for the number of the resolution levels $N_{RL} = 12$, and the CT acquisition protocol with the “LUNG”/”BONPLUS” reconstruction kernel and thin collimations (1.25 mm or less), in Table 7. It also stresses out the difficulty to quantitatively assess the performance of the proposed approach in the absence of a ground truth. The comparison with reference segmentations performed by experienced radiologists

encounters several difficulties related to different factors. First, the segmentation of the whole lung using manual contouring and labeling is tedious and prevents from building up a large reference database or pathologic atlases. Even for a specific case, our experience shows that the radiologist will generally concentrate only on one pathologic region and perform sparse segmentations on a subset of the axial CT images, which makes impossible a volumetric assessment. Second, the margins defined by the radiologist are relatively large and may include regions of textural properties similar with the normal lung which cannot be detected as pathological by the CAD system. Third, the CAD system operates according to a different logic than the human expert: it will detect the textural patterns different of the normal tissue, without making any association between the simultaneous presence of different patterns in a spatial neighborhood and the classification of the whole region as another class (as the radiologist will do). For example, fibrosis is a conglomerate of airspaces, HD reticulations, normal tissue and GDG, not all of these being simultaneously present. Also, for the same reasons, the class assigned to pathologic airspaces is different of what a radiologist would decide (e.g. EM instead of FHC, among a FHC cluster, or FHC zone inside a large emphysema region, because of the presence of noise). In this respect, further developments should be considered in order to include such type of association in the classification process.

Considering the follow-up analysis, a current major drawback is the impossibility to distinguish between pulmonary vessels and HD reticulations when they are connected to each other, namely in subjects with fibrosis.

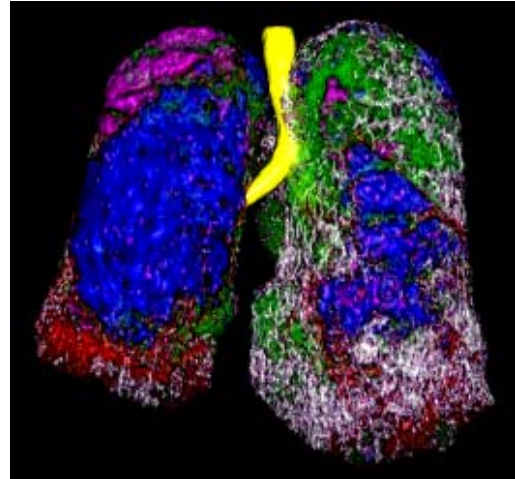
However, despite the fact that a quantitative assessment of the sensitivity and specificity of the developed approach could not be performed, visual investigations show a high detection rate of the lung pathologic patterns focused by this research. To conclude on these positive aspects, Fig. 86-Fig. 97 present 12 classification results obtained with the presented CAD system for different pathological subjects, illustrated using 3-D volume rendering. In each case, we show an original axial CT image, and the 3-D volume rendering including all normal/disease patterns, only EM+MEM, only FHC+GDG+HD, only GDG+HD, and only pathological patterns, respectively.

Table 7 The summarized recommendation values for the study

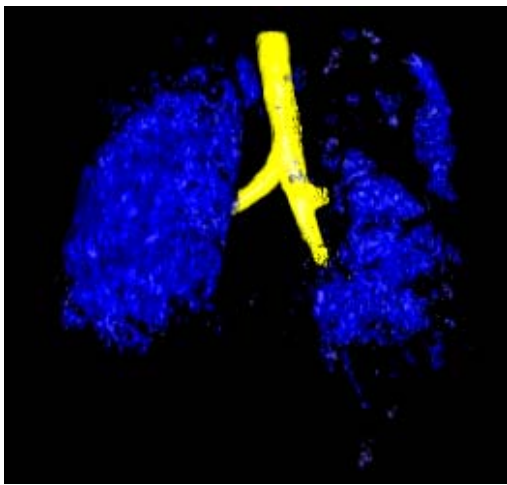
	Recommendation value
The number of resolution level (N_{RL})	12
The reconstruction kernel	“LUNG”/”BONEPLUS”
The X-ray beam collimation	≤ 1.25 mm



(a)



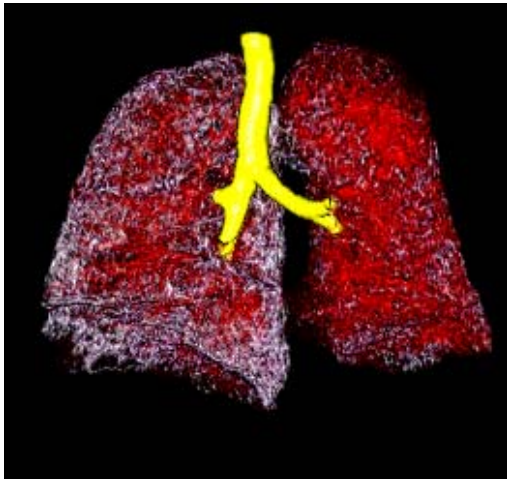
(b)



(c)



(d)



(e)



(f)

Fig. 86 The classification result obtained with the developed CAD system and illustrated using volume rendering: (a) original axial CT image, (b) all detected patterns, (c) only EM + MEM, (d) only FHC + HD + GDG, (e) only GDG + HD, and (f) only pathological patterns. Color code assignment:

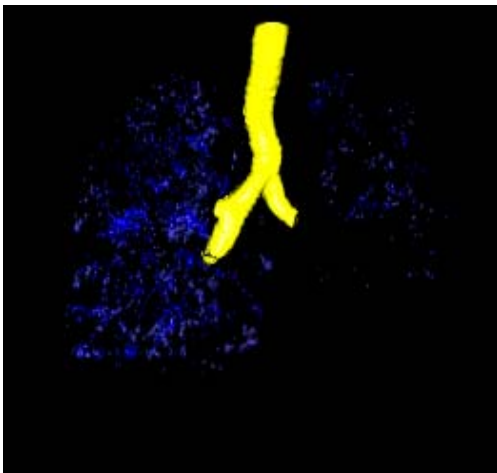
N ■ **MEM** ■ **EM** ■ **FHC** ■ **GDG** **HD** ■



(a)



(b)



(c)



(d)



(e)



(f)

Fig. 87 The classification result obtained with the developed CAD system and illustrated using volume rendering: (a) original axial CT image, (b) all detected patterns, (c) only EM + MEM, (d) only FHC + HD + GDG, (e) only GDG + HD, and (f) only pathological patterns. Color code assignment:

N ■ **MEM** ■ **EM** ■ **FHC** ■ **GDG** **HD** ■

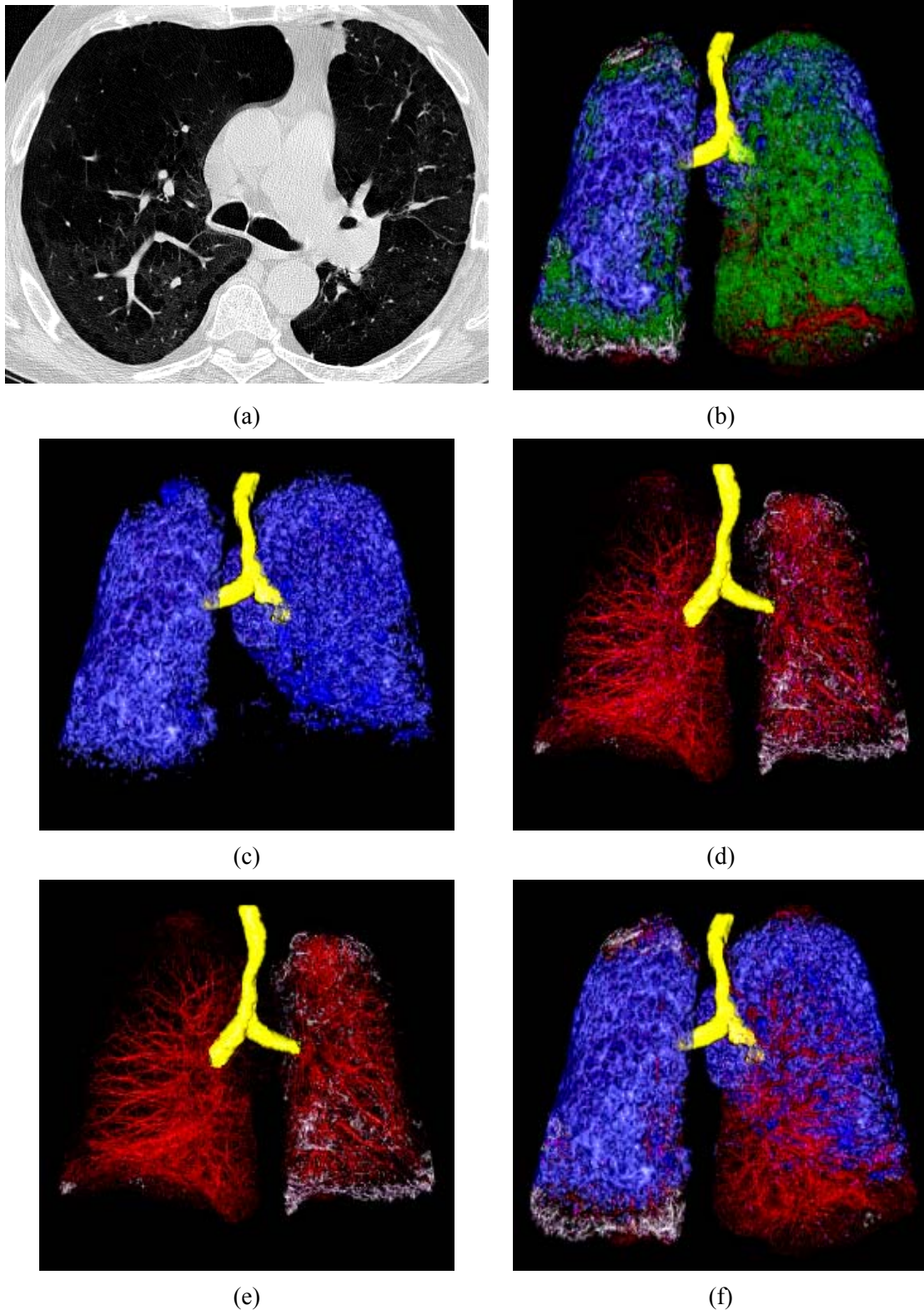


Fig. 88 The classification result obtained with the developed CAD system and illustrated using volume rendering: (a) original axial CT image, (b) all detected patterns, (c) only EM + MEM, (d) only FHC + HD + GDG, (e) only GDG + HD, and (f) only pathological patterns. Color code assignment:

N ■ MEM ■ EM ■ FHC ■ GDG HD ■.

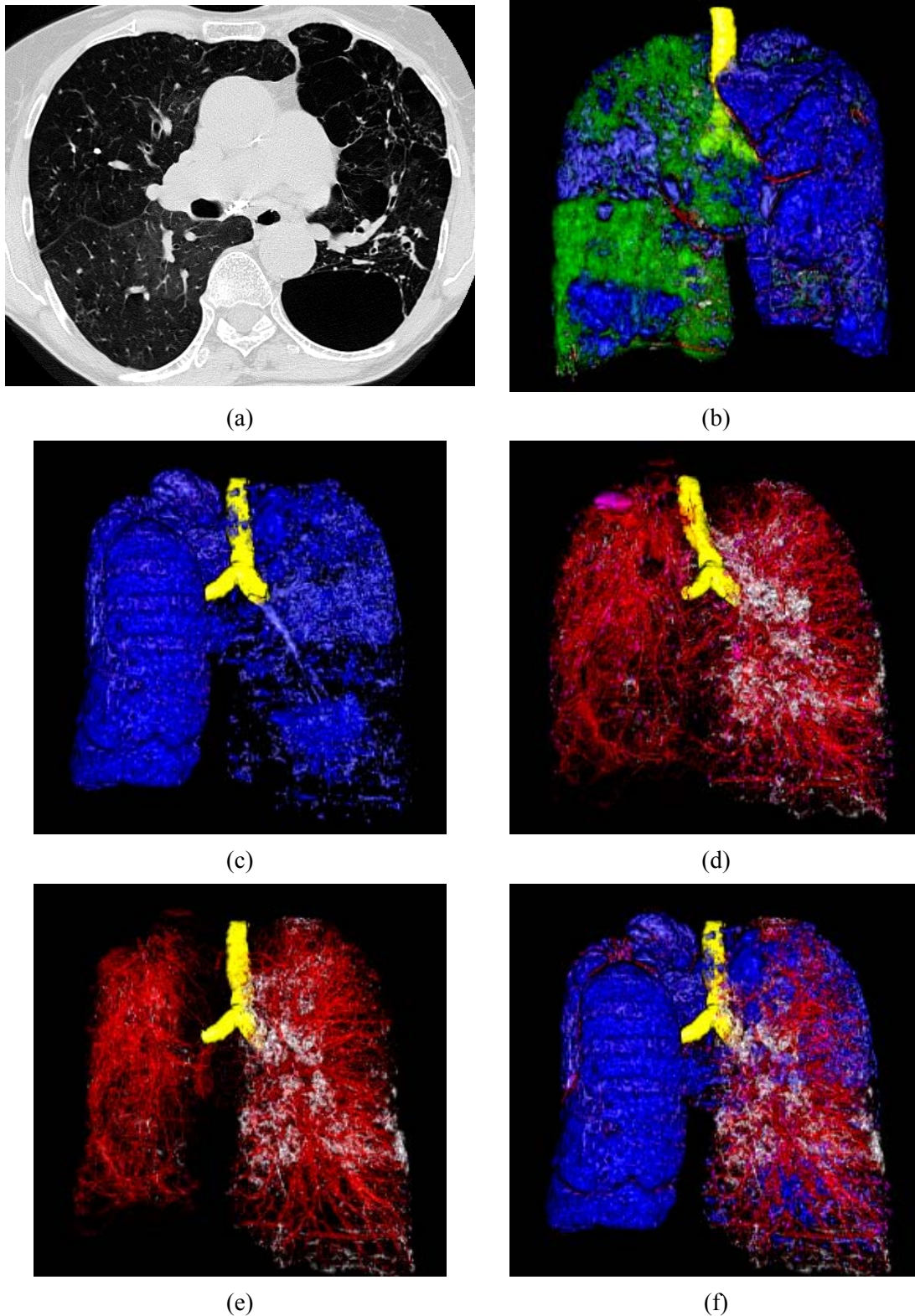
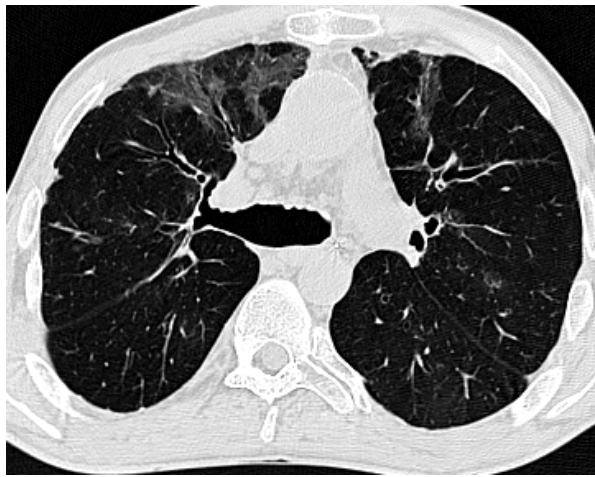
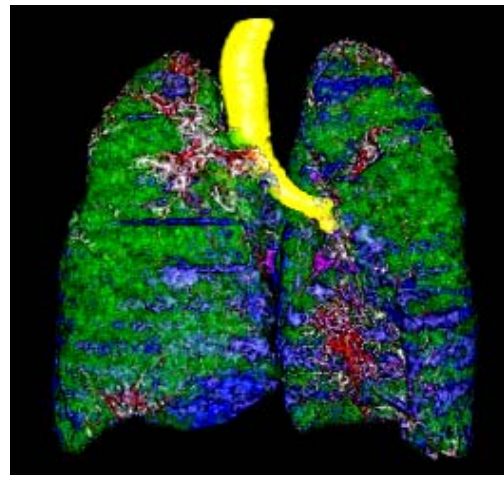


Fig. 89 The classification result obtained with the developed CAD system and illustrated using volume rendering: (a) original axial CT image, (b) all detected patterns, (c) only EM + MEM, (d) only FHC + HD + GDG, (e) only GDG + HD, and (f) only pathological patterns. Color code assignment:

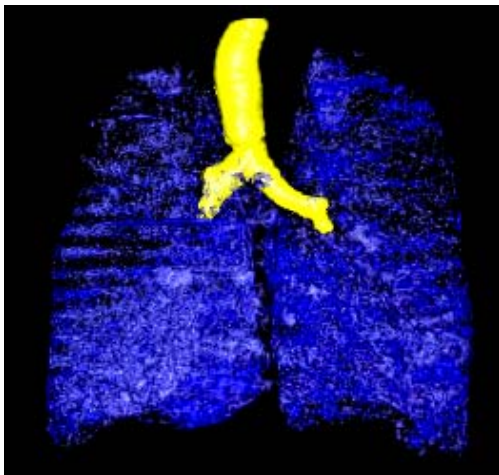
N MEM EM FHC GDG HD



(a)



(b)



(c)



(d)



(e)



(f)

Fig. 90 The classification result obtained with the developed CAD system and illustrated using volume rendering: (a) original axial CT image, (b) all detected patterns, (c) only EM + MEM, (d) only FHC + HD + GDG, (e) only GDG + HD, and (f) only pathological patterns. Color code assignment:

N ■ **MEM** ■ **EM** ■ **FHC** ■ **GDG** **HD** ■

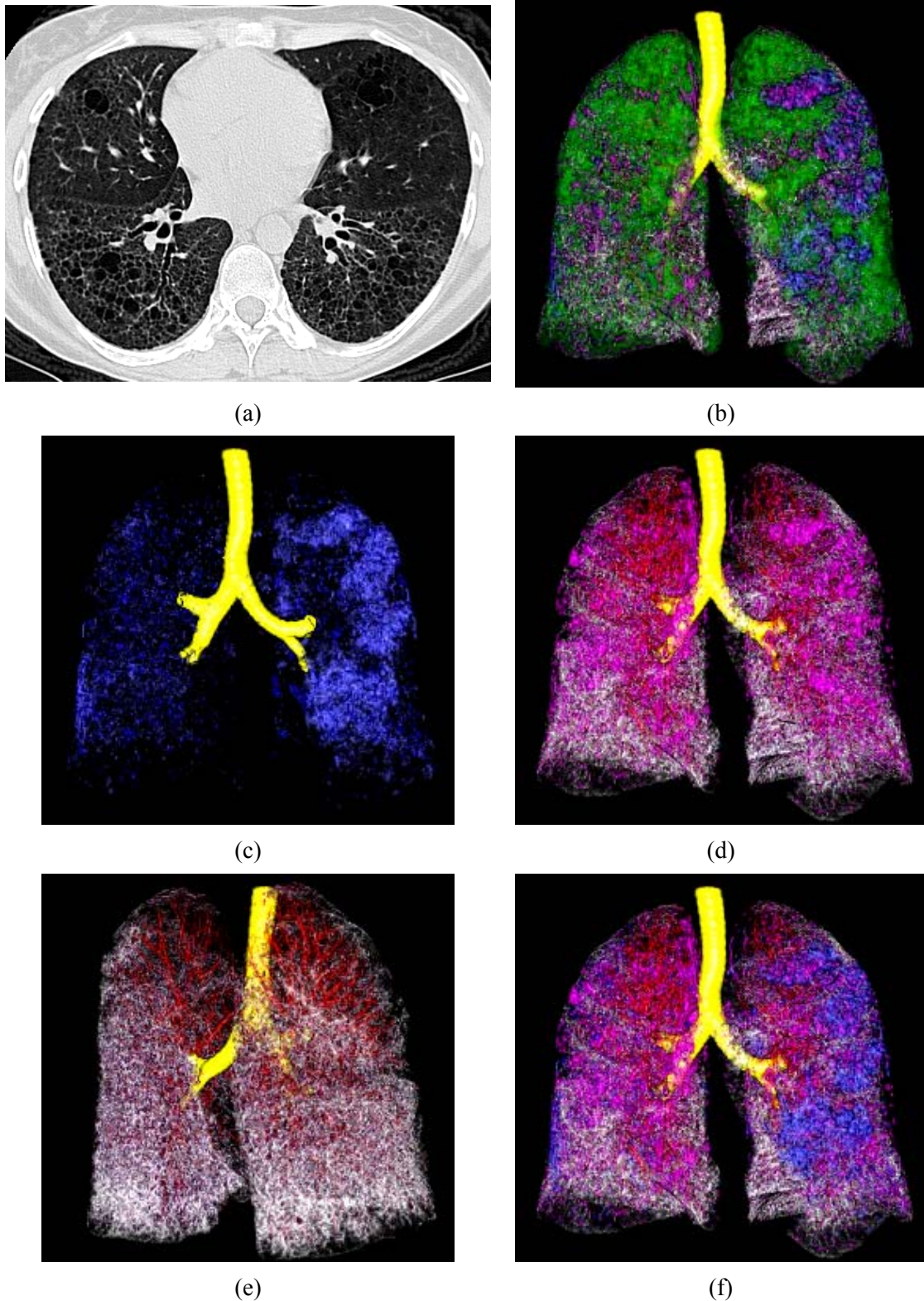


Fig. 91 The classification result obtained with the developed CAD system and illustrated using volume rendering: (a) original axial CT image, (b) all detected patterns, (c) only EM + MEM, (d) only FHC + HD + GDG, (e) only GDG + HD, and (f) only pathological patterns. Color code assignment:

N ■ **MEM** ■ **EM** ■ **FHC** ■ **GDG** ■ **HD** ■.

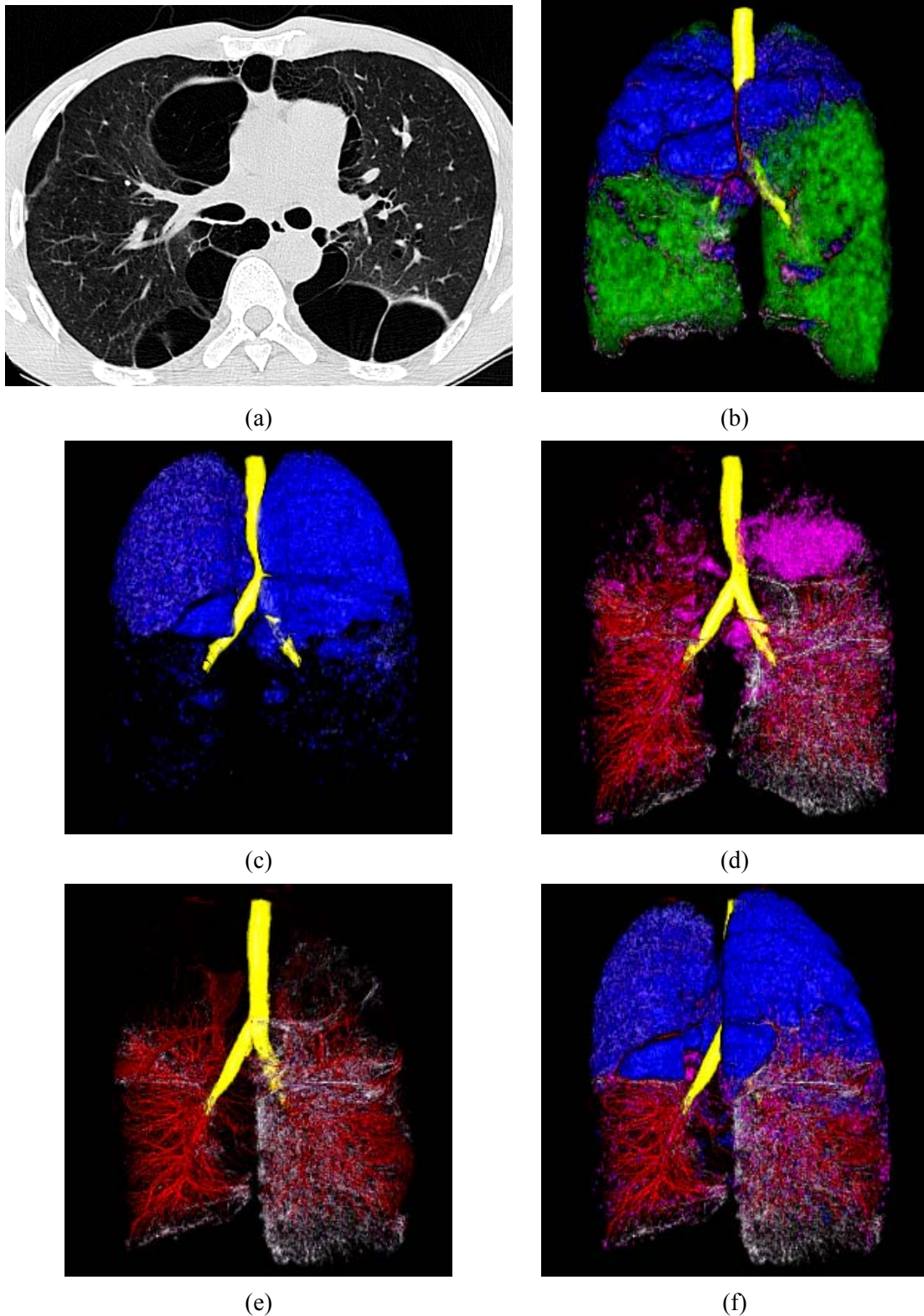
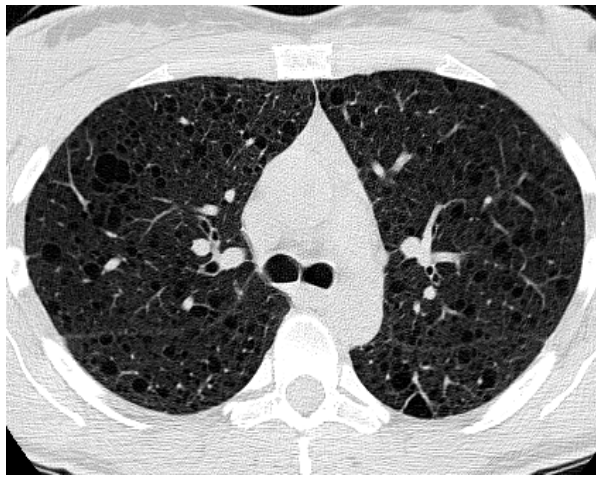
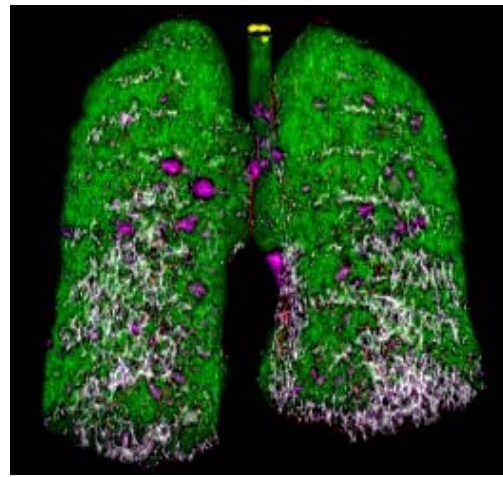


Fig. 92 The classification result obtained with the developed CAD system and illustrated using volume rendering: (a) original axial CT image, (b) all detected patterns, (c) only EM + MEM, (d) only FHC + HD + GDG, (e) only GDG + HD, and (f) only pathological patterns. Color code assignment:

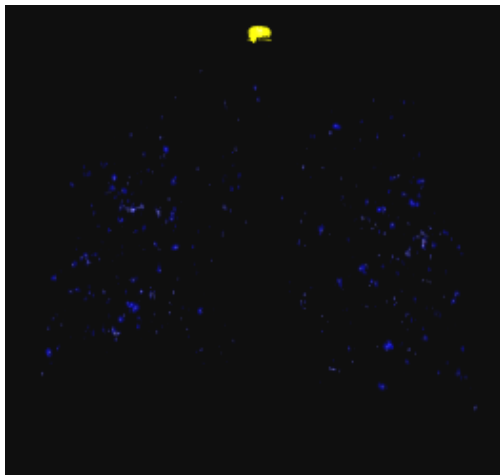
N (green) **MEM** (cyan) **EM** (blue) **FHC** (magenta) **GDG** (white) **HD** (red)



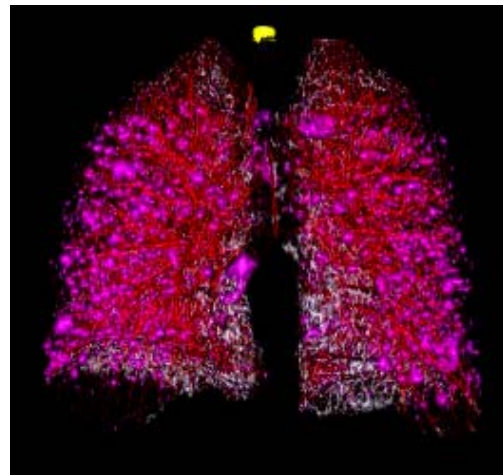
(a)



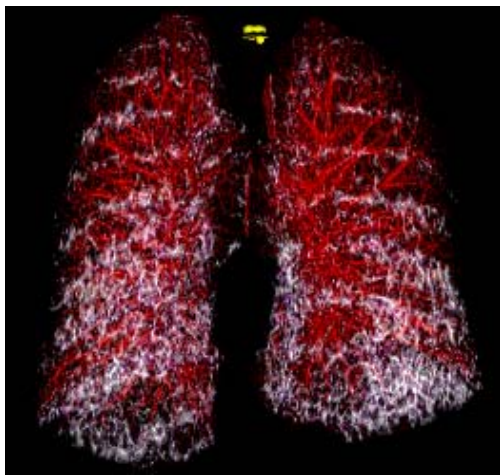
(b)



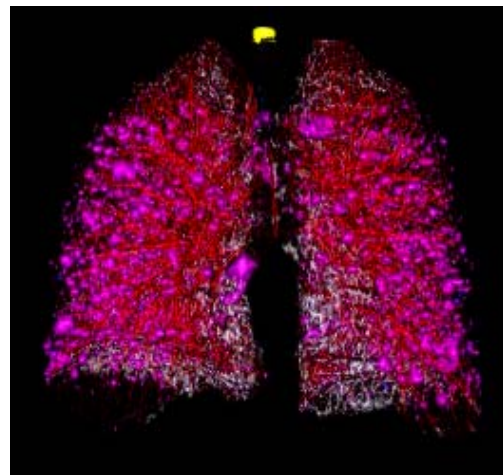
(c)



(d)



(e)



(f)

Fig. 93 The classification result obtained with the developed CAD system and illustrated using volume rendering: (a) original axial CT image, (b) all detected patterns, (c) only EM + MEM, (d) only FHC + HD + GDG, (e) only GDG + HD, and (f) only pathological patterns. Color code assignment:

N ■ **MEM** ■ **EM** ■ **FHC** ■ **GDG** **HD** ■

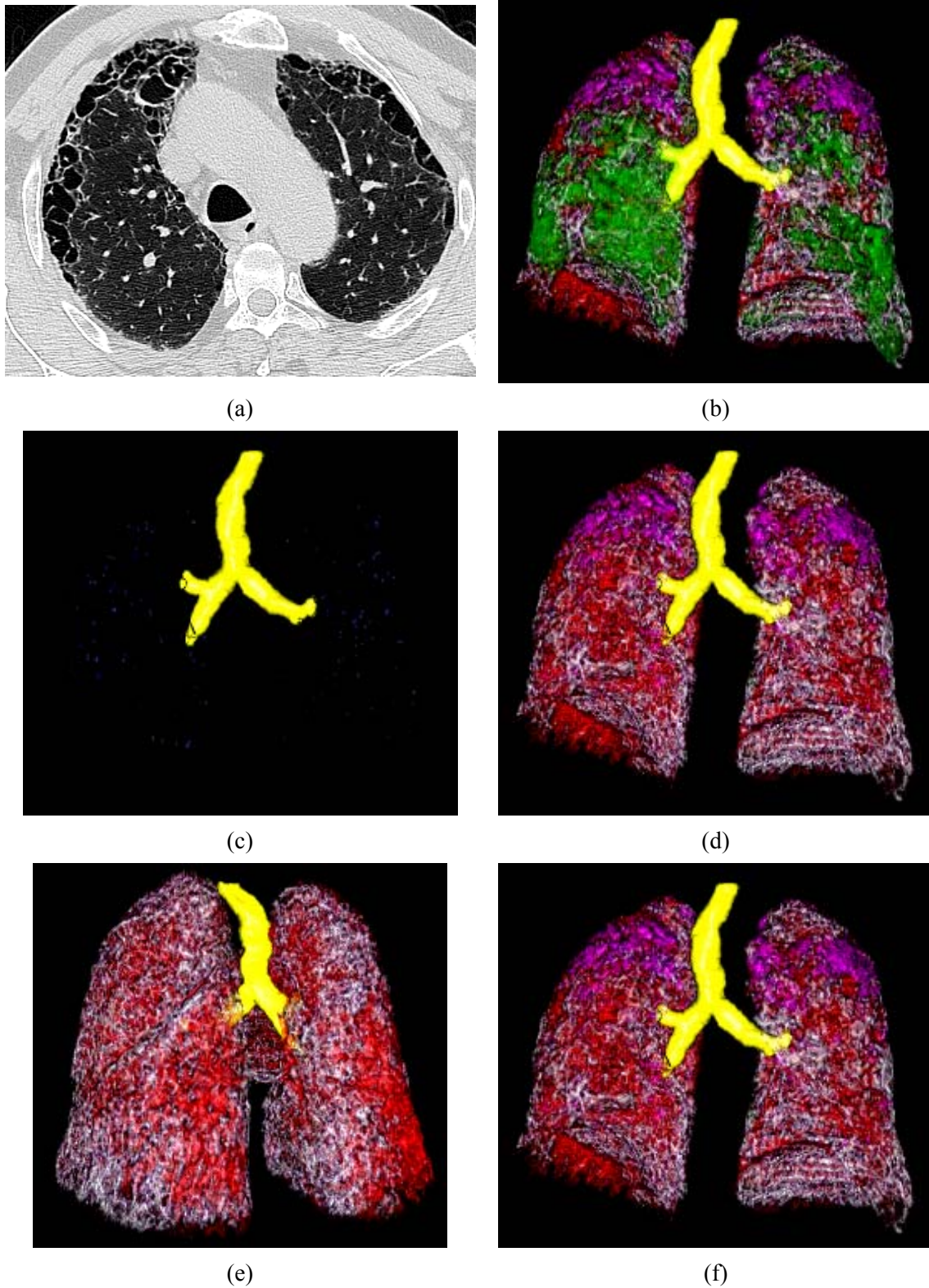


Fig. 94 The classification result obtained with the developed CAD system and illustrated using volume rendering: (a) original axial CT image, (b) all detected patterns, (c) only EM + MEM, (d) only FHC + HD + GDG, (e) only GDG + HD, and (f) only pathological patterns. Color code assignment:

N ■ MEM ■ EM ■ FHC ■ GDG HD ■.

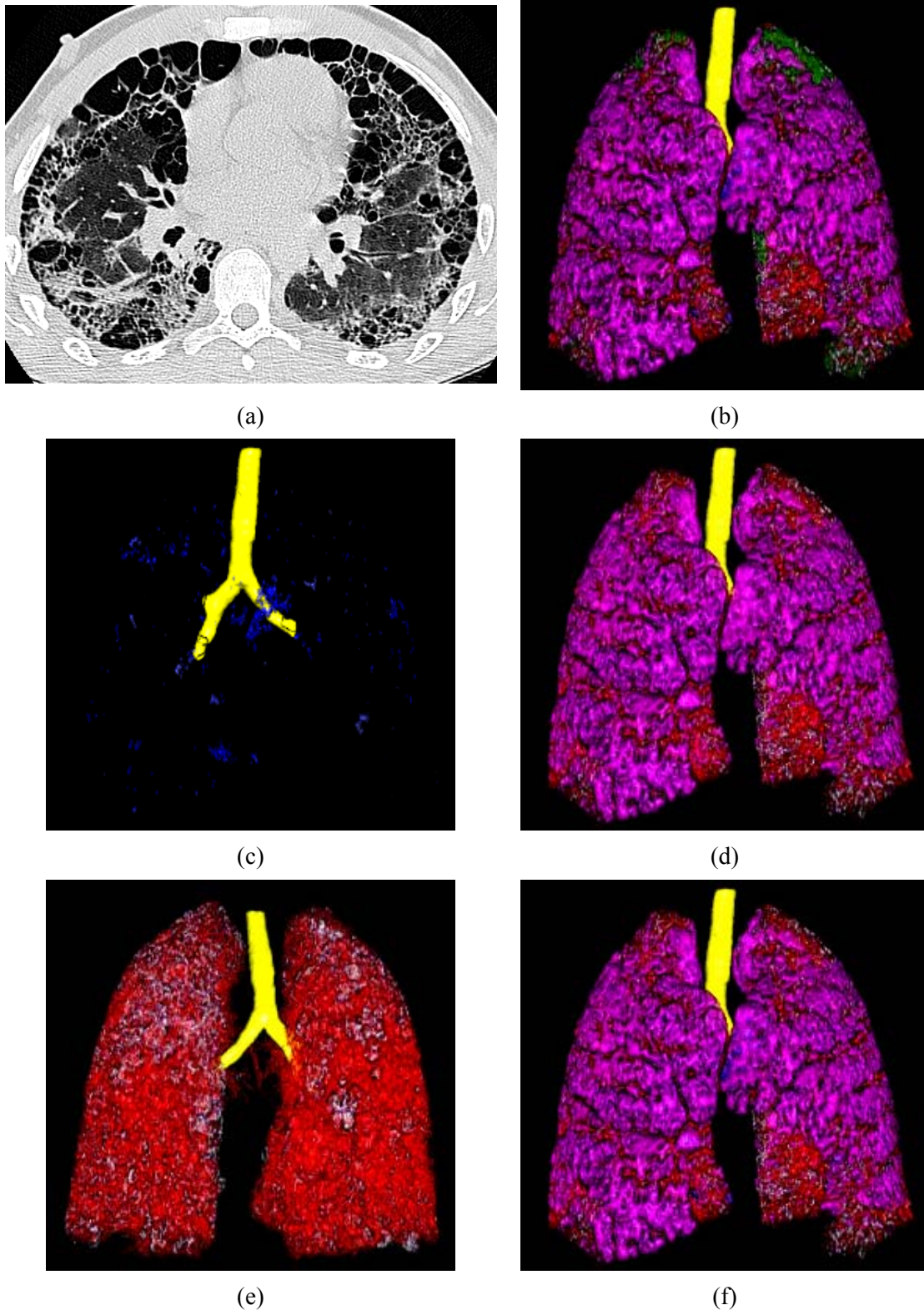


Fig. 95 The classification result obtained with the developed CAD system and illustrated using volume rendering: (a) original axial CT image, (b) all detected patterns, (c) only EM + MEM, (d) only FHC + HD + GDG, (e) only GDG + HD, and (f) only pathological patterns. Color code assignment:

N ■ **MEM** ■ **EM** ■ **FHC** ■ **GDG** **HD** ■

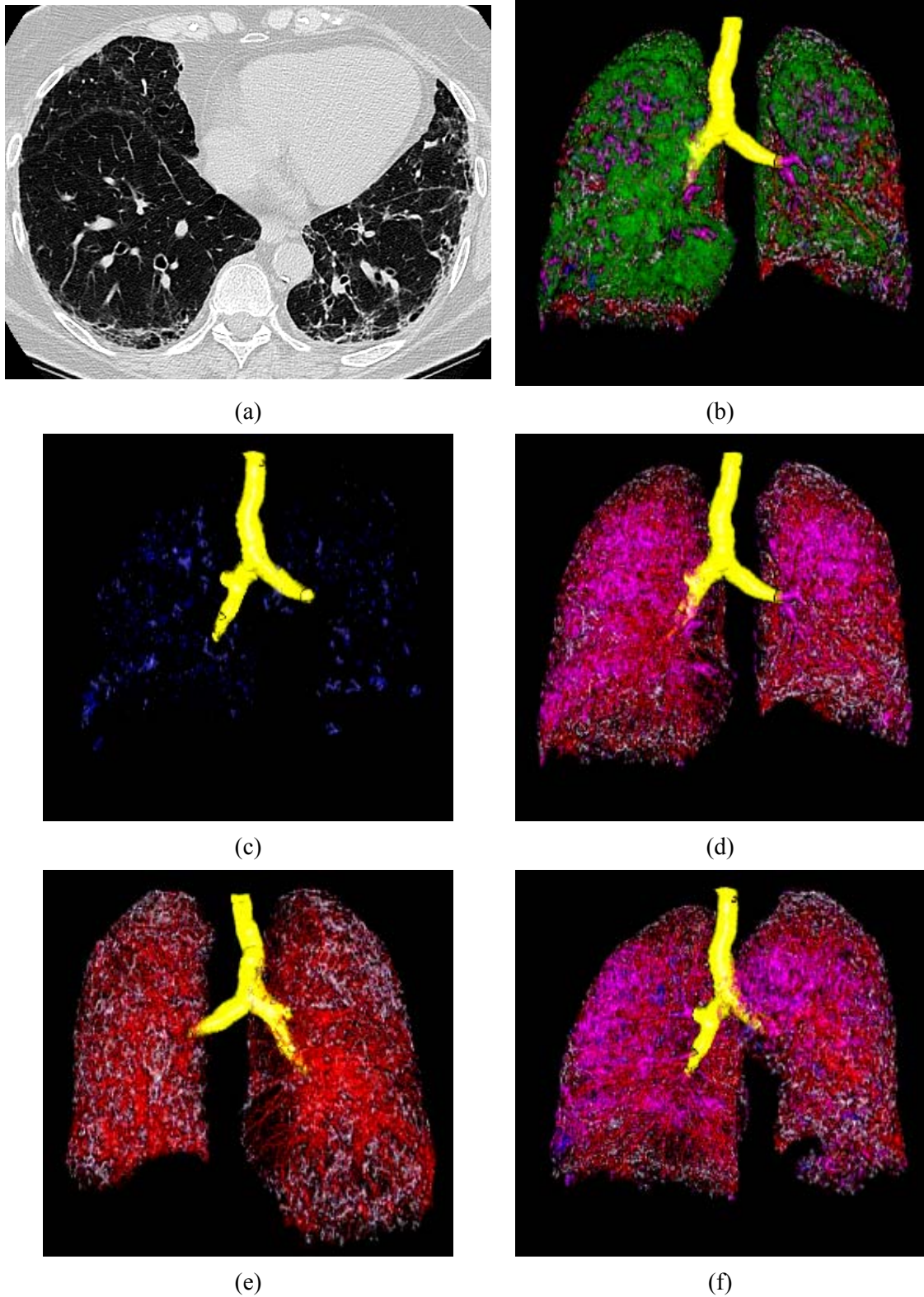


Fig. 96 The classification result obtained with the developed CAD system and illustrated using volume rendering: (a) original axial CT image, (b) all detected patterns, (c) only EM + MEM, (d) only FHC + HD + GDG, (e) only GDG + HD, and (f) only pathological patterns. Color code assignment:

N MEM EM FHC GDG HD

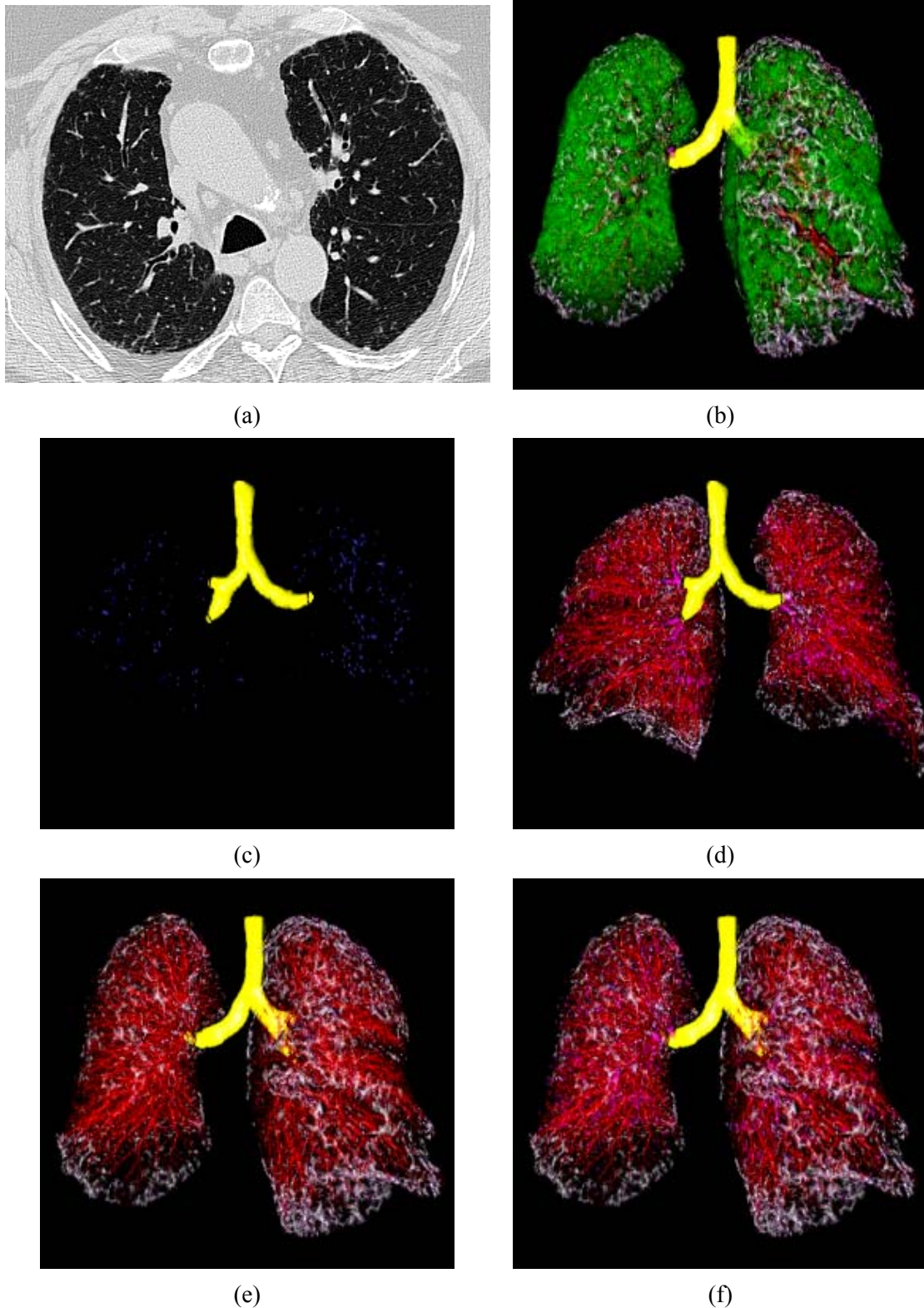


Fig. 97 The classification result obtained with the developed CAD system and illustrated using volume rendering: (a) original axial CT image, (b) all detected patterns, (c) only EM + MEM, (d) only FHC + HD + GDG, (e) only GDG + HD, and (f) only pathological patterns. Color code assignment:

N MEM EM FHC GDG HD

Conclusion and Perspectives

This research was performed in the clinical investigation framework of idiopathic interstitial pneumonias (IIPs) and emphysema in MSCT imaging. The objective was to develop a fully-automated computer-aided diagnosis (CAD) system targeting lung pathologies such as emphysema (EM), fibrosis/honeycombing (FHC) and ground glass (GDG) and providing quantitative information on the spatial distribution and volume of these pathological patterns. The ultimate clinical benefit aimed was the possibility to conduct quantitative follow-up studies which are critical for the therapeutic assays nowadays, when no efficient treatment is available for most IIPs.

The ability to perform follow-up studies thus requires that the quantitative information provided by CAD measurements should be three-dimensional and reported to the patient lung volume. Consequently, the detection and quantification approach involved by a target CAD system should necessarily be able to process the whole lung field of the patient. Such volumetric information is available from the MSCT imaging technology, which oriented our research towards fully 3-D image analysis methods.

The CAD system developed during this PhD research follows an original framework exploiting the textural properties of the disease patterns as they appear on MSCT images. For emphysema and fibrosis, the common characteristics refer to the presence of low-attenuated regions due to the tissue destruction, while ground glass is distinguished by medium-high intensity superior to the normal tissue. The idea exploited by the proposed approach is to detect EM and FHC by performing an analysis of the low-attenuated regions and to tackle the GDG on the remaining zones. Such analysis relied on a set of image features specific to each class of pathology which were identified in the CT data. They refer to size, clustering and gray-level distribution, both inside and around the patterns.

The analysis of the size property is addressed via a multi-resolution decomposition scheme of the lung volume relief based on a 3-D morphological filtering. It allows the identification (segmentation) of low-density patterns according to their sizes and also involves a local gray-scale analysis of each such pattern and its environment. Such a multi-resolution analysis results in a decomposition pyramid where textural patterns are identified at different scales. Note that the patterns extracted at different resolution levels may not be spatially disjoint and this property will be exploited to detect pattern clustering. Conversely, due to sometime locally low signal-to-noise ratio (mostly in the longitudinal axis of the MSCT scans), normal and pathological regions may be joint in the same pattern at a given resolution level. To overcome this potential drawback, we proposed combining the multi-resolution decomposition scheme with a texture-based spatial partitioning of the lung in ROIs of fixed

size and shape over all scales. This will produce smaller patterns at each resolution level and can thus capture local textural properties for a more accurate feature computation.

The resulting multi-resolution decomposition pyramid is further on described and analyzed by means of a hierarchic tree graph structure, where a node is associated with a given pattern at the given resolution level and the tree vertices correspond to the spatial connectivity between patterns at different resolution levels. Each node is assigned several spatial and textural features corresponding to the associated pattern. The analysis of the neighborhood of each node in the graph tree structure (parent - child - sibling) automatically provides the clustering information. The node (pattern) classification will exploit the multi-valued descriptive graph tree and is implemented by means of fuzzy-logic reasoning. For each pattern, six fuzzy membership functions were established for assigning a probability of association with a normal tissue or a pathological target. Finally, a decision step exploiting the fuzzy-logic assignments performs regions fusion and selects the target class of each lung pattern among the following categories: normal (N), emphysema (EM), fibrosis/honeycombing (FHC), and ground glass (GDG).

Note that a lung mask is built-up prior to the multi-resolution analysis by segmenting the lung fields. This is required for two reasons: first, obtaining the total lung volume (also allowing to restrain the processed data ROI) and second, providing information on the large airways (AW) and on high-density (HD) regions such as fibrosis reticulations occurring at the lung periphery and which may be disregarded by the multi-resolution analysis focusing on the low-attenuated patterns. The final volumetric classification results include all mentioned patterns (N, AW, EM, FHC, GDG, HD) and provides quantitative measurements.

The developed CAD system was tested on clinical routine studies including different types of emphysema and IIPs by visual inspection performed by experienced radiologists. The results obtained showed high accuracy in pathology detection with moderate discrimination between some small EM and FHC patterns, with EM being classed as FHC. This is due to high similarity of the computed features, mainly when the EM patterns are closely surrounded by HD regions or even by lung vessels, the differentiation between small vascular and HD structures not being trivial and currently not implemented in the lung mask detection procedure. Such class mix-up is also influenced by the presence of noise and, more generally, by the CT acquisition protocol which is not normalized between cases, even in follow-up examinations where this should be a major requirement. This induces grayscale differences of the same type of pathological patterns in different CT examinations, which may lead to erroneous assignments $EM \leftrightarrow FHC$, because the grayscale features in the fuzzy logic decision have an important weight.

We also noted the difficulty to quantitatively assess our CAD system because of the absence of an evaluation ground truth. When trying to define a pseudo ground truth by involving an expert radiologist to manually delineate pathologic regions, several difficulties

were encountered: the manual classification is restricted to a subset of the MSCT images thus preventing from a volumetric evaluation; the margins selected by the radiologist are larger, the drawn regions are generally convex and may include normal lung texture regions which will not be selected in the pathological patterns detected by the CAD system; finally, the human operator performs an additional (visual) clustering of the textural patterns observed and infer a pathological class for a larger region (e.g. an area including low-density patterns, HD reticulations and GDG can be assigned as FHC by the radiologist, while the CAD system may distinguish between some of these patterns).

The perspectives of this research are declined both in terms of methodological advancements and validation issues. In the developed analysis framework, the lung mask segmentation module would require a better discrimination between vascular structures and the other (fibrosis reticulations) high-density regions, which is a challenging problem for MSCT scans without use of contrast agent injection. A dedicated procedure for lung vessels segmentation should be thus developed and included in the CAD system. Also, the integration of a more accurate procedure for pulmonary airways segmentation, such as [125], would avoid the classification of intrapulmonary airways as EM or FHC patterns.

Concerning the fuzzy-based classification procedure, the introduction of new features less dependent on grayscale information would make the CAD system more robust to the CT acquisition protocol. Alternatively, the definition of a space transform where these new features could be inferred from should be considered. Finally, the decision step in the region fusion module may include a regularization approach with the objective to cluster different adjacent patterns into a defined pathology, similar with the radiologist's operating mode. However, this is an open discussion issue and depends on future clinical findings whether the quantification of different textural components inside a pathological region (such as HD reticulations or air sacs inside the fibrosis) presents a specific interest or not.

From the validation point of view, the quantitative assessment of the CAD systems targeting IIPs and emphysema requires the development of a specific ground truth like anatomic-pathologic atlases associated with representative MSCT datasets collected over several clinical centers, also involving data from follow-up studies. The building of such atlases is the most tedious task, as it involves interactive delineation of all pathological patterns, basically in 2-D, image by image for about 300-400 images per case. Additionally, such database should be constituted by at least two radiologist experts in order to minimize the intra-observer variability.

To conclude, the validated CAD system(s) targeting IIPs and emphysema have a great clinical potential in patient longitudinal follow-up and therapy design and evaluation, with a high impact expected on the socio-economical issues related to these pathologies.

Publications

- ◆ Ruey-Feng Chang, Kuang-Che Chang-Chien, Etsuo Takada, Jasjit S. Suri, Woo Kyung Moon, Jeffery H.K. Wu, Nariya Cho, Yi-Fa Wang, Dar-Ren Chen, “Breast Density Analysis in 3-D Whole Breast Ultrasound Images”, in 27th Annual Int. Conf. IEEE Engineering in Medicine and Biology Society, Sep. 2006, New York, USA
- ◆ Ruey-Feng Chang, Kuang-Che Chang-Chien, Etsuo Takada, Jasjit S. Suri, Woo Kyung Moon, Jeffery H.K. Wu, Nariya Cho, Yi-Fa Wang, Dar-Ren Chen, “Three Comparative Approaches for Breast Density Estimation in Digital and Screen Film Mammograms”, in 27th Annual Int. Conf. IEEE Engineering in Medicine and Biology Society, Sep. 2006, New York, USA
- ◆ Kuo-Hwa Chiang, Kuang-Che Chang-Chien, Ruey-Feng Chang, Hsuan-Yen Yen, “Tamper Detection and Restoring System for Medical Image Using Wavelet-based Reversible Data Embedding”, *Journal of Digital Imaging*, vol. 21, no. 1, pp. 77-90, 2007.
- ◆ Catalin Fetita, Kuang-Che Chang-Chien, Pierre-Yves Brillet, Françoise Preteux, and P. Grenier, "Diffuse parenchymal lung diseases: 3D automated detection in MDCT," in Proceedings 10th International Conference on Medical Image Computing & Computer Assisted Intervention, Brisbane, Nov. 2007, Australia, pp. 825-833.
- ◆ Catalin Fetita, Kuang-Che Chang-Chien, Pierre-Yves Brillet, Françoise Preteux, “Automated Diagnosis of Interstitial Lung Diseases and Emphysema in MDCT Imaging,” in Proceedings SPIE Conference on Mathematics of Data/Image Pattern Recognition, Compression, Coding, and Encryption with Applications X, San Diego, CA, vol. 6700, Aug. 2007, pp. 67000G: 1-12.
- ◆ Kuang-Che Chang-Chien, Catalin Fetita, Pierre-Yves Brillet, Françoise Preteux, Ruey-Feng Chang, “Detection and Classification of Interstitial Lung Diseases and Emphysema Using a Joint Morphological-fuzzy Approach,” in Proceedings SPIE Conference on Medical Imaging 2009: Computer-Aided Diagnosis, Lake Buena Vista, FL, vol. 7260, Feb. 2009.
- ◆ Jeon-Hor Chen, Chiun-Sheng Huang, Kuang-Che Chang-Chien, Etsuo Takada, Woo Kyung Moon, Jeffery H.K. Wu, Nariya Cho, Yi-Fa Wang, and Ruey-Feng Chang, “Breast Density Analysis for Whole Breast Ultrasound Images,” *Med. Phys.*, vol. 36, no. 11, pp. 4933-4943, Nov. 2009.

- ◆ Ruey-Feng Chang, Kuang-Che Chang Chien, Etsuo Takada, Chiun-Sheng Huang, Yi-Hong Chou, Chen-Ming Kuo, and Jeon-Hor Chen, “Rapid Image Stitching and Computer-aided Detection for Multi-pass Automated Breast Ultrasound,” *Med. Phys.*, vol. 37, no. 5, pp. 2063-2073, Apr. 2010.
- ◆ M. Wagner, O. Aidara, Kuang-Che Chang Chien, Catalin Fetita, M. W. Brauner, H. Nunes, D. Valeyre, Pierre-Yves Brillet, “Imagerie des PID chroniques en tomodensitométrie : du diagnostic à la quantification automatisée”, *Revue des maladies respiratoires*. (Accepted)
- ◆ Catalin Fetita, Kuang-Che Chang Chien, Pierre-Yves Brillet, Françoise Preteux, Ruey-Feng Chang, “Idiopathic Interstitial Pneumonias and Emphysema : Detection and Classification Using a Texture-discriminative Approach”, in *Proceedings SPIE Conference on Medical Imaging 2012*. (Accepted)

References

- [1] "American Thoracic Society/European Respiratory Society international multidisciplinary consensus classification of the idiopathic interstitial pneumonias," *Am. J. Respir. and Crit. Care Medicine*, vol. 165, no. 2, pp. 277-304, Jan 15 2002.
- [2] O. S. Al-Kadi and D. Watson, "Texture Analysis of Aggressive and Nonaggressive Lung Tumor CE CT Images," *IEEE Trans. on Bio-medical Eng.*, vol. 55, no. 7, pp. 1822-1830, 2008.
- [3] R. A. Blechschmidt, R. Werthschutzky, and U. Lorcher, "Automated CT image evaluation of the lung: a morphology-based concept," *IEEE Trans. on Med. Imaging*, vol. 20, no. 5, pp. 434-442, May 2001.
- [4] M. J. Gangeh, L. Sorensen, S. B. Shaker, M. S. Kamel, M. de Bruijne, and M. Loog, "A texton-based approach for the classification of lung parenchyma in CT images," *Med. Image Comput. Computer-Assisted Interv.*, vol. 13, no. Pt 3, pp. 595-602, 2010.
- [5] S. Hu, E. A. Hoffman, and J. M. Reinhardt, "Automatic lung segmentation for accurate quantitation of volumetric X-ray CT images," *IEEE Trans. on Med. Imaging*, vol. 20, no. 6, pp. 490-498, 2001.
- [6] L. Sorensen, S. B. Shaker, and M. de Bruijne, "Texture classification in lung CT using local binary patterns," *Med. Image Comput. Computer-Assisted Interv.*, vol. 11, no. Pt 1, pp. 934-941, 2008.
- [7] R. M. Summers, C. D. Johnson, L. M. Pusanik, J. D. Malley, A. M. Youssef, and J. E. Reed, "Automated polyp detection at CT colonography: feasibility assessment in a human population," *Radiology*, vol. 219, no. 1, pp. 51-59, Apr. 2001.
- [8] K. Suzuki, L. Feng, S. Sone, and K. A. D. K. Doi, "Computer-aided diagnostic scheme for distinction between benign and malignant nodules in thoracic low-dose CT by use of massive training artificial neural network," *IEEE Trans. on Med. Imaging*, vol. 24, no. 9, pp. 1138-1150, 2005.
- [9] E. M. Van Rikxoort, B. De Hoop, S. Van de Vorst, M. Prokop, and B. Van Ginneken, "Automatic Segmentation of Pulmonary Segments From Volumetric Chest CT Scans," *IEEE Trans. on Med. Imaging*, vol. 28, no. 4, pp. 621-630, 2009.
- [10] T. W. Way, B. Sahiner, H. P. Chan, L. Hadjiiski, P. N. Cascade, A. Chughtai, N. Bogot, and E. Kazerooni, "Computer-aided diagnosis of pulmonary nodules on CT scans: improvement of classification performance with nodule surface features," *Med. Phys.*, vol. 36, no. 7, pp. 3086-3098, Jul 2009.
- [11] J. P. Ko and D. P. Naidich, "Lung nodule detection and characterization with multislice CT," *Radiol. Clin. North Am.*, vol. 41, no. 3, pp. 575-597, May 2003.

- [12] T. Kobayashi, X. W. Xu, H. MacMahon, C. E. Metz, and K. Doi, "Effect of a computer-aided diagnosis scheme on radiologists' performance in detection of lung nodules on radiographs," *Radiology*, vol. 199, no. 3, pp. 843-848, June 1996.
- [13] H. MacMahon, R. Engelmann, F. M. Behlen, K. R. Hoffmann, T. Ishida, C. Roe, C. E. Metz, and K. Doi, "Computer-aided diagnosis of pulmonary nodules: results of a large-scale observer test," *Radiology*, vol. 213, no. 3, pp. 723-726, Dec. 1999.
- [14] A. P. Reeves and W. J. Kostis, "Computer-aided diagnosis for lung cancer," *Radiol. Clin. North Am.*, vol. 38, no. 3, pp. 497-509, May 2000.
- [15] K. Fujimoto, Y. Kitaguchi, K. Kubo, and T. Honda, "Clinical analysis of chronic obstructive pulmonary disease phenotypes classified using high-resolution computed tomography," *Respirology*, vol. 11, no. 6, pp. 731-740, Nov 2006.
- [16] J. C. Hogg, F. Chu, S. Utokaparch, R. Woods, W. M. Elliott, L. Buzatu, R. M. Cherniack, R. M. Rogers, F. C. Sciurba, H. O. Coxson, and P. D. Pare, "The nature of small-airway obstruction in chronic obstructive pulmonary disease," *New England J. Med.*, vol. 350, no. 26, pp. 2645-2653, Jun 24 2004.
- [17] H. Makita, Y. Nasuhara, K. Nagai, Y. Ito, M. Hasegawa, T. Betsuyaku, Y. Onodera, N. Hizawa, and M. Nishimura, "Characterisation of phenotypes based on severity of emphysema in chronic obstructive pulmonary disease," *Thorax*, vol. 62, no. 11, pp. 932-937, Nov 2007.
- [18] S. Matsuoka, T. Yamashiro, G. R. Washko, Y. Kurihara, Y. Nakajima, and H. Hatabu, "Quantitative CT assessment of chronic obstructive pulmonary disease," *Radiographics*, vol. 30, no. 1, pp. 55-66, Jan 2010.
- [19] G. L. Snider, L. J. Kleinerman, W. M. Thurlbeck, and Z. H. Bengali, "The definition of emphysema: report of a National, Heart, Lung and Blood Institute, Division of Lung Diseases Workshop," *Am. Rev. Respir. Dis.*, vol. 131, no. 1, pp. 182-185, Dec 1985.
- [20] M. C. O'Driscoll, E. D. Chan, and E. Fernandez, *Imaging of emphysema*. J. D. J. Newell and J. S. Lee, Eds. *Lynch DA: Imaging of diffuse lung disease*. B. C. Decker, Hamilton, 2000.
- [21] G. L. Snider, "Emphysema: the first two centuries--and beyond. A historical overview, with suggestions for future research: Part 2," *Am. Rev. Respir. Dis.*, vol. 146, no. 6, pp. 1615-1622, Dec 1992.
- [22] J. W. Gurney, "Pathophysiology of obstructive airways disease," *Radiol. Clin. North Am.*, vol. 36, no. 1, pp. 15-27, Jan 1998.
- [23] G. Raghu, H. R. Collard, J. J. Egan, F. J. Martinez, J. Behr, K. K. Brown, T. V. Colby, J. F. Cordier, K. R. Flaherty, J. A. Lasky, D. A. Lynch, J. H. Ryu, J. J. Swigris, A. U. Wells, J. Ancochea, D. Bouros, C. Carvalho, U. Costabel, M. Ebina, D. M. Hansell, T. Johkoh, D. S. Kim, T. E. King, Jr., Y. Kondoh, J. Myers, N. L. Muller, A. G.

- Nicholson, L. Richeldi, M. Selman, R. F. Dudden, B. S. Griss, S. L. Protzko, and H. J. Schunemann, "An official ATS/ERS/JRS/ALAT statement: idiopathic pulmonary fibrosis: evidence-based guidelines for diagnosis and management," *Am. J. Respir. and Crit. Care Medicine*, vol. 183, no. 6, pp. 788-824, Mar 15 2011.
- [24] M. Akira, H. Hamada, M. Sakatani, C. Kobayashi, M. Nishioka, and S. Yamamoto, "CT findings during phase of accelerated deterioration in patients with idiopathic pulmonary fibrosis," *Am. J. Roentgenol.*, vol. 168, no. 1, pp. 79-83, Jan 1997.
- [25] R. O. Crapo and R. E. I. Forster, "Carbon monoxide diffusing capacity," *Clin. Chest Med.*, vol. 10, no. 2, pp. 187-198, Jun 1989.
- [26] A. K. Jain, "Image Reconstruction from Projections," in *Fundamentals of digital image processing*: NJ: Prentice Hall, 1989.
- [27] M. Ahmed, V. Jacobi, and T. J. Vogl, "Multislice CT and CT angiography for non-invasive evaluation of bronchopulmonary sequestration," *Eur. Radiol.*, vol. 14, no. 11, pp. 2141-2143, Nov. 2004.
- [28] W. K. Chooi and S. K. Morcos, "High resolution volume imaging of airways and lung parenchyma with multislice CT," *Br. J. Radiol.*, vol. 77 Spec No 1, pp. S98-105, 2004.
- [29] D. Henzler, A. H. Mahnken, J. E. Wildberger, R. Rossaint, R. W. Gunther, and R. Kuhlen, "Multislice spiral computed tomography to determine the effects of a recruitment maneuver in experimental lung injury," *Eur. Radiol.*, vol. 16, no. 6, pp. 1351-1359, Jun 2006.
- [30] A. R. Hunsaker, "Multidetector-row CT and interstitial lung disease," *Semin. Roentgenol.*, vol. 38, no. 2, pp. 176-185, Apr 2003.
- [31] S. Iwano, T. Okada, H. Satake, and S. Naganawa, "3D-CT volumetry of the lung using multidetector row CT: comparison with pulmonary function tests," *Acad. Radiol.*, vol. 16, no. 3, pp. 250-256, Mar 2009.
- [32] F. L. Jacobson, "Multidetector-row CT of lung cancer screening," *Semin. Roentgenol.*, vol. 38, no. 2, pp. 168-175, Apr 2003.
- [33] A. F. Kopp, K. Klingenberg-Regn, M. Heuschmid, A. Küttner, B. Ohnesorge, F. T., S. S., and C. D. Claussen, "Multislice computed tomography: basic principles and clinical applications," *electromedica* 68 (2000), no. 2, 2000.
- [34] M. Uffmann and M. Prokop, "Multislice CT of the lung. Technique and clinical applications," *Radiologe*, vol. 41, no. 3, pp. 240-247, Mar. 2001.
- [35] S. G. Armato, 3rd and W. F. Sensakovic, "Automated lung segmentation for thoracic CT impact on computer-aided diagnosis," *Acad. Radiol.*, vol. 11, no. 9, pp. 1011-1021, Sep 2004.
- [36] N. Otsu, "A Threshold Selection Method from Gray-Level Histograms," *IEEE Trans. on Systems, Man and Cybernetics*, vol. 9, no. 1, pp. 62-66, 1979.

- [37] J. M. Reinhardt and W. E. Higgins, "Paradigm for shape-based image analysis," *Opt. Eng.*, vol. 37, no. 2, pp. 570-581, 1998.
- [38] J. K. Leader, B. Zheng, R. M. Rogers, F. C. Scieurba, A. Perez, B. E. Chapman, S. Patel, C. R. Fuhrman, and D. Gur, "Automated lung segmentation in X-ray computed tomography: development and evaluation of a heuristic threshold-based scheme," *Acad. Radiol.*, vol. 10, no. 11, pp. 1224-1236, Nov 2003.
- [39] D. M. Denison, M. D. Morgan, and A. B. Millar, "Estimation of regional gas and tissue volumes of the lung in supine man using computed tomography," *Thorax*, vol. 41, no. 8, pp. 620-628, Aug 1986.
- [40] L. W. Hedlund, R. F. Anderson, P. L. Goulding, J. W. Beck, E. L. Effmann, and C. E. Putman, "Two methods for isolating the lung area of a CT scan for density information," *Radiology*, vol. 144, no. 2, pp. 353-357, Jul 1982.
- [41] T. Sandor, D. K. Kido, W. B. Hanlon, and C. L. Rumbaugh, "Automated calvaria analysis from computerized axial tomographic scans," *Comput. Biomed. Res.*, vol. 14, no. 2, pp. 119-124, Apr 1981.
- [42] H. U. Kauczor, K. Heitmann, C. P. Heussel, D. Marwede, T. Uthmann, and M. Thelen, "Automatic detection and quantification of ground-glass opacities on high-resolution CT using multiple neural networks: comparison with a density mask," *Am. J. Roentgenol.*, vol. 175, no. 5, pp. 1329-1334, Nov 2000.
- [43] Y. Xu, M. Sonka, G. McLennan, J. Guo, and E. A. Hoffman, "MDCT-based 3-D texture classification of emphysema and early smoking related lung pathologies," *IEEE Trans. on Med. Imaging*, vol. 25, no. 4, pp. 464-475, Apr 2006.
- [44] L. Vincent and P. Soille, "Watersheds in digital spaces: an efficient algorithm based on immersion simulations," *IEEE Trans. on Pattern Anal. and Machine Intelligence*, vol. 13, no. 6, pp. 583-598, 1991.
- [45] N. Malpica, J. E. Ortuño, and A. Santos, "A multichannel watershed-based algorithm for supervised texture segmentation," *Pattern Recognition Letters*, vol. 24, no. 9-10, pp. 1545-1554, 2003.
- [46] S. Jianbo and J. Malik, "Normalized cuts and image segmentation," *IEEE Trans. on Pattern Anal. and Machine Intelligence*, vol. 22, no. 8, pp. 888-905, 2000.
- [47] S. Ukil and J. M. Reinhardt, "Anatomy-Guided Lung Lobe Segmentation in X-Ray CT Images," *IEEE Trans. on Med. Imaging*, vol. 28, no. 2, pp. 202-214, 2009.
- [48] Q. Wei, Y. Hu, J. H. MacGregor, and G. Gelfand, "Segmentation of Lung Lobes in Volumetric CT images for Surgical Planning of Treating Lung Cancer," in *Proc. IEEE Int. Conf. on Eng. Medicine and Biol. Soc.*, 2006, pp. 4869-4872.
- [49] I. C. Sluimer, M. Prokop, I. Hartmann, and B. van Ginneken, "Automated classification of hyperlucency, fibrosis, ground glass, solid, and focal lesions in high-resolution CT of the lung," *Med. Phys.*, vol. 33, no. 7, pp. 2610-2620, Jul 2006.

- [50] S. K. Tadikonda, M. Sonka, and S. M. Collins, "Region merging in medical image segmentation and interpretation," in Proc. IEEE Int. Conf. on Eng. Medicine and Biol. Soc., 1993, pp. 158-159.
- [51] U. Raeth, D. Schlaps, B. Limberg, I. Zuna, A. Lorenz, G. van Kaick, W. J. Lorenz, and B. Kommerell, "Diagnostic accuracy of computerized B-scan texture analysis and conventional ultrasonography in diffuse parenchymal and malignant liver disease," *J. Clin. Ultrasound*, vol. 13, no. 2, pp. 87-99, Feb 1985.
- [52] S. Delorme, M. A. Keller-Reichenbecher, I. Zuna, W. Schlegel, and G. Van Kaick, "Usual interstitial pneumonia. Quantitative assessment of high-resolution computed tomography findings by computer-assisted texture-based image analysis," *Invest. Radiol.*, vol. 32, no. 9, pp. 566-574, Sep 1997.
- [53] K. R. Heitmann, H. Kauczor, P. Mildenerger, T. Uthmann, J. Perl, and M. Thelen, "Automatic detection of ground glass opacities on lung HRCT using multiple neural networks," *Eur. Radiol.*, vol. 7, no. 9, pp. 1463-1472, 1997.
- [54] J. Malone, J. M. Rossiter, S. Prabhu, and P. Goddard, "Identification of disease in CT of the lung using texture-based image analysis," in Proc. IEEE Int. Conf. on Signals, Systems and Comput., 2004, pp. 1620-1624.
- [55] Y. Uchiyama, S. Katsuragawa, H. Abe, J. Shiraishi, F. Li, Q. Li, C. T. Zhang, K. Suzuki, and K. Doi, "Quantitative computerized analysis of diffuse lung disease in high-resolution computed tomography," *Med. Phys.*, vol. 30, no. 9, pp. 2440-2454, Sep 2003.
- [56] R. Uppaluri, G. McLennan, M. Sonka, and E. A. Hoffman, "Computer-based objective quantitative assessment of pulmonary parenchyma via x-ray CT," in Proc. SPIE Conf. on Med. Imaging, San Diego, CA, 1998, pp. 377-383.
- [57] R. M. Haralick, K. Shanmugam, and I. Dinstein, "Textural Features for Image Classification," *IEEE Trans. on Systems, Man and Cybernetics*, vol. 3, no. 6, pp. 610-621, 1973.
- [58] P. Korfiatis, C. Kalogeropoulou, A. Karahaliou, A. Kazantzi, S. Skiadopoulos, and L. Costaridou, "Texture classification-based segmentation of lung affected by interstitial pneumonia in high-resolution CT," *Med. Phys.*, vol. 35, no. 12, pp. 5290-5302, Dec 2008.
- [59] P. D. Korfiatis, A. N. Karahaliou, A. D. Kazantzi, C. Kalogeropoulou, and L. I. Costaridou, "Texture-based identification and characterization of interstitial pneumonia patterns in lung multidetector CT," *IEEE Trans. on Information Technol. Biomed.*, vol. 14, no. 3, pp. 675-680, May 2010.
- [60] D. H. Xu, A. S. Kurani, J. D. Furst, and D. S. Raicu, "Run-length encoding for volumetric texture," in 4th IASTED Int. Conf. on Visualization, Imaging, and Image Processing, Marbella, Spain, 2004.

- [61] A. H. Mir, M. Hanmandlu, and S. N. Tandon, "Texture analysis of CT images," *IEEE Eng. in Medicine and Biol. Magazine*, vol. 14, no. 6, pp. 781-786, 1995.
- [62] D. S. Raicu, J. D. Furst, D. Channin, D. H. Xu, A. Kurani, and S. Aioanei, "A texture dictionary for human organs tissues' classification," in *Proc. 8th. World Multi-conf. on Systemics, Cybermetics and Informatics*, Orlando, USA, 2004.
- [63] X. Tang, "Texture information in run-length matrices," *IEEE Trans. on Image Processing*, vol. 7, no. 11, pp. 1602-1609, 1998.
- [64] M. M. Galloway, "Texture analysis using gray level run lengths," *Computer Graphics Image Process*, vol. 4, no. 2, pp. 172-179, 1975.
- [65] B. B. Mandelbrot, *The fractal geometry of nature*. San Francisco: W. H. Freeman & Company, 1982.
- [66] N. Sarkar and B. B. Chaudhuri, "An efficient differential box-counting approach to compute fractal dimension of image," *IEEE Trans. on Systems, Man and Cybernetics*, vol. 24, no. 1, pp. 115-120, 1994.
- [67] S. Peleg, J. Naor, R. Hartley, and D. Avnir, "Multiple Resolution Texture Analysis and Classification," *IEEE Trans. on Pattern Anal. and Machine Intelligence*, vol. PAMI-6, no. 4, pp. 518-523, 1984.
- [68] C. C. Chen, J. S. DaPonte, and M. D. Fox, "Fractal feature analysis and classification in medical imaging," *IEEE Trans. on Med. Imaging*, vol. 8, no. 2, pp. 133-142, 1989.
- [69] E. L. Chen, P. C. Chung, C. L. Chen, H. M. Tsai, and C. I. Chang, "An automatic diagnostic system for CT liver image classification," *IEEE Trans. on Bio-medical Eng.*, vol. 45, no. 6, pp. 783-794, 1998.
- [70] A. P. Pentland, "Fractal-Based Description of Natural Scenes," *IEEE Trans. on Pattern Anal. and Machine Intelligence*, vol. PAMI-6, no. 6, pp. 661-674, 1984.
- [71] C. S. Fortin, R. Kumaresan, W. J. Ohley, and S. Hoefler, "Fractal dimension in the analysis of medical images," *IEEE Eng. in Medicine and Biol. Magazine*, vol. 11, no. 2, pp. 65-71, 1992.
- [72] A. E. Jacquin, "Fractal image coding: a review," *Proc. IEEE*, vol. 81, no. 10, pp. 1451-1465, 1993.
- [73] C. S. Tong and M. Pi, "Fast fractal image encoding based on adaptive search," *IEEE Trans. on Image Processing*, vol. 10, no. 9, pp. 1269-1277, 2001.
- [74] R. Uppaluri, T. Mitsa, and J. Galvin, "Fractal analysis of high resolution CT images as a tool for the quantification of lung diseases," in *Proc. SPIE Conf. on Med. Imaging*, San Diego, CA, 1995, pp. 133-142.
- [75] S. Deguy and C. Debain, "Classification of texture images using multi-scale statistical estimators of fractal parameters," in *Proc. 11th British Machine Vision Conf.*, 2000.
- [76] S. Prouteau, G. Ducher, P. Nanyan, G. Lemineur, L. Benhamou, and D. Courteix, "Fractal analysis of bone texture: a screening tool for stress fracture risk?," *Eur. J.*

- Clin. Invest., vol. 34, no. 2, pp. 137-142, Feb 2004.
- [77] D. Smutek, R. Sara, P. Sucharda, T. Tjahjadi, and M. Svec, "Image texture analysis of sonograms in chronic inflammations of thyroid gland," *Ultrasound Med. Biol.*, vol. 29, no. 11, pp. 1531-1543, Nov 2003.
- [78] R. O. Duda, P. E. Hart, and D. G. Stork, *Pattern classification*. Second ed. New York: Wiley, 1999.
- [79] W. Buntine, "Learning classification rules using bayes," in *Proc. 6th Int. Workshop on Machine Learning*, New York, USA, 1989, pp. 94-98.
- [80] A. A. Farag, A. El-Baz, G. Gimel'farb, and R. Falk, "Detection and recognition of lung abnormalities using deformable templates," in *Proc. 17th IEEE Int. Conf. on Pattern Recognition (ICPR)*, 2004, pp. 738-741.
- [81] R. Uppaluri, T. Mitsa, M. Sonka, E. A. Hoffman, and G. McLennan, "Quantification of pulmonary emphysema from lung computed tomography images," *Am. J. Respir. and Crit. Care Medicine*, vol. 156, no. 1, pp. 248-254, July 1997.
- [82] Y. Xu, E. J. van Beek, Y. Hwanjo, J. Guo, G. McLennan, and E. A. Hoffman, "Computer-aided classification of interstitial lung diseases via MDCT: 3D adaptive multiple feature method (3D AMFM)," *Acad. Radiol.*, vol. 13, no. 8, pp. 969-978, Aug 2006.
- [83] W. McCulloch and W. Pitts, "A logical calculus of the ideas immanent in nervous activity," *Bulletin of Mathematical*, vol. 5, pp. 115-133, 1943.
- [84] J. G. Taylor, *The promise of neural networks*. New York: Springer-Verlag, 1993.
- [85] V. N. Vapnik, *The nature of statistical learning theory*. New York: Springer-Verlag, 1995.
- [86] M. Kakar and D. R. Olsen, "Automatic segmentation and recognition of lungs and lesion from CT scans of thorax," *Computerized Med. Imaging Graphics*, vol. 33, no. 1, pp. 72-82, Jan 2009.
- [87] J. C. Bezdek, "A convergence theorem for the fuzzy ISODATA clustering algorithms," *IEEE Trans. on Pattern Anal. and Machine Intelligence*, vol. PAMI-2, no. 1, pp. 1-8, 1980.
- [88] J. C. Dunn, "A fuzzy relative of the ISODATA process and its use in detecting compact well-separated clusters," *J. Cybern.*, vol. 3, no. 3, pp. 32-57, 1973.
- [89] F. Farrokhnia and A. K. Jain, "A multi-channel filtering approach to texture segmentation," in *Proc. IEEE Int. Conf. on Comput. Vision and Pattern Recognition*, Maui, HI, 1991, pp. 364-370.
- [90] P. Korfiatis, A. Karahaliou, A. Kazantzi, C. Kalogeropoulou, and L. Costaridou, "Towards quantification of interstitial pneumonia patterns in lung multidetector CT," in *Proc. 8th IEEE Int. Conf. on BioInf. and BioEng.*, Athens, 2008, pp. 1-5.
- [91] X. Ye, X. Lin, J. Dehmeshki, G. Slabaugh, and G. Beddoe, "Shape-based

- computer-aided detection of lung nodules in thoracic CT images," *IEEE Trans. on Bio-medical Eng.*, vol. 56, no. 7, pp. 1810-1820, Jul 2009.
- [92] D. W. Hosmer and S. Lemeshow, *Applied logistic regression*. Second ed. New York: Wiley, 2000.
- [93] N. Arshadi and I. Jurisica, "Data mining for case-based reasoning in high-dimensional biological domains," *IEEE Trans. on Knowledge and Data Eng.*, vol. 17, no. 8, pp. 1127-1137, 2005.
- [94] M. D. Schluchter, M. W. Konstan, M. L. Drumm, J. R. Yankaskas, and M. R. Knowles, "Classifying severity of cystic fibrosis lung disease using longitudinal pulmonary function data," *Am. J. Respir. Crit. Care Med.*, vol. 174, no. 7, pp. 780-786, Oct 1 2006.
- [95] G. R. Washko, G. M. Hunninghake, I. E. Fernandez, M. Nishino, Y. Okajima, T. Yamashiro, J. C. Ross, R. S. Estepar, D. A. Lynch, J. M. Brehm, K. P. Andriole, A. A. Diaz, R. Khorasani, K. D'Aco, F. C. Sciurba, E. K. Silverman, H. Hatabu, and I. O. Rosas, "Lung volumes and emphysema in smokers with interstitial lung abnormalities," *New England J. Med.*, vol. 364, no. 10, pp. 897-906, Mar 10 2011.
- [96] L. A. Zadeh, "Fuzzy Sets," *Information and Control*, vol. 8, pp. 338-353, 1965.
- [97] L. A. Zadeh, "Fuzzy algorithms," *Information and Control*, vol. 12, no. 2, pp. 94-102, 1968.
- [98] L. A. Zadeh, "Outline of a new approach to the analysis of complex systems and decision processes," *IEEE Trans. on Systems, Man and Cybernetics*, vol. SMC-3, no. 1, pp. 28-44, 1973.
- [99] M. Sugeno and G. T. Kang, "Structure identification of fuzzy model," *Fuzzy Sets and Systems*, vol. 28, no. 1, pp. 15-33, 1988.
- [100] T. Takagi and M. Sugawno, "Fuzzy identification of systems and its applications to modeling and control," *IEEE Trans. on Systems, Man and Cybernetics*, vol. 15, no. 1, pp. 116-132, 1985.
- [101] L. Zhang, E. A. Hoffman, and J. M. Reinhardt, "Atlas-driven lung lobe segmentation in volumetric X-ray CT images," *IEEE Trans. on Systems, Man and Cybernetics*, vol. 25, no. 1, pp. 1-16, Jan. 2006.
- [102] M. N. Ahmed, S. M. Yamany, N. Mohamed, A. A. Farag, and T. Moriarty, "A modified fuzzy C-means algorithm for bias field estimation and segmentation of MRI data," *IEEE Trans. on Med. Imaging*, vol. 21, no. 3, pp. 193-199, Mar. 2002.
- [103] R. Hosseini, J. Dehmeshki, S. Barman, M. Mazinani, A. M. Jouannic, and S. Qanadli, "A fuzzy logic system for classification of the lung nodule in digital images in computer aided detection," in *4th Int. Conf. on Digital Soc.*, St. Maarten, 2010, pp. 255-259.
- [104] J. Cohen, "A coefficient of agreement for nominal scales " *Educational and*

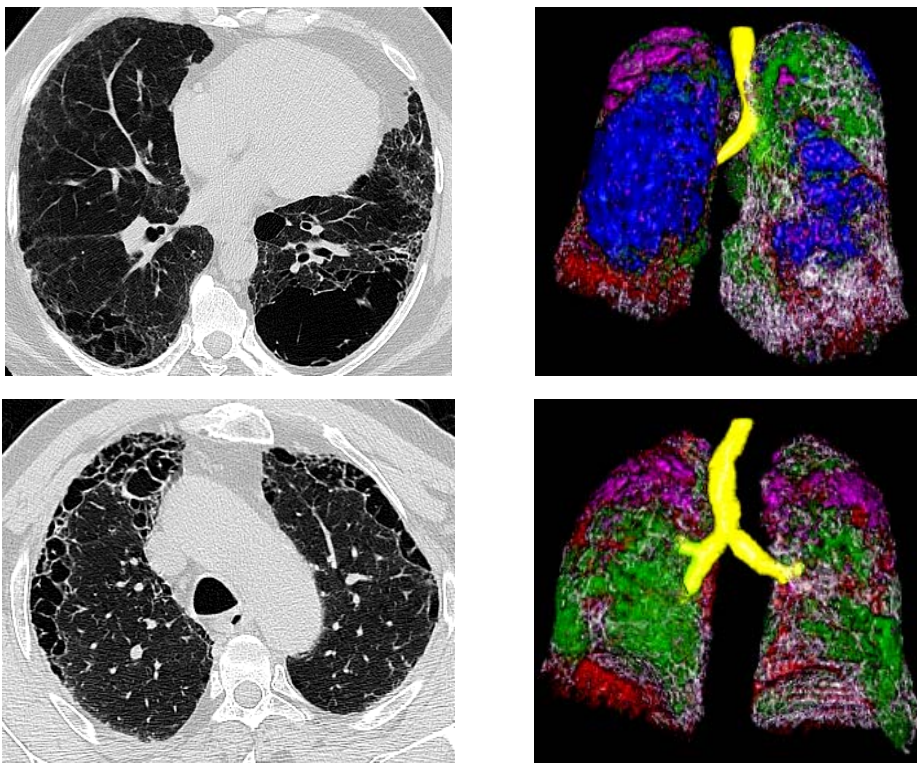
- Psychological Measurement, vol. 20, no. 1, pp. 37-46, 1960.
- [105] C. E. Metz, "ROC methodology in radiologic imaging," *Investigative Radiology*, vol. 21, no. 9, pp. 720-733, Sep 1986.
- [106] R. Shojaii, J. Alirezaie, and P. Babyn, "Automatic lung segmentation in CT images using watershed transform," in *Proc. IEEE Int. Conf. on Image Processing*, 2005, pp. 1270-1273.
- [107] H. Shikata, E. A. Hoffman, and M. Sonka, "Automated segmentation of pulmonary vascular tree from 3D CT images," in *Proc. SPIE Conf. on Med. Imaging*, San Diego, CA, USA 2004, pp. 107-116.
- [108] P. Perona and J. Malik, "Scale-space and edge detection using anisotropic diffusion," *IEEE Trans. on Pattern Anal. and Machine Intelligence*, vol. 12, no. 7, pp. 629-639, 1990.
- [109] F. Prêteux, On a distance function approach for gray-level mathematical morphology. in *Mathematical Morphology in Image Processing*, E. Dougherty, Ed. New York: Marcel Dekker, 1992.
- [110] C. Fetita, F. Prêteux, and P. A. Grenier, "3D reconstruction of the bronchial tree in volumetric CT: application to CT bronchography," *J. Electronic Imaging*, vol. 15, no. 2, pp. 023004-1:17, 2006.
- [111] C. Fetita, F. Prêteux, C. Beigelman-Aubry and P. A. Grenier, "Pulmonary airways: 3D reconstruction from multi-slice CT and clinical investigation," *IEEE Trans. on Medical Imaging*, vol. 23(11), pp. 1353-1364, 2004.
- [112] S. G. Armato, 3rd, M. B. Altman, J. Wilkie, S. Sone, F. Li, K. Doi, and A. S. Roy, "Automated lung nodule classification following automated nodule detection on CT: a serial approach," *Med. Phys.*, vol. 30, no. 6, pp. 1188-1197, Jun 2003.
- [113] J. Dehmeshki, J. Chen, M. V. Casique, and M. Karakoy, "Classification of lung data by sampling and support vector machine," in *Proc. IEEE Int. Conf. on Eng. Medicine and Biol. Soc.*, 2004, pp. 3194-3197.
- [114] M. K. Farrugia, S. A. Raza, S. Gould, and K. Lakhoo, "Congenital lung lesions: classification and concordance of radiological appearance and surgical pathology," *Pediatric Surg. Int.*, vol. 24, no. 9, pp. 987-991, Sep 2008.
- [115] I. Mariolis, P. Korfiatis, L. Costaridou, C. Kalogeropoulou, D. Daoussis, and T. Petsas, "Investigation of 3D textural features' discriminating ability in diffuse lung disease quantification in MDCT," in *Proc. IEEE Int. Conf. on Imaging Systems and Techniques (IST)*, 2010, pp. 135-138.
- [116] R. A. Ochs, J. G. Goldin, F. Abtin, H. J. Kim, K. Brown, P. Batra, D. Roback, M. F. McNitt-Gray, and M. S. Brown, "Automated classification of lung bronchovascular anatomy in CT using AdaBoost," *Med. Image Anal.*, vol. 11, no. 3, pp. 315-324, Jun 2007.

- [117] L. Srensen, S. B. Shaker, and M. de Bruijne, "Quantitative Analysis of Pulmonary Emphysema Using Local Binary Patterns," *IEEE Trans. on Med. Imaging*, vol. 29, no. 2, pp. 559-569, 2010.
- [118] T. W. Way, L. M. Hadjiiski, B. Sahiner, H. P. Chan, P. N. Cascade, E. A. Kazerooni, N. Bogot, and C. Zhou, "Computer-aided diagnosis of pulmonary nodules on CT scans: segmentation and classification using 3D active contours," *Med. Phys.*, vol. 33, no. 7, pp. 2323-2337, Jul 2006.
- [119] J. Yao, A. Dwyer, R. M. Summers, and D. J. Mollura, "Computer-aided diagnosis of pulmonary infections using texture analysis and support vector machine classification," *Acad. Radiol.*, vol. 18, no. 3, pp. 306-314, Mar 2011.
- [120] X. Y. Cheng, A. Ohya, M. Natori, and M. Nakajima, "Boundary extraction method for three dimensional ultrasonic echo imaging using fuzzy reasoning and relaxation techniques," in *Nuclear Science Symposium and Med. Imaging Conference*, 1993, pp. 1610-1614 vol.3.
- [121] A. Ronsenfeld, R. A. Hummel, and S. W. Zucker, "Scene labeling by relaxation operations," *IEEE Trans. on Systems, Man and Cybernetics*, vol. 6, no. 6, pp. 420-433, 1976.
- [122] S. W. Zucker, R. A. Hummel, and A. Ronsenfeld, "An application of relaxation labeling to line and curve enhancement," *IEEE Trans. on Comput.*, vol. C-26, no. 4, pp. 394-403, 1977.
- [123] E. H. Mamdani, "Application of fuzzy logic to approximate reasoning using linguistic synthesis," *IEEE Trans. on Comput.*, vol. C-26, pp. 1182-1191, 1977.
- [124] L. A. Zadeh, A theory of approximate reasoning. in *Machine Intelligence*, vol. 9, J. Hayes, D. Michie, and L. I. Mikulich, Eds. New York: Wiley, 1979, pp. 149-194.
- [125] C. Fetita, M. Ortner, P. Y. Brillet, F. Prêteux, and P. A. Grenier, "A morphological-aggregative approach for 3D segmentation of pulmonary airways from generic MSCT acquisitions," in *Proc. on Second International Workshop on Pulmonary Image Analysis, MICCAI*, 2009, pp. 215-226.
- [126] J. Serra, *Image Analysis and Mathematical Morphology*, Academic Press, London, 1982.
- [127] H. Minkowski, "Volumen und Oberfläche", *Math. Ann.*, vol. 57, pp.447-495, 1903.
- [128] L. Vincent, "Morphological grayscale reconstruction in image analysis: applications and efficient algorithms", *IEEE Trans. on Image Processing*, vol. 2(2), pp. 176-201, 1993.
- [129] M. Ortner, C. Fetita, P-Y Brillet, F. Prêteux, P. Grenier, "High-throughput morphometric analysis of pulmonary airways in MSCT via a mixed 3D/2D approach", *Proc. of SPIE Medical Imaging CAD conference*, Feb. 17, 2011.

Abstract This research focuses on the study of a specific category of non-neoplastic lung pathologies including emphysema and interstitial lung diseases (ILDs), and especially on idiopathic interstitial pneumonias (IIPs) – a variety of ILDs, and aims at developing a computer-aided diagnosis system of these pathologies exploiting the computed tomography imaging technology. The motivation of such a research comes from the increasing healthcare burden associated with this category of chronic diseases and from an unmet clinical need of efficient diagnosis and follow-up tools.

The fully automatic computer-aided diagnosis (CAD) solution developed in this thesis is based on 3-D mathematical morphology, texture and fuzzy logic analysis, and can be divided into four stages: (1) a multi-resolution decomposition scheme based on a 3-D morphological filter was exploited to discriminate the lung region patterns at different analysis scales. (2) An additional spatial lung partitioning based on the lung tissue texture was introduced to reinforce the spatial separation between patterns extracted at the same resolution level in the decomposition pyramid. Then, (3) a hierarchic tree structure was exploited to describe the relationship between patterns at different resolution levels, and for each pattern, six fuzzy membership functions were established for assigning a probability of association with a normal tissue or a pathological target. Finally, (4) a decision step exploiting the fuzzy-logic assignments selects the target class of each lung pattern among the following categories: normal (N), emphysema (EM), fibrosis/honeycombing (FHC), and ground glass (GDG).

The developed CAD system was tested on clinical routine studies including different types of emphysema and IIPs by visual inspection performed by experienced radiologists. The results obtained showed high accuracy in pathology detection with moderate discrimination between some small EM and FHC patterns. The developed solution has thus a great clinical potential in patient longitudinal follow-up and therapy design and evaluation, from which a high impact is expected on the socio-economical issues related to these pathologies.



Example of classification results obtained with the developed CAD system and illustrated using volume rendering: left - original axial CT image, right - corresponding lung patterns shown with 3-D volume rendering. Color code assignment:

N MEM EM FHC GDG HD